SYNTHESIS AND CHARACTERIZATION OF SUPPORTED SOLID ACID CATALYSTS FOR CONVERSION OF GREEN SEED CANOLA OIL TO BIODIESEL

A Thesis Submitted to the
College of Graduate and Postdoctoral Studies
In Partial Fulfillment of the Requirements
For the Degree of Doctor of Philosophy
In the Department of Chemical and Biological Engineering
University of Saskatchewan
Saskatoon

By

ANKEETA KURHADE

PERMISSION TO USE

In presenting this thesis/dissertation in partial fulfillment of the requirements for a Postgraduate degree from the University of Saskatchewan, I agree that the Libraries of this University may make it freely available for inspection. I further agree that permission for copying of this thesis/dissertation in any manner, in whole or in part, for scholarly purposes may be granted by Professor Ajay Kumar Dalai who supervised my thesis/dissertation work or, in their absence, by the Head of the Department or the Dean of the College in which my thesis work was done. It is understood that any copying or publication or use of this thesis/dissertation or parts thereof for financial gain shall not be allowed without my written permission. It is also understood that due recognition shall be given to me and to the University of Saskatchewan in any scholarly use which may be made of any material in my thesis/dissertation.

DISCLAIMER

The names of AXENS, Institut Francais du Pétrole, Evonik and Refining hydrocarbon technology were exclusively used to meet the thesis and/or exhibition requirements for the degree of doctor of philosophy at the University of Saskatchewan. Reference in this thesis/dissertation to any specific commercial products, process, or service by trade name, trademark, manufacturer, or otherwise, does not constitute or imply its endorsement, recommendation, or favoring by the University of Saskatchewan. The views and opinions of the author expressed herein do not state or reflect those of the University of Saskatchewan, and shall not be used for advertising or product endorsement purposes.

Requests for permission to copy or to make other uses of materials in this thesis/dissertation in whole or part should be addressed to:

Head of the Department of Chemical and Biological Engineering
57 Campus Drive
University of Saskatchewan
Saskatoon, Saskatchewan S7N 5A9 Canada

OR

Dean
College of Graduate and Postdoctoral Studies
University of Saskatchewan
116 Thorvaldson Building, 110 Science Place
Saskatoon, Saskatchewan S7N 5C9 Canada

ABSTRACT

Biodiesel, as a bioenergy source, is traditionally produced using alkaline catalysts which are limited to the use of refined vegetable oil feedstocks. The process tends to be environmentally non-benign because of undesired side reactions. It is important that this bioenergy is harnessed in a sustainable way. Heterogeneous solid acid catalysts can promote transesterification and esterification reactions from low-quality, unrefined feedstock without any side reactions like saponification or hydrolysis of triglycerides and minimize the effluent load downstream, thus, making them more desirable alternatives. The use of reactive and stable solid acid catalysts is one way of making the process sustainable. The primary aim of this research was to develop solid acid catalysts comprised of heteropolyacid like tungstophosphoric acid (HPW) and ordered mesoporous aluminosilicates such as MAS-7 and MAS-9. The work plan for this research was divided into five phases.

In phase one, commercial γ-alumina was tested for the heterogenization of HPW. HPW loading of 45 wt % was found to be optimum giving a methyl ester yield of 90.0 ± 2.8 wt % for biodiesel synthesis from refined canola oil under optimized reaction conditions that is 10 wt % of the catalyst loading, 17.5 methanol to canola oil molar ratio, 4 MPa, and 200°C for 10 hr. In case of biodiesel production from unrefined green seed canola oil, the methyl ester yield observed was 74.0 ± 1.9 % at the above reaction conditions. Porous oxide material with acidic properties was determined to be suitable for heterogenization of HPW. However, complete disintegration of HPW at loadings of high concentrations (55 and 65 wt %) was observed on the γ-Al_2O_3 surface and hence, reduced the catalytic activity. Therefore, to tailor their properties mesoporous aluminosilicates such as MAS-7 and MAS-9 were used as supports in the next phase.

The introduction of silica into the alumina framework has been shown to improve the textural and hydrothermal properties of alumina and hence in phase two, mesoporous aluminosilicates (MAS-7 and MAS-9) were selected as substitutes for γ-alumina as supports. A series of 5-45 wt % HPW on MAS-7/MAS-9 catalysts was prepared by a wet impregnation technique. Detailed insights into the surface chemistry of HPW supported on MAS catalysts were obtained with the help of Raman, Infrared, ^{29}Si magic-angle spinning and cross-polarization/MAS nuclear magnetic resonance (NMR), and X-ray absorption spectroscopy. The catalytic activities

were strongly correlated with the surface chemistry of the HPW supported on MAS-7 and MAS-9 catalysts. HPW supported on MAS-7 and MAS-9 exhibited favourable catalytic activity with a methyl ester yield of 76.5−88.7 wt % and stability sufficient for the simultaneous esterification and transesterification of low grade green seed canola oil. Based on this study, it was found that the MAS-7 and MAS-9 could serve as viable supports for the heterogenization of HPW.

Therefore, the main goal in phase three was to enhance catalytic performance by tuning the textural characteristics of these materials. This was achieved by the direct incorporation of HPW into aluminosilicates resulting in HPW-MAS-7 and HPW-MAS-9 composites. These composites were obtained via a facile one-step assembly between positively charged ZSM-5 precursors and negatively charged $PW_{12}O_{40}^{3-}$ species in the presence of the block copolymer. The textural characteristics of the composites were improved by introduction of HPW after the addition of an inorganic precursor to the template, leading to a material with a high BET surface area. Being novel heterogeneous solid acid catalysts, the activities of the composites were determined for biodiesel production from unrefined green seed canola oil, and yielded 95.4 ± 1.4 wt % of methyl esters in 10 h at 180 °C with 5.5 wt % of catalyst and a 15.5:1 methanol to oil molar ratio. Due to the high catalytic activity of these synthesized catalysts, it was decided to model the catalytic behaviour and investigate the techno-economic feasibility of scaling up this reaction for industrial application.

In the fourth phase, kinetic modelling, mechanistic and thermodynamic studies were undertaken using an optimized HPW-MAS-9 catalyst. The experimental data were fitted to a pseudo-homogeneous model (PH) and adsorption-based models such as Eley-Rideal (ER) Langmuir–Hinshelwood-Hougen–Watson (LHHW). The activity coefficients of the reactant and product species were estimated using the UNIQUAC method. The Eley-Rideal reaction pathway with the surface reaction of adsorbed methanol as the rate controlling step, was found to be a reliable representation of the observed kinetics.

In the fifth phase, techno-economic feasibility and life cycle analyses were conducted based on the results obtained in phase three. The economic analysis was performed using both deterministic and stochastic models. With the inclusion of tax incentives, the biodiesel selling price is approximately equal to $ 1.2 /kg and has a positive net present value (NPV) and an internal rate of return 25%. The results of these investigations revealed that the valorisation of green seed canola

oil can be achieved by using HPW-MAS-9 catalyst; provided that there are appropriate incentives for the production of biodiesel.

This research demonstrated that HPW-MAS-9 was not only an efficient heterogeneous catalyst for biodiesel synthesis, but also a material with tunable physicochemical properties that have potential relevance for industrial catalysis.

ACKNOWLEDGEMENTS

I would like to convey my sincere appreciation and gratitude to my PhD supervisor, Dr. Ajay Kumar Dalai, for his significant guidance, supervision and support during my doctoral study. I am also grateful for his encouraging mentorship in putting the best forward.

Also, I would like to express my deepest appreciation to the members of my advisory committee: Dr. Jafar Soltan, Dr. Catherine Niu (Department of Chemical and Biological Engineering), Dr. Yongfeng Hu (Canadian Light Source, Inc.), and Dr. Robert T. Tyler (College of Agriculture and Bioresources) for their thorough review, constructive comments and suggestions that helped to improve the quality of this research work.

I would also like to extend my thanks to Mr. Richard Blondin, Mr. R. Lee Prokopishyn, and Miss Heli Eunike for their technical assistance in the laboratory. Special thanks to Mr. Majak Mapoiur for his assistance in coding and insightful discussions. I am also grateful to Dr. Jianfeng Zhu (Saskatchewan Structural Sciences Centre) for helping with the NMR analysis. Funding from Natural Sciences and Research Council of Canada (NSERC) and Canada Research Chair Program is widely acknowledged.

I am profoundly indebted to my mother, Mrs. Rekha Kurhade, for being my inspiration and motivation throughout my life. I would like to thank her and my father, Mr. Hemantkumar Kurhade, and my brother, Mr. Sagar Kurhade, for their moral assistance and deep faith in me.

Special thanks to Mr. Bhavesh Patel (Diversey India Pvt. Ltd.) for his practical suggestions and motivation for a positive outlook toward this degree. My deepest appreciation goes to my friends for their kindness and support and always being there for me. Sincere thanks to colleagues in the Department of Chemical and Biological engineering for their excellent collaboration and support.

DEDICATION

Dedicated to

My dear brother, Mr. Sagar Kurhade and beloved parents, Ms. Rekha Kurhade and Mr. Hemantkumar Kurhade, who believed in me and encouraged me throughout the program.

TABLE OF CONTENTS

LIST OF TABLES

LIST OF FIGURES

LIST OF ABBREVIATIONS

APEA	Aspen process economic analyzer
ASTM	American society for testing and materials
BET	Brunauer-Emmett-Teller
CEPCI	Chemical engineering plant cost index
DBEP	Discounted break-even point
DCFROR	Discounted cash flow rate of return
DG	Diglyceride
ER	Eley-Rideal
FCI	Fixed capital investment
FFA	Free fatty acid
FT-IR	Fourier transform infrared spectroscopy
GL	Glycerol
GHG	Greenhouse gas
GSC	Green seed canola
HPA	Heteropolyacid
HPW	Tungstophosphoric acid
HPW/γ-Al_2O_3	HPW impregnated on gamma alumina
HPW/MAS	HPW impregnated on aluminosilicates MAS-7 or MAS-9
HPW-MAS	HPW incorporated in aluminosilicates during synthesis
LHHW	Langmuir-Hinshelwood-Hougen–Watson
MATLAB	Matrix laboratory
MG	Monoglyceride
MeOH	Methanol
NPT	Net payout time
NPV	Net present value
ODEs	Ordinary differential equations
PH	Pseudo-homogenous

^{29}Si CP/MAS NMR	Silicon cross polarisation ‑magic angle spinning nuclear magnetic resonance
TEM	Transmission electron microscopy
TG	Triglyceride
UNIQUAC	Universal quasichemical
XANES	X-ray absorption near edge spectroscopy
XAFS	X-ray absorption fine structure
XRD	X-ray diffraction

LIST OF NOMENCLATURES AND SYMBOLS

Nomenclatures

$^{[4]}$Al	Tetrahedral co-ordinated aluminium
$^{[6]}$Al	Octahedral co-ordinated aluminium
A	Pre –exponential factor
C_i	Concentration of component *i*, mol/L
$C_i\,(t)$	Concentration of component *i* at time *t*, mol/L
$C_i^{Exp}(t)$	Concentration of component *i* obtained from the experiments at time t, mol/L
[DG]	Diglyceride bulk concentration
E_a	Activation energy, kJ/mol
$\Delta G^{\ddagger}$	Free energy of activation, kJ/mol
$\Delta G^{0}_{R,T}$	Standard enthalpy change
[GL]	Glycerol bulk concentration
$\Delta H^{\ddagger}$	Enthalpy of activation, kJ/mol
h	Planck's constant, J. s.
ΔH^{0}	Standard enthalpy change
$\Delta H^{\ddagger}$	Enthalpy of activation, kJ/mol
$[i]$	Activity of the component *i*, mol/L
K_{eq}	Equilibrium constant for the overall transesterification reaction, dimensionless
k_1, k_3, k_5	Forward reaction rate constants for elementary reaction
k_2, k_4, k_6	Reverse rate constant for elementary reaction
K_{GL}	Equilibrium adsorption constant of glycerol
K_{DG}	Equilibrium adsorption constant of diglyceride
K_{eq}	Equilibrium constant for the overall transesterification reaction, dimensionless
K_{MG}	Equilibrium adsorption constant of monoglyceride
K_{MeOH}	Equilibrium adsorption constant of methanol
K_{ME}	Equilibrium adsorption constant of methyl ester
k_{MeOH}	Rate constant for methanol

K_{TG}	Equilibrium adsorption constant of triglyceride
k_B	Boltzmann constant J/K
l_i	A group of parameters
$\ln \Gamma_p^{(i)}$	Residual coefficient of group p with same type of molecules
[MG]	Methanol bulk concentration
[MeOH]	Methanol bulk concentration
[ME]	Methyl ester bulk concentration
n_1	No of parameters in model 1
n_2	No of parameters in model 2
N	No of experimental points
n_{DG_0}	Initial moles of diglyceride
n_{DG_i}	Moles of diglyceride at time = *t*
n_{MG_0}	Initial moles of monoglyceride
n_{MG_i}	Moles of monoglyceride at time = *t*
$nspc$	Total number of species
n_{TG_0}	Initial moles of triglyceride
P_{12}	Statistical criteria to compare model 1 and model 2
r_{DG}	Consumption rate of DG, mol/L
r_{GL}	Rate of generation of GL, mol/L
r_{MG}	Consumption rate of MG, mol/L
r_{ME}	Rate of generation of ME, mol/L
r_{MeOH}	Rate constant for methanol
r_{TG}	Consumption rate of TG, mol/L
ΔS^0	Standard entropy change
$\Delta S^{\ddagger}$	Entropy of activation, kJ/mol, K
T	Temperature of reaction in kelvin
x_i	mole fraction of the species *i*

Greek letters/symbols

$\boldsymbol{\gamma}$	Gamma
γ_i	Activity coefficient of species
γ_i^C	Combinatorial factor
γ_i^R	Residual factor
$\Psi_{m,p}$	Group interaction factor
Φ_i	Segment fraction
Γ_p	Residual group activity

GLOSSARY OF TERMS

Activity coefficient	A factor taken into account when the mixture of chemical substances deviates from an ideal behavior.
Chi-square	Defined as the ratio of the residual sum of squares of the errors between simulated and experimental values for concentration of species.
Catalyst wt %	Weight of the catalyst charged to the reactor based on the weight of oil.
Eley Rideal (ER) mechanism	This mechanism assumes that one of the reactants must be adsorbed on the catalyst in order to react. The reaction occurs by the other reactant passing by and interacting with the one on the surface.
HPW wt % loading	Weight of HPW/(Weight of HPW + Weight of support)
Langmuir-Hinshelwood	It is assumed that all reactants must be adsorbed on the catalyst in order to react.
Pseudo-homogeneous model	The model does not explicitly account for the presence of a heterogeneous catalyst in the reaction mixture.
P_{12} criterion	$P_{12} = \frac{\chi_1^2/(N-n_1)}{\chi_2^2/(N-n_2)}$, χ_1^2 and χ_2^2 in the equation are Chi-square. n_1 and n_2 represents the number of constants or parameters , for model 1 and 2. If $P_{12} < 1$, model 1 fits the data better compared to model 2 and vice a versa.
Pearson coefficient	The Pearson correlation coefficient is used to measure how two variables are linearly related and denoted by 'r'. r may range from -1 to 1. r = -1 suggests a negative linear relationship, r = 0 shows no linear relationship, and r = 1 suggests a perfect positive linear relationship.

Transition state	The configuration of highest potential energy along the path of lowest energy between reactants and products. Also, known as activated complex.
UNIQUAC method	Activity coefficient model used in description of phase equilibria.

CHAPTER 1

Introduction and Thesis Outline

1.1 Introduction

Efforts to develop clean technologies has been under progress worldwide, sparked by climate change and energy security. Energy contributes to two-third of the total greenhouse gas emission and 80% of CO_2 among the greenhouse gases. There was a growth in carbon emissions in 2018, relative to average of the previous five years as an outcome of the increase in energy demand. The increase in energy demand was majorly met by the fossil sources. Asia Pacific and North America regions were the main contributors to carbon dioxide emissions in 2018, accounting for 49.4% and 18.2% of total CO_2 emissions. Emissions were primarily due to the use of gas, oil and coal for combustion associated operations (BP statistical review of world energy, 2019). Oil consumption is heavily concentrated in Asia Pacific and North America and together, these regions account for 60% of the global consumption. Oil continues to be the most used fuel in the energy mix. The share of natural gas increased to 24% in 2018, whereas renewable contribution is just 4%. The consumption of the renewable power grew by 14% in 2018, contributing to 9% of world's electricity (BP statistical review of world energy, 2019). The share of the renewables in final energy usage is projected to be 18% by 2040, if progress continues at the same pace (https://www.iea.org/renewables2018/). This share is considerably below 28% benchmark for the IEA Sustainable Development Scenario. Renewables are essential for the decarbonisation process but are unlikely to be enough. In order to accelerate transition to a low-carbon energy system set out in the Paris-climate objectives, the development of renewable energy in the thermal, electricity and transport sectors must also be accelerated. Renewables in the transport sector come from biofuels and cover only a small share as compared to the electricity, power, and heat sectors. The growth in the biofuel sector is essential for the decarbonisation of the transport sector.

Energy derived from the conversion of biological material into gaseous or liquid biofuel is called bioenergy. Only bioenergy that reduces lifecycle GHG emissions has a future in decarbonisation energy system under favourable market and policy conditions. Hence, sustainability is key to the growth of bioenergy–as solid, liquid or gaseous biofuel. Advanced biofuels are produced from non-food feedstock. They usually offer significant reductions in greenhouse gas emissions compared to fossil fuels and standard biofuels. Amongst the biofuel synthesis route, the catalytic conversion of the vegetable oil to liquid transportation fuel is called the transesterification route. In this route, the higher alcohol, i.e. glycerol moiety in triglyceride is substituted by a lower alcohol such as ethanol or methanol in presence of catalyst resulting in alkyl ester of long chain fatty acid termed as biodiesel and glycerol as a by-product.

Commercial technologies for biodiesel production like the one from Refining Hydrocarbon Technology involves esterification of free fatty acids (FFA) using an acid catalyst. Later, the transesterification reaction is carried over a fixed bed of solid alkaline catalysts. However, the main problem associated with solid alkaline catalysts is leaching of catalytic active sites into glycerol (Busca, 2014). Institut Francais du Pétrole has developed an EsterFipH process for transesterification reaction using solid catalysts based on zinc aluminate (Scharff et al., 2013). The main advantage of the process is that it produces high quality glycerol but requires partially refined vegetable oil in order to avoid operating problems (Scharff et al., 2013).The alkaline catalysts are particularly suitable for refined oils with low FFA content. The process tends to be uneconomical because of high feedstock cost and undesired side reactions. On the contrary, heterogeneous solid acid catalysts, promote transesterification and esterification reaction from low-quality, unrefined feedstock without any side reactions like saponification; thus, making them more desirable alternatives. In solid acid catalysis, keggin–type heteropolyacid (HPW, chemical formula - $H_3PW_{12}O_{40}$) are an interesting class of compounds with superacidity and versatile structure (Noshadi et al. 2012; Grinenval et al. 2010). Heteropolyacids (HPAs) readily dissolve in polar solvents in their native form. Substantial efforts have been made to improve their chemical stability by dispersing them over traditional metal oxide supports. However, development of these heterogeneous solid acid catalysts for the production of biodiesel to meet the industrial demand

remains a daunting task in terms of the stability, surface properties and catalytic performance and hence, comprises the major part of this research work.

Technological developments in catalyst and reactor design are essential to utilize potential low grade feedstock for the sustainable biodiesel production. The use of stable and active catalysts is the preferable option owing to improved efficiency process by minimal waste generation, product quality and easy catalysts recovery.

The background of the research is explained in terms of the literature review present in the chapter 2.

1.2 Knowledge gaps

Literature review (Chapter 2) carried out for the biodiesel production using the solid acid catalyst showed the knowledge gaps as mentioned below:

1. There are limited reported studies on interaction of support γ-Al_2O_3 with heteropolyacid for the biodiesel production.
2. Mesoporous aluminosilicates MAS-7 and MAS-9 are yet to be studied as support for heteropolyacids. Research using HPW supported on MAS-7 or MAS-9 is non-existent.
3. Direct incorporation of HPW in the synthesizing step of MAS-7 and MAS-9 is unexplored. The influence of HPW introduction on catalysts properties and the catalytic activity for the biodiesel production is yet to be investigated.
4. Kinetics for HPW-MAS catalysed transesterification reaction is unknown.
5. Techno-economic and life cycle assessment for biodiesel process from green seed canola oil (FFA content -5.5 wt %) using HPW – MAS catalysts is undetermined.

1.3 Hypotheses

Based on the above knowledge gaps, the hypotheses are stated below

1. It is anticipated that the interaction between HPW and γ-Al_2O_3 with varying HPW loading would affect the physicochemical structure of the catalysts and the catalytic activity for biodiesel synthesis.
2. MAS-7 and MAS-9 supports would be expected to have a strong interaction with HPW leading to minimal/no leaching of HPW anions. Also, they too have an ordered mesoporous

structure and hence, would have limited diffusion and could provide the fine dispersion of HPA on MAS-7 and MAS-9 and a strong acidity favoring the biodiesel production with minimal deactivation of catalyst.

3. Direct synthesis approach would influence the morphological and textural characteristics, which in turn will influence the activity.
4. Kinetic study would provide insights to actual mechanism of HPW-MAS catalysts for biodiesel synthesis.
5. The techno-economic analysis and life cycle study would help in assessing the economic, commercial viability and sustainability of the biodiesel synthesis from green seed canola oil using HPW-MAS catalysts.

1.4 Research objectives

The principle research objective of this Ph.D. work is to develop novel heterogeneous supported solid acid catalysts for esterification and transesterification reaction for biodiesel synthesis. To meet the overall objectives the research step includes the synthesis of supported heterogeneous acid catalyst with Brønsted and Lewis acidities, improved hydrothermal stability and surface area. The following phases describe the sub-objectives of the research work.

Phase 1: *To investigate γ-Al_2O_3 as a support for HPW using characterisation techniques and test its catalytic activity for biodiesel synthesis*

- Preparation of a series of HPW supported γ-Al_2O_3 catalysts with varying HPW loading, catalysts characterisation, and catalyst preparation

Phase 2: *To investigate mesoporous aluminosilicate supports MAS-7 and MAS-9 for dispersion of HPW and catalytic performance for biodiesel production*

- Synthesis of supports MAS-7 and MAS-9 from zeolite β and ZSM-5 precursor solution respectively. Preparation of supported HPW-MAS-7/MAS-9 catalysts.
- Characterization of the supports and catalysts, catalytic performance and stability.

Phase 3: *Develop hybrid catalysts comprising of HPW and mesoporous aluminosilicates MAS-7 and MAS-9 via hydrothermal synthesis*

- Inclusion of $H_3PW_{12}O_{40}$ and mesoporous aluminosilicates MAS-7 and MAS-9 formed from zeolite beta and ZSM -5 using block copolymer template.
- Ascertaining structural features of developed catalysts with the help of characterization techniques and correlating with the activity for biodiesel synthesis.

Phase 4: *Conduct kinetic studies for the best catalysts for the transesterification reaction to produce biodiesel*

- Develop kinetic model for the transesterification reaction using the best catalysts at the optimized reaction conditions.
- Investigate thermodynamic parameters and deduce reaction mechanism.

Phase 5: *Conduct techno-economic and life cycle assessment for heterogeneous catalysed reaction*

- Design, develop and simulate biodiesel process using Aspen Plus V10 and conduct techno-economic analysis.
- Conduct life cycle assessment the heterogeneously catalysed biodiesel synthesis from green seed canola oil using SimaPro 9.0.

1.5 Organisation of the thesis

This PhD thesis is structured according to the manuscript-style thesis guidelines of College of Graduate and Postdoctoral studies. The introduction to subject matter and background of the research in terms of literature survey are given in Chapters 1 and 2, respectively. A substantial portion of the dissertation consists of published manuscripts. The manuscripts were drafted and presented after the completion of the corresponding stages to peer reviewed publications. The manuscripts described in the Chapters 3, 4, 5, and 6 were all published in various journals. It is intended that manuscript for Chapter 7 be prepared and submitted to journal for possible publication. Chapter 8 provides the overall conclusions and suggestions from this research study. The references for all the Chapters are collected in the reference section as well as the appropriate additional information are provided in the parts of appendices.

1.6 Manuscript content of the thesis

The subject of each Chapter and how it addresses the research goals of the thesis are described below. It is important to note that the use of manuscript–style theses can result in overlap between parts of the materials. Efforts to minimize such possible redundancies have been made.

The first phase of the study examined γ-Al_2O_3 as a support for HPW owing to its high mechanical strength and large volume open mesoporosity. HPW/γ-Al_2O_3 catalysts were prepared using a wet impregnation method with varying loadings of HPW (5-65 wt %) and characterized for their physicochemical properties. The performance of HPW/γ-Al_2O_3 catalysts was studied via the transesterification of canola oil to yield methyl esters. Optimum HPW loading on γ-Al_2O_3 as well as optimum reaction conditions for the biodiesel synthesis have been established. The outcomes and findings from this phase of the work are detailed in Chapter 3 as a published manuscript. However, the catalytic activity of the catalyst for the transesterification of green seed canola oil was not high enough and it was hypothesized that adding silica would help tailor the support properties to improve the activity of catalysts.

Mesoporous MAS-7 and MAS-9 aluminosilicates assembled from zeolite β and ZSM 5 respectively, combine the advantages of both mesoporous materials (large pores) as well as hydrothermal stability and zeolites (strong acidity). It is essential to consider support stability while preparing supported acid catalysts and is desirable in catalytic application. In consideration of this, in phase two of this research, MAS-7 and MAS-9 supports were regarded to be another option for HPW heterogenization. The main focus of this phase was to test the viability of mesoporous aluminosilicates such as MAS-7 and MAS-9 as the supports for HPW and to gain insights into the surface chemistry of the catalysts when HPW is deposited on MAS-7 and MAS-9 supports and their influence on the transesterification reaction. The details are given as published manuscript in Chapter 4.

To meet the demands of industrial application, the need to further optimize these HPW-aluminosilicate catalysts with the goal of enhancing reactivity towards simultaneous esterification and transesterification reaction was important. Therefore, Phase 3 research was conducted to enhance the catalytic efficiency of this material by tuning the physicochemical characteristics through the synthesis technique. To achieve this goal, composites were synthesized through a facile one-step assembly in the presence of block copolymer template. Efforts were made to obtain stable

and reactive mesoporous composite with the improved catalytic performance. Chapter 5 presents the results and outcomes are presented as a published manuscript.

The kinetic and reaction mechanism for the transesterification of unrefined green seed canola oil using the best catalysts was studied in the fourth phase of this research. A less complicated Pseudo-homogenous (PH) and adsorption –based models such as Langmuir-Hinshelwood-Hougen–Watson (LHHW) and Eley-Rideal (ER) are explored to possibly determine the rate-controlling step. In relation to reaction kinetics, on the grounds of statistical analysis, the thermodynamic parameters for the stepwise transesterification processes are also assessed using the best model. Chapter 6 discusses the results of this research as published manuscript.

Chapter 7 offers an assessment of the economic feasibility and the life cycle of the heterogeneously catalysed biodiesel process using green seed canola oil as a feedstock. The discussion and overall conclusions are presented in Chapter 8. This Chapter also discusses the scope for future work as a recommendation section followed by list of references. From this research, it was shown that the biodiesel can be produced from green seed canola oil using MAS-9 supported HPW catalysts with an efficiency of 95.4 ± 1.4 wt % and the process can be scaled up for the industrial application if adequate incentives are present.

Additional data related to this research is provided in Appendix A. Aspen plus simulation outcomes for biodiesel plant are given in Appendix B. Calculations for catalysts synthesis and calibration curves for GC and HPLC are given in Appendix C and Appendix D, respectively. Appendix E provides the code for Matlab programming. The sample calculations for absence of external and internal mass transfer limitations, BET surface area, and activity coefficients using UNIQUAC method are provided in Appendix G, H, and I, respectively.

CHAPTER 2

Literature Review

Contribution of this chapter to overall study

This section gives an overview of the current scenario for biodiesel production, application of various types of solid catalysts; supported metal oxides in particular, to identify the most suitable supports, acid catalysts and the most efficient parameters for catalytic efficiency.

2.1 Introduction

Biodiesel is a global, commonly used and viable, sulphur-free, biodegradable and non-toxic fuel substitute for diesel. Sodium methylate solution is the most commonly used biodiesel catalysts. Sodium methylate solution catalyst accounted for 82.9% of production share in 2016. This share will rise over the next five years as expected by biodiesel catalysts market report 2019. Evonik is one of the major players in the global biodiesel catalyst sector with 30% sodium methylate solution in methanol as the leading transesterification catalysts for biodiesel synthesis. The alkaline catalysts, however, are compatible with the oil, preferably with FFA content less than 1 % (Pruszko, 2015).

To date, the production of biodiesel by homogenous and solid alkaline catalysts dominates the present industries. The zinc-aluminate-based Esterfip^{TM} technology created by French business AXENS has been introduced in large-scale plants in France, Malaysia, Sweden and the USA. These plants are equipped with fixed-sheet adiabatic tower reactors with a catalyst divided into two areas and equipped with instruments to ensure a homogeneous combination and plug-flow. The nature and quality of the feedstock limit the design and operation of these reactors (Dimian and Rothenberg, 2016). The technology is suitable for conventional vegetable oils with low FFA content. Also, the robustness of the catalysts, is the main problem here as the method utilizes large quantities of catalysts.

Despite excellent technological accomplishments in recent years, the catalysts type and its particular design are still fraught with many difficulties. Deep insight into catalysis for biodiesel production and optimum operating conditions remains cutting-edge research.

2.2 Biodiesel process and reaction mechanism

Biodiesel is a C_{12} –C_{22} blend of monoalkyl fatty acid esters (FAMEs) (Su and Guo, 2014). Biodiesel is produced in the presence of a catalyst by transesterification/esterification of triacylglycerol (present in vegetable oils) or fats using short-chain alcohol such as methanol or ethanol. As illustrated in Eqs. 2.1, 2.2, and 2.3, the transesterification of triglyceride into fatty acid alkyl esters occurs in three successive reversible reactions, resulting in diglyceride (DG), monoglyceride (MG) and then FAME (Zabeti et al., 2009). Stoichiometrically, the ratio of oil to alcohol is three moles of alcohol per mole of oil. Hence, the molar excess of alcohol favors the formation of esters by shifting the equilibrium according to Le Chatellier's principle. For each transformed TG mole, the total net reaction is 3 mol of alkyl fatty acid esters and 1 mol of glycerol (Eq. 2.4). If free fatty acids (FFAs) are present in the feedstock, FFAs undergo esterification reaction to produce FAMEs. These reactions can be performed either through non-catalytic or catalytic procedures. Non-catalytic transesterification process is slow and usually requires high temperature and pressure for the completion (Zabeti et al., 2009). Catalytic transesterification can either proceed via base catalyzed mechanism or acid catalyzed mechanism.

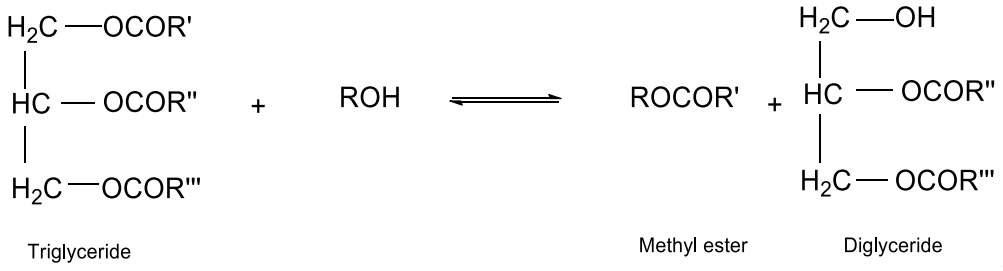

Triglyceride Methyl ester Diglyceride .…….(2.1)

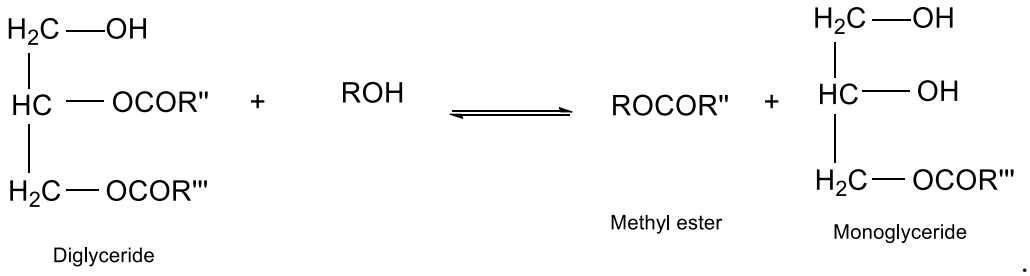

Diglyceride Methyl ester Monoglyceride ……(2.2)

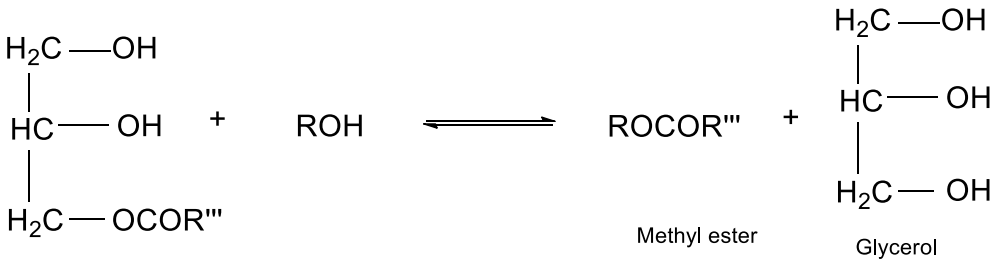

……..(2.3)

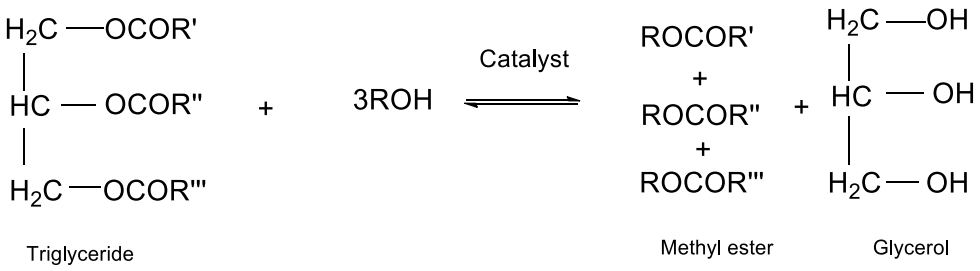

……(2.4)

2.2.1 Reaction mechanism

Uncatalyzed

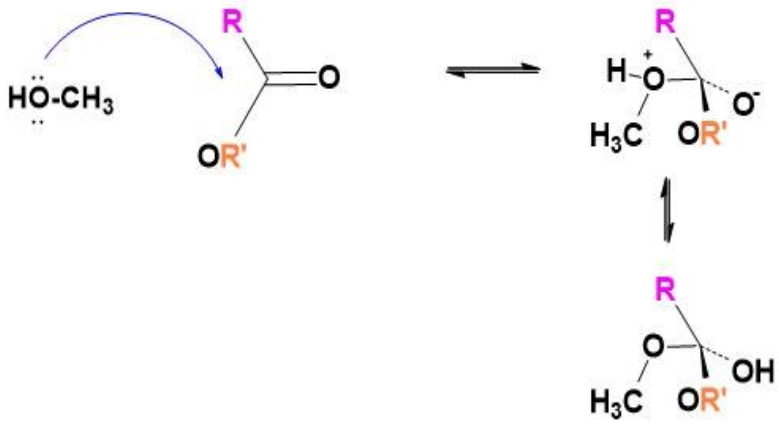

Figure 2.1. Uncatalyzed reaction mechanism.

Figure 2.1 illustrates the uncatalyzed addition of the nucleophile methanol to a carbonyl compound. The nucleophile attack of the methanol on carbonyl compound produces a dipolar tetrahedral intermediate. Species' alternatives include return to starting materials, proton transfer to give the isomeric uncharged tetrahedral intermediate, and undergo further reaction (Maskill, 1996).

Acid-catalyzed

The nucleophile and the electrophile are both neutral in the above reaction, although they can both be polar molecules. However, a small equilibrium level of carbonyl oxygen protonation will occur in acidic environment. The carbonyl compound's conjugate acid thus formed will be much more electrophilic, i.e. much more vulnerable to nucleophile attack. The initial product of this acid-catalyzed nucleophile is the tetrahedral intermediate (Maskill, 1996).

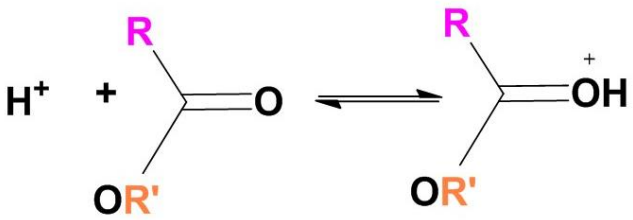

Figure 2.2. Acid- catalyzed nucleophilic addition to carbonyl compound

Base –catalyzed

A pre-equilibrium deprotonation of methanol can also achieve catalysis in order to give much more reactive nucleophile. Hence, alkaline catalysts are most widely employed for this reaction (Maskill, 1996).

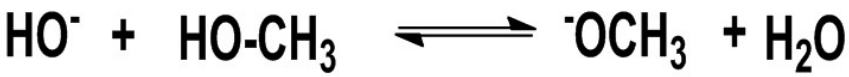

Figure 2.3. Base-catalyzed nucleophilic addition to carbonyl compound

However, feedstocks with more than 2.5 wt % FFA react with alkali catalyst resulting into soap formation. This is an undesirable reaction because the soap formation affects the biodiesel yield and in turn makes it difficult to separate esters from glycerol. It also binds to the catalyst, i.e. more catalyst will be needed, resulting in increased cost (Leung et al., 2010). Not only this, but the

water liberated during the saponification reaction can affect the transesterification by hydrolysing the triglyceride, forming more FFA. Vegetable oil/fat with FFA content over 2.5 wt % requires an additional step of pre-treatment for the removal of FFA before the transesterification reaction is carried out thereby increasing the processing cost. In addition solid alkaline catalysts, such as MgAl hydrotalcites (Benedictto et al., 2018), bamboo charcoal-based magnetic solid base catalyst (K/BC-Fe_2O_3) (Liu et al., 2018), and mixed metal oxides (CaO-MgO, CaO-La_2O_3, CaO-ZnO, and MgO-ZnO) (Lee et al., 2016) are quite effective with high conversion and biodiesel yield. However, strong adsorption of FFA, water, and formation of soap can deactivate the active basic sites. Nonetheless, leaching and related deactivation mechanisms for alkaline catalysts are still a challenge. These drawbacks associated with the alkaline catalysts limit the use of low-grade feedstocks and raise concerns about the sustainability of the process. With the use of solid acid catalysts, the above constraints regarding solid alkaline catalysts can be overcome as they can promote simultaneous esterification and transesterification reaction without saponification and hydrolysis reaction.

2.3 Solid acid catalysts

Solid acid catalysts are used for a multitude of acid-promoting processes in organic synthesis (Gupta and Paul, 2014). A large number of inorganic and polymeric solid acids for the acid-catalyzed transesterification reaction have been explored previously. Wang and colleagues explored mesoporous sulfated zirconia (MSZ550 and MSZ600) for transesterification of soybean oil and simultaneous (trans)esterification of soybean oil / oleic acid. However, the reaction of ionic sulfate species with methanol during the recycling runs resulted in catalysts deactivation (Wang et al., 2019). In case of sulfonated magnetic solid acid catalysts, Wang et al. (2019) found that calcined $Zr_{1.0}Fe_{1.0}$-CMC-SO_3H could be continuously used for the five cycles for esterification of oleic acid, with a biodiesel yield higher than 85.4%.

While the catalytic activities of solid acid catalysts are enhanced to some extent. There is a need to further enhance the catalytic activity of solid acid for frequent applications in the production of biodiesel. The heteropolyacid catalysts are common acidic catalysts and are regarded eco friendly alternatives to standard acid catalysts due to their non toxicity (Gupta and Paul, 2014; Su and Guo, 2014). HPAs have a distinct and mobile ionic framework in contrast to zeolites and metal oxides. They have high Brønsted acidity and have redox features that can be tuned by variable

chemical composition. Selective oxidation and acid catalysis are the main areas for catalytic applications of HPAs. Heteropolyacid catalytic system is primarily addressed in this subject of the thesis.

2.4 Keggin –type heteropolyacids

Heteropolyanions with keggin structures are most commonly researched as catalysts owing to their stability and ease of synthesis (Kozhevnikov, 2007; Okuhara et al., 1996). The ideal α-type keggin structure has T_d symmetry and is represented by the formula $[XM_{12}O_{40}]^{n-}$, with X being the heteroatom (Si^{4+}, P^{5+}, etc.) and M being the addendum atom (W^{6+}, Mo^{6+}, etc.). The heteropoly anion frame consists of a central XO_4 tetrahedron and is surrounded by a corner and 12 edges of a metal-oxygen octahedron (MO_6). $H_3PW_{12}O_{40}$, $H_4SiW_{12}O_{40}$ and $H_3PMo_{12}O_{40}$ are the most common HPAs. Among them, $H_3PW_{12}O_{40}$ (tungstophosphoric acid, phophotungstic acid or dodecatungstophosphoric acid) is the most stable of all HPAs and has the highest Brønsted acidity. (Moffat, 2001; Okuhara et al., 1996). Hence, in the present work $H_3PW_{12}O_{40}$ is the subject of review and henceforth the abbreviation HPW is used.

In HPW, P is located between in the center of $(PW_{12}O_{40})^{3-}$ and $12W_3O_{13}$ octahedra (4 X W_3O_{13}) is surrounded by a PO_4 tetrahedron (Chen et al., 1992). Brønsted acidity occurs when the net charge of $(PW_{12}O_{40})^{3-}$ heteropolyanion is satisfied by three protons (Yadav, 2005). In heteropolyanions, the negative charge of similar value is spread across much larger anions than those formed in mineral acids. The electrostatic interaction between the proton and anion in heteropolyacids is much less than for mineral acids.

The change in the electronic charge induced by deprotonation can spread across the whole unit. Therefore, the acid strength of the heteropolyanions is higher than mineral acids. Protons play an important part in connecting the adjacent heteropolyanions. As shown in Figure 2.4, the protons in crystalline $H_3PW_{12}O_{40}.6H_2O$ exist as $H_5O_2^+$ species which connects the adjacent heteropolyanions to terminal W-O_d oxygen atoms via hydrogen bonding (Okuhara et al., 1996).

The significant drawbacks associated with heteropolyacids involve low thermal stability and low surface area, thus the synthesis, characterization and catalytic features of HPAs, particularly supported ones have been of great importance in recent years.

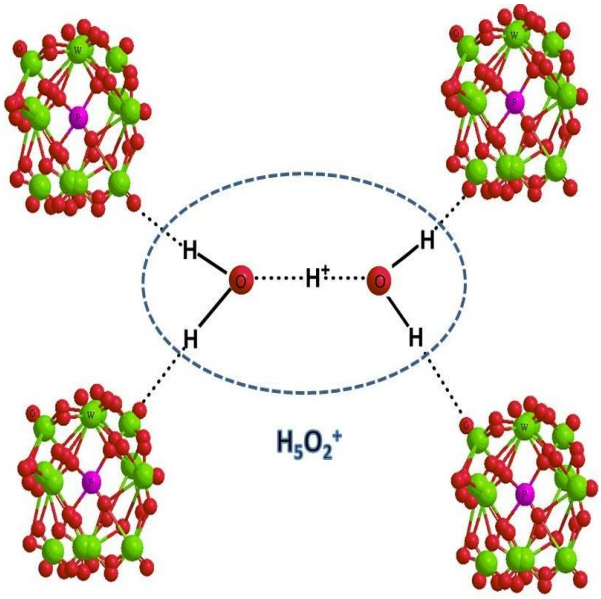

Figure 2.4. Example of secondary structure. $H_3PW_{12}O_{40}$. $6H_2O$. Each $H_5O_2^+$ bridges four polyanions (Okuhara et al., 1996).

2.5 Supports for heteropolyacids

It is essential in heterogeneous catalysis using heteropolyacids, to disperse these strong acids on a material with a large surface area. The supported heteropolyacid catalysts consist of heteropolyacid as the active phase and a support. There may be an electronic interaction between the active phase and support, which is why the support may also influence the catalytic behavior of the catalysts. The porous structure also makes it easy for the reactant or product species to diffuse in and out (Hanif et al., 2017). The most commonly used supports are metal oxides like aluminium oxides, silica gels, aluminosilicates, magnesium oxides, zirconium oxides, and titanium oxides owing to their high specific surface area, thermal and mechanical stability and large pore size.

Gopinath et al. (2018) examined Cs exchanged silicotungstic acid supported by Zr-KIT-6 (Cs-STA /ZK) solid acid catalyst for oleic acid esterification and transesterification of pongamia oil, neem oil and castor oil. The authors observed that the mesoporous nature of the catalysts could prevent Cs-STA from leaching during the recycle run. The deactivation of the catalysts after two cycles was observed, which was mainly attributed to blocking of active sites by product and reactant species. The catalyst's small pore size may have resulted in pore blockage.

Atia et al. (2008) explored silica, alumina, and aluminosilicate supports for the immobilisation of $H_3PMo_{12}O_{40}$, $H_3PW_{12}O_{40}$, $H_4SiW_{12}O_{40}$, and $(NH_4)_3PMo_{12}O_{40}$. Tungsten–based heteropolyacid demonstrated the excellent activity and stability. The authors discovered that the alumina was a better support than the silica in terms of catalytic activity and selectivity for the glycerol dehydration reaction and proposed the reason as a strong interaction between the HPAs and the support surface.

The gamma phase of alumina is primarily used as carriers (Schoenfeldt, 2008) and is preferred material due to its flexibility, tailoring structural properties, and low cost (Mochida and Choi 2006). A literature study demonstrates that only Badday et al. (2013) evaluated γ- alumina supported tungstophosphoric acid for ultrasound–assisted transesterification of crude Jatropha oil. The highest yield achieved in this research was 64.3% with 25 wt % catalyst loading and 20:1 methanol to oil molar ratio and 1 hour reaction time. The reaction time was short, which could have led to lack of contact time between the reactants resulting in low yield.

Zeolites have also been explored as a support for HPAs owing to their distinctive micropore structure and high thermal stability. In its frame work, zeolite should have a moderate number of aluminum atoms for efficient encapsulation of HPA. The cations that promote the formation of HPA precursors occupy the cation- induced sites of these aluminum atoms (Mukai et al., 2001). In the research conducted by Baroi et al. (2014) it was found that HPW loading creates hierarchal pores in the H-β zeolite framework by attaching itself to the four membered alumina and silica resulting in the breaking of the Si-O-Al bond. In addition, Baroi and Dalai (2014) found that strong acidity and thermal treatment alter the zeolite structure, which creates secondary pores from 12-300 Å, making it easier for the keggin unit with a diameter of 12 Å to be deposited in pores. In particular, silica based mesoporous materials and zeolite supported HPW were researched as a catalyst for the transesterification of biodiesel production. Maximum conversion was achieved when HPW/H-β/H-Y zeolite was used as a catalyst as compared to MCM-48 and SBA-15.

Various kinds of microporous crystal aluminosilicates, zeotypes like ZSM-5, zeolite Y, L and beta exhibit acidity. For instance, ZSM-5 is an efficient catalyst in shaped selective catalysis, while zeolite Y is an important FCC catalyst, whereas beta zeolite exhibits high activity in catalytic alkylation (Lin et al., 2004). However, H-ZSM 5, beta and Y showed poor catalytic activity in esterification due to the limited diffusion of bulky fatty acid reactants into zeolite pores (Bart et al.,

2010). It is essential to design a material with larger pores and channels with zeolites to obtain the high catalytic efficiency. In contrast to microporous zeolites, the pore diameter of the mesoporous material is between 2 and 50 nm (Mansir et al., 2017). Mesoporous materials as catalyst have been widely used for esterification reaction. Mesoporous materials like MCM-41, in particular, are not sufficiently acidic to promote esterification reactions. Pérez-Pariente et al. (2003) discovered that esterification of oleic acid with glycerol over Al-MCM-41 was less effective than that over zeolite β. In addition, low acid strength and low hydrothermal stability are the primary issues when using mesoporous material. The applications of these materials in the catalytic system where acidity plays a significant role are very limited, despite their exceptional textural characteristics.

Efforts have been made to improve the catalytic effectiveness, acidity and stability of these materials through acid modification or controlled dispersion of metal atoms. Margeta et al. (2013) synthesized hydrothermally stable Ti-SBA-15 by direct substitution of Ti into SBA-15 materials, however, the amorphous walls of these materials limit their practical applications. In addition, extra Lewis acid sites are created during synthesis due to the weakness of Brønsted acid sites. Due to this issue, the pore distinguishing properties of the catalysts are adversely affected.

Another approach to overcome this issue is to assemble protozeolitic nanoclusters into a framework structure to form aluminosilicates with mesoporosity, acidity and stability. The main benefit of this technique is that, compared to microporous zeolites, mesoporous material overcomes the constraint of zeolite pore and facilitates the diffusion of bulk molecules (Liu and Pinnavaia, 2002). The concept of using zeolites seeds as precursors for the assembly of large porous materials that are hydrothermally stable and strongly acidic has been expanded to include mesostructured hexagonal SBA-15 analog, MAS-7.

2.5.1 Supports of interest

Mesoporous aluminosilicates such as MAS-7 are assembled using beta zeolite seeds in strongly acidic media, whereas MAS-9 is assembled from ZSM-5 precursors. Compared to mesoporous materials such as SBA-15 and Al-SBA-15, the wall thickness (4-5 nm) of MAS-7 was found to be sufficient to assemble the zeolite precursors (2-3 nm) (Xiao, 2005). The mesoporosity therefore remains unchanged. The aluminum atoms are assimilated into the tetrahedral co-ordination of the silica framework similar to that seen in zeolites, thus maintaining acidity and crystallinity. Furthermore, this was verified by NMR spectra showing the existence of 4 and 6 co-

ordinated Al, indicating the incorporation of the Al species within the framework of MAS-7 (Han et al., 2001). In addition, it was found that the chemical shift of Al in MAS-7 occurred similar to that in zeolite beta, suggesting aluminium environment in MAS-7 is very similar to that of beta-zeolite. The surface area (959 m^2/g), pore volume (1.24 cm^3/g), and average pore size (7.6 nm) of MAS -7 were higher than those of Al-SBA-15 and H-beta, indicating a better catalytic performance (Lin et al., 2004).

MAS-9, which is assembled from preformed ZSM-5 nanoclusters with polymer surfactant (P123), has a thickness of 5.4 nm, higher than that of the zeolite subunit cell (~3.0 nm), thus allowing a nanometer-sized ZSM to remain in mesoporous walls, increasing stability while preserving the mesoporous structure (Liu and Pinnavaia, 2002). The IR spectrum of MAS-9 revealed the existence of five T-O-T member rings (T = Si or Al) as in zeolite crystals. In addition, MAS-9 NMR spectra confirmed the four co-ordinated Al atoms in the MAS-9 framework. These four co-ordinated Al atoms are associated with the Brønsted acid site. Comparing the pore size, micropore volume and surface area of MAS-9 with other mesoporous materials, it was found that the MAS-9 exhibited a pore size of 8 nm, micropore volume of 0.16 cm^3/g and surface area of 961 m^2/g higher than those of SBA-15 and Al-SBA-15 (Liu and Pinnavaia, 2002). The large micropore volume of MAS-9 can be ascribed to the presence of zeolite units in the mesoporous walls. The excellent textural features of these materials make them appealing to explore as the supports in catalytic systems. Together with support pore structure, the distinct structural characteristics contribute to the catalytic activity of esterification and transesterification reactions. The stability of the supported acid catalysts must be taken into consideration. N_2 isotherms and XRD results show that MAS-9 maintains an orderly hexagonal structure with a surface area of 680 m^2/g after 120 h of boiling water treatment, while SBA-15 and Al-SBA-15 lose most of their mesostructured surface area of less than 200 m^2/g (Xiao, 2005).

2.6 Preparation of supported acid catalysts

The physicochemical characteristics and catalytic effectiveness of the final catalysts (active material+ support) will depend on the preparation technique. Typically, the wet impregnation method is considered to be the most feasible technique to introduce HPAs on the supports. The impregnation method includes wetting the solid support matrix with a liquid solution comprising of dissolved metal oxide. The technique is described as dry or incipient wetness when the

impregnating solution is almost the same quantity as the pore volume of support. However, the impregnation is the wet one when surplus impregnating solution is required. Using this technique, HPAs can be highly dispersed on to the support over a large surface area to improve the catalytic performance. In case of silica support, however, there exists a weak interaction between HPAs and silica support (Atia et al., 2008). As a result, HPAs tend to leach out of support, particularly in polar media, leading to catalyst deactivation. The grafting technique could be used to immobilize HPA to prevent leaching (Ren et al., 2010). This technique could improve the reusability of the catalysts, but limitations such as decrease in the effectiveness of mass transfer still exist due to reduced pore size. The one-step template assisted path could be designed to satisfy this requirement, as detailed in Chapter 6.

2.7 Choice of feedstock

A variety of feedstocks are used for the biodiesel synthesis, ranging from standard edible and non-edible oils, used vegetable oils or animal fats (Su and Guo, 2014). Selection of feedstock is strongly dependent on local accessibility. Soybean oil is widely used in the United States and South America, whereas Palm oil is a dominant feedstock in Asian counties such as Malaysia and Indonesia (Lee et al., 2014).

Green seed in canola is a downgrading factor that causes annual losses of more than $ 150 million and is of major concern in North America. (https://www.topcropmanager.com/crushing-the-green-seed-problem-in-canola-21343/). Furthermore, finding the market for these seeds and moving off the farm has been a challenge. Green seed occurs when the chlorophyll in seed has not degraded or cleared owing to several environmental variables, the most important being frost and extreme warm dry weather. According to Canadian grain commission, No.1 canola has <2 percent green seed and < 25 ppm chlorophyll; No.2 canola contains 2-6 percent green seed and 26-45 ppm chlorophyll; No.3 canola has 6-20 percent green seed and 46-100 ppm chlorophyll; Sample canola contains > 20 percent green seed and >100 ppm chlorophyll. Only 75% of the samples were graded Canola No.1 in 2018, based on analyses of 2,505 individual canola samples from western Canadian canola provinces (Alberta-Peace River, Saskatchewan and Manitoba).

Due to high chlorophyll concentrations, the quality of oil produced from processing green seeds is compromised, making it unsuitable for human consumption. Treating the oil for the edible purpose is expensive. Oleic acid constitutes the major fatty acid in green seed canola oil composition followed by linoleate acid.

The green seed canola oil was procured from Milligan Bio-Tech Inc. (Formerly known as Milligan Biofuels Inc.), Foam Lake, Saskatchewan. The plant has their own mechanical seed crushing and extraction facility. Clean and dried seeds are conveyed into the crushing plant and run through a cold-press extraction process. The oil is filtered to remove waxes and gums. Table 2.1 shows the fatty acid composition of the green seed canola oil.

The FFA % based on the oleic acid is estimated to be 5.4 ± 1.36 based on AOCS-D6751 method. Usually, the FFA content in the refined oil is ≤ 0.05%. The peroxide value for the green seed canola oil was found to be 13.77 ± 0.94 meq/kg of oil. Green seed can be categorized as a low-quality feedstock. In present research, green seed canola oil served as the option of feedstock for biodiesel production using supported solid acid catalysts.

Table 2.1. Fatty acid composition of green seed canola oil

Fatty acid		Molecular weight	Weight fraction	Fatty acid %
C14:0	Methyl myristate	228.9	0.001	0.10
C16:0	Methyl palmitate	257.118	0.0525	5.26
C18:0	methyl stearate	285.16	0.02	2.00
C18:1	methyl oleate	283.09	0.7	70.00
C18:2	Methyl linoleate	280.44	0.1913	19.14
C18:3	Methyl linolenate	278.46	0.00628	0.63
C20:0	Methyl arachidate	312.5	0.00520	0.52
C20:1	Methyl cis-11-eicosenoate	310.5	0.01851	1.85
C22:0	Methyl behenate	340.58	0.00230	0.23
C22:1	Methyl cis-13-docosenoate	338	0	0.00
C24:0	Methyl tetracosanoate	367.38	0.00235	0.24
	Total		0.99965	99.96

2.8 Summary

Solid alkaline catalysts are mostly employed for the biodiesel production from partially refined feedstock or involves two-step (trans)esterification steps. Solid acid catalysts have significant advantages in separation, recycling, and environmental friendliness in heterogeneous acid catalyzed transesterification and esterification reactions. Numerous supports have been studied for the heteropolyacids immobilization and have been used extensively for biodiesel production as a supported solid acid catalyst. These catalysts demonstrate acceptable reactivity towards esterification and transesterification reaction. However, some constraints such as leaching and coke formation still exist when it comes to the reusability of these catalysts. In order to meet this challenge, choosing the support with large pore diameter, high surface area as well as pore volume can decrease the mass transfer limitation of the species. The electronic interaction between the support and active material can enhance the catalytic performance and prevent leaching of the active phase. The catalysts preparation routes should also be carefully designed to strengthen the interaction between support framework and active sites. Based on the aforementioned literature study, alumina and alunminosilicate supports were selected for heterogenization of HPW for this dissertation topic. To begin with γ-Al_2O_3 was used as support for the immobilization of HPW as illustrated in Chapter 3.

CHAPTER 3

Physicochemical Characterization and Support Interaction of Alumina-Supported Heteropolyacid Catalyst for Biodiesel Production

The content of this chapter has been published in Asia Pacific journal of chemical engineering cited below and presented in the following conferences:

Citation:

Kurhade, A., Dalai, A.K., 2018. Physiochemical characterization and support interaction of alumina-supported heteropolyacid catalyst for biodiesel production. Asia-Pacific J. Chem. Eng. 13, 1–13. https://doi.org/10.1002/apj.2249

Conference Proceedings:

Kurhade, A., Dalai, A.K. Alumina-supported heteropolyacid catalysts for biodiesel production: physicochemical characterisation and support interaction. 66th Canadian Chemical Engineering Conference, Quebec city, Quebec, Canada, October 16-19, 2016.

Kurhade, A., Dalai, A.K. Development of alumina and ordered mesoporous aluminosilicates-supported heteropolyacid for biodiesel production. North American Catalysis Society Meeting, Denver, United States, June 4-7, 2017.

Contribution of the Ph.D. Candidate

Experiments were designed in consultation with Dr. Ajay K. Dalai and executed by Ankeeta Kurhade. Material synthesis, catalysts characterization and data interpretation were performed out by the student. The manuscript was drafted by Ankeeta Kurhade with guidance and suggestions provided by Dr.Ajay K.Dalai.

Contribution of this Chapter to Overall Ph.D. Research

The first phase of the research is addressed in this section: to investigate γ-Al2O3 as a support for HPW using characterization techniques and test its catalytic activity for biodiesel synthesis. This section demonstrates the necessary physicochemical characteristics of the support for HPW immobilization and its effect on the catalytic activity for biodiesel production from partially refined canola oil.

3.1 Abstract

Tungstophosphoric acid (HPW) supported on γ-Al_2O_3 catalysts were prepared with varying loadings of HPW. Catalysts characteristics were assessed using BET surface area analysis, TGA, XRD, Raman, Pyridine adsorbed FT-IR spectroscopy and ^{13}C hpdec (high- power ^{1}H decoupling) NMR, while surface morphology was examined using SEM and TEM analysis. Catalysts with higher HPW loadings (55-65 wt %) showed the presence of WOx species. The catalytic activity of HPW impregnated catalysts was evaluated for biodiesel synthesis from canola oil. A methyl ester yield of 90.0 ± 2.8 % was obtained for the transesterification of canola oil (FFA content- 2.5 wt %) under the optimized conditions i.e 10 wt % of the catalyst loading, 17.5 methanol to oil molar ratio, 4 MPa and at 200 ºC in 10 hours.

3.2 Introduction

The known disadvantages of the traditional base-catalyzed transesterification reaction have attracted much attention towards the development of viable and greener chemical process with the aim of reduction in effluent generation and catalysts recovery. Owing to this, the solid acid catalysts in heterogeneous form are being preferred than base catalysts or liquid acids.

The commonly used industrial process for biodiesel synthesis is the alkali-catalyzed transesterification of triglycerides in presence of methanol (Agarwal et al., 2012; Wong et al., 2014). The major issue with the alkali catalyzed transesterification is saponification and the effluent generation, rendering it environmental non benign (Luque and Melero, 2012; Wong et al., 2014). In such a case, heterogeneous catalytic process offers several advantages over the homogenous (Patel and Narkhede, 2012) one, to enlist some, facilitation of separation and

purification steps, easy reusability of the catalyst. Considering heterogeneous solid acid catalysis, heteropoly acids (HPAs) supported on the carriers have garnered huge interest in biodiesel production because of their structural mobility and super acidity. They are supported on acidic or neutral carriers like Al_2O_3 or SiO_2 owing to their low surface area and lack of thermal stability (Atia et al., 2008). Amongst all HPAs, tungstophosphoric acid (HPW, $H_3PW_{12}O_{40}$) has a higher acidity as compared to the other HPAs (Saifuddin et al., 2015)

Supported HPAs on MCM-48, Al–MCM-48, MCM-41, and SBA 15 have been employed for synthesis of benzoic acid (Chen et al., 2014; Meng et al., 2014; Wu et al., 2014). Studies have been reported using $H_3PW_{12}O_{40}$ in supports to name a few such as Hβ, ZrO_2, SBA-15, TiO_2/SiO_2, Cs/Nb_2, as a catalyst for biodiesel production (Brahmkhatri and Patel, 2011; Kaur et al., 2018; Narkhede et al., 2015; Oliveira et al., 2010; Patel and Narkhede, 2012; Surasit et al., 2017). In addition, HPW supported on MCM-41, Al-MCM-41, 3D graphene aerogel and reduced graphene oxide have been studied for esterification of levulinic acid (M Wu et al., 2016; Min Wu, Zhao, Li, Su, et al., 2016; Min Wu, Zhao, Li, Wu, et al., 2016; Zheng et al., 2017). Atia et al. (2008) reported that alumina and aluminosilicates supported heteropolyacids are more active as compared to silica supported catalyst when investigated for glycerol dehydration. HPW supported Al_2O_3 has been explored as a catalyst for Friedel-Crafts alkylation and esterification reactions (Bhatt and Patel, 2011 ; Sharma et al. 2004). It was reported that HPW can be supported on alumina for esterification reactions however, the catalysts have not been explored to their fullest potential for biodiesel synthesis.

γ- Alumina itself possess large volume open mesoporosity and acidic catalytic behavior due to the presence of the surface hydroxyl groups (Schoenfeldt, 2008; Sinkler et al., 2006). Typically, it is the acidic behavior of these hydroxyl groups which can be utilized for the immobilization of the substance on to the alumina surface. In addition, it is widely produced, easily accessible, and economically feasible.

Therefore, HPW supported γ-Al_2O_3 catalyst was examined for biodiesel production. The synthesized catalysts were characterized for XRD, Raman and Pyridine adsorption FTIR to know the keggin anion environment on γ-Al_2O_3 surface. The textural and thermal analysis of all the synthesized catalysts were performed. The optimum reaction parameters were deduced using factorial and response surface methodology. An attempt was made to relate the activity of the

synthesized catalysts with the catalysts' physicochemical properties such as HPW loading, Brønsted to Lewis acidic site band (B/L) ratio and surface area of the catalysts.

3.3 Experimental section

3.3.1 Materials

Tungstophosphoric acid ($H_3PW_{12}O_{40}$. H_2O, HPW) and γ-Al_2O_3 were acquired from Alfa-Aesar, Massachusetts, USA. Methanol (99.9%), was supplied by VWR, Mississauga, Ontario, Canada.

3.3.2 Catalysts preparation

Catalysts containing 5-65 wt % of HPW supported on γ-Al_2O_3 were prepared by wet impregnation method. 3 g of support was impregnated with HPW using methanol as a solvent (4 mL/g of support). The catalysts were allowed to air dry overnight. The dried catalyst was then calcined at 450 °C. The catalysts are denoted as M wt % HPW/ γ-Al_2O_3 in which the values of M were 5, 15, 25, 35, 45, 55 and 65.

3.3.3 Catalyst characterization

The catalysts physicochemical properties were determined by Micrometrics equipment (Model ASAP 2000). Before the analysis, the sample was degassed at 200 ºC. Brunauer-Emmett-Teller (BET) method was used to calculate the surface area, whereas BJH method was employed for pore volume and diameter. The catalysts thermal stabilities were assessed by Thermo Gravimetric Analyses (TGA) using TGA Q analyzer. Raman analysis was carried out using Raman Invia Reflex Raman microscope spectrometer (785nm).

The X-ray diffraction (XRD) patterns were obtained on an Advance diffractometer (Bruker D8) with Cu *Kα* radiation. The crystallite size was calculated using Scherrer's equation (Cullity and Stock, 2001)

$$d = k\lambda/\beta cos\theta \quad \text{(3.1)}$$

Where k is the crystallite shape constant (≈0.94, assuming the spherical powdered crystal), β is the reflection width the wavelength of X-ray source and θ is the Bragg angle.

Scanning electron microscope depictions were recorded on FE-SEM-cold field emission scanning electron microscope (Hitachi SU8010). TEM analysis was carried out on Hitachi HT7700 TEM instrument with accelerating voltage 80 kV. Methanol was used as a solvent to disperse the sample. Solid state^{13}C NMR hpdec studies of pyridine adsorbed on HPW/γ-Al_2O_3 were carried out. ^{13}C spectra's were recorded at a carbon frequency of 125.75 MHzon Avance NMR spectrometer with a spinning rate of 10 kHz and pulse repetition time of 4s.

The total surface acidity of the catalysts was calculated using acid –base titration. 0.1 g of catalysts in 20 mL of 0.1 M NaOH was agitated for 3 hours at room temperature to allow ion exchange. After centrifugation, the suspension was titrated with 0.1 M HCl in presence of phenolphthalein indicator. The surface acidity was expressed in mol of H^+/g of catalyst.

3.3.4 Catalytic activity study

The performance of the catalysts was studied via the transesterification of canola oil (containing 2.5 wt % FFA) in a Parr reactor. 35 g of canola oil in the reactor was first pre-heated to 50 °C followed by addition of catalysts and methanol into the reactor. The pressure of the system was maintained at 4 MPa. The reactor was pressurized using N_2 inert gas. The screening reaction parameters of 3 wt % catalyst (based on weight of canola oil), 20:1 methanol to oil molar ratio at 200 °C and a reaction time of 10 h based on the literature (Baroi and Dalai, 2012) were selected for the optimization study.

The product was analyzed using HPLC (Agilent Technologies 1100 series) equipped with a PL gel column. 5μm two Phenogel column (100 Å 300 × 7.80) connected in series were used for the analysis. The mobile phase THF was introduced for 20 min at 1 mL/min. The sample was injected at a volume of 20 μL, whereas the detector temperature, and column temperature was kept at 35 °C and 24 °C (Baroi and Dalai, 2012). The ester yield (wt %) was determined using Eq. (3.2)

$$Ester\ yield\ (wt.\%) = \frac{methyl\ ester\ weight}{Weight\ of\ oil\ phase} \times 100 \quad \text{.....(3.2)}$$

The triglyceride (TG) conversion was calculated using Eq (3.3)

$$TG\ conversion\ (\%) = \frac{TG_{Eq.}(t)}{TG_{Eq.}(t=0)} \times 100 \quad \text{..... (3.3)}$$

$$TG\ equivalent\ = Triglyceride + \frac{2}{3}\ Diglyceride + \frac{1}{3} Monoglyceride + \frac{1}{3}\ Free\ Fatty\ acid$$

The catalysts were studied in successive reaction runs. The catalysts were filtered from the reaction mixture and solvents like hexane and methanol were used for removal of the polar and non-polar compounds.

The turnover frequency (TOF) was deduced as per the equation (Patel and Narkhede, 2012)

$$TOF = \frac{Moles\ of\ reacted\ substrate}{moles\ of\ catalysts \times time\ of\ reaction} \quad \text{..... (3.4)}$$

3.4 Results and discussions

3.4.1 Textural properties of catalysts

Table 3.1. Surface characteristics of γ-Al_2O_3 and HPW/ γ-Al_2O_3

Catalyst	BET surface area (m^2/g)[a]	Total pore volume (cm^3/g)[b]	Average pore size (nm)[c]	Keggin anion density (nm^{-2})[d]	Total Surface acidity (moles of H^+/g of catalyst)
γ-Al_2O_3	256	0.73	7.5	0.0	12.5±0.46
5 wt % HPW/ γ-Al_2O_3	233	0.65	7.0	0.04	13.6
15 wt % HPW/ γ-Al_2O_3	227	0.56	6.1	0.14	13.6
25 wt % HPW/ γ-Al_2O_3	215±3	0.57±0.01	6.4±1.3	0.24	13.9
35 wt % HPW/ γ-Al_2O_3	205	0.52	6.2	0.36	14.1
45 wt % HPW/ γ-Al_2O_3	192±6	0.39±0.04	6.9±0.9	0.50	14.4
55 wt % HPW/ γ-Al_2O_3	155	0.33	6.3	0.74	13.5
65 wt % HPW/ γ-Al_2O_3	119	0.21	7.0	1.14	13.9

[a]specific surface area calculated by the BET method; [b]From BJH desorption method; [c]From BJH desorption method; [d]Keggin anion density

$$= [HPW(wt\%)/100] \times 6.02 \times 10^5 / [BET surface\ area\ (m^2/g) \times 2880.2]$$

Typical isotherms for N_2 gas adsorption–desorption for γ-Al_2O_3 and HPW supported γ-Al_2O_3 are given in Figure 3.1.The catalysts exhibited IV type of isotherms as per IUPAC

nomenclature, likely characteristic of mesoporous materials and exhibited H1 hysteresis loop (Hernández-Cortez et al., 2010).

This type of hysteresis loop can considered to be due to adsorption in unconnected pores with a relatively narrow pore size distribution. When HPW is impregnated onto the support, the hysteresis loop type is maintained i.e to say the main part of the hysteresis loop remained in the same relative pressure.

The catalyst synthesized by using wet impregnation method had a BET surface area between 119-233 m^2/g (see Table 3.1). As expected, the BET surface area decreased with increase in HPW. Also, a decrease in pore volume was observed, suggesting HPW is deposited inside the mesopores of γ-Al_2O_3 support. Similar kind of observations was reported in the literature for HPW supported on MCM-41 (Chen et al., 2013 ; Shringarpure and Patel, 2011). The average pore size ranged from 6.1-7.5 nm.

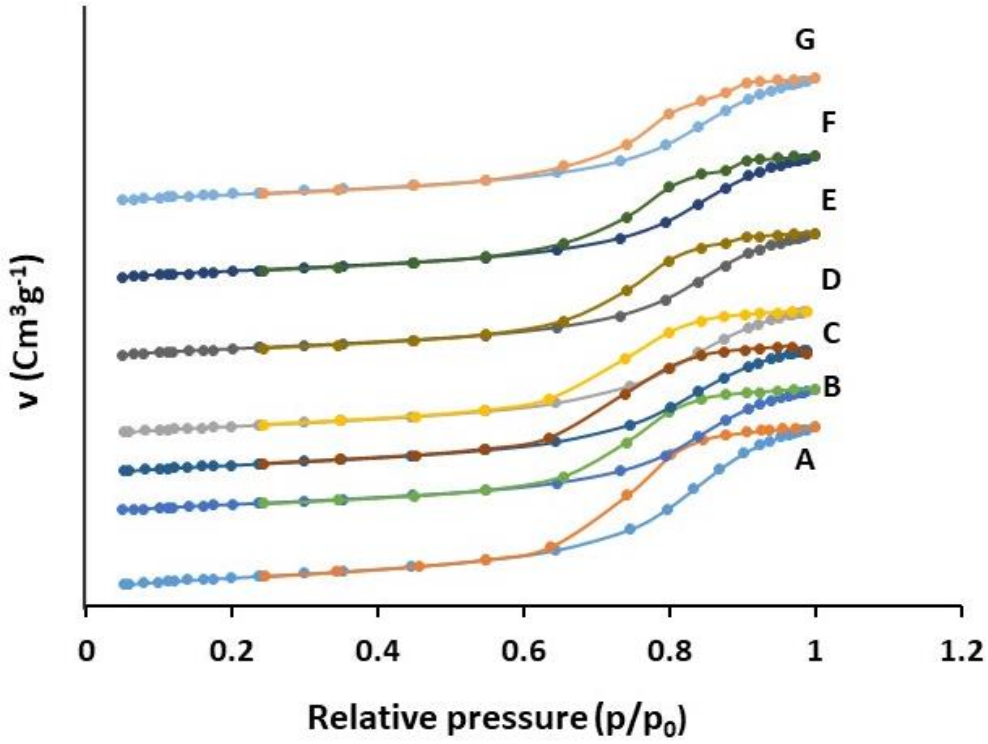

Figure 3.1. N_2 adsorption-desorption isotherms of A) γ-Al_2O_3 (B) 5 wt % HPW/γ-Al_2O_3, (C) 15 wt % HPW/γ-Al_2O_3, (D) 25 wt % HPW/γ-Al_2O_3, (E) 35 wt % HPW/γ-Al_2O_3, (F) 45 wt % HPW/γ-Al_2O_3, and (G) 55 wt % HPW/γ-Al_2O_3.

The total surface acidity of the synthesized catalysts ranged from 12.5-14.4 mole of H^+/g of catalysts. The total surface acidity increased of up to 45 wt % of HPW loading.

3.4.2 Raman spectroscopy

To affirm the presence of the keggin anion on Al_2O_3 surface, the supported HPW catalysts were examined by Raman spectroscopy (see Figure 3.2). The heteropolyacids mostly represents $PW_{12}O_{40}^{3-}$ anion framework in which tetrahedron PO_4 is surrounded by $12WO_6$ octahedra. Since, groups of these are linked by corner-sharing oxygens, four types of oxygen bands between 1200 and 700 cm^{-1} are observed (Caliman et al., 2005).

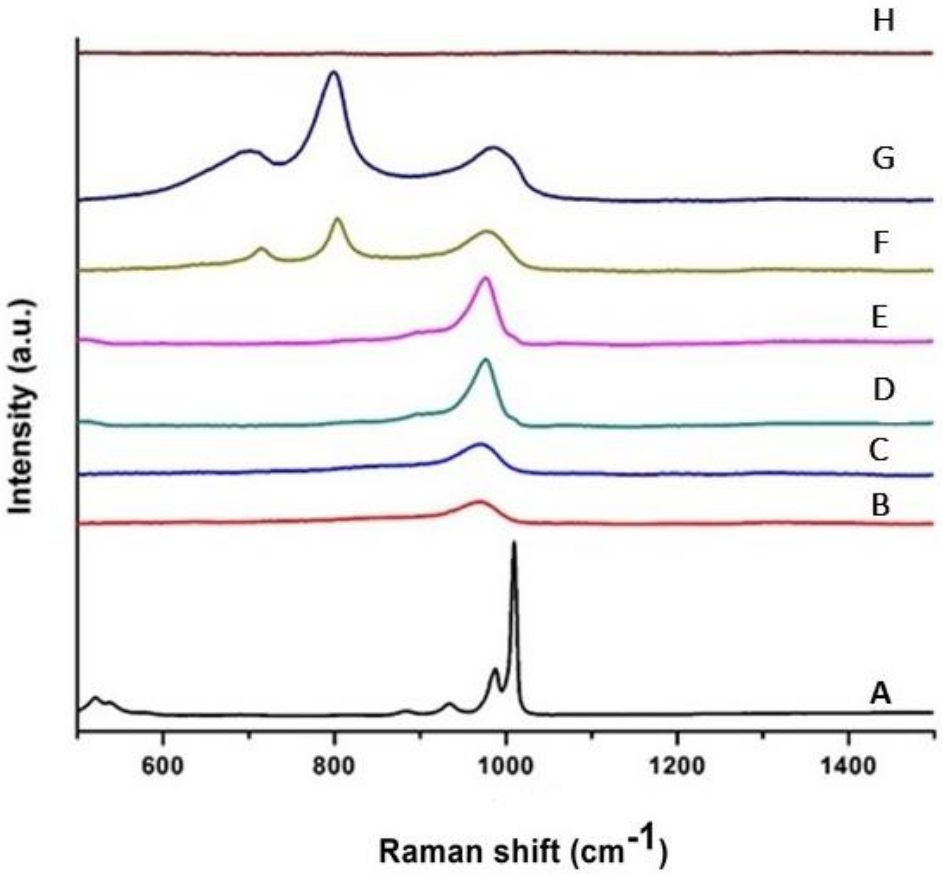

Figure 3.2. Raman spectra of (A) HPW , (B) 5 wt % HPW/γ-Al_2O_3 , (C) 15 wt % HPW/γ-Al_2O_3 , (D) 25 wt % HPW/γ-Al_2O_3, (E) 45 wt % HPW/γ-Al_2O_3, (F) 55 wt % HPW/γ-Al_2O_3, (G) 65 wt % HPW/γ-Al_2O_3 , and (H) γ-Al_2O_3.

The Raman spectra of HPW show characteristic peak at 1010 cm^{-1} ascribed to W=O symmetrical stretching while the band at 990 cm^{-1} is associated with the antisymmetric stretching

of W=O. Bands observed between 500 and 600 cm^{-1} are related to W-O-W and O-P-O symmetric stretching and asymmetric deformation vibration, respectively.

For the alumina support no band was observed and can be because of Al-O bond's ionic character (Wachs, 1996). With the increase in HPW loading on γ-Al_2O_3 up to 45 wt %, the characteristic band between 900 and 1000 cm^{-1} was found to be broadened and shifted.

This shifting of the peak position can be attributed to keggin unit and γ-Al_2O_3 support interactions, interfering with keggin unit symmetry (Guo et al., 2008). However, prolonged calcination at 450°C might have resulted in anhydride form of keggin. But no decomposition of keggin anion into WOx species was observed until a HPW loading of 45 wt %. As such, hardly any decomposition was observed in TGA profiles for the supported catalysts. Thereafter, with further increase in the loading resulted in decreased intensity of these bands and showed an additional bands at 714 cm^{-1} and 803 cm^{-1},attributed to W-O-W stretching and W-O stretching, respectively. According to Xu et al. (2014) Raman spectra of WO_3 also showed peaks centered at 807 cm^{-1} and 717 cm^{-1}. WO_3 appears at keggin anion surface densities above 0.5nm^{-2}. Their presence in the Raman spectra suggests that the loadings of 55 wt % (0.74 nm^{-2}) and 65 wt % (1.14 nm^{-2}) possibly could have led formation of WO_x species and subsequent agglomeration into WO_3. As the surface density of keggin anion increases, the intensity of band at 712 $cm^{-1}$and 803 cm^{-1} increases, while for the band 990 cm^{-1} decreases. The ratio of peak areas of W-O stretch (803 cm^{-1}) and the symmetric stretch of W=O (990 cm^{-1}) area (Figure not shown) for HPW/γ-Al_2O_3 samples was calculated at various keggin anion surface densities (0.04-1.14 nm^{-2}). It was found that the intensity increases to larger values as tungsten oxide crystallites becomes evident. Above 0.5 nm^{-2} keggin anion density, W-O bonds increases in the number (Figure 3. 2 (G, F)) while the intensity of W=O bond decreases. This increase in W-O band intensity suggests that the concentration of WO_x increases as keggin anion density increases. This also conveys that upon the formation monolayer on alumina excess loosely held WO_X species aggregate into crystallites of tungsten oxide.

3.4.3 XRD analysis

Further, the presence of keggin anion on the support was confirmed by XRD analysis. XRD patterns for γ-Al_2O_3, HPW, and catalysts are shown in Figure 3.3. Three reflection peaks at 2θ =

37.1, 46.0 and 66.6° were noticed, associated to the reflections of planes of γ-Al_2O_3 ((311), (400), and (440)) (JCPDS, no. 10-0425), respectively. It has been stated in the literature that the specific peaks related to tungsten kegging structure occurs at 2θ = 10.28, 20.68, 25.38, 29.48 and 34.68. On comparison of the XRD patterns of HPW/ γ-Al_2O_3 with that of pure HPW revealed that up to 55 wt % HPW loading (i.e. keggin anion density 0.74 nm^{-2}) none of the catalysts revealed crystalline phase of HPW, thus suggesting that HPW is better dispersed on the support. This can be associated with the supports mean pore diameter (7.5 nm) (Table 3.1) and the diameter of the keggin anion (1.2 nm) (Badday et al., 2013; Kozhevnikov, 1995). The difference in the pore diameter would allow a uniform dispersion of HPW on alumina's surface, reducing the possible agglomerations of HPW which could lead to formation of crystals and plugging of pores.

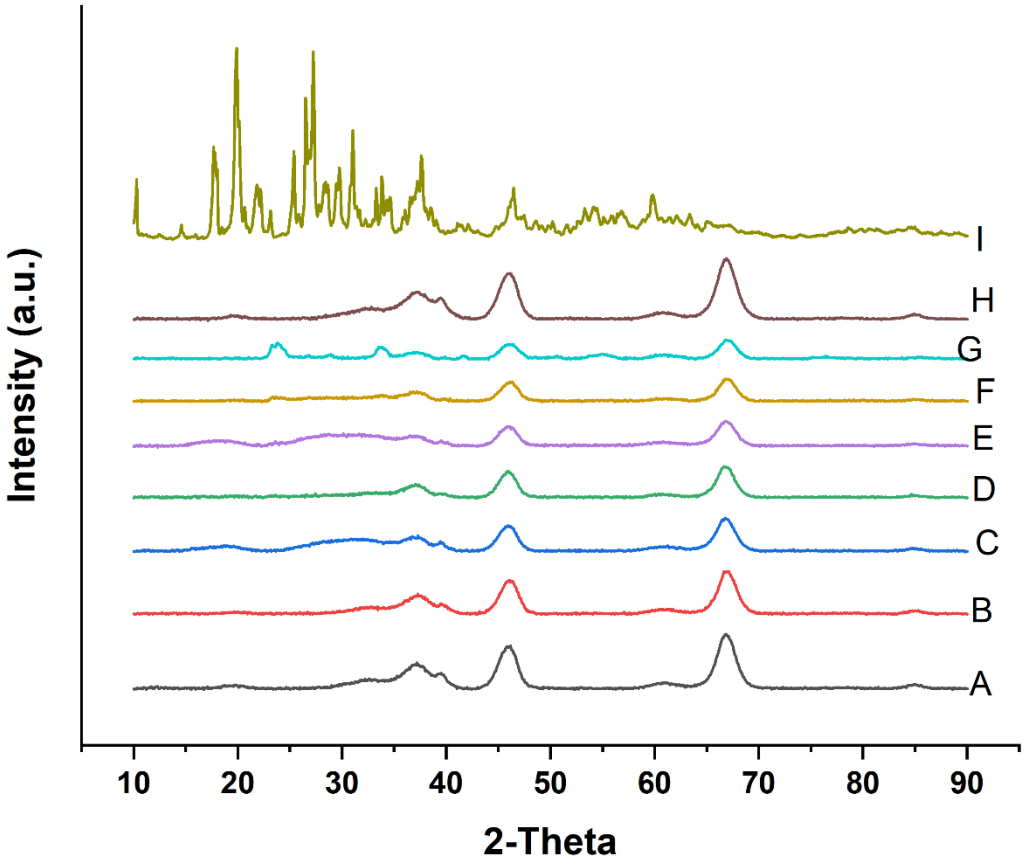

Figure 3.3. XRD graph for A) 5 wt % HPW/γ-Al_2O_3, (B) 15 wt % HPW/γ-Al_2O_3, (C) 25 wt % HPW/γ-Al_2O_3, (D) 35 wt % HPW/γ-Al_2O_3, (E) 45 wt % HPW/γ-Al_2O_3, (F) 55 wt % HPW/γ-Al_2O_3,(G) 65 wt % HPW/γ-Al_2O_3, (H) γ-Al_2O_3, and (I) HPW.

At a higher HPW loading of 65 wt %, an additional diffraction peak was observed at 23 and 35° which can be assigned to the reflections associated with WO_3 species. The peak at $2\theta = 23°$ is distinct of WO_3 species (Balzer et al., 2014). However, in Raman spectroscopy, WO_3 crystallite was observed not only for 65 wt % but also for a loading of 55 wt %. Hence, in accordance to XRD and Raman spectroscopy, formation of WOx species are observed at higher HPW loadings (55-65 wt %).

As HPW content increased from 5-45 wt %, the intensity of diffraction peaks at $2\theta = 37.1$, 46.0 and 66.6° associated with γ-Al_2O_3 was found to be decreased, thus indicating a decrease in crystallinity in HPW supported sample in comparison to unloaded Al_2O_3 support. Hence, the size of Al_2O_3 crystallites were calculated using Scherrer's equation. It was observed that the crystallite sizes of Al_2O_3 decreased from 4.4 to 4 nm as HPW content increased from 5-45 wt %. This suggests that HPW could occupy Al_2O_3 lattice site thus preventing the growth of Al_2O_3 crystalline grains thereby pointing towards better dispersion of HPW onto the support. In impregnation and drying process, HPW is attached to Al_2O_3 through interaction of the heteropolyanion proton with $Al\text{-}O^-$ site or via electrostatic binding with Al^{3+} sites in the lattice. This agrees with the literature, a decrease in crystallite size of SnO_2 was observed by Ahmed et al. (2011) when the HPW content was increased from 3 to 30%.

3.4.4 SEM and TEM analysis

Changes in the surface morphology upon impregnation of HPW on γ-Al_2O_3 were studied using scanning electron micrograph. As observed on the micro scale (Figure 3.4 (A, B)), hardly any change in the surface morphology was observed for 45 wt % HPW/γ-Al_2O_3 catalysts suggesting the dispersion of HPW inside the pores.

Further down the scale (Figure 3.4 (C, D)), the crystallite aggregates were observed for the support γ-Al_2O_3, while for supported HPW catalyst such crowding of the crystallites was not observed. This compliments the findings from XRD analysis where a decrease in γ-Al_2O_3 crystallite size (4.4 nm) was observed upon HPW impregnation, indicating the restricted growth of γ-Al_2O_3 crystalline grains and leading to better dispersion of HPW at a loading of 45 wt %.

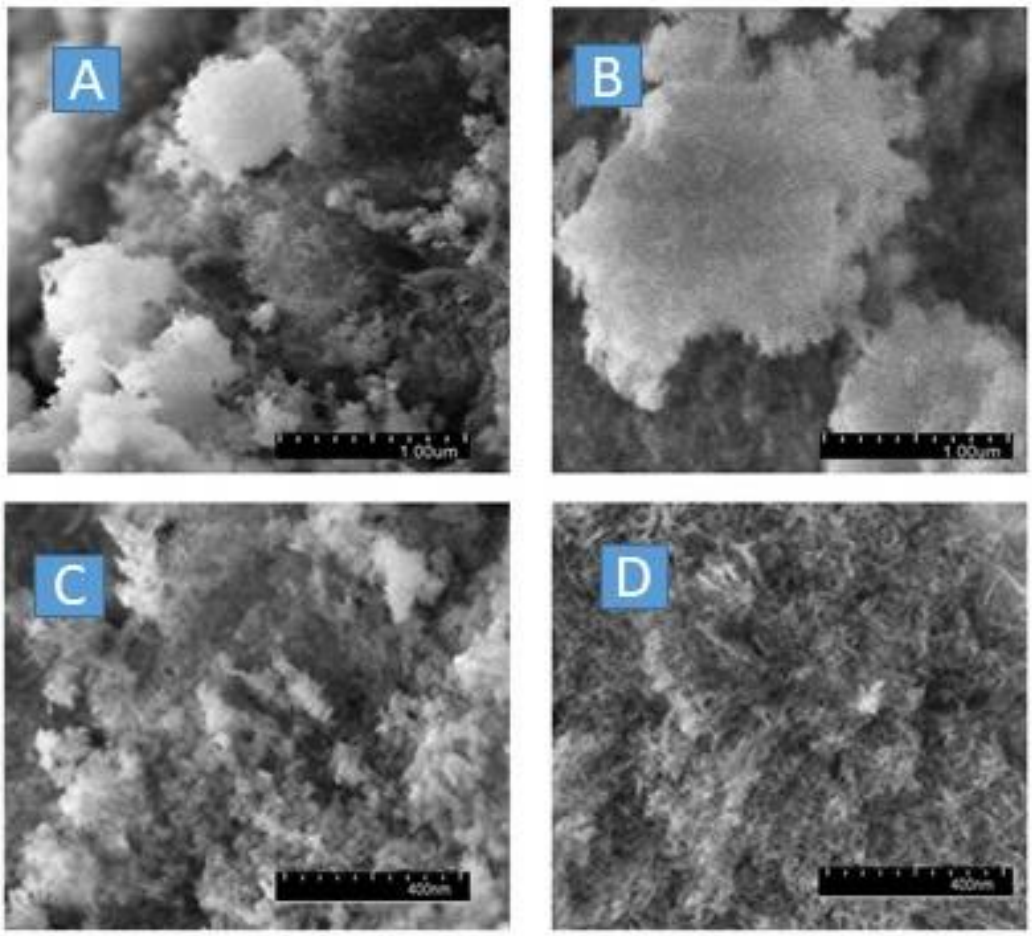

Figure 3.4. SEM images of (A, C) γ-Al_2O_3, and (B, D) 45 wt % HPW/ Al_2O_3 at different magnifications

The TEM images of the support and 45 wt % HPW loaded on γ-Al_2O_3 are shown in Figure 3.5 (A, B). A worm like mesostructure was observed for the support γ-Al_2O_3 whereas the image of HPW supported on γ-Al_2O_3 showed the existence of the keggin anions as round particles (indicated by arrow in Figure 5B) dispersed over the alumina support. The difference in the diameter between the support and HPW allowed HPW to reside inside the pores as confirmed by appearance the dark particles. Similar observations were reported by the author Badday et al. (2013).

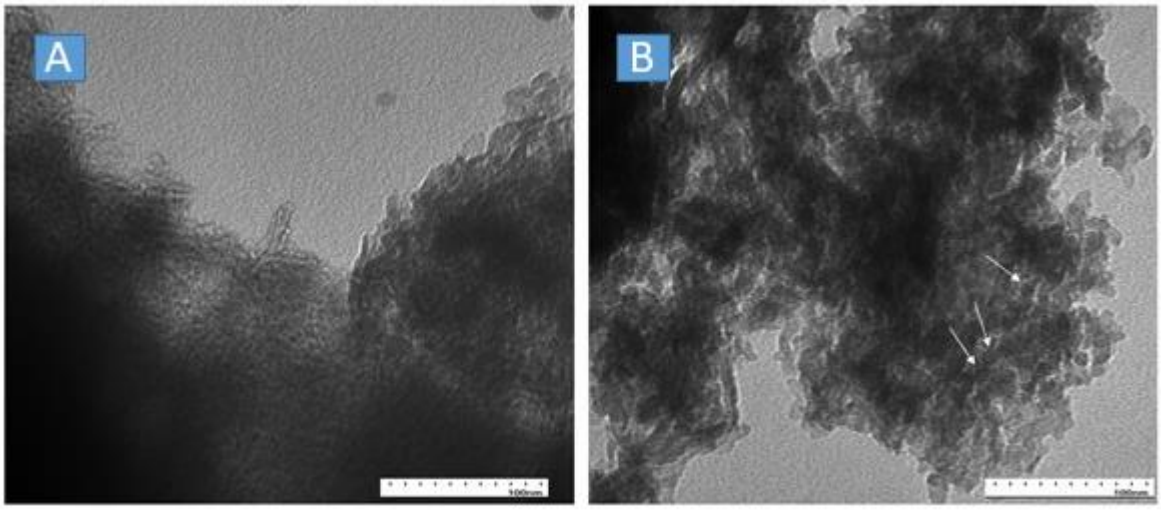

Figure 3.5. TEM images of (A) γ-Al_2O_3, and (b) 45 wt % HPW/ Al_2O_3

3.4.5 Thermal stability

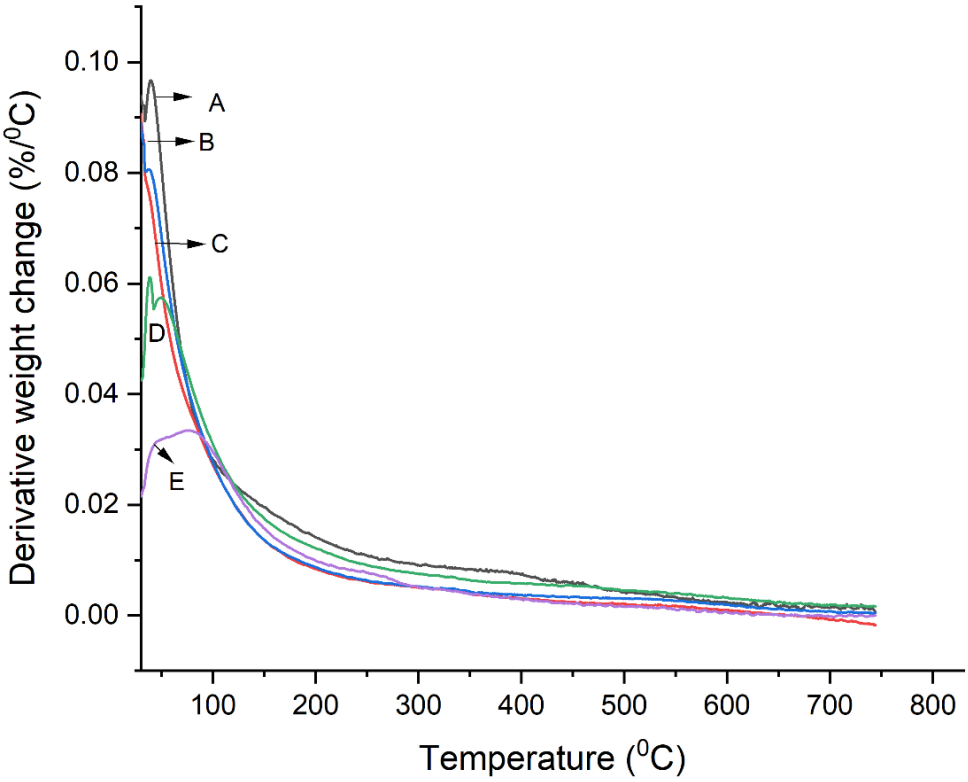

Figure 3.6. Thermogravimetric analysis of A) γ-Al_2O_3, (B) 5 wt % HPW/γ-Al_2O_3, (C) 25 wt % HPW/γ-Al_2O_3, (D) 45 wt % HPW/γ-Al_2O_3, and (E) 65 wt % HPW/γ-Al_2O_3.

TGA curves of alumina and the HPW supported alumina are given in Figure 3.6. A loss of physisorbed water was found in the temperature range 100-200 °C. More water was absorbed by γ-Al_2O_3 and 5 wt % HPW/γ-Al_2O_3 which could be due to vacant Al-OH bonds in the material, being slightly hydrophilic to adsorb water.

A lesser loss of water molecule was observed at higher loadings (65 wt %), which could possibly be due to the formation of tungsten oxide species as detected in XRD and Raman spectroscopy. The hydrophobic nature of tungsten oxide would have been responsible for lesser water absorption (Hoo and Abdullah, 2014). The support and HPW supported synthesized catalysts were found to be stable up to 750 ˚C.

3.4.6 FT-IR with pyridine adsorption

The adsorbed pyridine IR spectra were used to characterize the acidic sites of the catalysts (Figure 3.7). The peak at 1441 cm^{-1} correlates to ring motions, due to pyridine interacting with medium strength Lewis acids indicating the existence of Lewis acid sites, whereas the feature at 1579 cm^{-1} is because of protonation of pyridine by Brønsted sites present on HPW (Araujo et al., 2006; Zaera, 2014).The intensity of the bands at 1483 cm^{-1} (PyL, PyH^+) and 1579 cm^{-1} (PyH^+) increased with HPW loadings, especially for those samples having keggin anion surface density > 0.24 nm^{-2} , followed by a decrease in intensity at 1.14 nm^{-2}. According to Ramis et al. (1992), these spectral features are related to acidity of W-OH groups which is also consistent with the absence of band at 1579 cm^{-1} in the spectra shown by γ-Al_2O_3 and low loading of HPW on Al_2O_3. It was found that the Lewis acid site always prevail despite the HPW content and might be due to the free electrons in the tungsten (Hernández-Cortéz et al., 2003). In Montmorillonite K10 Modification with tungstophosphoric Acid, Sliwa et al. (2014) reported the prevalence of the Brønsted acidity, while the Lewis acid pre-dominance was observed. This could be due to HPW and γ-Al_2O_3 interacting differently, depending on the degree of hydroxylation. In order to favour the exchange, the HPW needs three localised OH^{-1}. In case of higher degree of hydroxylation the exchange might proceed as

$$H_3[W_{12}PO_{40}]+Al(OH)_3\rightarrow[W_{12}PO_{40}]Al+3H_2O \quad \text{.....(3.5)}$$

As neutralisation takes place completely, Lewis acidity is retained. Similar kind of results were observed for sol-gel zirconia in the presence of heteropolyacid (Hernández-Cortéz et al., 2003),

while for supported WO_3 on TiO_2, it was observed that Lewis acidity prevails and its strength is decreased with an increase in WO_3 surface density (Ladera et al. 2013). If enough OH^{-1} are not present then an exchange as $[W_{12}PO_{40}]$ H^{2-} with Brønsted acidity is required (Hernández-Cortéz et al., 2003).

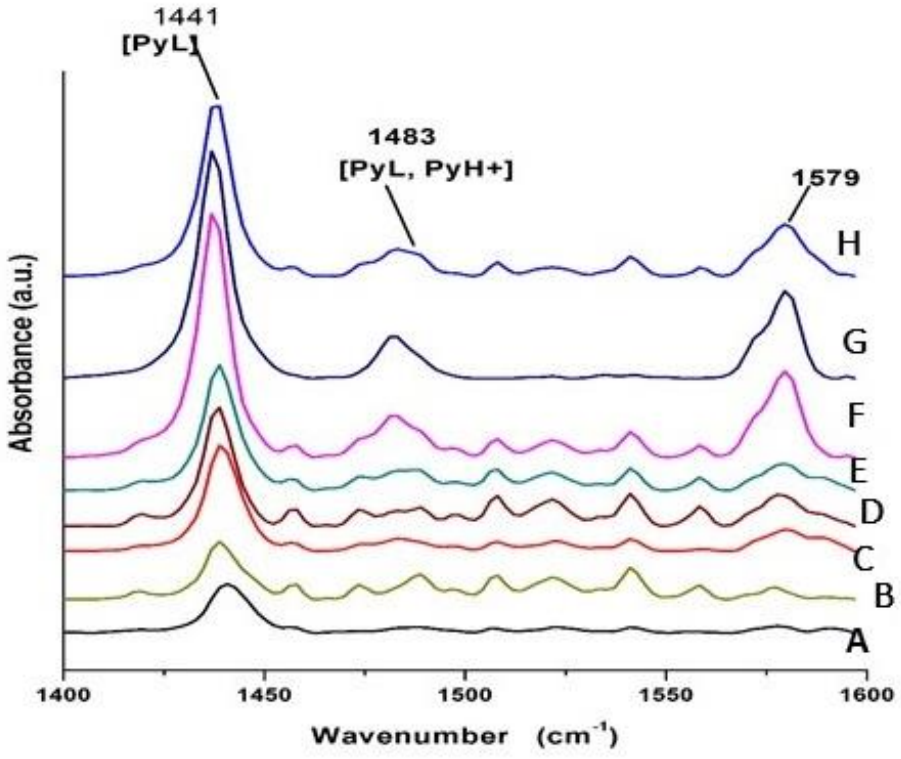

Figure 3.7. Infrared spectra after pyridine adsorption and subsequent desorption A) γ-Al_2O_3,(B) 5 wt % HPW/γ-Al_2O_3, (C) 15 wt. % HPW/γ-Al_2O_3, (D) 25 wt % HPW/γ-Al_2O_3, (E) 35 wt % HPW/γ-Al_2O_3, (F) 45 wt % HPW/γ-Al_2O_3, (G) 55 wt % HPW/γ-Al_2O_3, and (H) 65 wt. %-HPW/γ-Al_2O_3

3.4.7 ^{13}C hpdec NMR

The data for ^{13}C chemical shift for adsorbed pyridine on HPW/γ-Al_2O_3 are summarized in Table 3.2. The intramolecular α-β and α-γ ^{13}C chemical shift differences are reported as the chemical shift for β and γ carbons in pyridine changes because of the complex formation (Maciel et al., 1983) Also, the way the pyridine molecule is attached on the surface has been studied by α- and β and α- and γ chemical shift differences.

Table 3.2. ^{13}C Chemical shift differences for HPW/γ-Al_2O_3

Sample	(α-β)[a]	(α-γ)[b]	Remarks
5 wt % HPW/ γ-Al_2O_3	25.7	-	γ peak not well determined
25 wt % HPW/ γ-Al_2O_3	21	8.5	
35 wt % HPW/ γ-Al_2O_3	25	13	
45 wt % HPW/ γ-Al_2O_3	22.7	8.9	
55 wt % HPW / γ-Al_2O_3	18	-	γ peak not well determined
65 wt % HPW / γ-Al_2O_3	18.9	-	γ peak not well determined

[a] ^{13}C Chemical shift difference between α- and β- carbons of pyridine in HPW/γ-Al_2O_3; [b] ^{13}C Chemical shift difference between α- and γ- carbons of pyridine in HPW/γ-Al_2O_3.

5 wt % and 35 wt % HPW/γ-Al_2O_3 showed difference in α-β chemical shift at 25.7 ppm and 25 ppm, respectively (Figure not shown), mostly representing differences in chemical shift α-β carbons of hydrogen-bonded pyridine (Kawashima et al., 1997; Maciel et al., 1983), while for 25 wt % and 45 wt % HPW/γ-Al_2O_3, it was found to be 21 and 22.7 ppm. Based on the reference data (Maciel et al., 1983), it can be interpreted that most of the pyridine existed as Lewis acid-base complexes with Al surface. Hence, it can be said that the sample has chemisorbed pyridine at the Lewis acid site. This is also persistent with infrared data that alumina acidic sites were Lewis type centered and the apparent Brønsted acidity arise at higher loadings from pyridine protonation by Brønsted sites present on HPW. For the higher loadings of 55 wt % HPW/γ-Al_2O_3 and 65 wt % HPW/γ-Al_2O_3, the observed chemical shift differences were found to be associated to hydrogen bonded pyridine (Maciel et al., 1983).

3.4.8 Mechanism of HPW immobilization on the γ- alumina surface

A mechanism of HPW immobilization on γ-Al_2O_3 can be proposed based on the keggin nature and the acidity of the supports. The surface concentration of the acidic site on the alumina

is involved in distortion of heteropolyanion (Raman (Figure 3.2A), XRD (Figure 3.3I.)).Compared with the bulk heteropolyacid, among the supported HPW/γ-Al_2O_3, the state of the adsorbed poloxymetalate moiety at lower HPW loadings /monolayer coverage with the alumina surface remained unaffected (XRD, Raman) and retains acidity in methyl ester synthesis. This could be because of interaction of protons with the γ-Al_2O_3 support. The possible adsorption mechanism of HPW is depicted in Figure 3.8. It includes the dehydroxylation of the surface hydroxyl groups on γ-Al_2O_3 surface which creates e -donor sites and e-acceptor sites (Rao et al., 2005; Schoenfeldt, 2008). HPW is attached to γ-Al_2O_3 as one of the protons of the heteropolyanion interacts with Al-O^- site.

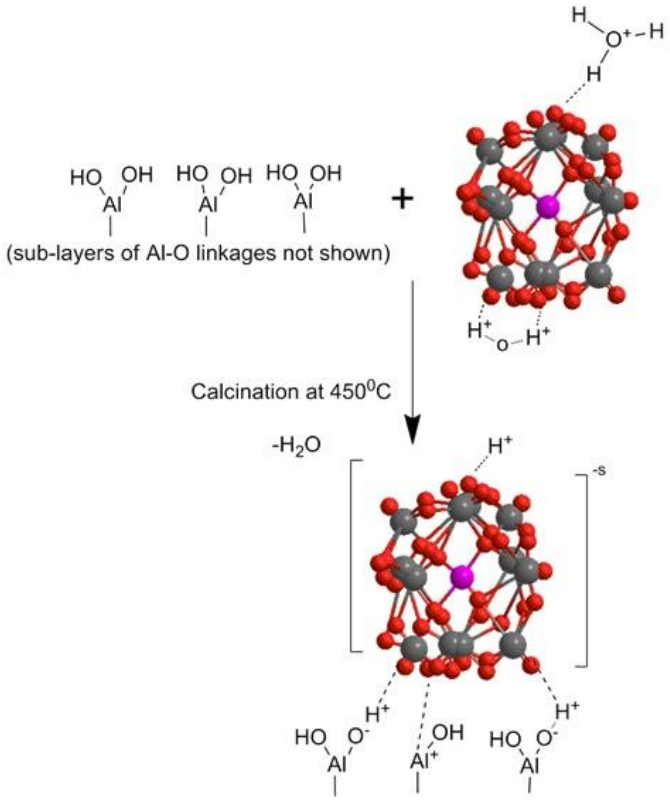

Figure 3.8. Probable interaction of HPW with γ-Al_2O_3.

This results in negative charge *(δ−)* at the keggin unit and it binds to Lewis acid site via electrostatic binding. This reflects the involvement of number of basic and acidic sites in immobilizing $H_3PW_{12}O_{40}$ species.

3.5 Catalytic activity study

3.5.1 Effects of HPW loading on γ-Al_2O_3

The effects of HPW loading (between 5 and 65 wt %) supported on γ-Al_2O_3 on the ester yield were investigated. The reaction operating parameters were 3 wt % loading of the catalysts 200 °C, 10 hr, and 20:1 methanol to oil molar ratio. With low HPW anions loading, 5 wt % HPW/γ-Al_2O_3 would be less reactive in comparison to higher HPW/Al_2O_3 solid catalysts due to less number of active sites. It was observed that increasing HPW loading beyond 45 wt % hardly affected the ester yield (Figure 3.9). The TOF for the supported catalysts was found in the range of $9.7*10^{-4}$ -$8.8*10^{-2}$ min^{-1}.

To better understand the HPW loading effect, the acidic properties of the catalysts were correlated with the catalytic activity.

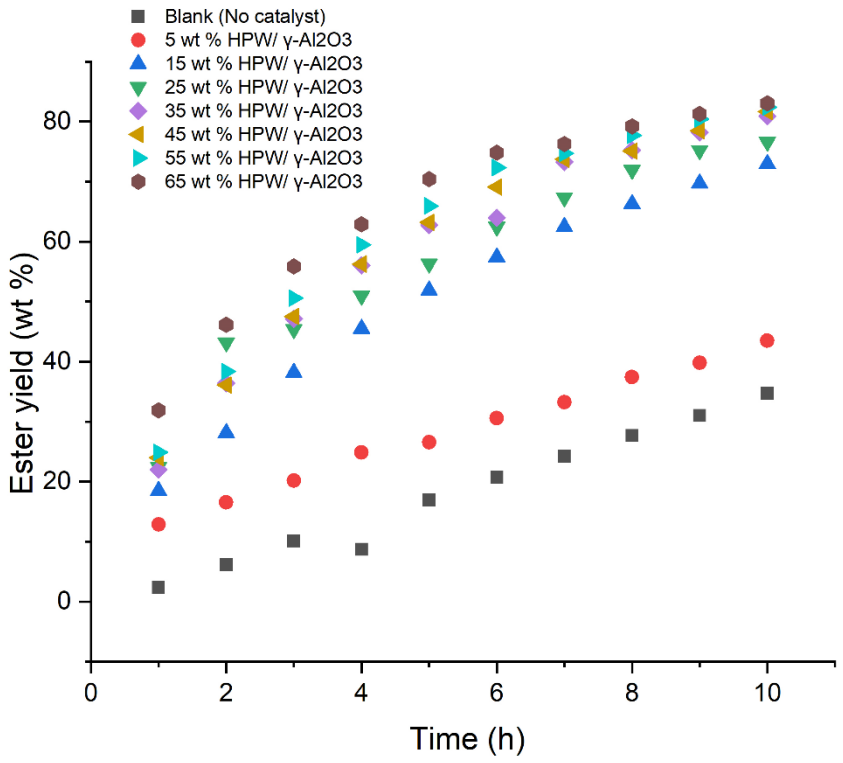

Figure 3.9. Screening of HPW + γ-Al_2O_3 for biodiesel synthesis (3 wt % catalyst loading, 20:1 methanol to oil molar ratio, 200 °C, 4 MPa and 10 h).

3.5.2 Acidic properties and correlation with catalytic activity

Figure 3.10 shows the correlation of B/L ratio (intensity ratio of Brønsted acid to Lewis acid site band) with the catalytic activity as a function of HPW loading. A direct correlation between B/L ratio and activity of catalysts is observed based on the results. With the increase in the B/L ratio up to HPW loading of 45 wt %, the catalytic activity also increased and then decreased with decrease in B/L ratio at higher keggin densities. This decrease in catalytic activity can be because of the loss of acidity at higher keggin densities due to the occurrence of tungsten oxides as marked by the appearance of WO_3 peaks in XRD & Raman spectroscopy. Further, the agglomeration of these crystallites on the catalyst with the reduced BET surface area of the catalysts could lead to blockage of mesopores. As a result, the acidic sites in these mesopores are inaccessible at the time of the reaction and, as a result, HPW loadings of more than 45 wt % showed decreased catalytic activity. From the trend followed by the B/L curve, it can be said that an optimal level of Lewis acid and Brønsted acid site influences the transesterification reaction positively (Shi et al., 2012).

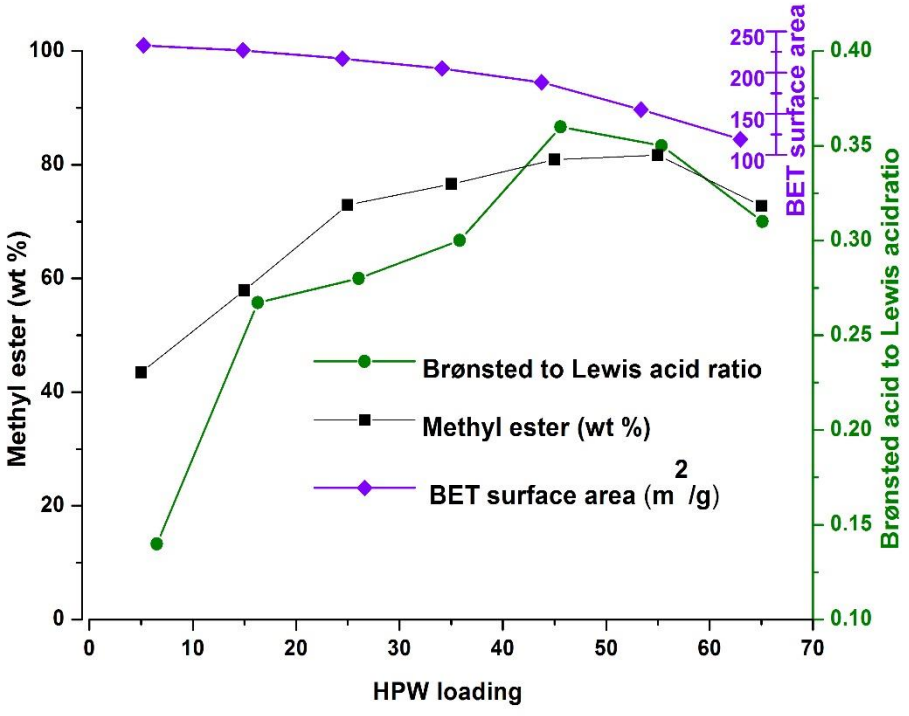

Figure 3.10. Correlation of B/L ratio with catalytic activity (3 wt % catalyst loading, 20:1 methanol to oil molar ratio, 200 °C, 4 MPa and reaction time of 10h).

3.6 Process optimization

The reaction parameters influencing the methyl ester synthesis from canola oil using HPW/γ-Al_2O_3 were optimized with 2^2 factorial design and RSM (Response surface Methodology). The conversion of triglyceride was taken as a response. The factors were selected considering, optimization of process economically. The factors consist of catalyst weight and methanol: oil molar ratio. The reaction temperature was fixed at 200 ^{0}C based on the kinetic study. Although, the ester yield increases with the increase in reaction temperature it was observed that increasing temperature beyond 200 °C leads to the formation of the polymeric product due to the oil subjected at the higher temperature (225 °C) for 10 h (Ladera et al., 2013). The stirring speed was maintained at 600 rpm in order to abstain limiting mass transfer (Vicente et al., 2005).

The levels were chosen as per the preliminary experiments. The catalyst loading levels were selected at 3 and 9 wt %, while those of methanol to oil molar ratio were 10:1 and 25:1. Table 3.3 shows 2^2 factorial design. The last column shows the triglyceride conversion obtained experimentally for each run. Five additional runs were carried out at the center point, for estimation of experimental error and curvature effect.

The following expression was obtained on fitting the experimental results to a linear model

$$Conversion\ (\%) = 85.47 + 0.99A + 8.96\ B - 5.035A * B \quad \text{.....(3.6)}$$

$(R^2 = 0.99)$

Where, response is predicted value of triglyceride conversion (%), A and B are coded values

(-1, 0, 1) of loading of catalyst (wt %) and methanol: oil molar ratio.

From the statistical analysis it was observed that the curvature effect was significant at 95 % confidence. As a result, 2-level factorial model was not enough to illustrate the system, and hence a second-order model in two variables was required to fit the data.

The curvature effect was significant. Thus, the design was modified to a central composite design with additional runs (Star points, highlighted in Table 3.3).The statistical model for response surface is expressed as:

$$Conversion(\%) = 97.53 + 1.97A + 9.58B - 2.25A * A - 8.45B * B - 5.04A * B \ldots\ldots (3.7)$$

$(R^2 = 0.97)$

Where, response is predicted value of triglyceride conversion %, A and B are coded values (-1, 0, 1) of catalyst loading (wt %) and methanol: oil molar ratio. The model has R-square value of 97% meaning it can explain 97% variations in the conversion.

Table 3.3. Experimental matrix for the factorial designs, center points and star points

Experimental runs	PtType	Blocks	Catalysts weight (%)	Methanol: oil molar ratio	Response (%)
1	-1	1	10.2	17.5	98.6
2	-1	1	6	6.9	67.6
3	0	1	6	17.5	97.5
4	0	1	6	17.5	97.6
5	1	1	3	25.0	98.5
6	0	1	6	17.5	98.1
7	-1	1	1.8	17.5	90.2
8	1	1	9	10.0	82.5
9	0	1	6	17.5	95.9
10	1	1	3	10.0	70.5
11	1	1	9	25.0	90.4
12	-1	1	6	28.1	96.4
13	0	1	6	17.5	98.6

Star points

The 3D surface plot depicting the response (triglyceride conversion) as a function of catalysts loading and methanol: oil molar ratio is plotted for the experimental range considered (Figure 3.11). The second order model shows that for low methanol concentration triglyceride conversion increases with increasing catalyst loadings. This improvement can be ascribed to the presence of the active sites on the catalyst (Lau et al., 2016). The catalyst loading is a significant

factor and has a positive effect. At a high methanol to oil molar ratio, conversion increases at intermediate loading of catalysts but as catalyst loading increases, the conversion decreases. This is because of the negative methanol to oil molar ratio- catalyst interaction and hence, a negative concentration quadratic coefficient. The increase in methanol to oil molar ratio will contribute to the transesterification reaction, thereby increasing the conversion to an optimum value. At a high methanol-to-oil ratio, however, the solubility of glycerol could be facilitated by the formation of monoglycerides, which would lead to a glycerolysis of the biodiesel and lower the final product yield (Mansir et al., 2017). It can also reduce the yield due to the dilution effect of the catalysts, which causes the insolubility of methanol in oil. A decrease in conversion was observed on increasing the catalysts loading above 6 wt % for 25:1 methanol to oil molar ratio which probably could be because of mixing problem of catalyst and reactants (Zabeti et al., 2010).

The precision of quadratic model was evaluated in this study. On comparison of the predicted results with that of experimental, the error obtained was 1.6 % suggesting model is accurate enough to estimate the triglyceride conversion. A triglyceride conversion of 94.9 ± 2.9 % and methyl ester yield of 90.0 ± 2.8 wt % were observed at the optimized reaction conditions of 10 wt % of the catalyst loading, 17.5 methanol to oil molar ratio, 200 ^{o}C and 4 MPa in 10 hours.

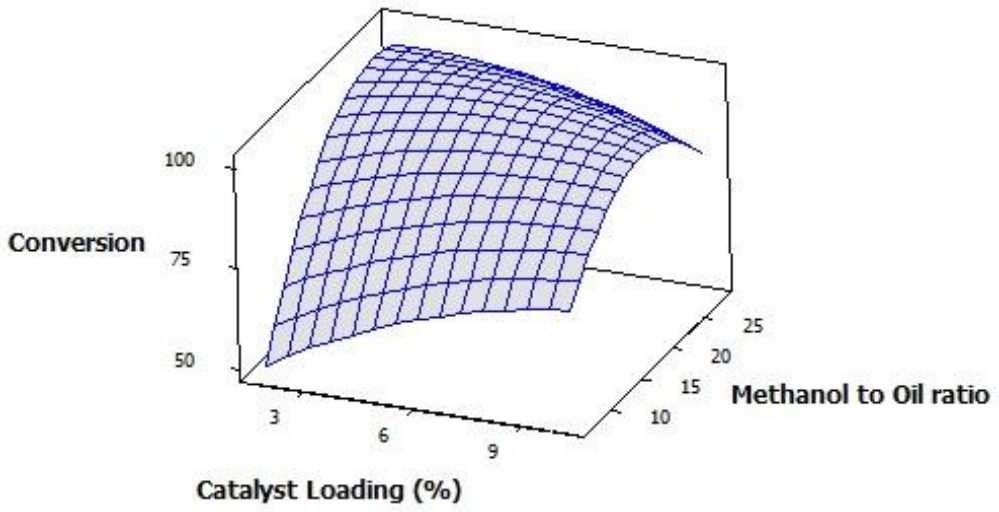

Figure 3.11. Response surface plot as a function of catalyst loading and methanol to oil molar ratio at catalyst loading levels of 3 and 9 wt %, methanol to oil molar ratio levels of 10:1 and 25:1 , 200 °C, 4 MPa and reaction time of 10 h.

HPW/γ-Al_2O_3 catalysts with optimized loading of 45 wt % was studied for successive reaction runs. A triglyceride conversion of 94.9 % (σ = 2.9) was obtained in the first run while the second run showed a conversion of 90.3 % (σ = 4.3) respectively. There was no statistically significant difference observed between the conversion values of two runs when tested by two-sample t-test. The pyridine adsorbed FT-IR spectra of the reused catalyst was carried out (Figure 3.12) and the B/L ratio (intensity ratio of Brønsted acid to Lewis acid band) was determined. The first run showed a B/L ratio of 0.42 while 0.37 was observed in the second run. There was insignificant decrease in B/L. This suggests that the catalyst was able to retain the acidic sites after the subsequent reuse.

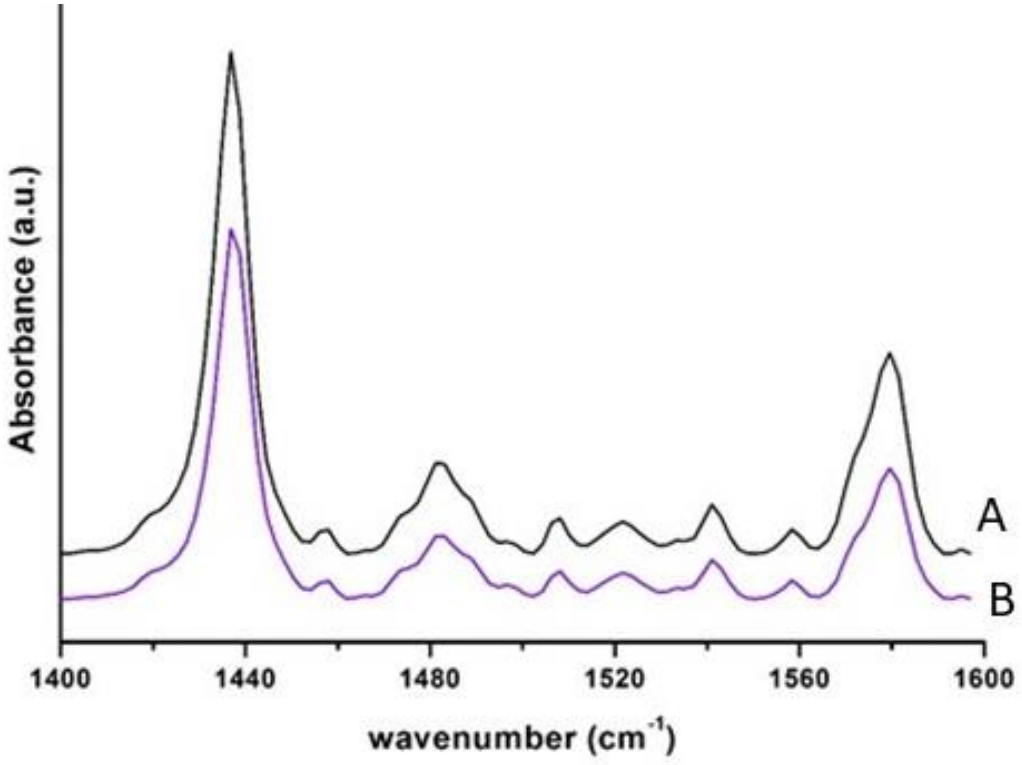

Figure 3.12. Infrared spectra after pyridine adsorption and subsequent desorption (A) 45 wt % HPW/γ-Al_2O_3, and (b) 45 wt % HPW/γ-Al_2O_3 (spent catalyst after 1st reuse).

3.7 Application of the catalyst on low-grade green seed canola oil

In order to determine catalysts robustness, the simultaneous transesterification and esterification was carried out using green seed canola oil at the optimized reaction conditions. The

methyl ester yields at the optimized reaction conditions of 10 wt % of the catalyst loading, 17.5 methanol to oil molar ratio, 200 °C and 4 MPa in 10 hours are shown in Table 3.4.

The FFA content of canola biodiesel was found to be 0.38% (0.76 mg KOH/g). On the other side, the conversion of the green seed canola oil was likely to be limited to the FFA content of the feedstock.

Table 3.4. Methyl ester yield obtained with green seed canola oil and canola oil feedstocks.

Parameters	Canola oil	Green seed canola oil
Ester content (wt %)	90.0	74.0
FFA content (%)	0.38 (0.76 mg KOH/ g)	1.2 (2.35 mg KOH/ g)

The FFA content of green seed canola ester mixture was comparatively large (FFA content-1.2 %). It is indicated that the probable hydrolysis of esters may occur in the presence of water, producing free fatty acids.

The catalysts 45 wt % HPW/γ-Al_2O_3 showed some robustness towards the transesterification of canola oil, but the utilization of green seed canola oil as a feedstock was limited. This can also be attributed to the limited density of Brønsted acid sites on the catalysts surface. The Brønsted acid sites serve as H^+ donor, providing a hydrophobic environment and protecting the actives sites from the poisoning effect of water.

3.8 Conclusions

Surface morphological studies (SEM and TEM) indicated that HPW is well dispersed at a loading of 45 wt %, whereas tungsten oxide species were observed at HPW higher loadings (55-65 wt %). It was established that the surface acidity of γ-alumina plays a role in the immobilization of HPW. Upon partial dehydroxylation, γ-alumina exhibits Lewis acid sites (Al^{3+}), Lewis base sites ($Al\text{-}O^-$), and Brønsted acid sites and serves as a binding site for keggin anion. Porous oxide materials with acidic characteristics were therefore determined to be suitable for the heterogenization of HPW.

The catalysts characterization result revealed that 45 wt % HPW loading is favorable for acid catalyzed transesterification reaction and can be attributed to the occurrence of Brønsted acidity at this loading and giving the optimal B/L ratio. A methyl ester yield of 90.0 ± 2.8% was achieved for

the biodiesel production from canola oil, whereas an ester yield of 74.0 ± 1.9% was obtained with green seed canola oil at the optimized reaction conditions.

Activity of alumina-based solid acid catalysts towards the transesterification of green seed canola was limited. Therefore, there was a need to improve the catalysts' characteristics. The addition of the silica is shown to enhance the textural and hydrothermal properties of alumina. The co-existence of SiO_4 and AlO_4 in an aluminosilicate framework induces strong Brønsted acid sites over the support surface that is stronger than the acidity of mere alumina. These characteristics make aluminosilicates materials of interest for use as supports for transesterification reactions. As a result, aluminosilicates such as MAS-7 and MAS-9 were used as supports for the catalysts moving forward as outlined in Chapter 4.

CHAPTER 4

Surface Investigation of Tungstophosphoric Acid Supported on Ordered Mesoporous Aluminosilicates for Biodiesel Synthesis.

The content of this chapter has been published in ACS Omega cited below and presented in the following conferences:

Citation:

Kurhade, A., Zhu, J., Hu, Y., Dalai, A.K., 2018. Surface investigation of tungstophosphoric acid supported on ordered mesoporous aluminosilicates for biodiesel synthesis. ACS Omega 3, 14064–14075. https://doi.org/10.1021/acsomega.8b01931

Conference Proceedings:

Kurhade, A., Dalai, A.K. Development of alumina and ordered mesoporous aluminosilicates-supported heteropolyacid for biodiesel production. North American Catalysis Society Meeting, Denver, United States, June 4-7, 2017.

Kurhade, A., Hu, Y., Dalai, A.K. Surface investigation of tungstophosphoric acid (HPW, $H_3PW_{12}O_{40}$) supported on ordered mesoporous aluminosilicates for biodiesel synthesis. 67th Canadian Chemical Engineering Conference, Edmonton, Alberta, Canada, October 22-25, 2017.

Kurhade, A., Zhu, J., Hu, Y., Dalai, A.K. Surface investigation of tungstophosphoric acid supported on ordered mesoporous aluminosilicates for biodiesel synthesis. 25th Canadian Symposium on Catalysis, Saskatoon, Saskatchewan, Canada, May 8 -11, 2018.

Contribution of the Ph.D. Candidate

Experiments, catalysts characterization, and data interpretation were carried out by Ankeeta Kurhade in consultation with Dr.Ajay K. Dalai.

Dr. Yongfeng Hu and Dr. James Dynes helped in XANES analysis of W L_1 and L_3 edges and Al-K edge. Dr. Jianfeng Zhu helped with solid state NMR of catalysts samples and provided guidance in analysing the data. The manuscript was written by Ankeeta Kurhade based on the suggestions provided by Dr.Ajay K. Dalai and Dr.Yongfeng Hu.

Contribution of this Chapter to Overall Ph.D. Research

This chapter demonstrates the prospects of using MAS-7 and MAS-9 supports for HPW in biodiesel synthesis from green seed canola oil.

4.1 Abstract

MAS-7 & MAS-9 aluminosilicates with ordered hexagonal mesopores and uniform size were obtained from zeolite beta assembly and ZSM-5 precursors respectively, using P123 surfactant via co-operative self-assembly pathway. A series of tungstophosphoric acid (HPW) supported on MAS-7, and MAS-9 ($H_3PW_{12}O_{40}$/MAS-7/MAS-9) catalysts for biodiesel production were synthesized via wet impregnation technique. Characterization of supports and catalysts was done using N_2 adsorption-desorption analysis, X-ray diffraction (XRD), pyridine adsorption Fourier-transform IR and Raman. Also, ^{29}Si MAS and CP/MAS NMR techniques were employed to study MAS-7/MAS-9 and supported solid acid catalysts surfaces. Nitrogen sorption analysis and XRD patterns indicated the formation of well-defined mesoporous materials, whereas IR spectroscopy confirmed the presence of four distinct types of OH group with varying degrees of acidity. ^{29}Si MAS NMR signified a stronger interaction between the framework of mesoporous aluminosilicates and $H_3PW_{12}O_{40}$. The X-ray absorption near-edge spectra (XANES) of the L_1 and L_3 edge tungsten showed that W in $H_3PW_{12}O_{40}$/MAS-9 sample is in W^{6+}, indicating tungsten environment similar to H_2WO_4 with O_h symmetry. The catalytic activity of the synthesized catalysts was investigated for biodiesel synthesis using unrefined green seed canola oil as a feedstock giving methyl ester yield of 76.5-88.7 wt % under the optimized reaction conditions. Catalysts activities were strongly correlated with the surface chemistry MAS-7 and MAS-9 supported HPW catalysts.

4.2 Introduction

One of the routes leading to the production of the green fuel is the transesterification /esterification of vegetable oil/ animal fat to produce biodiesel. The green properties of these fuels

are as a result of the fact that they are obtained from biomass. In addition, this fuel is substantially free of sulfur, and aromatic compounds.

The transesterification reaction is often catalyzed either by addition of alkali or acid catalysts. In case of the alkali-catalyzed transesterification reaction, there are several problems associated with the catalysts including the product separation from catalyst and formation of the soap due to the free fatty acids present in the feedstock, thus making it undesirable for cheap feedstock (Haas et al., 2006; Marchetti and Errazu, 2008). Different catalyst systems have been used to promote these reactions (Lee et al., 2014).

Heterogeneous solid acids were found to be more useful for the low quality or unrefined oils (Lee et al., 2014) than their solid base analogs and are expected to enhance esterification of FFA and transesterification of triglycerides simultaneously. It is highly desirable to synthesize biodiesel from low-cost feedstock to avoid the cost associated with refined vegetable oil. This cost can account for up to 85% of the biodiesel production cost (Luque and Melero, 2012; Marchetti and Errazu, 2008).

Considering heterogeneous solid acid catalysis, supported heteropoly acids (HPAs) have achieved enormous interest in biodiesel synthesis because of their structural mobility and super acidity. Since HPAs lack thermal stability and has a low surface area, they are incorporated on acidic /neutral carriers like Al_2O_3 or SiO_2. Tungstophosphoric acid (HPW, TPA, $H_3PW_{12}O_{40}$) has a higher acidity as compared to the other HPAs (Saifuddin et al., 2015). Atia et al. (2008) reported that alumina and aluminosilicates supported heteropolyacids are more active than the silica supported catalyst for glycerol dehydration. As far as zeolites are concerned, they possess high thermal stability and acidity related to their unique Al in building units, but small pore size restricts their use when large molecules are involved during catalytic reaction. However, in the case of mesoporous aluminosilicates with ordered pore structure, low acid strength and thermal stability are of primary concern. In such a scenario, the zeolite molecules can be assembled into a framework structure such that the salient features of zeolite and mesoporous aluminosilicates materials are maintained. Hence, the mesoporous aluminosilicates MAS-7 and MAS-9 were synthesized via P123 surfactant with as formed zeolite beta and precursors of ZSM-5. Further, these mesoporous aluminosilicates can serve as a support for HPA owing to their exposed surface area available and ordered mesoporosity and in turn improving the acidity of the catalysts.

In the existing literature, aluminosilicates with ordered mesoporosity assembled directly from zeolite precursors are yet to be explored for the synthesis of biodiesel. This work focusses on HPW impregnated mesoporous materials with zeolite nanocrystallites like MAS-7 and MAS-9 as new catalysts for the biodiesel synthesis in a batch reactor. This chapter provides detailed insights into the surface chemistry of the catalysts when HPW is incorporated on MAS-7, and MAS-9 supports and its correlation with the catalytic activity.

A series of 5-45 wt % HPW on MAS-7/MAS-9 catalysts were prepared by wet impregnation technique. The synthesized supports and catalysts were employed for the biodiesel synthesis from low-quality oil like unrefined green seed canola oil. It is accessible in large quantities in the western provinces of Canada. The synthesized catalysts facilitated simultaneous transesterification and esterification reactions.

4.3 Experimental

4.3.1 Synthesis of MAS-7 and MAS-9 supports

Hydrothermally stable mesoporous aluminosilicates MAS-7 and MAS-9 with ordered hexagonal structures were synthesized from the assembly of tri-block polymer surfactant (P123, Fisher Scientific) with a precursor of zeolite beta and ZSM-5 in strongly acidic media according to the report Han et al. (2001) and Xia et al. (2014). The syntheses for MAS-7 and MAS-9 are as follows:

(1) The zeolite beta precursor solution was prepared by mixing 0.4 g of NaOH, 0.83 g of $NaAlO_2$, and 16.8 g of fumed silica into 75 mL of tetraethylammonium hydroxide (TEOAH, 1M in water, Aldrich) with molar ratios of 1.0/60/2.5/22/800 for $Al_2O_3/SiO_2/Na_2O/TEAOH/H_2O$. The mixture thus obtained was aged at 140 °C for 4 h. (2) The precursor solution with ZSM-5 was obtained by adding 0.35 g of $NaAlO_2$ in 14 mL of tetrapropylammonium hydroxide solution (TPAOH, 1M in water, Aldrich), and 24 mL of tetraethyl orthosilicate (TEOS, >98%, Aldrich) with 68 mL of water. The molar ratios of $Al_2O_3/SiO_2/Na_2O/(TPA)_2O/H_2O$ were maintained at 1.0/50/1.0/7/1800. The precursor solution was then aged at 100 °C for 3 h. (3) 10 g of polymer surfactant (P123) was dissolved in acidified water (265 mL of water mixed with 98 mL of 10 M HCl). The precursor solution obtained in step (1) or (2) was introduced dropwise to the polymeric solution and stirred at 40 °C for 20 h. Then, the mixture was then transferred into an autoclave at 100 °C for 36 h. (4)

The white product obtained was filtered, dried in an oven and calcined at 550 °C for 5 h for template removal.

4.3.2 Preparation of HPW/MAS-7/MAS-9 catalysts

A series of 5-45 wt % HPW anchored MAS-7/MAS-9 catalysts were prepared using a wet impregnation method. A 10 mL of the methanolic solution of HPW was used to impregnate 1 g of MAS-7/MAS-9 supports. The samples were stirred at room temperature, and oven dried at 110 °C and was further calcined.

4.4 Catalyst characterization

The BET isotherms were assessed using Micrometrics ASAP 2000. The samples were degassed at 300 ^{0}C for 3 h. The surface area was obtained with the Brunauer–Emmett–Teller (BET) method. The pore size distribution was obtained with the help of the Barrett-Joyner-Halenda (BJH) model.

The low angle and wide angle diffractions were obtained on a D8 Advance Powder diffractometer. [Monochromatic Cu Kα (λ=1.54Å) radiation]. Supports and catalysts samples were scanned from 1.5° to 10° and 10-90° with a 2θ step size of 0.01°.

For FT-IR spectroscopy of pyridine adsorption, the measurements were performed on Fourier transform spectrometer (Vertex 60 Bruker, Germany) between the region 4000-400 cm^{-1} with a resolution of 4 cm^{-1}. Raman spectra of the catalysts were obtained on a Raman Invia Reflex Raman microscope spectrometer in the spectral range 98 to 1497 cm^{-1} using a 785 nm solid state diode (Renishaw Inc.) and a 1200 1/mm grating.

^{29}Si NMR technique was applied to study the chemical environment of ^{29}Si nuclei in these mesoporous aluminosilicates.^{29}Si solid-state NMR experiments were carried on AVANCE III HD Bruker spectrometer operated at 99.36 MHz (^{1}H frequency at 500.13MHz), with a DOTY CP-MAS probe of 4mm. Both ^{29}Si MAS and CP/MAS (Cross Polarization) experiments were carried out at 6 kHz spinning speed, along with ^{1}H decoupling. For ^{29}Si MAS experiments, 1024 – 4096 scans were accumulated for different samples, with a 45° pulse and a 5 s recycle delay. For ^{29}Si CP/MAS experiments, 2048 – 4096 scans were accumulated for different samples, with a 2s recycle delay and a 5.0 ms of contact time. ^{29}Si Chemical shifts are referenced to a Na-DSS (4, 4-dimethyl-4-silapentane-1-sulfonic acid sodium salt) at 0 ppm.

The X-ray absorption near edge spectra analysis was carried out to study the environment of W in HPW supported catalysts. The X-ray absorption spectra were obtained on the IDEAS beamLine at CLS (Canadian Light Source Inc., Canada.). Ge (220) double crystal monochromator was employed to cover the energy range of tungsten L_1 and L_3-edges in transmission mode and fluorescence yield using a Si drift detector. Reference compounds, such as Na_2WO_4 H_2O, and H_2WO_4 were measured in transmission mode for comparison and energy calibration. All XANES data were processed using the Athena program.

The Al structure in HPW supported on aluminosilicates was obtained from the Al K-edge spectra. Samples were pressed onto a carbon tape and the Al K-edge spectra was obtained using SGM beamline at CLS.

The total surface acidity of the synthesized supports and HPW impregnated catalysts were determined by the acid-base titration. 100 mg of catalyst was dissolved in 20 mL of NaOH (0.1M). The solution was agitated at room temperature for 3 h to facilitate ion exchange. The supernatant obtained after centrifugation was titrated with 0.1 M HCl using phenolphthalein indicator. The surface acidity was indicated in terms of mol of H^+/g of the catalyst.

4.5 Catalytic activity

The performance of synthesized catalysts was determined via simultaneous transesterification and esterification of green seed canola oil (Free Fatty Acid (FFA) content- 5.5 wt %). 100 mL of the Parr reactor was used to carry out the reaction. 35 g of green seed oil was preheated to 60 °C. A weighed amount of catalysts was introduced into the reactor vessel followed by methanol. The preliminary experiments for the catalysts were conducted at 200 °C, methanol to oil molar ratio of 20:1, 2.5 wt % catalyst (weight of the catalysts based on green seed canola oil) and 600 rpm.

After the reaction, the contents were filtered to separate the catalysts. For ester phase analysis, HPLC was used (Agilent Technologies). A Hewlett-Packard 1100 series was employed in ester content analysis. Two Phenogel columns (5µ 100 Å 300 X 7.80 mm) with a column temperature of 24 °C were used. Tetrahydrofuran at 1 mL/min for 20 min was used as a mobile phase. The detector temperature was maintained at 35 °C whereas the sample injection consists of 20 µl. The equation (4.1) determines the ester yield (wt %)

$$Ester\ yield\ (wt\ \%) = \frac{Methyl\ ester\ weight\ in\ ester\ phase}{Ester\ phase\ weight} \times 100 \quad \text{.....(4.1)}$$

The acid value (AV) of the produced biodiesel was calculated as per AOCS-D6751 method, and the equation (4.2) determines the conversion of free fatty acid.

$$Conversion(\%) = \frac{AV(initial) - AV(final)}{AV\ (initial)} \times 100 \quad \text{.....(4.2)}$$

The leaching test of HPW supported mesoporous aluminosilicates was performed with methanol as solvent. Methanol is one of the reactants in transesterification and esterification reaction, and HPW is highly soluble in the polar solvent. Hence, the supported catalysts were evaluated by adding 50 mL of methanol to 0.02 g of the solid at room temperature and kept under magnetic stirring for one hour. An aliquot was withdrawn at regular intervals using a 1 mL syringe with a 0.2 µm filter. The concentration of HPW was measured by UV-vis spectrophotometer (UV mini 1240 Shimadzu) with a scanning 200-800 nm wavelength.

4.6 Results and discussions

4.6.1 Characterization of the support and catalysts

Surface analysis

The synthesized catalysts, 0–45 wt % HPW/MAS-7, had a high surface area in the range of 374–998 m^2/g. For 0–45 wt % HPW/MAS-9, it ranged from 333 to 740 m^2/g. The introduction of the HPW anions significantly changes the surface characteristics as the surface area decreases with an increase in the HPW content. From Table 4.1, it can be seen that as more HPW anions are incorporated, more depositions occurred on the external surface and resulted in the lowering of the surface area (Hoo and Abdullah, 2014). However, in case of 25 wt % HPW/MAS-7 and 15 wt % HPW/MAS-9, an increase in micropore area was observed which might be due to the development of abnormalities in the pores. Also, for the other catalysts, a decrease in micropore and mesopore areas and pore volume was observed after HPW loading, thus suggesting that HPW is deposited in the mesoporous channels and dispersed well on the surface of supports with ordered mesopores. In case of MAS-7, the average pore size, as well as the unit cell parameter, hardly showed any change

with HPW loading, but the values obtained slightly varied from the values of MAS-7/MAS-9. The reason behind this phenomenon can be explained by the fact that MAS-7/MAS-9 possesses both micropores and mesopores.

The *t*-plot analysis showed that MAS-7 and MAS-9 possessed microporous areas of 131.6 and 74.1 m^2/g, respectively. MAS-7 and MAS-9 possessed microporosities of 0.07 and 0.04 cm^3/g, respectively, whereas for the synthesized samples HPW/MAS-7/MAS-9, they varied in a nonsystematic way with HPW loading. The presence of microporosity in both MAS-7 and MAS-9 can be accredited to the occurrence of the respective primary units of zeolite MFI in the mesoporous walls (Han et al., 2001).

Table 4.1. Textural properties of the mesoporous aluminosilicate supports and HPW supported catalysts.

Catalyst	S_{BET} (m^2/g)	S_M (m^2/g)	S_{Ext} (m^2/g)	D_a (nm)	V_{micro} (cm^3/g)	V_T (cm^3/g)	V_{meso} (cm^3/g)	d_{100} (nm)	a_0 (nm)
MAS-7	998	131.6	866.3	4.2	0.07	1.1	1.1	11.0	12.7
5 wt % HPW/MAS-7	833	102.2	731.2	4.1	0.05	1.0	0.9	10.2	11.7
15 wt %HPW/MAS-7	739	55.0	684.0	4.4	0.03	0.9	0.8	10.3	11.9
25 wt %HPW/MAS-7	574	74.6	499.1	4.5	0.04	0.7	0.7	10.4	12.0
35 wt %HPW/MAS-7	503	62.0	440.4	4.4	0.03	0.6	0.6	10.4	12.0
45 wt %HPW/MAS-7	374	28.3	355.7	4.5	0.01	0.5	0.5	9.9	11.5
MAS-9	740	74.1	665.7	8.5	0.04	1.5	1.5	9.8	11.3
5 wt % HPW/MAS-9	649	43.4	605.9	8.7	0.02	1.4	1.4	1.0	11.5
15 wt % HPW/MAS-9	551	181.0	370.3	11.0	0.09	0.8	0.7	10.4	12.0
25 wt % HPW/MAS-9	426	69.6	356.5	8.0	0.04	0.9	0.8	9.9	11.5
35 wt %HPW/MAS-9	339	39.2	300.3	10.4	0.02	0.8	0.7	10.3	11.9
45 wt% HPW/MAS-9	333	30.6	302.2	8.4	0.02	0.7	0.7	9.9	11.5

a_0, unit- cell parameter determined from the position of the (100) diffraction line as $a_0 = 2d_{100}\sqrt{3}$; S_{BET} – surface area calculated by BET method; S_M- Micropore area; S_{Ext} – External surface area; D_a- mean pore diameter; V_{micro} – micropore volume ;V_T - Total pore volume; V- Mesopore volume.

Adsorption isotherm

The isotherms of N_2 for pure MAS-7 and MAS-9 and HPW supported catalysts are shown in Figures. 4.1 and 4.2. The isotherms of all catalysts are of type IV as per IUPAC categorization marked by step increase due to capillary condensation (relative pressure of 0.2 to 0.4) and exhibited H1 hysteresis loop characteristic of mesoporous solid with closure at around $p/p_0 = 0.45$ and 0.54 for MAS-7 and MAS-9, respectively.

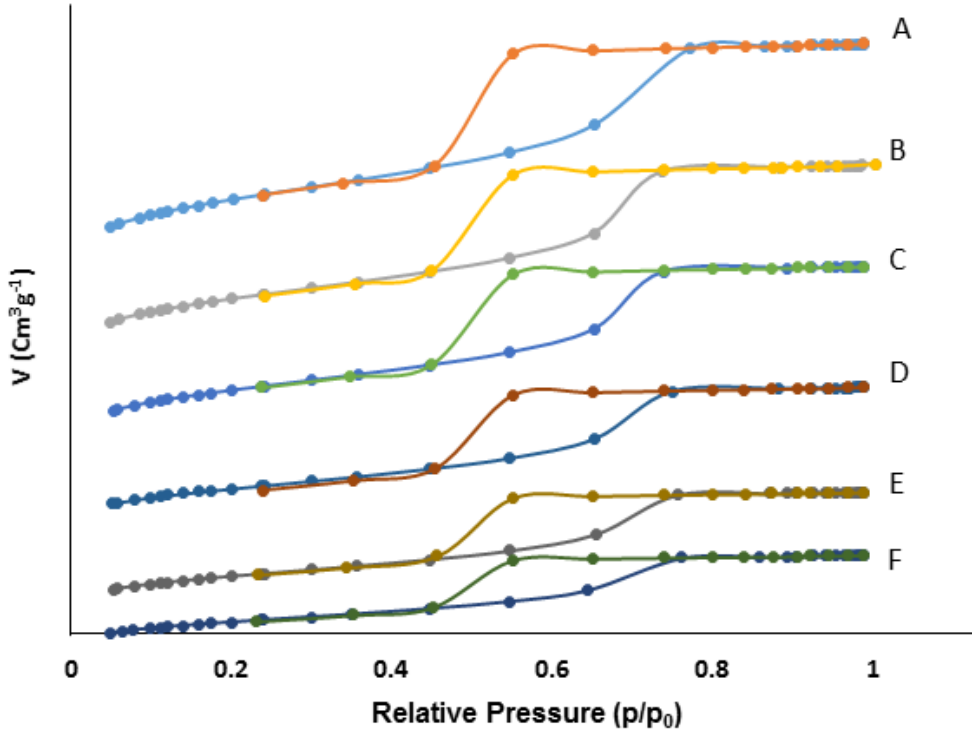

Figure 4.1. BET isotherms of (A) MAS-7, (B) 5 wt % HPW/MAS-7, (C) 15 wt % HPW/MAS-7, (D) 25 wt % HPW/MAS-7, (E) 35 wt % HPW/MAS-7, and (F) 45 wt % HPW/MAS-7.

The adsorption isotherms of HPW-impregnated MAS-7 catalysts hardly varied significantly, indicating that the mesoporosity of MAS-7 was unaffected by HPW loading, that is, for 5–45 wt % HPW/MAS-7, the shapes of the isotherms were similar to that of MAS-7, and the main part of the hysteresis loop remained at the same relative pressure. For 15–45 wt % HPW/MAS-9, the desorption branches extended to a lower relative pressure ($p/p_0 = 0.45$) compared to that of 5 wt % HPW/MAS-9 and MAS-9. It has been reported that HPW anions may occupy or

block the mesopores of the aluminosilicates, thus increasing the average pore size and decreasing the surface area (Kozhevnikov et al., 1996).

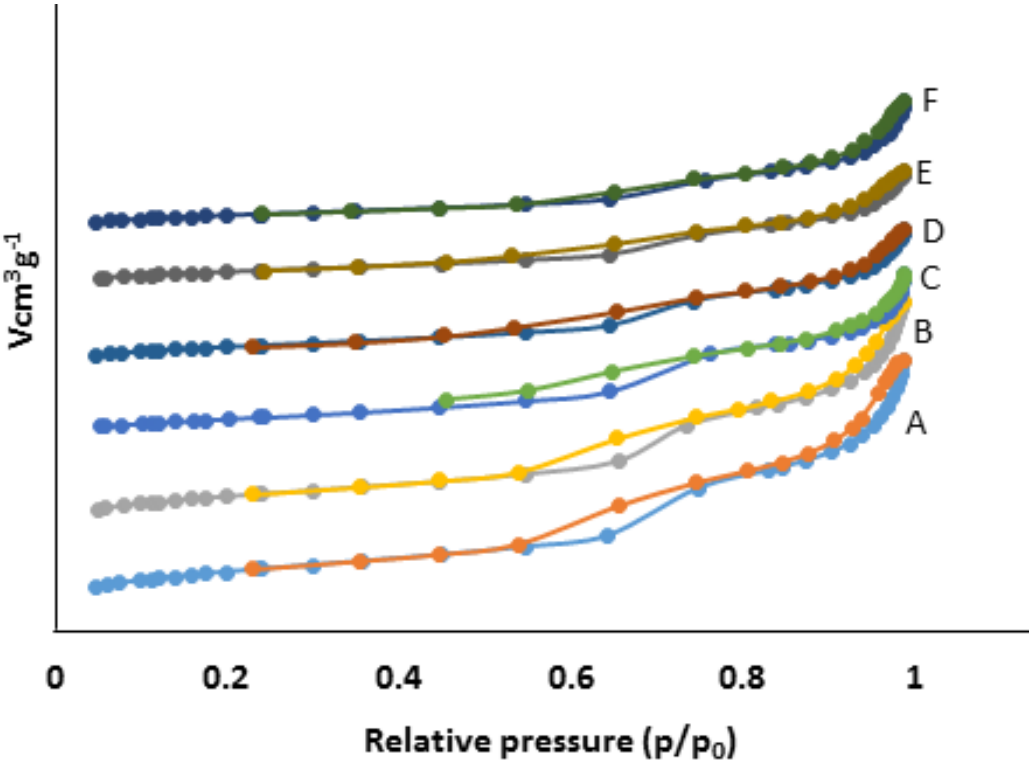

Figure 4.2. BET isotherms of (A) MAS-9, (B) 5 wt % HPW/MAS-9, (C) 15 wt % HPW/MAS-9, (D) 25 wt % HPW/MAS-9, (E) 35 wt % HPW/MAS-9, and (F) 45 wt % HPW/MAS-9.

X-Ray diffraction

The small-angle X-ray diffraction (XRD) patterns (0.5–10°) of MAS-7 possessed the strongest and weak diffraction peaks at 0.87° and 1.5°, ascribing to the (100) and (110) crystal planes, typical of the P6mm well-ordered hexagonal arrays of mesopores (Xia et al., 2014) (Appendix A, Figure A.1). The sharp (100) diffraction peaks for MAS-7 and MAS-9 at $2\theta = 0.87$ and 0.9, respectively, gave the d-spacing values of 11.0 and 9.8 nm. The cell parameters a_0 were 12.7 and 11.3 nm, respectively, for MAS-7 and MAS-9 based on the relationship $a_0 = 2d_{100}\sqrt{3}$. The wall thickness values calculated using the equation "wall thickness = a_0-pore diameter" were found to be 8.5 and 2.8 nm for MAS-7 and MAS-9, respectively. It has been reported that longer reaction duration and higher temperatures result in enlarged pore size and decreased wall thickness (Si et al., 1997). However, MAS-7, which was synthesized at a higher temperature of 140 °C as compared

to MAS-9 (synthesized at 100 °C), had a greater wall thickness and smaller pore size. The other factor, which can play a role in increasing wall thickness, is the nature of silica (Mokaya, 1999). Fumed silica, which is used in the synthesis of MAS-7, has a smaller unit of silicates and possesses a lower degree of polymerization with higher diffusion rates in solution as well as aggregates, resulting in the formation of thicker walls.

For the supported catalysts, hardly any change in the planes corresponding to the long-range structural ordering of MAS-7 and MAS-9 after HPW impregnation was observed. Hence, it can be concluded that the supports MAS-7 and MAS-9 retained their symmetry even after HPW loading.

The wide-angle diffraction patterns for HPW in bulk, supports, and 5–45 wt % HPW/MAS-7/MAS-9 catalysts are shown in Figures 4.3 and 4.4. A broad peak was observed at a 2θ value of 22.8° corresponding to an amorphous structure of silica, which was more pronounced in case of the MAS-7 and HPW/MAS-7 catalysts compared to that of HPW-supported MAS-9 catalyst. It can be attributed to the source of silica used in the preparation of both the supports, which was fumed silica in case of MAS-7 and tetraethyl orthosilicate (TEOS) for MAS-9.

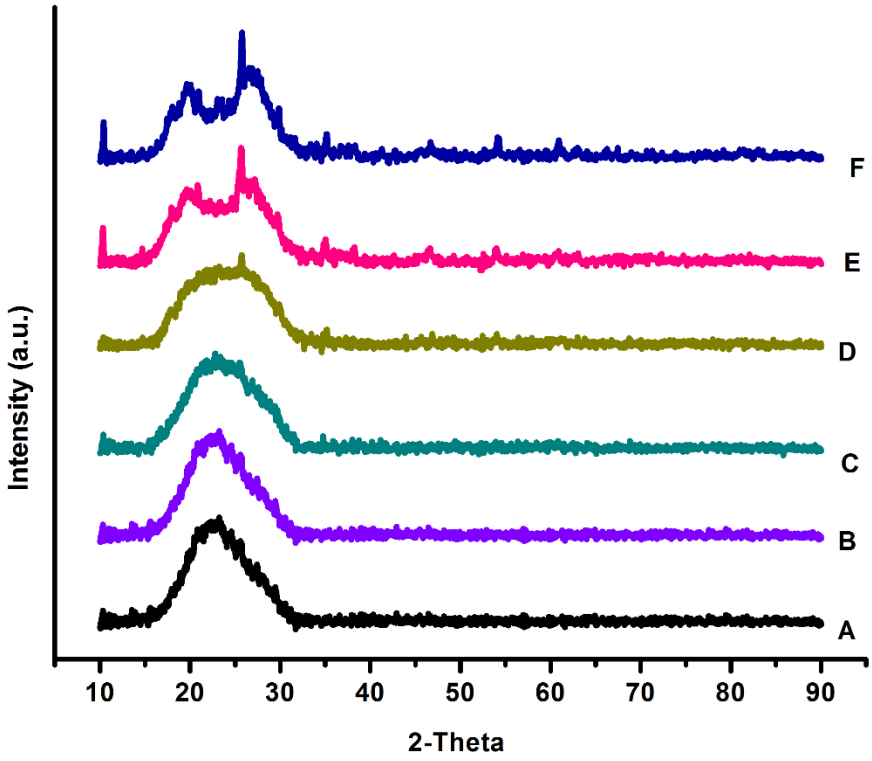

Figure 4.3. Wide-angle XRD patterns for (A) MAS-7, (B) 5 wt % HPW/MAS-7, (C) 15 wt % HPW/MAS-7, (D) 25 wt % HPW/MAS-7, (E) 35 wt % HPW/MAS-7, and (F) 45 wt % HPW/MAS-7.

This peak was observed up to the loadings of 25 and 15 wt % for MAS-7 and MAS-9 supports, respectively. The absence of the characteristic peaks of HPW at these loadings signified that HPW was well-distributed on the support surface and also inside the hexagonal channels and in the aluminosilicate pore walls, as the pore size of MAS-7 and MAS-9 (4.2 and 8.5 nm) is higher than that of HPW (1.9 nm) crystals. As the loading increases from 25 to 45 wt %, peaks related to HPW gradually occur. As the XRD patterns are related, irrespective of the presence or absence of clear crystals, the diffraction patterns for HPW on MAS-7 and MAS-9 show that HPW introduced is precisely distributed on the MAS-7 and MAS-9 surfaces at a higher loading of 15 wt %. As the loading of HPW increases, some HPW exists as a crystal phase.

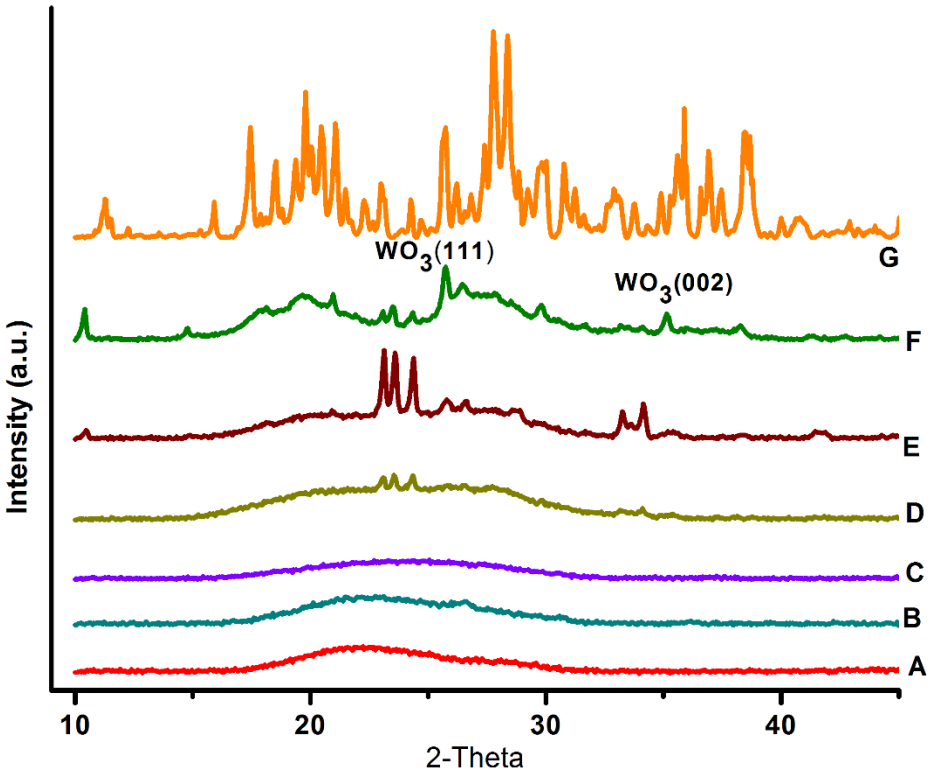

Figure 4.4. Wide-angle XRD patterns for (A) MAS-9, (B) 5% HPW/MAS-9, (C) 15% HPW/MAS-9, (D) 25% HPW/MAS-9, (E) 35% HPW/MAS-9, (F) 45% HPW/MAS-9, and (G) HPW

Raman spectral analysis

Further, the nature of impregnated HPW was studied using Raman spectroscopy. The spectra of HPW supported on MAS-7 and MAS-9 are shown in Figures 4.5 and 4.6. The crystalline HPW shows the characteristic bands at 1009.8 cm^{-1} (symmetric stretching of PO_4 sites), 991 cm^{-1} [antistretching (vas) of $W=O_t$], and 931 [ν_{as} (W–O–W)], which is in good agreement with the literature data (Guo et al., 2008; Ross-Medgaarden et al. 2008). The low-intensity bands appearing at 538 and 516 cm^{-1} are attributed to W–O–W {symmetric stretching [ν(s)]} and O–P–O [asymmetric deformation (ν_{as})] (Holclajtner-Antunović et al., 2010). After the impregnation of HPW into the MAS-7 and MAS-9 lattices, the peaks corresponding to the PO bond and W═O vibrations were broadened; therefore, a broad peak was seen in the range of 921–1053 cm^{-1}. For 5 wt % loadings, the characteristic keggin bands for supported HPW are hardly observed, whereas 15 and 25 wt % loadings show only broad- and low-intensity main bands at about 985 and 1010 cm^{-1}, suggesting an interaction of the keggin unit and the MAS-7/MAS-9 framework.

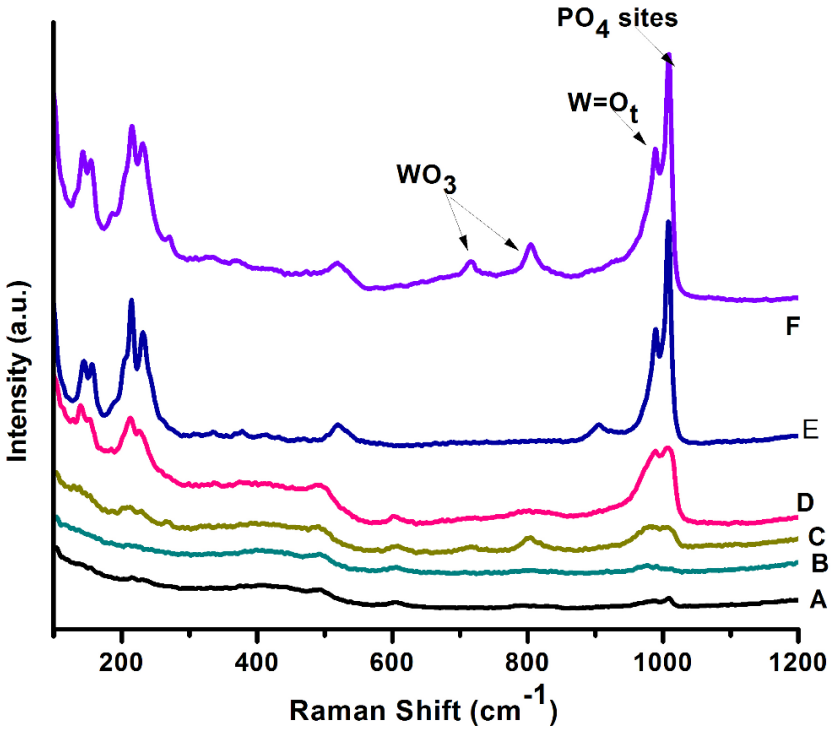

Figure 4.5. Raman spectra of (A) MAS-7, (B) 5 wt % HPW/MAS-7, (C) 15 wt % HPW/MAS-7, (D) 25 wt % HPW/MAS-7, (E) 35 wt % HPW/MAS-7, and (F) 45 wt % HPW/MAS-7.

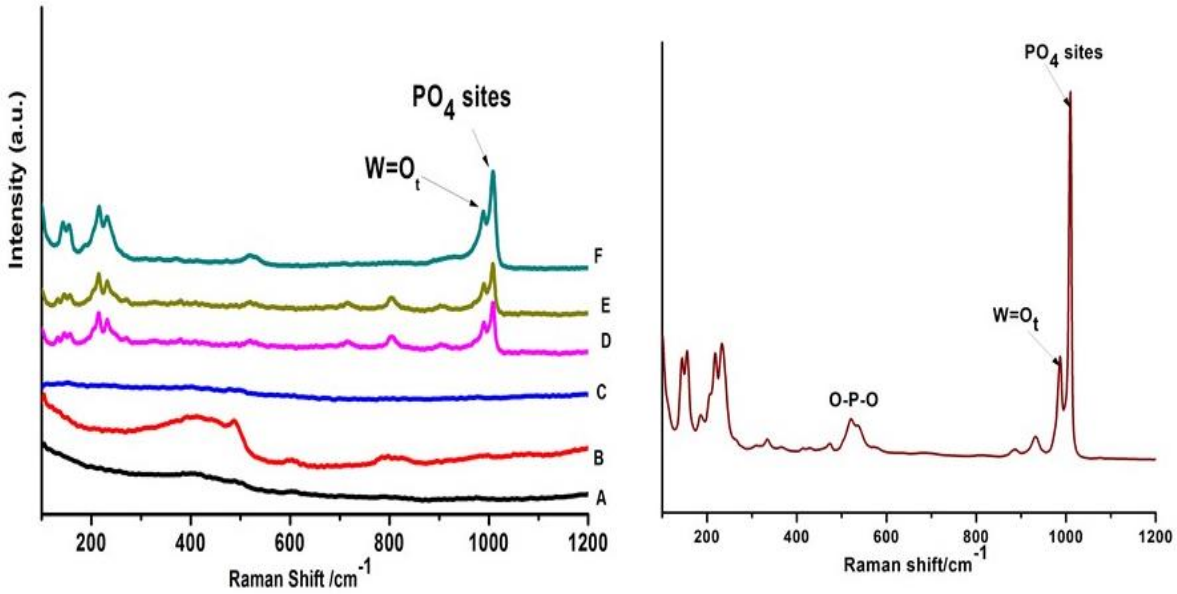

Figure 4.6. Raman spectra of (A) MAS-9, (B) 5 wt % HPW/MAS-9, (C) 15 wt % HPW/MAS-9, (D) 25 wt % HPW/MAS-9, (E) 35 wt % HPW/MAS-9, (F) 45 wt % HPW/MAS-9, and (G) HPW.

However, in the case of 35 and 45 wt % HPW loadings, sharp and higher intensity peaks were observed resembling that of pure HPW, thus indicating that the keggin unit environment is identical to that of HPW and hence confirms the retainment of the keggin structure even after anchoring to the supports. However, for 45 wt % HPW/MAS-7, additional peaks occurred at 710 and 804 cm^{-1}, attributed to the presence of crystalline WO_3 (Xu et al., 2014). This suggests that despite the retainment of the keggin unit, there was some tungsten oxide formation on the surface.

^{29}Si Magic angle spinning (MAS) and CP/MAS NMR studies

The interaction of impregnated HPW with the mesoporous aluminosilicate framework was studied via ^{29}Si nuclear magnetic resonance (NMR). $^{1}H \rightarrow {}^{29}Si$ cross-polarization (CP, via dipolar coupling) detects the NMR signal of silicon nuclei that are close to protons, which makes it a reliable and sensitive technique for the detection of silicon nuclei at or close to the surface of the MAS-7/MAS-9 materials. Figure 4.7 B, D shows the ^{29}Si CP/MAS NMR spectrum of the support MAS-7 and the synthesized catalyst HPW/MAS-7 sample obtained at room temperature. The spectra showed three ^{29}Si signals at about −93, −102, and −110 ppm, reflecting the presence of Q_2, Q_3, and Q_4 units (Figure 7B,D) (Brahmkhatri and Patel, 2011). A dominating resonance is observed at −102 ppm, and it is ascribed to Si* nuclei within the X silicon linkages of $XOSi^*(OSi)_3$

(Q_3), where X is H or HPW. The shoulder at −93 ppm resembles the silicon atoms on the surface with two siloxane bonds and either single- or hydrogen-bonded germinal silanol sites, $(SiO)_2{*}(SiOX)_2$ (Q_2), whereas at −110 ppm the resonance is due to the hydroxyl-free Q_4 (siloxane) units—no heterolinkages (either Si–O–H or Si–O–HPW) (Roberge et al., 2002). Note that this signal at −110 ppm dominates the ^{29}Si MAS NMR spectra of the corresponding system (Figure 4.7A,C), which makes sense as there are much more silicon atoms inside the framework than on the surface. The reason leading to a weak ^{29}Si signal for the Q_4 unit in the CP/MAS spectra is that the signal intensities of the CP/MAS spectra rely on the number of protons and the dipolar coupling strength (i.e., the distance) between ^{1}H and ^{29}Si, rather than on the amount of silicon nuclei. Therefore, CP/MAS is not a suitable technique for quantitation. ^{29}Si MAS NMR should be applied for this purpose.

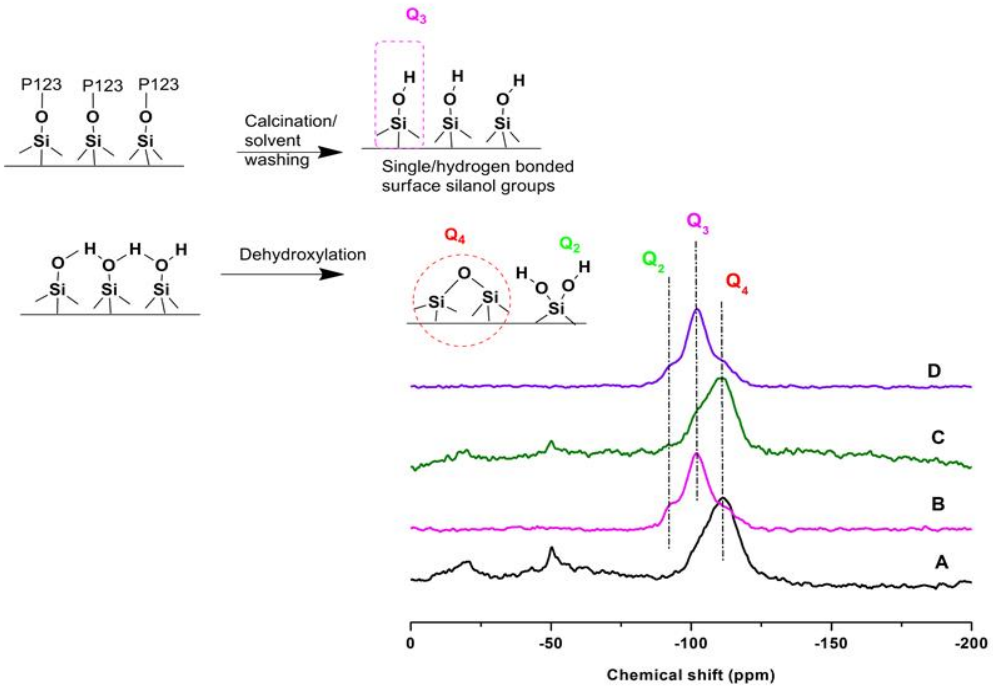

Figure 4.7. ^{29}Si{^{1}H} MAS spectra of (A) MAS-7 and (C) 35 wt % HPW/MAS-7; ^{29}Si CP/MAS NMR spectra of (B) MAS-7 and (D) 35 wt % HPW/MAS-7.

Figure 4.7 A,C shows the ^{29}Si MAS NMR spectra with proton (^{1}H) decoupling of MAS-7 and HPW/MAS-7. The signal at about −110 ppm, originated from Q_4 units, dominates the spectra, especially for MAS-7. The signals from Q_2 and Q_3 can be clearly seen in the ^{29}Si MAS spectrum

of HPW/MAS-7. The spectra were therefore deconvoluted into three components, with the ^{29}Si chemical shifts at about −93, −102, and 110 ppm corresponding to the silicon nuclei in the Q_2, Q_3, and Q_4 units, respectively. Using the signal intensities from spectral deconvolution (Table 4.2), the fractional population of the surface germinal hydroxyl silanol sites and isolated silanol sites was calculated. From the fractional populations, we can calculate the surface SiOH concentration and the number of OH groups per square nanometer (η_{OH}).

Table 4.2. Quantification of Peak Areas in the ^{29}Si MAS NMR spectra of mesoporous aluminosilicates and HPW supported catalysts and the number of hydroxyl groups per unit area.

	Q_2 % $(SiO)_2*(SiOX)_2$	Q_3% $XOSi*(OSi)_3$	Q_4% $(SiO)_4*Si$	$(Q_2+Q_3)/Q_4$	η_{OH} /nm^2
MAS-7	7.2	32.1	60.8	0.6	4.3
HPW/MAS-7	2.1	41.5	56.4	0.8	7.5
MAS-9	13.3	37.8	48.9	1.0	7.7
HPW/MAS-9	11.3	42.8	45.8	1.2	17.5

Where X= H/HPW

According to Léonardelli et al. (1992), if the different chemical species in Q_2, Q_3, and Q_4 are proportioned as x, y, and z, the number of OH groups, assuming that all the hydroxyl groups are on the outer surface, i.e., on the surface measured by the BET method is given by

$$\eta_{OH} = \frac{f_s(1+f_g)}{S}\frac{N_A}{60+9f_s(1+f_g)} \quad \text{.....(4.3)}$$

where $f_g = x/(x + y)$, $f_s = x + y$, and N_A is the Avogadro number. The concentrations of x, y, and z can be given as $x = fgfs$, $y = fs(1 – fg)$, $z = 1 – fs$. The η_{OH} values for the supports MAS-7 and MAS-9 and the synthesized catalysts, as well as the distribution of Q_2, Q_3, and Q_4 units and their relative values, are shown in Table 4.2. The intensity redistribution of these silicon sites is thought to be due to the reactions of the surface SiOH groups with HPW. During impregnation, the protons of HPW ($H_3PW_{12}O_{40}$) are transferred to the OH groups of the silica surface, mainly with the germinal silanols of the support. Thus, the terminal W═O groups within the keggin unit interact with the surface $(AlO)(HO)Si*(OSi)_2$ groups via W–O–Si(Al) covalent bonding. Hence, the variation in the distribution of Q_4 units in the supported catalysts was observed because of the

formation of heterolinkages. Also, the distribution of Q_3 unit in the HPW-supported catalysts was found to increase, which could be probably due to the conversion of two germinal units into silanol sites (Q_3) upon subsequent dehydroxylation. Therefore, a higher value of $(Q_2 + Q_3)/Q_4$ was observed for the HPW-supported catalysts, thereby suggesting an interaction between the framework of mesoporous aluminosilicates and HPW. A similar kind of distribution of Q_2, Q_3, and Q_4 units was observed for the HPW/MCM-41 catalysts (Brahmkhatri and Patel, 2011).

Hydroxyl framework and Lewis and Brønsted acidity

Figure 4.8 A shows the infrared (IR) νOH spectra of the mesoporous aluminosilicate MAS-7 before exposure to the pyridine (Py) atmosphere. The band appearing at 3741 cm^{-1} can be assigned to the external silanols, whereas the other having a vibrational frequency of 3600 cm^{-1} is associated with the Brønsted acidity, and the intensity of this band corresponds to the aluminum content of the zeolite and with the extent of proton exchange (Wang and Nicholson, 2004).

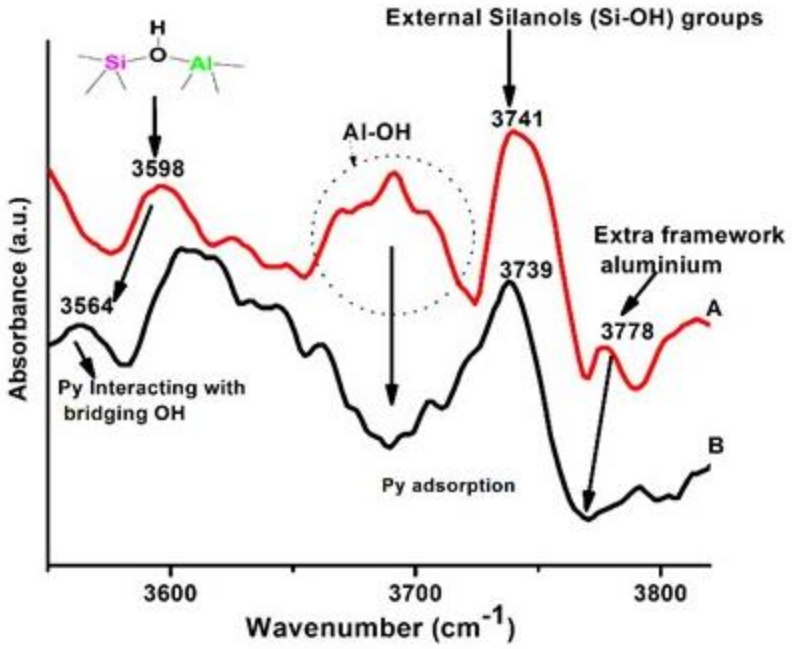

Figure 4.8. FTIR spectra of the hydroxyl stretching vibrations between 3820 and 3550 cm^{-1} of the mesoporous aluminosilicates (A) MAS-7 and (B) pyridine-desorbed MAS-7 at 150 °C.

Further, the relative intensity of external silanol when correlated with that of the Brønsted acid band indicates smaller primary crystallites and higher external surface area and agrees well

with the BET and XRD analyses. The νOH spectra also show the occurrence of a weak band and a broadband at 3778 and 3720–3652 cm^{-1}, respectively, ascribed to small noncharged extra-framework aluminum and to the OH stretching vibrations of Al–OH, where Al would be linked with the framework by chemical bonds (Roberge et al., 2002).

Figure 4.8 B represents the νOH spectra of the pyridine-desorbed MAS-7 sample. The signal at 3600 cm^{-1} reappeared after pyridine desorption at 150 °C, shifting to a lower wavenumber, thus indicating an interaction with the bridging OH group, whereas the band at 3720–3652 cm^{-1} was found to be absent. The disappearance of the band at 3720–3652 cm^{-1} perhaps is due to the adsorption of pyridine on the Al hydroxyl species with the subsequent dispersal of νOH vibration. Also, the band appearing at 3778 cm^{-1} was found to be completely removed, and hence it can be concluded that it is fully available for pyridine adsorption. On the basis of the weak base interaction, it has been reported that the band at 3778 cm^{-1} associated with the Al–OH species is moderately acidic (Roberge et al., 2002). Moreover, the bands in the region 3880–3700 cm^{-1} are usually present on aluminum oxides, in which Al is present in the tetrahedrally coordinated part (Trombetta et al., 2000). Hence, it can be proposed that OHs are present over the tetrahedral Al cations and are also associated with the formation of Lewis sites (because of the coordinatively unsaturated Al^{3+} cations). On the other hand, the band at 3746 cm^{-1} of the OH vibration stretching of silanol remains unaltered. Isernia (2013) reported a similar observation.

To conclude, MAS-7 showed four distinct types of OH groups with varying degrees of acidity, except for the terminal OH groups. The occurrence of these different OH groups on the metal oxide surface can promote the bonding to metal sites of different coordinations. Hence, this allows us to propose that the interaction of the HPW keggin structure can take place at these sites.

The identity of the acidic sites (Brønsted and Lewis acids) present in mesoporous aluminosilicates and HPW-supported catalysts with varying loadings has been deduced from the IR spectra of the framework vibrations of the adsorbed pyridine (Figures 4.9 and 4.10). The pyridine adsorption on MAS-7 and MAS-9 yields IR bands at 1448, 1602, and 1634 cm^{-1}. The peak at 1448 cm^{-1} corresponds to the hydrogen-bonded pyridine and hence ascertains the surface OH group accessibility (donor H-bond sites), whereas the bands at 1602 and 1634 cm^{-1} indicate the formation of LPy species (exposing the unsaturated metal sites) and Brønsted acid sites, respectively. The intensity at 1535 cm^{-1}, attributed to the formation of BPy species, resulted in an

increased intensity at higher HPW loading (>25 wt % for MAS-7 and >15 wt % for MAS-9). The increase in Brønsted acidity with increasing HPW surface coverage can correspond to the polytungstate clusters, which can delocalize the protons among the neighboring tungsten trioxide species. Their occurrence was noticed in the Raman spectra by the presence of W–O–W bands at a loading of 45 wt % (Figure 4.5 F). Similarly, the occurrence of the peaks at 1486 and 1624 cm^{-1}, corresponding to the formation of adjacent Lewis and Brønsted and Lewis acidic sites, was observed at higher HPW loadings.

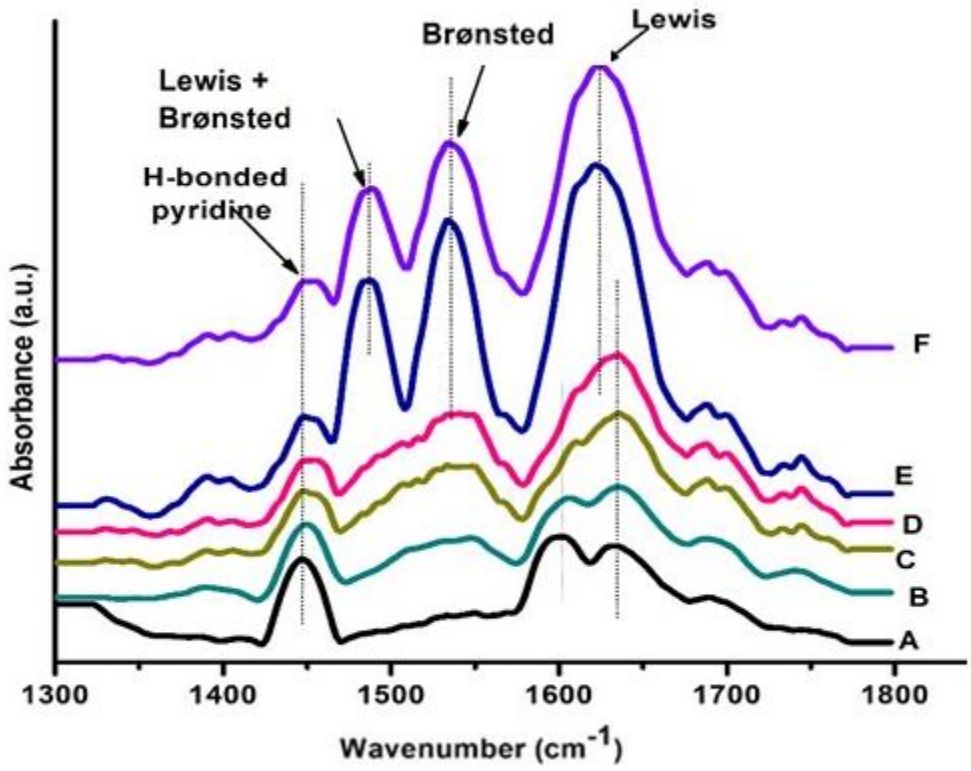

Figure 4.9. FTIR spectra in the 1300–1800 cm^{-1} range after pyridine desorption at 150 °C of (A) MAS-7, (B) 5 wt % HPW/MAS-7, (C) 15 wt % HPW/MAS-7, (D) 25 wt % HPW/MAS-7, (E) 35 wt % HPW/MAS-7, and (F) 45 wt % HPW/MAS-7.

A sudden increase in peak for Lewis and Brønsted acidity was observed for MAS 7 compared to MAS-9 at a HPW loading of 35 and 45 wt %. This may be due to the different interactions of the HPW with MAS-7 and MAS-9 support hydroxyl groups and the amount of HPW dispersed. MAS-7 support had OH group density (4.3 η_{OH} /nm^2) lower than that of MAS-9 (7.7 η_{OH} /nm^2) and the amount of HPW adsorbed is lower. As HPW loading increases, there is a separate phase and the

apparent Brønsted acidity arises due to W-OH groups (Ramis et al., 1992). The increase in peak for Lewis acidity can be due to the free electrons in the tungsten (Hernández-Cortéz et al., 2003).

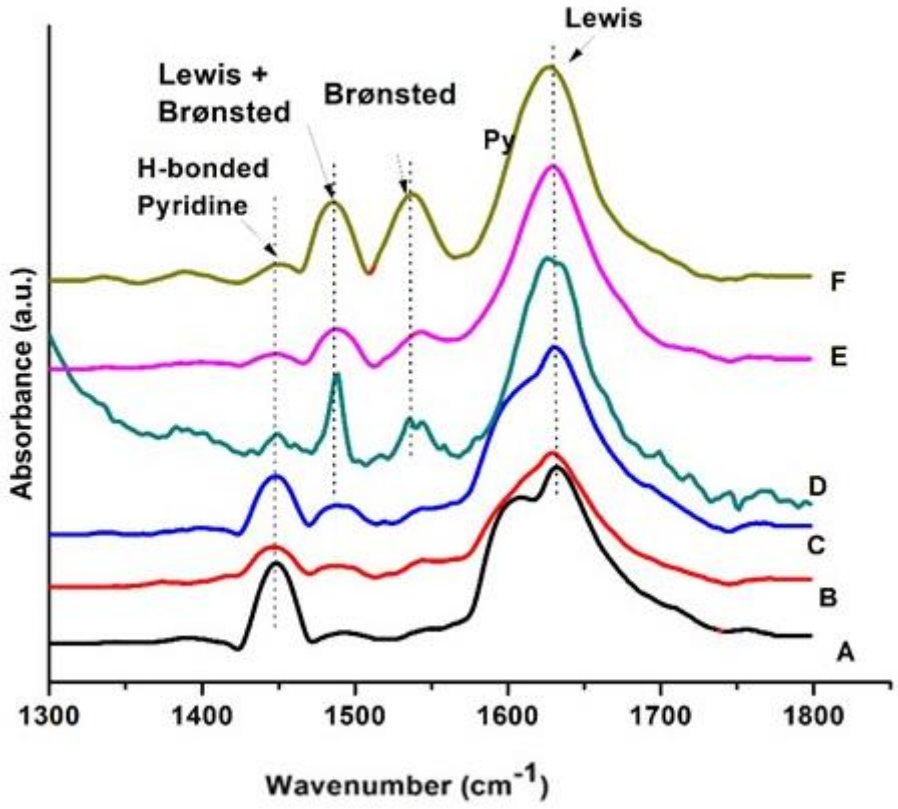

Figure 4.10. FTIR spectra in the 1300–1800 cm^{-1} range after pyridine desorption at 150 °C of (A) MAS-9, (B) 5 wt % HPW/MAS-9, (C) 15 wt % HPW/MAS-9, (D) 25 wt % HPW/MAS-9, (E) 35 wt % HPW/MAS-9, and (F) 45 wt % HPW/MAS-9.

W L_1 and L3 –Edge XANES

W L_3 –Edge

W - L_3 edge spectra exhibit prominent features referred to as white line arises due to electronic transition from 2*p* 3/2 state to 5*d* unoccupied states accompanied by several excitations for hybridized W 5d–O 2p conduction band. Figure. 4.11 (I) depicts the L_3 edge spectra of tungsten for the reference samples (A) H_2WO_4, (B) Na_2WO_4 H_2O, and synthesized catalyst sample (C) 45 wt % HPW/MAS-9. The W-L_3 spectrum of HPW/MAS-9 was found to be similar to that of H_2WO_4

but different from Na_2WO_4, H_2O. Hence, it can be said that 45 wt % HPW/MAS-9 has O*h* symmetry as H_2WO_4 exhibit O*h* symmetry while Na_2WO_4 showed T_d symmetry.H_2WO_4 shows a broad peak, whereas unsymmetrical peak is observed for Na_2WO_4. These dissimilarities in the white line shape are because of tungsten 5d states ligand field splitting. Yamazoe et al. (2008) stated that 5d orbitals splitting of tungsten tetrahedral unit is smaller than an octahedral unit. The second order derivative spectra were used in order to describe the splitting of the 5d orbitals in t_{2g} (d_{xy}, d_{xz}, d_{yz}) and e_g (d_z^2, $d_{x^2-y^2}$). Figure. 4.11 (II) shows the 2nd order derivatives XANES spectra of W-L_3 of 45 wt % HPW/MAS-9 and reference samples. The ligand field splitting was more readily observed for tungstic acid (H_2WO_4) in the second-order derivative plot, and the energy gap indicates the d-orbital splitting. H_2WO_4 is having nearly an octahedral symmetry, and the lower energy peak is referred as a transition to orbital t_{2g} vacancy, whereas the peak at higher energy is ascribed to excitation to an orbital e_g vacancy. The crystal field splitting [$\Delta d = E(e_g) - E(t_{2g})$] for H_2WO_4 and 45 wt % HPW/MAS-9 was found to be 3.5 and 4.09 eV, respectively, whereas the WO_4 units, as in case of Na_2WO_4, show a minima in lower energy as the 5d orbital split is small in the tetrahedral tungsten unit. The crystal filed splitting or the energy gap for Na_2WO_4 between the shoulder and the large peak was found to be 1.5 eV, which is pretty much closer to the value reported in the literature (Yamazoe et al., 2008).

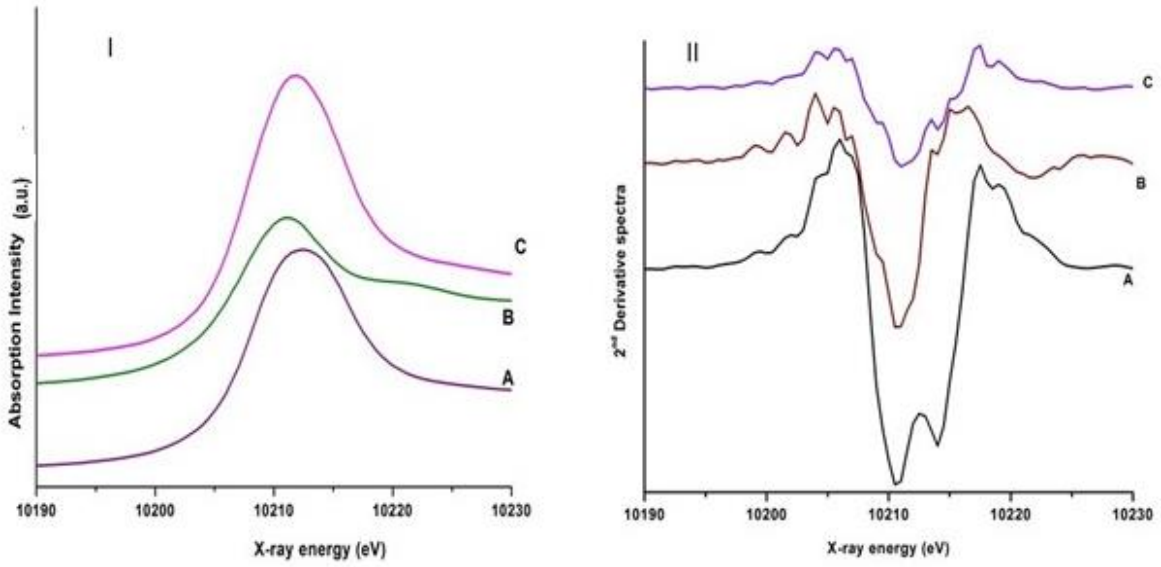

Figure 4.11. W L_3 XANES spectra (I) and second derivative spectra (II) of (A) H_2WO_4, (B) $Na_2WO_4 \cdot H_2O$, and (C) 45 wt % HPW/MAS-9.

L_1 – Edge

The pre-edge feature in W L_1 spectra is ascribed to 2s to d-p orbitals transition, sensitive to W bonding environment symmetry. The p-orbitals unoccupied hybridize strongly with d band in case of tetrahedral symmetry but not for regular octahedral. For tetrahedral symmetry, the unoccupied p orbitals strongly hybridize with d band but not for regular octahedral symmetry.

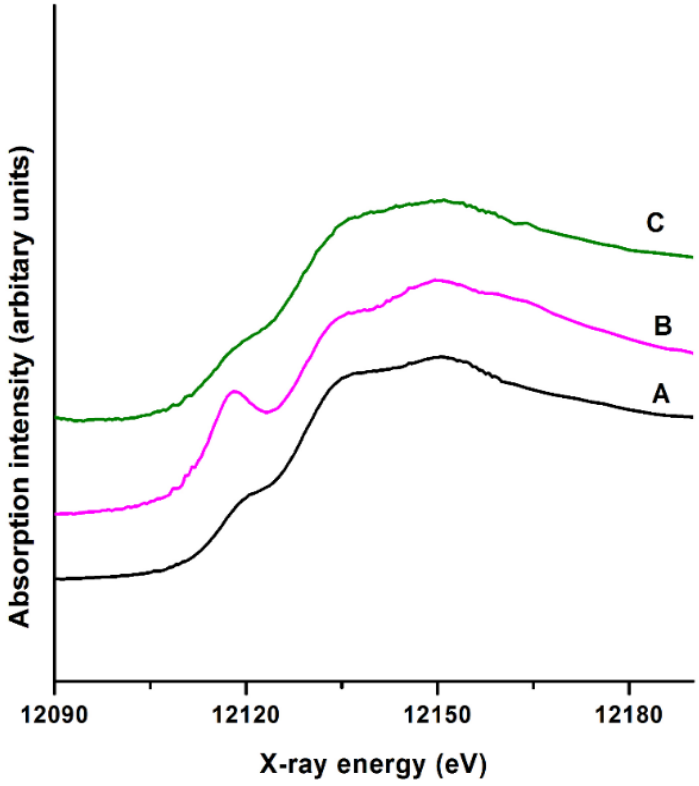

Figure 4.12. W L_1-edge XANES (A) H_2WO_4 (B) $Na_2WO_4 \cdot H_2O$ (C) 45 wt % HPW/MAS-9.

45 wt % HPW/MAS-9 and H_2WO_4 with W in octahedral symmetry show small pre-edge peaks.

As 2s → 5d transition is formally dipole-forbidden, regardless of the symmetry, however, in case of distortion from the ideal symmetry, the hybridization of 5p/5d orbitals makes 2s → 5d transition possible, and therefore the pre-edge peak of Na_2WO_4 having the tetrahedral units of W is much more intense than the other reference samples (Figure 4.12).

Curve-fitting for W L_1-edge was done using an arctangent and Lorentz function similar to the pre-edge peak derivation from the L_3-edge (Appendix A, Figure A.2). As H_2WO_4 and 45 wt % HPW/MAS-9 lack the hybrid d and p orbitals, mainly quadrupole electron transition could take place from 2s to t_{2g} and e_g orbitals of 5d. Hence, the pre-edges of H_2WO_4 and 45 wt % HPW/MAS-

9 were fitted with two Lorentz functions, whereas the pre-edge of Na_2WO_4 was fitted with one Lorentz function.

Conjointly W L_1 and L_3 - edge XANES

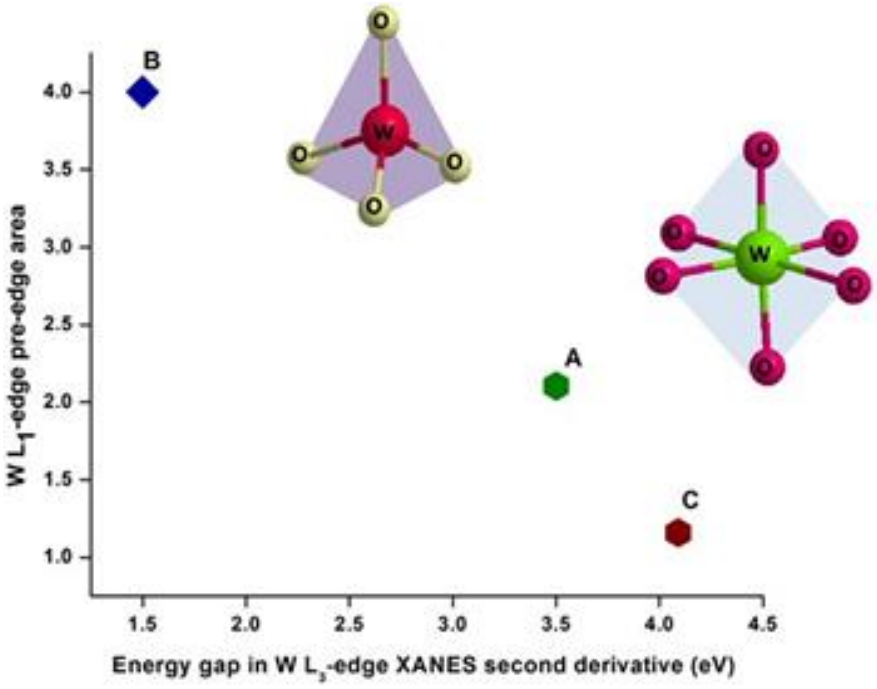

Figure 4.13. Relationship between the area of the pre-edge peak in L_1-edge XANES and the splitting of the minima in the L_3-edge XANES second derivatives: (A) H_2WO_4 (B) $Na_2WO_4 \cdot H_2O$, and (C) 45 wt % HPW/MAS-9.

On plotting the pre-edge area of the L_1-edge versus L_3-edge energy gap split, it was observed that 45 wt % HPW/MAS-9 and H_2WO_4 with octahedral coordination comprised a smaller pre-edge area and a large energy gap, as shown in Figure 4.13, whereas $Na_2WO_4 \cdot H_2O$ with a tetrahedrally coordinated W is recognized with a small energy gap (L_3-edge) and a larger pre-edge area (L_1-edge).

Consequently, from the W L_1 edge, L_3 edge, and combined analysis, it was confirmed that tungsten in the synthesized catalyst samples exists as W^{6+}, residing in an octahedral environment. In three-dimensional heteropolytungstates, WO_X octahedral are connected within the wrapped surface and not by the central atom. The terminal group, W═O of HPW, interacts with the surface hydroxyls of the mesoporous framework (congruent with the ^{29}Si NMR studies), leading to the

formation of larger polyanions. These larger heteropolyanions generate Brønsted acidity by effectively delocalizing the negative charge and aid in the release of protons effectual for the transesterification and esterification reactions. This also agrees well with the pyridine-adsorbed Fourier transform infrared (FT-IR) spectroscopy measurements, in which an increase in Brønsted acidity was found at higher HPW loadings corresponding to the polyanion clusters.

XAFS study of Al-K edge

The Al standards examined included $AlPO_4$, which has only 4-fold coordinated Al and gibbsite Al $(OH)_3$ which has only 6 –fold coordinated Al. The white line peak at 1566 eV is referred to AlO_4 corresponding to allowed transition of Al 1s to antibonding t_2 (3p) like states, while the peak at 1568 eV is assigned to AlO_6 (Figure 4.14). Both, $^{[4]}$ Al and $^{[6]}$ Al were observed in synthesized catalyst samples, thus indicating the Al species are introduced in mesostructured via the self-assembly of ZSM -5 nanoclusters surrounding the surfactant. A sharp white line with relatively high intensity is observed at 1566 eV for 35 wt % HPW/MAS-9 catalysts as compared to MAS-9 and 45 wt % HPW/MAS-9 samples. This indicated different Al coordination distributions in the samples. Hence, $^{[4]}$ Al and $^{[6]}$ Al were quantitatively determined by curve fitting analysis using arc tangent and two Gaussian curves.

Table 4.3 shows the variation of Al co-ordination in HPW supported MAS-9 catalysts. For, 35 wt % HPW/MAS-9 sample, the 4 fold co-ordinated Al was higher whereas for MAS-9 and 45 wt % 6-fold co-ordinated Al was higher. It has been reported that, Lewis acid sites exists in ZSM -5 in tetrahedral symmetry. Since, ZSM -5 is precursor for synthesis of MAS-9, we posits that ^{4}[Al] are potential Lewis acid centres and is also in accordance to FT-IR spectra of OH stretching vibrations where bands in the region 3880-3700 cm^{-1} were observed due to OHs present over tetrahedral Al cation associated with the formation of Lewis sites (due to co-ordinatively unsaturated Al^{3+} cations).

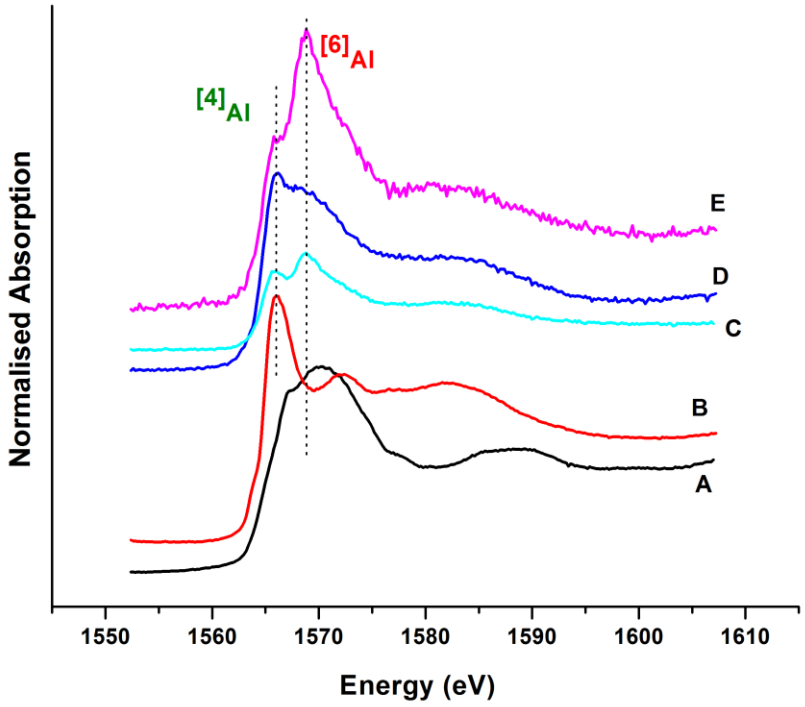

Figure 4.14. Al-K XANES spectra of A) gibbsite $Al(OH)_3$, (B) $AlPO_4$, (C) MAS-9, (D) 35 wt % HPW/MAS-9, and (E) 45 wt % HPW/MAS-9.

Table 4.3. Variation of Al- co-ordination in MAS-9 catalysts

Catalysts	$^{[4]}$Al		$^{[6]}$Al		$^{[4]}$Al: $^{[6]}$Al
	Peak	Area	Peak	Area	
MAS-9	1565.6	3.4	1568	4.5	43:57
35 wt % HPW/MAS-9	1566	4.3	1567.8	0.5	89:11
45 wt % HPW/MAS-9	1565.6	1.7	1568	5.2	25:75

4.6.2 Catalytic activity

Effects of HPW loading on MAS-7 and MAS-9

The effects of HPW loading varying from 5 to 45 wt % in MAS-7 and MAS-9 supports on methyl ester yield were investigated (Figures 4.15 and 4.16). In this study, the operating parameters of reaction were fixed at 2.57 wt % (loading of catalysts), methanol to green seed canola oil molar

ratio of 20:1, 200 °C, and 8 h.The supported solid acid catalysts gave the methyl ester yield between 60 and 79 wt % in 8 h as compared to MAS-7 that only showed 41 wt %. It is well-known that acidity favors the transesterification and esterification reactions. Hence, with the low HPW loading, expectedly a low activity of 5 wt % HPW/MAS-7 was observed in comparison to other HPW on MAS-7/MAS-9 catalysts because of the lower number of acidic sites. However, 25 wt % HPW/MAS-7 showed a higher activity as compared to 35 wt % HPW/MAS-7 and 45 wt % HPW/MAS-7.

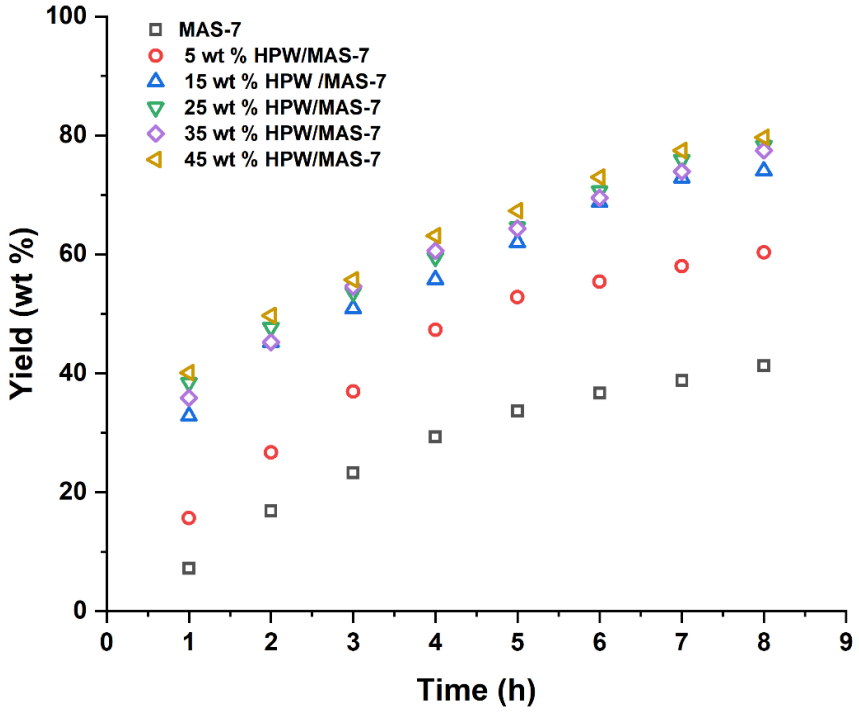

Figure 4.15. HPW loading screening for MAS-7 (2.57 wt % catalyst, methanol-to-oil molar ratio of 20:1, 200 °C, 4 MPa, and 8 h).

The results in Figure 4.15 suggest that at a HPW loading higher than 25 wt %, the acidic sites ingrained in the mesopores could have been unavailable because of the plugged mesopores, confirmed by the BET analysis, leading to an insignificant increase in the yield of ester.

Hence, the activities of the two catalysts did not significantly increase the methyl ester yield as compared to the 25 wt % HPW/MAS-7 catalyst in which most of the HPW anions were well-dispersed on to the support. This optimum dispersion was confirmed by the XRD analysis (Figure 4.3D). Hence, 25 wt % HPW loading was found to be optimum for the MAS-7 support.

For the support MAS-9, despite higher HPW loading, 45 wt % HPW/MAS-9 showed reduced activity as compared to 35 wt % HPW/MAS-9 (Figure 4.16). For instance, to obtain a methyl ester of 72, 35 wt % HPW/MAS-9 required only 5 h, whereas 45 wt % HPW-supported catalysts required up to 6 h. The maximum ester yield obtained in 8 h was 89.7 wt % at a HPW loading of 35 wt % in the case of MAS-9 support.

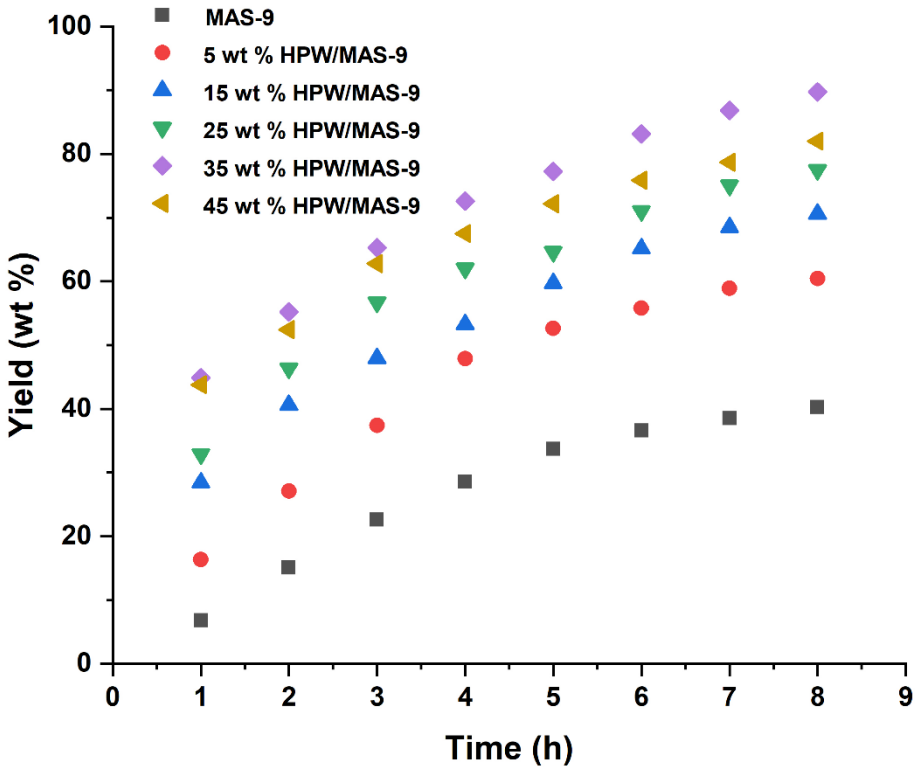

Figure 4.16. HPW loading screening for MAS-9 (2.57 wt % catalyst, methanol to oil molar ratio 20:1, 200 °C, 4 MPa, and 8 h).

Effects of surface acidity on catalytic activity

Figure 4.17 A, B shows the quantitative correlation of surface acidity with the catalytic activity (methyl ester yield) as a function of different HPW loadings for MAS-7 and MAS-9, respectively. The results indicated a direct relationship between the catalytic activity and the total surface acidity of the catalysts, that is, the catalytic activity increases with the total surface acidity. Figure 17 A shows that 25 wt % HPW-supported MAS-7 exhibits a higher catalytic activity and can be related to the highest total surface acidity because of the better dispersion of the keggin

anions on the surface of the catalyst, with an optimum surface area and pore diameter facilitating the simultaneous transesterification and esterification reactions.

However, with the higher amount of HPW loading on the catalyst surface, hardly any significant increase was found in the catalytic activity and this can be interpreted by the surface area, and pore volume decreases with the amount of HPW loading (Table 4.1) and the decreasing accessibility by the triglyceride molecules.

Hence, the total surface acidity was found to decrease, which in turn affected the catalytic activity despite the retainment of the keggin anions at the HPW loadings (determined by XRD and Raman analyses) as high as 45 wt %. 35 wt % HPW supported on MAS- 9 showed the highest catalytic activity attributed mostly to the surface acidity of this catalysts. Also, as marked by the Al-K edge spectra for 35 wt % HPW/MAS-9, 89% of tetrahedral co-ordinated Al corresponding to the Lewis acid centres were observed. In addition, the Lewis acid dominance was marked by Pyridine adsorbed FT-IR for a loading of 35wt % HPW/MAS-9.

Besides, it was observed that HPW/MAS-9 had a higher acidic strength than HPW/MAS-7, as the MAS-9 precursor ZSM-5 is more acidic than the MAS-7 precursor zeolite β.

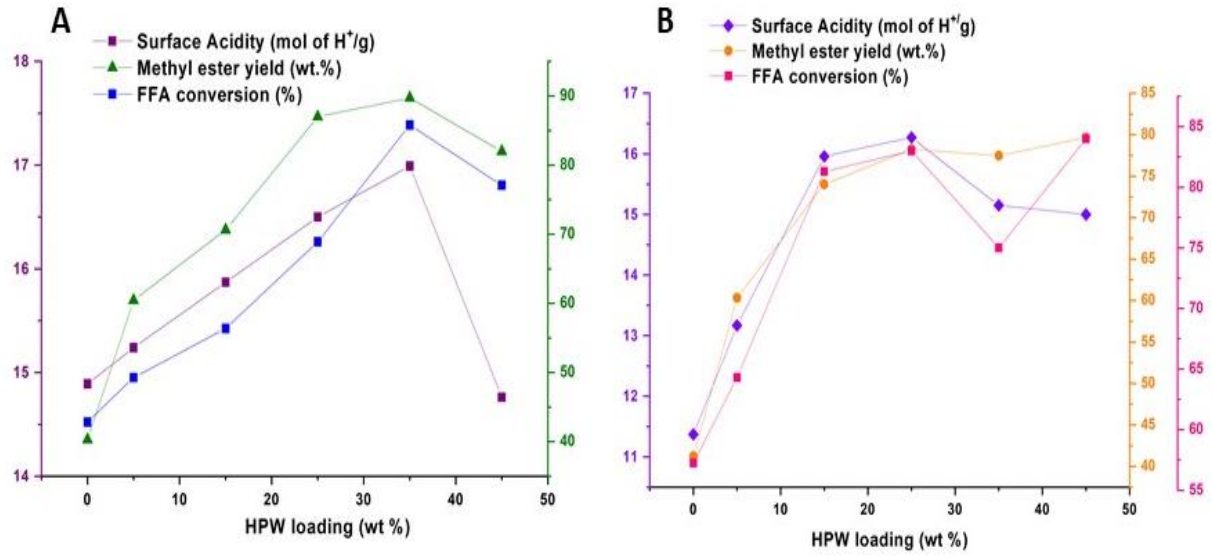

Figure 4.17. Correlation of the catalytic activity with the surface acidity of the catalysts as a function of HPW loading: (A) HPW/MAS-7, and (B) HPW/MAS-9.

4.6.3 Statistical analysis

The ester yield was determined at different combinations of the catalyst weight, alcohol/oil ratio, and reaction time for the 25 wt % HPW/MAS-7 catalyst. Table 4.4 gives the minimum and maximum limits of each factor used. The quadratic model equation was derived using response surface design of experiments (DOE) for determining the combinations of these three factors giving the maximum ester yield. The model has an *R*-square value of 0.90, meaning it is capable of explaining 90 % of variations in the yield. The maximum ester yield predicted by the model is 76.7% (95% confidence interval—66.8, 86.6%), with the optimal settings of factors being 5.5 wt % of the catalyst, 14.9:1 methanol/oil ratio, and 10 h of reaction time. However, it was seen from the Pareto chart of standardized effects (Figure 4.18) and the main effect plots of yield for factors and their interactions (Figure 4.19) that only the methanol/oil ratio and the reaction time have a statistically significant impact on the ester yield. The catalyst weight when varied between 1 and 10 wt % did not have any statistically significant impact on the ester yield. However, at 5.5 wt % catalyst, the ester yield is maximized. Previous researchers have also reported that the catalyst loading did not influence the ester yield significantly (Jacobson et al., 2008).

Table 4.4. Factor and limits for DOE.

Factor	Unit	Minimum	Maximum
Catalyst weight	wt %	1	10
Methanol: oil ratio	mol	6:1	25:1
Reaction time	hour	4	10

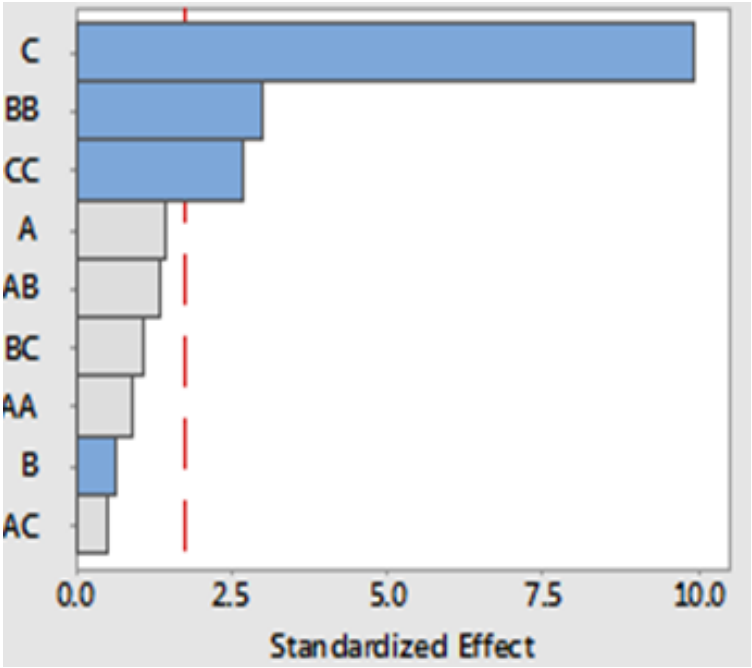

A – catalyst weight, B-methanol to oil molar ratio; C- reaction time

Figure 4.18. Pareto chart of standardized effects.

The yield of ester increased with the increase in reaction time, whereas for methanol/oil molar ratio, it increased until the midpoint, and after that decreased. A similar trend was observed by the authors Xie and Li (2006). The catalyst 35 wt % HPW/MAS-9 gave an ester yield of 88.7 ± 4.2 wt % at the above-optimized conditions. Polyoxometalate supported on various meso/macroporous oxides resulted in 82–96% of oleic acid conversion at 200 °C. The most stable catalysts against the leaching of active material were heteropolyacid supported on 3.5% SiO_2–ZrO_2 and SiO_2–Al_2O_3 (Avramidou et al., 2017). The use of HPMo/Nb2O5 resulted in 99.7% ester yield at conditions of 20 wt % catalyst loading, 90:1 ethanol-to-oil molar ratio, a reaction temperature of 210 °C, and a reaction time of 4 h (da Conceição et al., 2017). Phosphotungstic acid-functionalized

magnetic nanoparticles (HPW-PGMA-MNPs) gave 98% FAME yield after 24 h at 122 °C, with the catalyst loading of 4 wt % and 33:1 methanol/grease molar ratio (Zillillah et al., 2014).

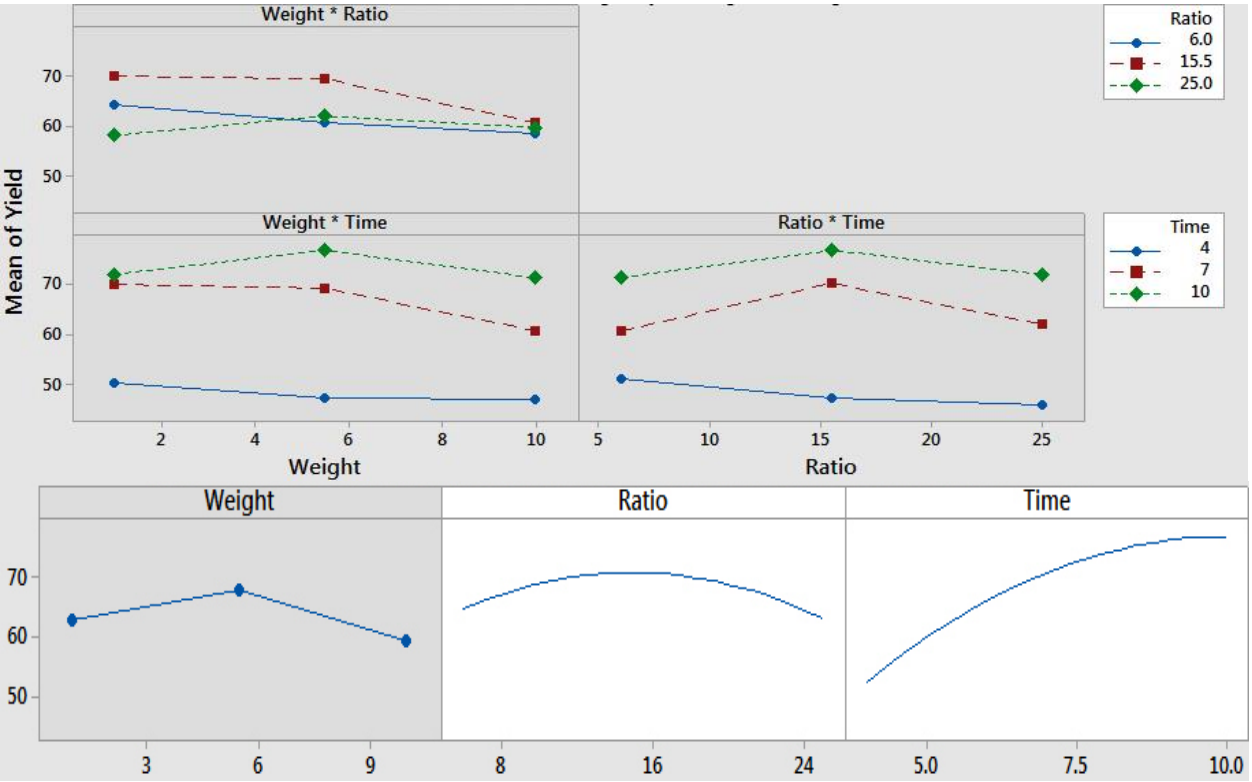

Figure 4.19. Interaction and main effect plots for methyl ester yield.

4.7 Reusability study of supported catalysts

The separated catalyst was washed between successive reaction runs with tetrahydrofuran (THF) for the removal of nonpolar and polar components and then subsequently regenerated by drying at 100 °C for 24 h. The results obtained for the first three cycles are presented in Figure 4.20 along with the surface acidity (mole of H^+/g) of the catalysts. Reduction of 3.3 and 4% in the catalytic activity was observed for 35 wt % HPW/MAS-9 and 25 wt % HPW/MAS-7, respectively, after the first reuse. However, not a significant decrease in the ester yield was observed from the successive reaction runs. The small loss in the activity could be attributed to the loss of amount of catalysts during handling.

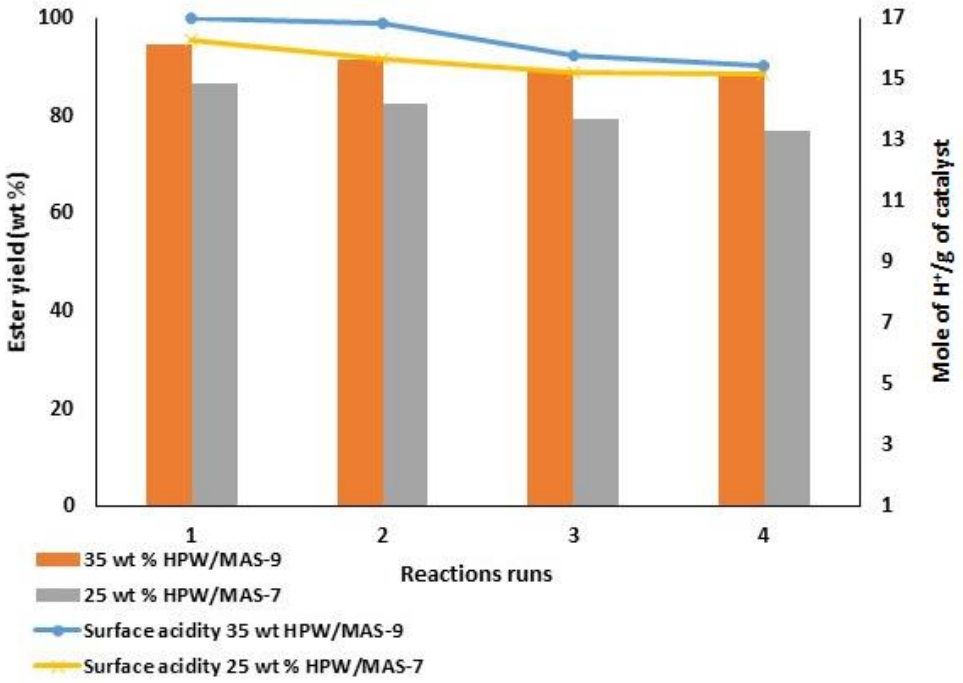

Figure 4.20. Methyl ester yield (wt. %) and surface acidity of the catalysts (mole of H^+/g) after successive reaction runs.

The presence of active material in the present study, that is, HPW was monitored by UV–vis based on 253 nm absorption, ascribed to the transfer of the charge terminal/bridging oxygen 2p to the tungsten 5d orbital (W–O–W and W–Od) (Marchena et al., 2015). For the leaching of HPW in methanol, a calibration curve was constructed with the standard solution of HPW in methanol at concentrations of 1.5, 3.1, 6.2, and 12.4 ppm. The concentration of the catalysts before and after the reaction was deduced from the curve obtained. The results hardly showed any significant leaching (0.002 and 0.001%) of the active phase from the supports MAS-7 and MAS-9 and can be associated to the interaction of the keggin anion with the supports, confirmed by the ^{29}Si NMR studies. This study is supported by Kozhevnikov et al. (1996), who stated that the reaction was truly heterogeneous and that the leaching of active phase was negligible.

Bala et al. (2017) showed that the PTA/KIT-5 catalysts exhibited the highest conversion of 83% for used cooking oil and 100% for palmitic acid at optimum conditions, and their catalyst recycling studies indicated 22% loss in conversion at the end of four cycles because of the leaching of acid from the framework. HPW-supported cesium-containing Niobia (HPW/Cs1.0/Nb_2O_5) when

employed for the esterification of palm fatty acid distillate (PFAD) gave an ester yield of 90% at 65 °C after 8 h, with 15 wt % catalyst loading and 15:1 methanol/PFAD ratio. However, the catalysts showed poor reusability, marked by 15% decrease in the catalytic activity, at the fifth run because of the blockage of active sites and the alteration in the structure of the catalysts. Moreover, the catalysts were unable to reactivate via calcination (Surasit et al., 2017). The 20% H_3PW/ZrO_2 catalyst with an oleic acid conversion of 88% in 4 h at 100 °C with 1:6 oleic acid/ethanol molar ratio and 10 wt % catalyst loading resulted in the leaching of 8 wt % of H_3PW after the first reuse (Oliveira et al., 2010).

4.8 Conclusions

$H_3PW_{12}O_{40}$ on MAS-7/MAS-9 catalysts were synthesized by wet impregnation. As per the BET analysis, the mesoporosity of the synthesized catalysts was found to be preserved after the impregnation of HPW at a loading as high as 45 wt %. XRD and Raman studies confirmed the retainment of the keggin anions on the support, whereas ^{29}Si NMR suggested a stronger interaction between the framework of mesoporous aluminosilicates and $H_3PW_{12}O_{40}$. Hence, no leaching of HPW from the support was observed. X-ray absorption fine structure spectroscopy of W L_1 and L_3 edges indicated that W in the HPW-supported catalysts is in an octahedral-like coordination, hence the system was effective for the transesterification and esterification reactions. The synthesized catalysts showed suitable physicochemical properties for the biodiesel production. The acidic strength of HPW/MAS-9 was higher than that of HPW/MAS-7, as the precursor of MAS-9 was more acidic than the MAS-7 precursor. 35 wt % HPW/MAS-9 and 25 wt % HPW/MAS-7 showed catalytic activities of 88.7±4.2% and 76.5±2.5 wt %, respectively, with unrefined green seed canola oil under optimized reaction conditions. Further, the catalysts separated by filtration and drying at 100 °C confirmed their reusability without a considerable decrease in activity.

Results from this phase of the work indicated that the mesoporous aluminosilicates like MAS-7 and MAS-9 can be used as optimal supports for HPW and both the materials synergistically provide the surface chemistry which is favorable for the simultaneous esterification and transesterification reaction. However, it was observed that the methyl ester yield obtained was less than 90% and therefore research was conducted to enhance the catalytic efficiency of these materials by tuning the physicochemical properties through synthesis technique described in following Chapter.

CHAPTER 5

Meso-Structured HPW-MAS-7 and HPW-MAS-9 Composite Catalysts for Biodiesel Synthesis from Unrefined Green Seed Canola Oil

The content of this chapter has been published in Industrial Engineering and Chemistry Research cited below and presented in the following conferences:

Citation:

Kurhade, A., Zhu, J., Dalai, A.K., 2019. Meso-structured HPW-MAS-7 and HPW-MAS-9 composite catalysts for biodiesel synthesis from unrefined green seed canola oil. Ind. Eng. Chem. Res. 58, 15772–15786. https://doi.org/10.1021/acs.iecr.8b06479

Conference Proceedings:

Kurhade, A., Zhu, Dalai, A.K. Meso-structured HPW-MAS-7 & HPW-MAS-9 composite catalysts for biodiesel synthesis from unrefined green seed canola oil. Canadian Chemical Engineering Conference, Toronto, Ontario, Canada, October 28-31, 2018

Kurhade, A., Zhu, Dalai, A.K. Self- assembled heteropolyacid acid-MAS-9 mesoporous hybrids for acid- catalyzed biodiesel production from green seed canola oil. North American Catalysis Society Meeting, Chicago, Illinois, United States, June 23-28, 2019.

Contribution of the Ph.D. Candidate

Experiments and catalysts characterization were planned in consultation with Dr.Ajay K. Dalai and carried out by Ankeeta Kurhade. Dr. Jianfeng Zhu helped with the ^{29}Si MAS and ^{31}P NMR analysis and data interpretation. The manuscript was prepared by Ankeeta Kurhade based on the guidance and suggestions provided by Ajay K.Dalai.

Contribution of this Chapter to Overall Ph.D. Research

A slight change in the synthesis procedure can have profound effect on the structure morphology and stability of the resulting material. This chapter highlights the value of controlled synthesis method in assessing the convergence of porous oxide material with highly reactive and tunable class of HPW for the development of new class of functional materials having potential significance for industrial acid or oxidation catalysts.

5.1 Abstract

$H_3PW_{12}O_{40}$-MAS-7 and $H_3PW_{12}O_{40}$-MAS-9 composite catalysts exhibiting different structural orderings were assembled from zeolite beta and ZSM-5 precursors by a one-pot template-assisted self-assembly mechanism. Characterization results suggest that $H_3PW_{12}O_{40}$ was encapsulated into the mesoporous framework of the aluminosilicates without alteration of mesoporosity of the composites. The sequential introduction of $H_3PW_{12}O_{40}$ during the synthesis of MAS-7 and MAS-9 affected the surface morphologies. The textural characteristics of the composites were improved owing to the introduction of HPW after the addition of an inorganic precursor to the template leading to a material with a high BET surface area. As novel heterogeneous solid acid catalysts, the activity of the composites was determined for the biodiesel synthesis from the unrefined green seed canola oil, giving 95.4 ± 1.4 wt % methyl ester in 10 h at 180 °C with 5.5 wt % of catalyst and a 15.5:1 methanol to oil molar ratio. The recyclability of the composites is evaluated through four consecutive reactions.

5.2 Introduction

The remarkable characteristics of heteropoly compounds in the solid form are well-known due to their superacidity, high proton mobility, and nontoxicity (Misono, 2001; Su and Guo, 2014). In solid acid catalysis, keggin-type heteropolyacid (HPW, $H_3PW_{12}O_{40}$) and the Wells-Dawson type ($H_6P_2W_{18}O_{62}$) are widely used for a variety of acid-catalyzed reactions(Grinenval et al., 2010; Noshadi et al., 2012). Unfortunately, heteropolyacids readily dissolve in polar solvents, rendering them less useful for heterogeneous catalysis. Considerable efforts are made to heterogenize heteropolyacids (HPAs) by making use of porous oxide materials. These oxides form an interesting class of solids that are used in catalysis owing to their thermal stability, rigidity, and porous structure. Materials possessing an ordered porous structure and high surface area serve as suitable supports for deposition of the active species (Dufaud and Lefebvre, 2010). The heterogenization

of heteropolyacids can be done in two major ways: (i) depositing or dispersing HPA in the preformed oxide by wet impregnation and (ii) direct incorporation of HPA to oxide in the synthesis procedure. The impregnation method is simple but results in an overall decrease in the surface area with higher HPA loadings, whereas the direct synthesis method leads to a material with a larger surface area and pore sizes, thus enhancing the performance of these composites.

The lack of the thermal stability and durability of the encapsulated heteropolyacid in the porous composite that occurs due to the leaching of these active species makes them undesirable for industrial processes. Nikseresht et al. (2017) reported the encapsulation of phosphotungstic acid (PTA) acid in MIL-53(Fe) via ultrasound irradiation as an efficient catalyst for the esterification of oleic acid with ethanol and n-butanol. However, 5% of PTA leaching was observed during the recovery process. Alcañiz-Monge et al. (2018) employed tungstophosphoric acid immobilized zirconia obtained via the sol–gel/hydrothermal method for the esterification of palmitic acid with methanol. A reduction in the catalytic activity was observed for the successive reaction runs due to the leaching and fouling of the material.

Among supports used to heterogenize heteropolyacids, siliceous mesoporous materials have been investigated for direct incorporation of HPW via the sol–gel process or surfactant templated method. Further, it has been reported in the literature that HPA interacts weakly with silica and can easily leach out when a polar solvent is used (Su and Guo, 2014). The overall acidity of these composites is contributed mostly by HPAs as silica is mildly acidic. Surfactant-templated ordered siliceous material such as meso SiO_2, SBA-15, and SBA-3 has been used for the direct incorporation of HPA during synthesis (Gagea et al., 2009). 12-phosphotungstic acid (PWA)–SiO_2 composite could maintain the mesostructure only up to a PWA loading of 30 wt % (Yun et al., 2004). Similarly, when $H_5PMo_{10}V_2O_{40}$ or $H_3PW_{12}O_{40}$ was directly incorporated in the synthesis of SBA-3 type silica, a collapse of the mesostructure was observed due to the leaching (Nowińska et al., 2003). The instability and loss of mesostructure could result from the thin wall structure. In case of $H_3PW_{12}O_{40}$–SBA-15, the composite exhibited a BET surface area in the range of 604–753 m^2/g. It had a well-defined pore structure, but with $H_3PW_{12}O_{40}$ loading of less than 20 wt % (Guo et al., 2008). The incorporation of this bulky HPW during the synthesis can lead to significant alteration in the resulting assemblies giving rise to the disordered structure. Moreover, HPW decomposes in alkaline pH and, hence, limits the synthesis in an alkaline condition or using

templates like cationic alkylammonium halide. This suggests that slight changes in the synthesis procedure can have a significant influence on the morphology, structure, and stability of the solids as formed. Therefore, it is imperative as well as challenging to maintain HPW stability and the surface characteristics of the composites.

Our previous investigation reported $H_3PW_{12}O_{40}$ supported on MAS-7 and MAS-9 catalysts with 2D mesoporous structure and exhibited good stability and catalytic activity for the simultaneous esterification and transesterification of green seed canola oil (Kurhade et al., 2018). These mesoporous aluminosilicates MAS-7 and MAS-9 are choices of support, as they are assembled using beta zeolite seeds and ZSM-5 in strongly acidic media. Compared with mesoporous materials like SBA-15 and Al-SBA-15, the wall thickness of MAS-7 and MAS-9 is thick enough to assemble the zeolite precursor (Han et al., 2001). Thus, the Al species in the mesostructures are mostly placed at zeolite-like sites, thereby preserving the acidity and crystallinity while also improving hydrothermal stability. These unique features and synthesis in acidic media make them attractive for the direct incorporation of HPW into the framework. Well-ordered pores of MAS-7 and MAS-9 aluminosilicates assembled from zeolite-β and ZSM-5 precursor solutions, respectively, serve as nanochannels for HPW inclusion, mass transport, or conduit for shape selective catalysis. In the present research, efforts were made to obtain stable and reactive mesoporous composites with intact HPW. These composites were synthesized through a facile one-step assembly between the positively charged ZSM-5 precursors and negatively charged $PW_{12}O_{40}^{3-}$ species in the presence of the block copolymer. The effects of sequential introduction of HPW on the composite properties and catalytic activity were investigated, which makes this study unique. We designed two routes for the preparation of these composites with the difference related to the sequence of introduction of HPW in synthesis. Consequently, the composites were tested as novel heterogeneous solid acid catalysts for biodiesel production from unrefined green seed canola oil (acid value, 10.8 mg KOH/g). It was found that the sequential introduction of HPW influenced the textural characteristics of the composites. The introduction of HPW after the addition of the zeolite precursor gel to copolymer solution resulted in the composites with thermodynamically stable structure exhibiting larger BET surface area and long-range ordering. The 2D morphology with long-range ordering promoted the efficient transport of the reactants and easier diffusion to the active sites, thus exhibiting higher reactivity for the transesterification reaction. Besides this, the efficiencies of $H_3PW_{12}O_{40}$ incorporated MAS-7 and MAS-9 were

compared. The particular structures of these composites formed from zeolite beta and ZSM-5 combined with their acidic characteristics make those potentially efficient heterogeneous solid acid catalysts for the transesterification reactions. The findings highlight the value of a controlled synthesis method in assessing the convergence of porous oxide material with a highly tunable class of HPW for the development of a new class of functional material having potential relevance for industrial or oxidation catalysts.

5.3 Experimental section

5.3.1 Preparation of HPW-MAS-7 and HPW-MAS-9 composite catalysts

HPW-MAS-7 and HPW-MAS-9 composite catalysts were synthesized via a one-pot–Pluronic123 template-assisted self-assembly mechanism with an initial HPW loading of 25 wt %. HPW-MAS-7 composites were prepared from zeolite beta precursor solution, whereas HPW-MAS-9 composites were obtained from the ZSM-5 precursor solution. Two routes were employed for the preparation of composites related to the sequential introduction of HPW in the synthesis procedure.

Route 1: (I) 10 g of Pluronic 123 was mixed with 295 mL of water and 98 mL of HCl. The calculated amount of HPW dissolved in water was added dropwise to the polymeric solution and stirred for 3 h. (II) The zeolite beta precursor mixture with molar ratios of 1.0/60/2.5/22/800 for $Al_2O_3/SiO_2/Na_2O/TEAOH/H_2O$ was aged at 140 °C for 4 h. (III) The ZSM-5 precursor solution prepared with molar ratios of 1.0/50/1.0/7/1800 for $Al_2O_3/SiO_2/Na_2O/(TPA)_2/H_2O$ was aged at 100 °C for 3 h. The precursor solution obtained in step II or III was added to the above polymeric solution (I) and stirred at 40 °C for 20 h. Later, the mixture was poured into a 500 mL autoclave and stored at 100 °C for 36 h. The final product was filtered, washed, and dried in a vacuum oven at 60 °C. The solids were then calcined at 400°, 500°, and 550 °C under static air for 4 h at a rate of 2 °C/min. The resulting solids are denoted as HPW-MAS-7 1 X/HPW-MAS-9 1 X, where 1 stands for the composite synthesized by route 1 and X represents the calcination temperature.

Route 2: The zeolite beta precursor solution or ZSM-5 precursor solution was added to 10 g of pluronic 123, mixed with 295 mL of water and 98 mL of HCl and stirred for 3 h. Later, a calculated amount of HPW dissolved in water was added to the above solution dropwise and stirred at 40 °C for 20 h. The admixture was poured into a 500 mL autoclave and stored at 100 °C for 36 h. After vacuum drying at 60 °C, the solids were then calcined at 400°, 500°, and 550 °C under static air

for 4 h at a rate of 2 °C/min. The solids are denoted as HPW-MAS-7 2 X/HPW-MAS-9 2 X, where 2 stands for composite synthesized by route 2 and X represents the calcination temperature.

5.3.2 Catalyst characterisation

The adsorption and desorption isotherms were obtained using a Micrometrics ASAP 2000. A total of 0.2 g of the sample was degassed at 300 °C at a ramp rate of 10 °C/min under a vacuum pressure of 0.5 μm of Hg for 3 h. The surface areas of HPW-MAS-7 and HPW-MAS-9 composites were computed using the Brunauer–Emmett–Teller (BET) method, whereas the pore-size distributions were determined using the Barret–Joyner–Halenda (BJH) model.

Small angle X-ray diffraction (SXRD) patterns were determined on a D8 Advance Powder Diffractometer equipped with GE monochromator emitting a monochromatic Cu Kα (λ = 1.54 Å) radiation. The composites were scanned from 0.5° to 10° with a step size of 0.01. The generator was operated at 40 kV and 40 mA. The data were processed using DIFFRAC.SUITE.

^{29}Si-MAS, ^{29}Si CP/MAS NMR, and ^{31}P {^{1}H} spectra were obtained on a Bruker Avance NMR spectrometer. The ^{29}Si-MAS and ^{31}P MAS were obtained using a 45° excitation pulse, ^{1}H decoupling, 6 kHz spinning speed and 5 s relaxation delay while CP/MAS experiments employed a relaxation delay of 2 s, spinning speed of 6 kHz and CP contact time of 5 ms.

The FT-IR spectra of the composites were obtained on Vertex 70v vacuum spectrometer (Bruker, Germany) equipped with DLaTGS detector, and MIR source. The spectras were recorded in the range 1400–1800 cm^{-1} using 32 scans and a resolution scan of 4 cm^{-1}. The FT-IR spectra of the samples were measured in the absorption mode. The OPUS 7.5 spectroscopy software was used for data acquisition.

Raman spectra of the composites were obtained on a Raman Invia Reflex Raman microscope spectrometer in the spectral range 98 to 1497 cm^{-1} using a 785 nm solid state diode (Renishaw Inc.) and a 1200 1/mm grating. The laser was focused onto the sample using a 50× (NA = 0.75) microscope objective lens. The laser power set to 50% was 65.2 mW, and an exposure time of 10 s was applied. The samples were photobleached for 60 s to eliminate any background fluorescence. The instrument was calibrated with Si (110), which was measured at 520 cm^{-1}. The data were processed using the Renishaw Wire (V3.4) software.

The morphologies of the composites were studied via high-resolution transmission electron microscope (HRTEM). The sample preparation involved the dispersion of the composites in ethanol for the analysis. The suspensions on the carbon-coated copper grid were observed on a Hitachi HT7700. Imaging was done at an 80 kV accelerating voltage using magnifications ranging from 10 to 500 K.

The particle size of the composites was determined by using a Malven Mastersizer 3000 with a Hydro EV (MAZ3400) wet dispersion unit. Obscuration was used to help set the concentration of the samples when added to dispersant and ultrasonicated for 10 s. Water was used as a dispersant having a refractive index of 1.33. Materisizer V3.71 was used to process the data.

The Brønsted-acid site density of the composites was calculated using the acid–base titration. A total of 100 mg of the powdered composite was dissolved in 20 mL of NaOH solution, and the mixture was stirred for 3 h. The supernatant was titrated with 0.1 M HCl using a phenolphthalein indicator. The Brønsted acid site density was calculated from the amount of HCl consumed (blank, mL of HCl for the composite solution) and is expressed as millimoles of H^+/g of the composite.

5.4 Catalytic activity

The transesterification reaction of unrefined green seed canola oil with methanol was carried out in a 100 mL batch reactor (Parr Instrument Co., IL, USA) to produce biodiesel. The typical experiment included 35 g of green seed canola oil (acid value, 10.8 mg KOH/g), 25 g of methanol, and 0.9 g of the catalyst (2.57 wt % of a catalyst based on 35 g of oil). Preliminary runs were carried out at a reaction temperature of 150 °C, 8 h, and 4 MPa.

After separation of the catalysts by filtration, the ester wt % was determined by HPLC (Agilent Technologies). The components were separated using two 5 μL, 100 Å, 300 × 7.8 mm phenogel columns (column temperature of 24 °C) in series with a guard column. Tetrahydrofuran solvent was used as the mobile phase. The detector temperature was kept at 35 °C, and the sample injection volume was 20 μL. The ester (wt %) was obtained using Eq (5.1):

$$\text{Ester wt \%} = \frac{\text{Methyl ester weight in ester phase}}{\text{Ester phase wieght}} \times 100 \quad \text{.....(5.1)}$$

The leaching test of the HPW from the composite framework was performed using a UV–vis spectrophotometer (UV mini 1240 Shimadzu). A total of 20 mg of the solid was dissolved in 50 mL of methanol as it is one of the reactants and was stirred for 1 h. A calibration curve was constructed with HPW standard solutions in methanol at concentrations of 1.5, 3.1, 6.2, and 12.4 ppm ($A = 9.7 \times 10^{-3} + 0.002$) .The concentration of HPW in an aliquot withdrawn at regular intervals was measured by the spectrophotometer with a scanning 200–800 nm wavelength.

5.5 Results and Discussion

5.5.1 Postulated synthesis mechanism - effects of sequential introduction of HPW on the catalysts properties

In this work, the sequential introduction of HPW in the direct synthesis of aluminosilicates was conceived to obtain composite catalysts with a better dispersion of HPA and surface properties. The morphological changes taking place during the intermediate synthesis of these composites were observed via TEM studies.

Mesoporous aluminosilicates like MAS-7 and MAS-9 follow the $S°H^+X^-I^+$ pathway. S° represents a nonionic surfactant (P123); H^+, hydronium ions; and Cl^-, anions. The interaction between the organic template and inorganic species guides the synthesis mechanism. In an aqueous solution, the nonionic surfactant P123 forms a micelle, and upon addition of HCl, the ethoxy groups of P123 are protonated to H_3O^+ ions. The positive charge on P123 is neutralized by Cl^- anions (Gagea et al., 2009). At this stage, P123 is stabilized and HPW is added (route 1, Figure 5.1). HPW anions appear around the P123 micelle shell (Figure 5.2A, TEM image). The darker shade in the image represents the form of surfactant aggregate in the micelle, and HPW anions are marked by light gray small aspherical particles. The weak conjugate base of HPW can replace some of the Cl^- anions surrounding the micelle (Gagea et al., 2009). From Figure 5.2B, it was observed that after the addition of a zeolite precursor solution into the HPW+P123 solution, the P123 block copolymer aggregated into flower-like micelles. This suggests that when zeolite precursors are added at a very low pH, they rapidly hydrolyze and try to interact with a negative anionic shell of P123 surrounding micelle. So, to decrease the overall free energy of the micellization, the morphology of the P123 converts into flower-like micelles from the spherical one.

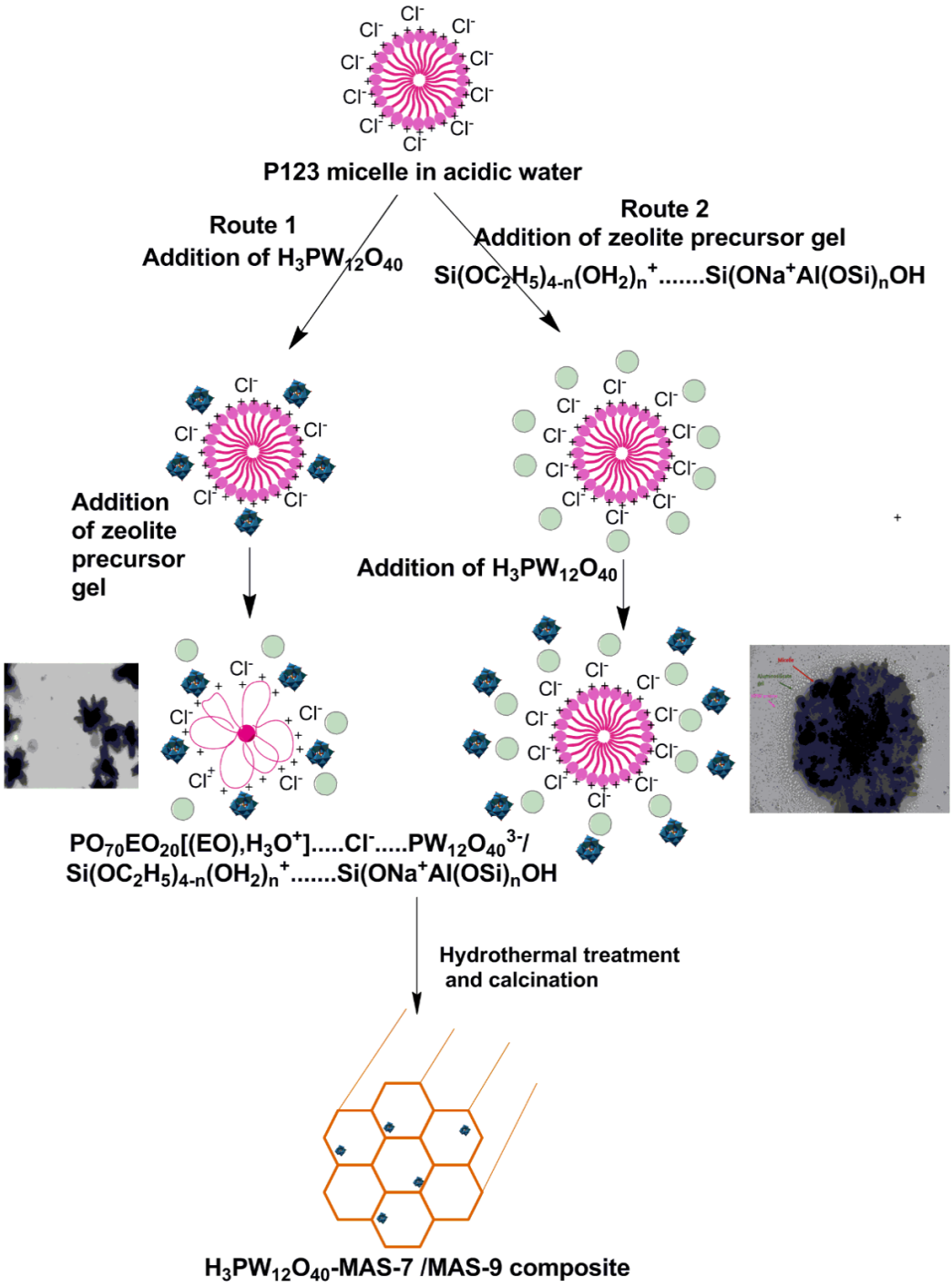

Figure 5.1. Designed routes for the synthesis of HPW-MAS-7/HPW –MAS-9 composite differing in sequence of addition of HPW

Hence, the aggregation of flower-like micelles results from balancing the interfacial energy of the hydrophobic chains in the core. However, from the TEM image, it could be seen that HPW is molecularly dispersed (gray small spherical properties).

Subsequently, cohydrolysis and condensation of inorganic species and surfactant organization in the presence of $H_3PW_{12}O_{40}$ result in the formation of $PO_{70}EO_{20}[(EO)\cdot H_3O^+]...Cl^-$ $...PW_{12}O_{40}^{3-}/Si(OC_2H_5^-)_{4-n}(OH_2^+)_n...SiONa^+Al(OSi)_n(OH)$ species.

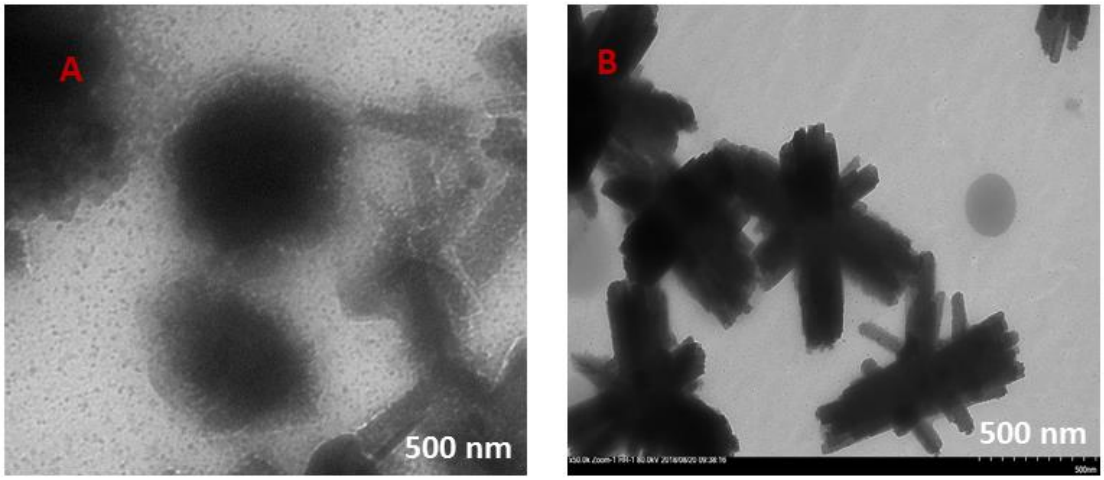

Figure 5.2. TEM images of (A) HPW+ Polymer system after 3 hours stirring and, (B) after the addition of zeolite precursor solution in HPW+ Polymer system.

In route 2 (Figure 5.1), the zeolite precursor solution is first added to the polymer system and then the HPW anions are introduced. In this way, the precursor solution is first hydrolyzed with block copolymer without affecting the development of the micellar structure and the onset of long-range order.

The solubilization of nonionic surfactant in the acidic media (HCl + water) is due to the hydronium ion associated with the EO moieties. Hence, this positive charge is neutralized by Cl^- anions similar to route 1. Upon the addition of the zeolite precursor solution, the charge associated species are assembled together via electrostatic forces. This leads to the strong interaction, and thus the layer of the aluminosilicate appears surrounding the micelle and can be observed from the TEM image, Figure 5.3. Such type of electrostatic interactions between the silica species and EO units has been reported during the synthesis of the $H_3PW_{12}O_{40}$-silica composite by Guo et al.(2008).

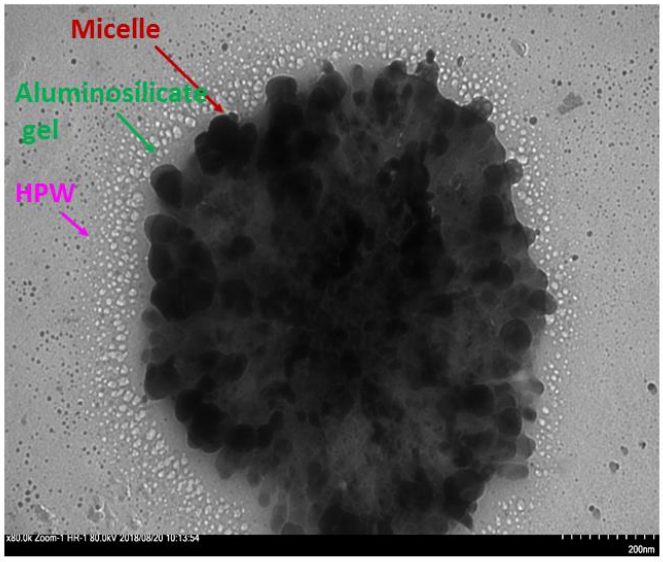

Figure 5.3. TEM image after addition of HPW solution to zeolite precursor + Polymer system.

The EO moieties with H_3O^+ ions first interacts with the cationic species by a hydrogen bonding or electrostatic interactions forming

$PO_{70}EO_{20}[(EO).H_3O^+] \ldots . Cl^- / Si(OC_2H_5^-)_{4-n}(OH_2^+)_n \ldots SiONa^+Al(OSi)_n(OH)$ species.

Later, the solution is mixed with HPW. It could be seen from the TEM image (Figure 5.3) that HPW anions are well dispersed around the micelle. The above observation suggests that the products are formed with a thermodynamically stable structure without disordering of the mesostructure or causing a decrease in surface area. Hence, the composite catalysts synthesized via route 2 exhibited a higher BET surface area as compared to route 1.

In both the synthesis routes, the gel was subjected to hydrothermal treatment for the polymerization to occur. Further, to reinforce the interactions between the HPW and aluminosilicate gel, controlled calcination was performed to obtain the HPW-MAS composites.

5.5.2 Morphology, mesostructure, and porosity of the composites

Morphology and structural ordering of the composites synthesized by route 1 and route 2 were characterized by TEM analysis and small-angle XRD analysis. Figure 5.4A reveals that in the composite obtained by route 1, the hexagonal areas are visible but with low areas of an ordered

structure, whereas the HPW-MAS-9 2 500 °C composite synthesized by route 2 exhibits well-ordered 2D hexagonal arrays of mesopores (Figure 5.4B). The different morphologies are related to the synthesis routes. In route 2, the introduction of HPW after zeolite precursor gel into the polymer system gives a well-ordered structure, suggesting prehydrolysis of aluminosilicate gel is vital to forming ordered mesostructured composites. Also, the TEM images in Figure 4.2B reveal the presence of flower-like micelles in route 1, resulting in a thermodynamically unstable structure. Furthermore, the TEM images of the as-synthesized HPW-MAS 9 composites regardless of morphologies indicate that the materials are phase pure as no individual phases are observed. Hence, the interaction of the keggin unit with the aluminosilicate can be inferred to be chemical rather than physical adsorption (Li et al., 2009).

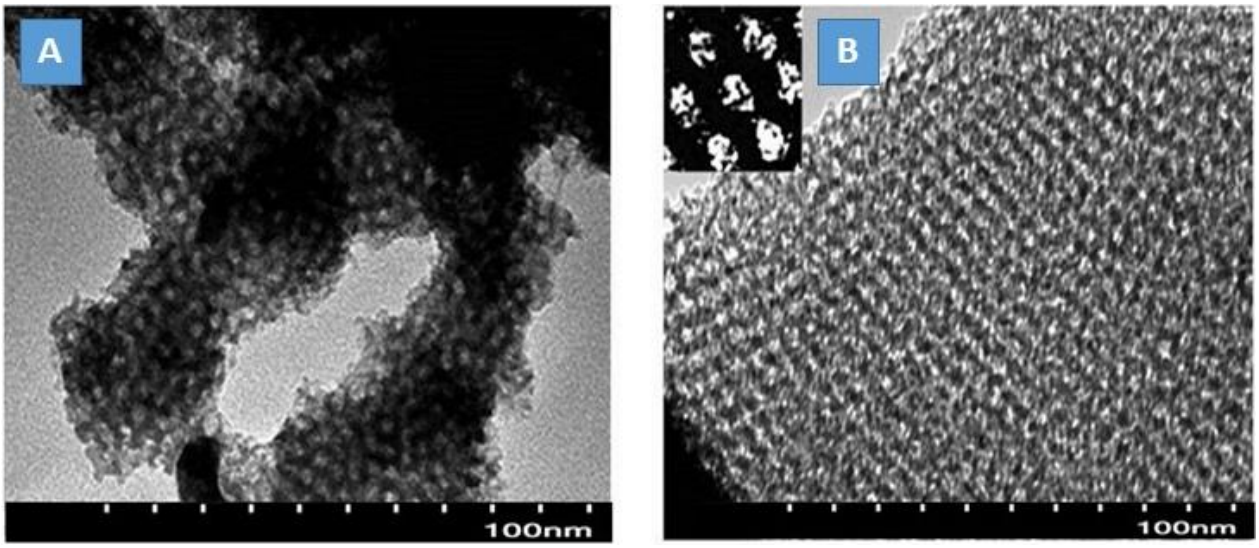

Figure 5.4**.** The representative TEM images of composites with 25 wt. % HPW loading A) HPW-MAS 9 1 500 °C, and B) HPW-MAS 9 2 500 °C.

The small angle XRD results are in accordance with the above observations. The small angle XRD patterns for P123-directed HPW-MAS-9 500 °C composites synthesized by route 1 and route 2 are shown in Figure 5.5. The composite HPW-MAS-9 2 500 °C exhibits the Bragg reflections $2\theta = 0.86°$, 1.5°, and 1.9°, respectively (Figure 5.5A). The d values determined from the Bragg equation are 10, 6, and 5 nm. The ratios of these values are $1:1/\sqrt{3}:1/2$ and are indexed as [100], [110], and [200] diffractions. Hence, this suggests that the composites synthesized by route 2 show highly ordered 2D hexagonal p6mm symmetry mesostructure. The lattice parameter a_0 calculated by equation $a_0 = 2d_{100}/\sqrt{3}$ is 12 nm, whereas the composite HPW-MAS-9 1 500 °C

(Figure 5.5B) exhibits only one intense Bragg reflection at 2θ = 0.86°. This suggests that the composite has mesostructure but it lacks long-range ordering. The above observations were found to be true in the case of HPW-MAS-7 composites (Appendix A, Figure A.3).

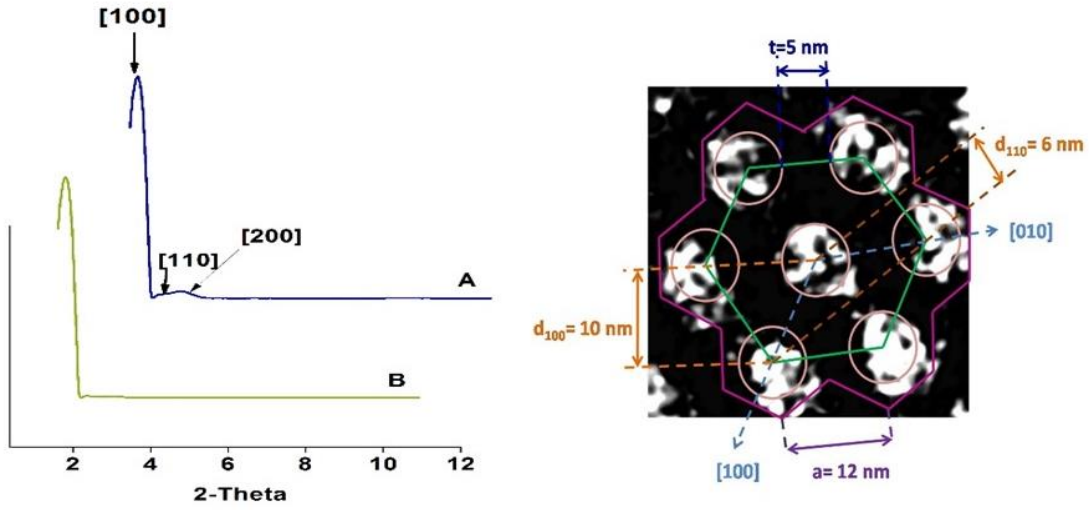

Figure 5.5. Small angle XRD of representative composites A) HPW-MAS-9 2 500 °C, and B) HPW-MAS-9 1 500 °C. On the right -TEM image of HPW-MAS-9 2 500 °C with lattice parameters.

N_2 gas adsorption–desorption isotherms and BJH pore size distribution of representative HPW-MAS-7 and HPW-MAS-9 composites are presented in Figures 5.6 and 5.7. The isotherms for all the catalysts indicate type IV isotherms. The composites HPW-MAS-7 1 500 °C and HPW-MAS-7 2 500 °C exhibit H1 type hysteresis typical of rigid mesoporosity, possessing regular, even pores without an interconnecting channel (Beale et al., 2012). For the composite HPW-MAS-7 1 500 °C, a sharp inflection with primary mesopores with an average pore width of 7 nm is observed with p/p_0 between 0.64 and 0.80. A distinct nature of adsorption and desorption branch is observed in case of the composite synthesized by route 2 (HPW-MAS-7 2 500 °C) leading to the abrupt closure of the hysteresis loop. And, this can be because of the rapid decrease in adsorbed volume along the desorption branch in p/p_0 = 0.44. This event is often referred to as the tensile strength effect (Gagea et al., 2009; Groen et al., 2003). Hence, the contribution around 4 nm in BJH pore size distribution for these catalysts is attributed to the tensile strength effect phenomenon

(Figure 5.6, II). Apart from this, a unimodal and narrow pore size distribution is observed for HPW-MAS-7 composites irrespective of the synthesis route.

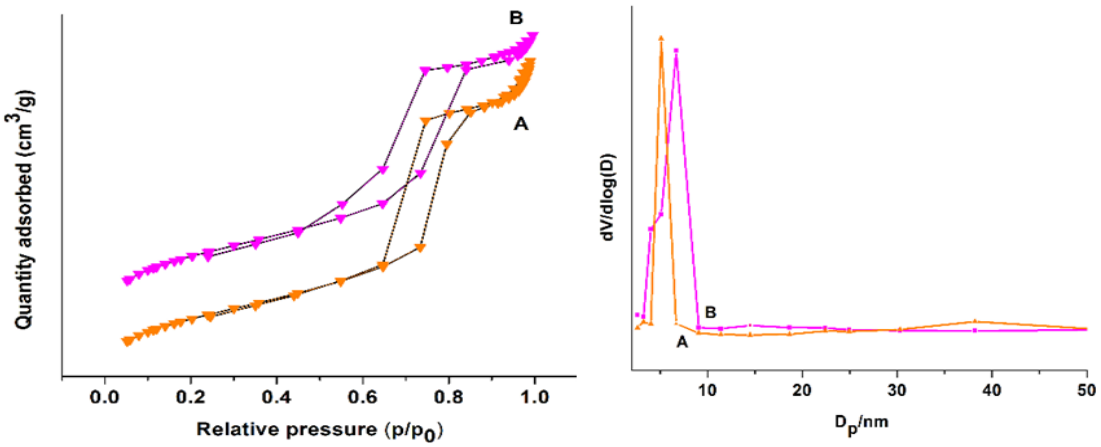

Figure 5.6. Nitrogen porosimetry isotherms (I) and pore size distribution curve (II) of composites A) HPW-MAS-7 1 500 °C and, B) HPW-MAS-7 2 500 °C.

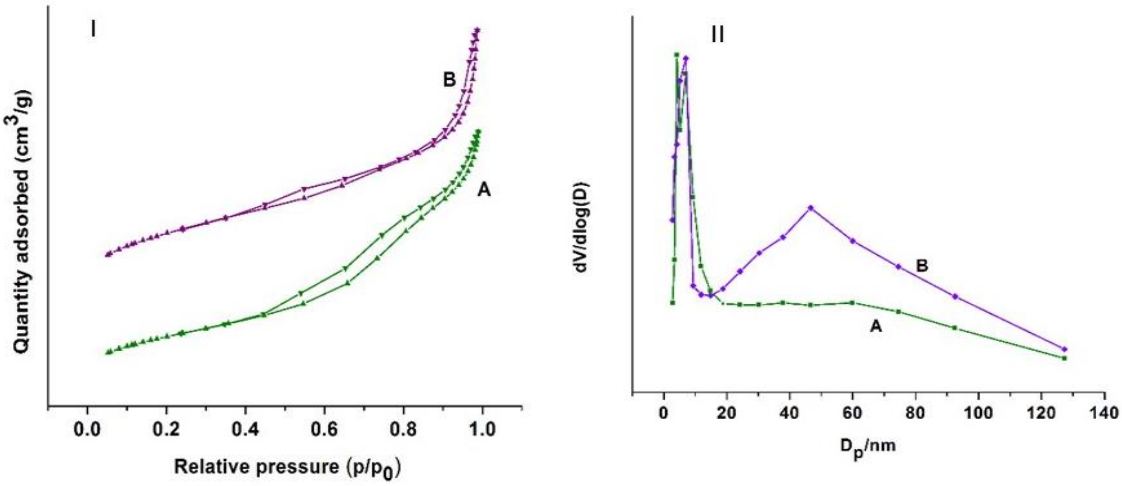

Figure 5.7. Nitrogen porosimetry isotherms (I) and pore size distribution curve (II) of composites A) HPW-MAS-9 1 500 °C and, B) HPW-MAS-9 2 500 °C.

For, HPW-MAS-9 1 500 °C, the isotherm exhibits capillary condensation steps at a relative pressure p/p_0 = 0.44–0.98 and exhibits H3 type hysteresis indicative of slit-shaped pores (Beale et

al., 2012). In case of HPW-MAS-9 2 500 °C, it possesses two capillary condensation steps at a relative pressure of p/p_0 = 0.44–0.74 and p/p_0 = 0.83–0.98 and classifies as H1–type hysteresis.

The textural parameters of the composites are listed in Table 5.1. It is found that both HPW-MAS-7 and HPW-MAS-9 composites synthesized by route 2 exhibit higher surface area than the ones obtained by route 1, also confirming the reproducibility of synthesis route 2. It can be a result of initial interaction between the Pluronic P123 and framework wall species rendering the species to be ordered at the beginning and ultimately leading to a mesostructure with a high surface area. The diameter of the pore calculated from the BJH desorption isotherm is in the range of 6–7 nm and 7–8 nm for the HPW-MAS-7 and HPW-MAS−9 composites.

Table 5.1. Textural characteristics of the HPW-MAS composite catalysts

	Route 1			Route 2		
HPW-MAS-7 composites						
Calcination temperature	Surface area (m^2/g)	Pore volume (cm^3/g)	Pore size (nm)	Surface area (m^2/g)	Pore volume (cm^3/g)	Pore size (nm)
400 °C	839	1.3	8.5	1115	1.3	6.0
500 °C	748	1.1	7.0	842	1.1	6.0
550 °C	735	1.1	7.4	931	1.2	6.0
HPW-MAS-9 composites						
400 °C	613	1.2	7.6	886	0.9	7.7
500 °C	608	1.0	7.0	810±4	0.99±0.11	8±0.06
550 °C	595	1.1	7.2	761	1.1	7.9

The decrease in surface area with the increase in the calcination temperature can be attributed to the removal of the organic template P123 as the complete elimination of the organic template requires a high temperature (T > 500 °C) (Bérubé and Kaliaguine, 2008). Kleitz et al.

(2003) reported that after completion of the oxidation process of the template at 350 °C, the remaining organic components are converted to carbon dioxide, water, or residual carbonaceous species. The residual carbon content decreases gradually at high temperatures. The total pore volume almost remains unchanged irrespective of the synthesis route, whereas the mesopore size decreases for the composites synthesized by route 1 with the increase in calcination temperature from 400 to 500 °C. The removal of the copolymer takes place inside the primary mesopores, with a fragmentation of the carbon chain. The decrease in the pore size suggests that the lattice shrinkage takes place at these temperatures in accordance with the results reported by Bérubé and Kaliaguine (2008). However, in case of the composites synthesized by route 2, the pore volume and pore size remained almost unchanged. The observed increase in surface area for HPW-MAS-7 synthesized by route 2 and calcined at 550 °C might be caused by the disintegration of the large heteropolyanions into small tungsten oxide species.

5.5.3 ^{29}Si MAS and CP/MAS NMR studies

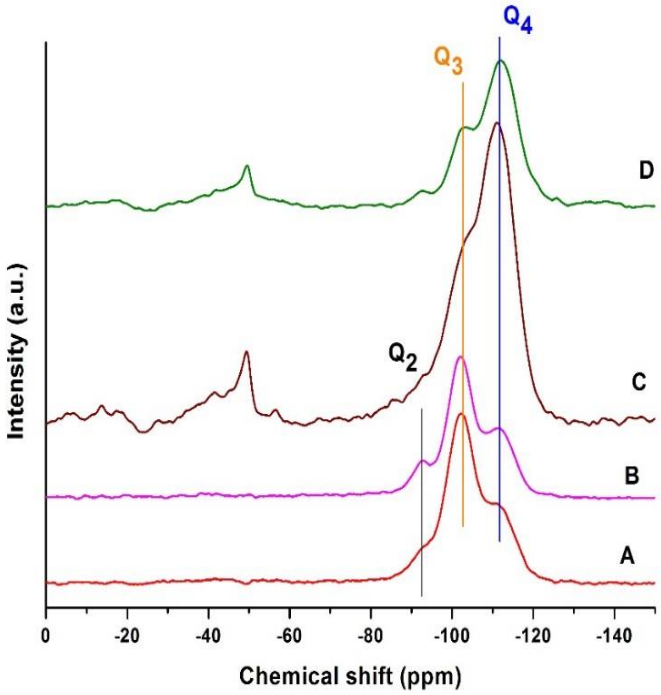

Figure 5.8. ^{29}Si CP/MAS NMR spectra of (A) HPW-MAS-9 2 500 °C, and (B) HPW-MAS-9 1 500 °C; ^{29}Si ^{1}H DEC/MAS NMR spectra of (C) HPW-MAS-9 2 500 °C, and (D) HPW-MAS-9 1 500 °C.

The extent of formation of a highly condensed organosilicate hybrid framework and interaction of HPW with the framework was determined via ^{29}Si studies. The ^{29}Si CP/MAS and ^{29}Si MAS spectra for the representative composites HPW-MAS-9 500 °C synthesized by route 1 and route 2 are shown in Figure 5.8. $^{1}H \rightarrow {}^{29}Si$ cross-polarization detects the NMR signal of silicon nuclei that are close to protons.

In general, as expected, ^{29}Si CP/MAS spectra showed three characteristic peaks at −93, −103, and −111 ppm indicating the presence of Q_2, Q_3, and Q_4 silicon nuclei. Q_2 corresponds to $(SiO)_2{*}(SiOX)_2$ and Q_3 to $XOSi{*}(OSi)_3$, where X can be H or an interacting keggin unit with the surface hydroxyls, and Q_4 represents $Si–(O–Si)_4$ in the mesoporous framework (Brahmkhatri and Patel, 2011). The Q_2 and Q_3 units possessing one or two OH groups are found mostly on the surface and edges of the mesopores (Cattaneo et al., 2016). The $Si–(O–Si)_4$ units are located inside the framework instead of on the surface and exhibit the dominant resonance in ^{29}Si MAS spectra (Figure 5.8C and D). For the HPW-MAS-9 2 500 °C composite, a very weak ^{29}Si signal for Q_2 is observed when compared to the one synthesized by route 2. This suggests the different distribution of the silicon units in the synthesized composites via route 1 and route 2. The MAS spectra were therefore deconvoluted using the ^{29}Si chemical shifts from the ^{29}Si CP/MAS spectra. The distribution of Q_2, Q_3, and Q_4 units for the HPW-MAS-9 500 °C composite is shown in Table 5.2. A higher fraction of Q_3 units is observed for the composite (HPW-MAS-9 2 500 °C) synthesized by route 2 and indicates more surface reactions of SiOH groups with the HPA. During the synthesis procedure (route 2), the keggin unit interacts with the silica matrix in the presence of block copolymer $EO_{20}PO_{20}EO_{20}$ and results in the formation of $EO_{20}PO_{70}EO_{20}–Si(OC_2H_5^{-})_{4-n}(OH_2^{+})/H_3PW_{12}O_{40}$. Also, supported by the TEM image (Figure 5.3), the layer of precursor gel is surrounded by a micelle followed by HPW molecules.

Table 5.2. Quantification of different silicon species from ^{29}Si MAS spectra

Catalysts	Q_2%	Q_3%	Q_4%
HPW-MAS-9 1 500°C	1	29	69
HPW-MAS-9 2 500°C	1	49	49

5.5.4 The compositional and structural stability of keggin unit in composite catalysts

The structural stability of the keggin unit in the catalysts was investigated via ^{31}P MAS NMR spectroscopy. Figures 5.9 and 5.10 show the ^{31}P MAS NMR obtained on HPW and HPW-MAS-7 and HPW-MAS-9 composites synthesized via route 1 and route 2. ^{31}P MAS NMR characterizes two HPA species. The one at −15.1 ppm suggests the intact keggin structure and the other at around 12.9 ppm with a different structure (species B). The ^{31}P NMR spectrum of HPW exhibits a single intense signal at −15.5 ppm (fwhm = 0.04 ppm) attributed to the resonance of PO_4 units within the $H_3PW_{12}O_{40}$ environment. This ^{31}P chemical shift corresponds to a keggin anion having six protons.

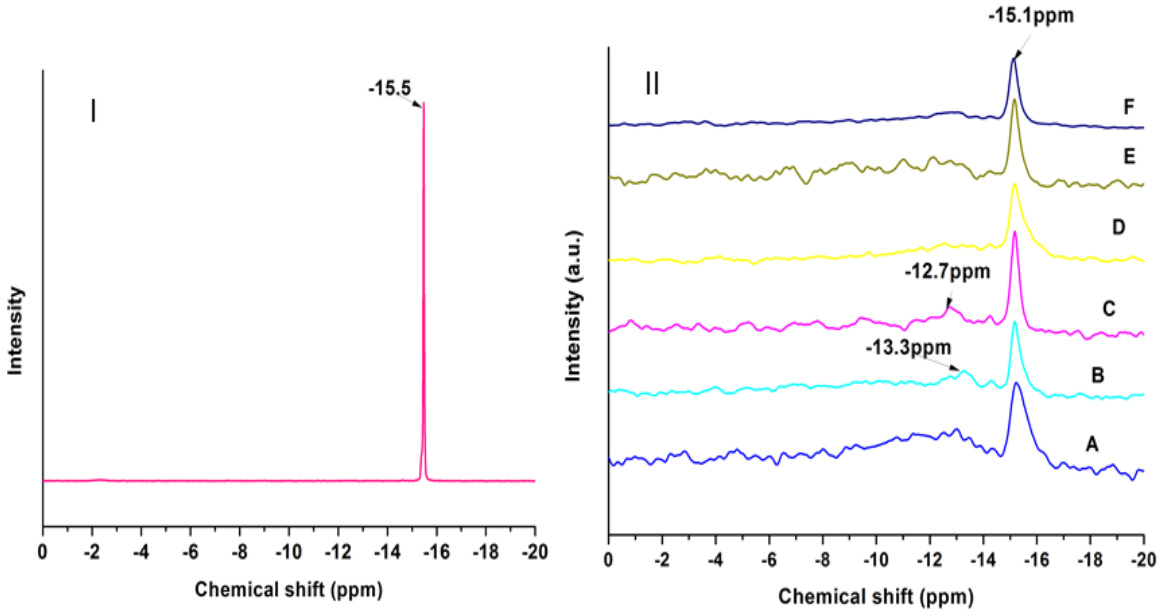

Figure 5.9. ^{31}P NMR spectra of (I) HPW and (II) composites synthesized by route 1 A) HPW-MAS-7 1 400 °C, B) HPW-MAS-7 1 500 °C, C) HPW-MAS-7 1 550 °C; ^{31}P NMR spectra of composites synthesized by route 2 D) HPW-MAS-7 2 400 °C, E) HPW-MAS-7 2 500 °C, F) HPW-MAS-7 2 550 °C.

The protonated water, $H(H_2O)_2^+$, is connected to the heteropolyanion by hydrogen-bonding at terminal oxygens ($W{=}O{-}H^+(H_2O)_2$) (Okuhara et al., 1996). The composite catalysts HPW-MAS-7 and HPW-MAS-9 synthesized via route 1 and route 2 also show similar features at −15.1 ppm noticeable by a small shift (0.4 ppm) from a bulk HPW signal. This small chemical shift

difference can be the result of a slight variation in the hydration degree experienced by phosphorus. Hence, the line at −15.1 correlates to the crystalline HPW molecule with different hydration states. Also, the signal at 15.1 is considerably broadened (fwhm = 1.1). This can be a result of the distribution of different isotropic chemical shifts of ^{31}P due to the different electronic environments of HPW in the composite. This different electronic environment can be because of the interaction of keggin with aluminosilicates forming species $(Si(OSi)_2OAlOH_2)_n^+$ $[H_2PW_{12}O_{40}]^-$ at the interface.

Further, an increase in intensity is observed for this spectral feature at −15.1 ppm with the increase in the calcination temperature. This suggests the reinforcement of interactions with the keggin unit. However, a weak and broad signal around −12.9 or −13.3 ppm is observed at calcination temperatures of 400 and 550 °C (Figure 5.10E and F).

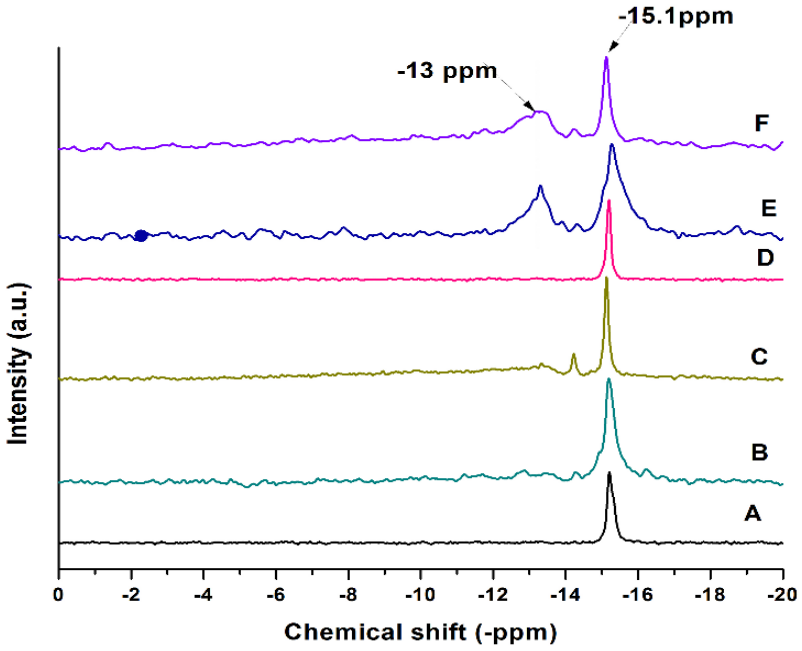

Figure 5.10. ^{31}P NMR spectra of composites synthesized by route 1 A) HPW-MAS-9 1 400 °C, B) HPW-MAS-9 1 500 °C, C) HPW-MAS-9 1 550 °C; ^{31}P NMR spectra of composites synthesized by route 2 D) HPW-MAS-9 2 400 °C, E) HPW-MAS-9 2 500 °C, and F) HPW-MAS-9 2 550 °C.

According to existing literature, it is supposed to be originating either from the interacting keggin species (Olejniczak et al., 2000) or from the partial transformation of the keggin structure and lacunary species like $P_2W_{18}O_{62}^{6-}$ or $P_2W_{21}O_{71}^{6-}$ (Kozhevnikov et al. 1996; Okuhara et al.,

1996). In order to confirm this signal at −12.9 or −13.3 ppm, the ^{31}P MAS NMR spectra of mechanical mixture HPW and HPW-MAS-9 2 500 °C were obtained. The spectra gave rise to a single signal at −15.5 ppm similar to the spectrum of pure HPW (Appendix A, Figure A.4). Thus, this verifies that the keggin structure interacts with the aluminosilicates and causes a shift in the main hexahydrate HPW signal and gives rise to an additional signal at −12.9 or 13.3 ppm. Hence, from ^{31}P NMR, it can be concluded that HPA molecules in the composites have different hydration states irrespective of the synthesis route and can be a result of interactions between the keggin unit and aluminosilicate.

Further, the interactions of the keggin unit with aluminosilicate were confirmed via Raman spectroscopy.

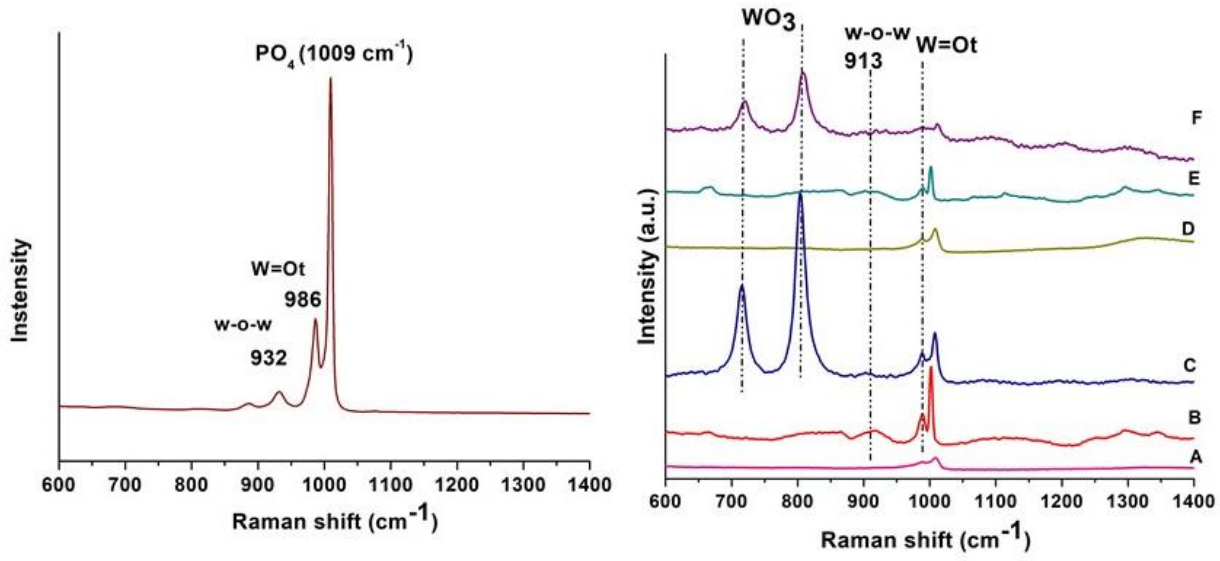

Figure 5.11**.** Raman spectra of (I) HPW and (II) HPW-MAS-7 composites synthesized via route 1 and 2 (A) HPW-MAS-7 1 400 °C, (B) HPW-MAS-7 1 500 °C, (C) HPW-MAS-7 1 550 °C , (D) HPW-MAS-7 2 400 °C , (E) HPW-MAS-7 2 500 °C, and (F) HPW-MAS-7 2 550 °C.

Raman spectroscopy is very sensitive to the keggin unit, and the signals originate from HPW alone without any interference from the mesoporous aluminosilicate. Figures 5.11 and 5.12 show the Raman spectra for bulk HPW and representative composites HPW-MAS-7 500 °C and HPW-MAS-9 500 °C synthesized via route 1 and route 2. HPW exhibits three characteristic bands at 1009 cm^{-1} (symmetric stretching of PO_4 sites), 991 cm^{-1} (antistretching (ν_{as}) of W═Ot), and 932

(ν_{as} (W–O–W) (Holclajtner-Antunović et al., 2010). These peaks are also observed for the composites with decreased intensity and some shifts of the peak positions.

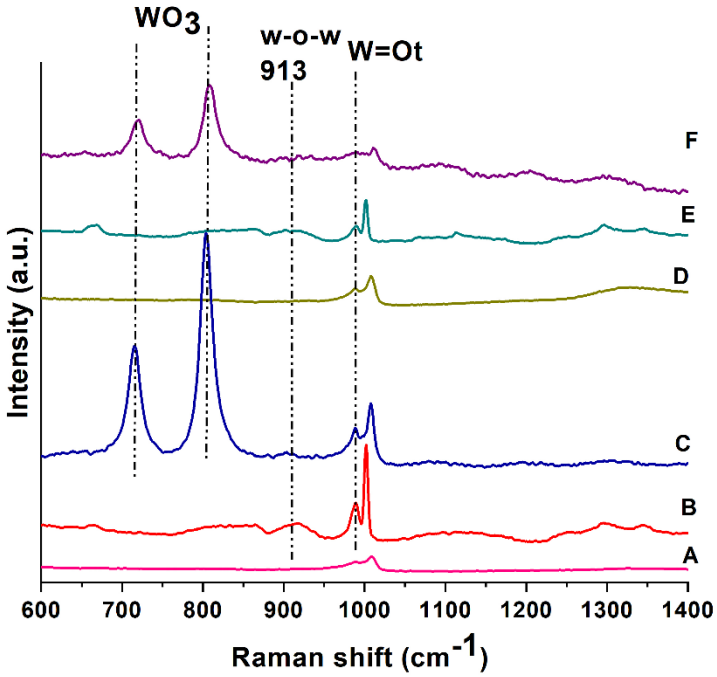

Figure 5.12. Raman spectra of HPW-MAS-9 composites synthesized via route 1 and 2 (A) HPW-MAS-9 1 400 °C, (B) HPW-MAS-9 1 500 °C, (C) HPW-MAS-9 1 550 °C , (D) HPW-MAS-9 2 400 °C , (E) HPW-MAS- 9 2 500 °C and, (F) HPW-MAS -9 2 550 °C.

The red-shift of these peak positions is associated with the interaction of the keggin anion and mesoporous aluminosilicates via proton transfer (Guo et al., 2008). Concurrently, the intensity of the peak related to the W–O–W bond became very weak or negligible, which was noted prominently in the composites synthesized by route 2. This confirmed that the keggin unit strongly interacted with the mesoporous framework. These interactions can take place at either terminal oxygen atoms (O_t and O_c) or bridge oxygen atoms (O_b) in the keggin unit and can be expressed as $W{=}O_t...HO(SiO)_2{*}(AlOSi)_2$, $W–O_c...HO(SiO)_2{*}(AlOSi)_2$, and $W–O_b...HO(SiO)_2{*}(AlOSi)_2$. However, for the composites calcined at 550 °C, the signal at 900–1005 cm^{-1} is broadened, and additional peaks corresponding to crystalline WO_3 appear at 710 and 805 cm^{-1}. This implies the decomposition of HPW. For the $H_3PW_{12}O_{40}$–silica composite, the HPW decomposition was observed at an HPW loading of 15.7 wt % and a calcination temperature of 520 °C (Guo et al.,

2008). The above observations related to Raman spectra suggest that the basic structure of keggin is preserved at a calcination temperature of 400 and 500 °C, and the interaction between mesoporous aluminosilicates and the keggin unit still exists.

5.5.5 The identity of the acidic sites in the composites via pyridine FT-IR

Different types of acid sites in as-synthesized composites were investigated using pyridine FT-IR. The pyridine FT-IR of the representative composites HPW-MAS-7 500 °C and HPW MAS -9 500 °C synthesized via route 1 and route 2 are shown in Figures 5.13 and 5.14. Four characteristic peaks are observed for the composites at 1448, 1490, 1602 and 1631 cm^{-1}. The one at 1448 cm^{-1} corresponds to the hydrogen bonded pyridine, whereas the peak at 1602 cm^{-1} relates to the occurrence of Lewis acid sites. This peak at 1602 cm^{-1} can be due to the pyridine co-ordinatively bonded to Al^{3+} sites.

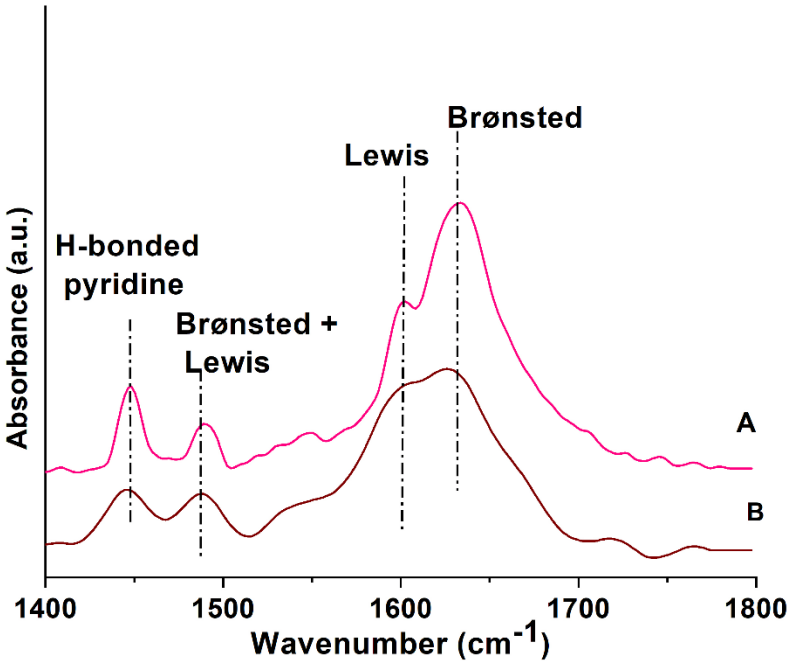

Figure 5.13**.** FT-IR spectra in 1300-1800 cm^{-1} range after pyridine desorption at 150 °C of A) HPW-MAS-7 1 500 °C, and B) HPW-MAS-7 2 500 °C.

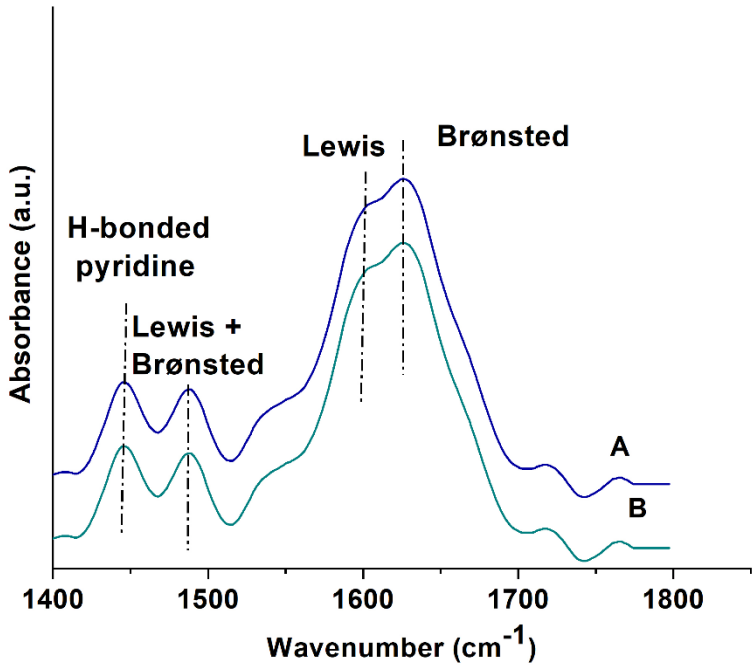

Figure 5.14**.** FT-IR spectra in 1300-1800 cm^{-1} range after pyridine desorption at 150 °C of A) HPW-MAS-9 1 500 °C, and B) HPW-MAS-9 2 500 °C.

The Brønsted acid peak at 1634 cm^{-1} is contributed from the surface $(AlO)(HO)Si^*(OSi)_2$ groups and the protons of HPW. The characteristic peak at 1490 cm^{-1} confirms the presence of the coexistence of Brønsted and Lewis sites. Hence, the above results indicate that the synthesized HPW-MAS composites are bifunctional, i.e., exhibit both Brønsted and Lewis acid sites regardless of the morphology.

5.6 Evaluation of the catalytic activity of HPW-MAS-7 and MAS-9 composites synthesized by route 1 and route 2

The influence of pore morphology, mesostructure, porosity and acidity of HPW-MAS composites on its catalytic performance was investigated by simultaneous esterification and transesterification of unrefined green seed canola oil to synthesize biodiesel. The catalytic activity was evaluated at the preliminary reaction conditions of 20:1 molar ratio of methanol to oil, 2.57 wt % catalyst (grams of a catalyst based on the weight of green seed canola oil), at 150 °C, 8 hours, and 4 MPa. Figure 5.15 shows the catalytic activity of the composites at varying calcination temperature synthesized by route 1 and route 2. The methyl ester yield is found to increase with

the increase in calcination temperature from 400 °C to 500 °C irrespective of the synthesis route and pore morphologies.

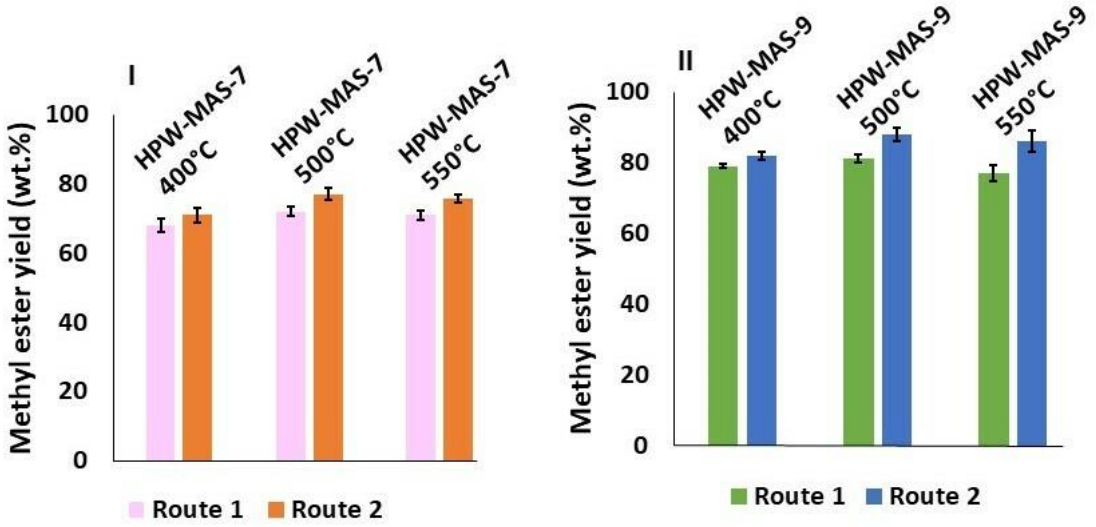

Figure 5.15. Methyl ester yield (wt. %) of (I) HPW-MAS-7 and (II) HPW-MAS-9 composites with 25 wt. % HPW loading at varying calcination temperature. Conditions- 20:1 methanol to oil molar ratio, 0.9 g of catalyst (2.57 wt.% of catalyst based on 35 g of oil), 150 °C, 8 hours, 4 MPa.

The increase in the methyl ester yield can be explained with the increase in Brønsted acidity. The increase in the Brønsted acid site density with the increase in calcination temperature from 400 to 500 °C can be attributed to the formation of larger polyanions due to an interaction between polyanions and the mesoporous framework. The formation of these larger heteropolyanions can effectively delocalize the negative charge required for the formation of Brønsted acids and promote the release of protons effectual for the transesterification reaction.

Hence, an increase in the catalytic activity can be as a result of $(Si(OSi)_2OAlOH_2)_n^+$ $[H_2PW_{12}O_{40}]^-$ species and bring about the protonation of the triglyceride molecule, which is a vital step for the transesterification reaction via acid catalysis (Figure 5.16). The presence of these species is evident from ^{31}P NMR studies. Also, from the ^{29}Si MAS–NMR studies, a higher fraction of Q_3 units, which are usually located at the edges of pores, is observed.

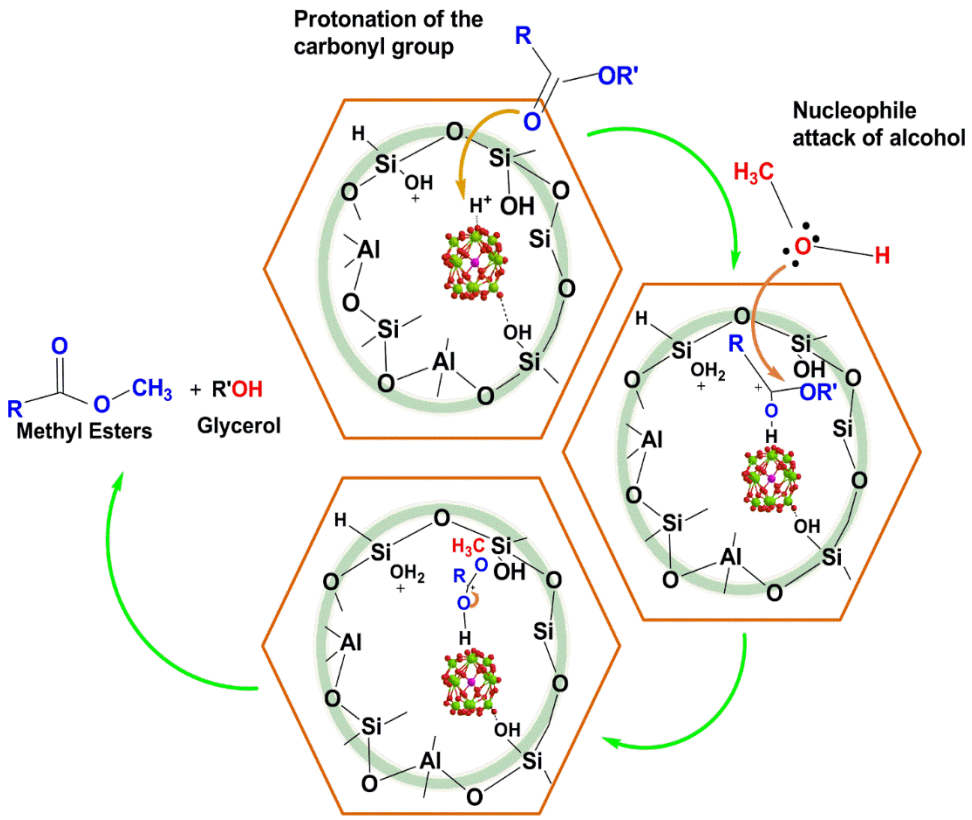

Figure 5.16. The pore composition of HPW-MAS composite catalysts as well as the mechanism of the transesterification reaction taking place on the surface of the composite.

This suggests more surface reactions of Q_3 silanols with HPW and creates a hydrophobic environment. Hence, it can be inferred that the pore channels in these composites are in favor of enrichment of hydrophobic reactants like triglyceride, whereas the hydrophilic glycerol is easily expelled. A higher yield of 88.7 ± 3.0 wt % is observed for HPW-MAS-9 500 °C composite obtained by Route 2 among all the composite catalysts. Thus, the interaction of the HPW with the aluminosilicate hydroxyl groups plays an important role in improving the acidity. This interaction can be recognized as the interaction of stronger Brønsted acid with a weaker Brønsted acid. The addition of the stronger acid to the weaker acid leading to stronger Brønsted acidity is well established.

$$Si(OSi)_2OAlOH)_n + H_3PW_{12}O_{40} \rightarrow (Si(OSi)_2OAlOH_2)_n^+ [H_2PW_{12}O_{40}]^- \quad \text{.....(5.2)}$$

On the other hand, the Lewis acidity of these composites comes from co-ordinatively unsaturated Al^{3+} sites. This Al^{3+} ion can interact directly with triglyceride molecules and behave as an electron acceptor and, thus, contribute to the catalytic activity.

Further, a strong interaction between the surface hydroxyl groups of aluminosilicates and HPW is observed at a higher calcination temperature of 500 °C. However, at the calcination temperature of 550 °C, hardly any significant increase in the methyl ester is observed. This can be a result of partial disintegration of HPW into tungsten trioxide, which is apparent from the Raman spectra (Figures 5.11F and 5.12F) of composites at a calcination temperature of 550 °C.

Concurrently, the structural orderings and pore geometries of the HPW-MAS-7 and HPW-MAS-9 composites also influence the catalytic activity. From Figure 5.15, it is observed that the composites synthesized by route 2 showed a higher catalytic activity compared to the ones synthesized via route 1. From, the SXRD and BET analyses, it can be seen that the sequential introduction of HPW affected the textural properties of the composites. For the composites synthesized by route 2, a transitional periodicity of hexagonal arrays is observed with large BET surface areas, higher pore diameter, and as well as uniform pore distribution. A larger BET surface and long-range orderliness can provide composites with a higher population of active sites and easy transport of triglyceride and methanol reactant. This contributes to the enhanced activity, whereas the composite synthesized by route 1, the translational periodicity, is absent. As indicated in the SXRD (Figure 5.5), there is no long-range order.

The smaller BET surface area and pore diameter can lead to an increased mass transfer limitation of the bulky triglyceride molecule and contribute to the lower activity of composites synthesized by route 1. The difference in the yield of the composite obtained with route 1 and route 2 can also be ascribed to a higher fraction of Q_3 units observed for the composite synthesized by route 2 and indicated more surface reactions of SiOH groups with HPW (^{29}Si MAS–NMR studies) providing active $W^{6-n}O_X$–(n-H^+) centers. This is also evident from Table 5.3, wherein a higher density of H^+ is observed for the composite synthesized by route 2 as compared to route 1. This contributes to the higher transesterification yield obtained with composites synthesized by route 2.

Table 5.3. Brønsted acid site density of the composites synthesized by route 1 and route 2 (with 25 wt % HPW loading) at different calcination temperatures.

Millimoles of H^+/g of composites		
HPW-MAS-7 composites		
Calcination temperature	Route 1	Route 2
400 °C	20520	23652
500 °C	22400	27792±549
550 °C	19540	25419
HPW-MAS-9 composites		
400 °C	29980	30980
500 °C	32670	35830±826
550 °C	30560	31230

On the basis of the physicochemical results and catalytic testing of the synthesized composites, it was found that the route 2 synthesis approach gave the composites with a well-ordered structure. This can decrease the mass transfer limitation of triglyceride and esters to and from active sites. Therefore, the composites synthesized by route 2 exhibited better catalytic activity in the transesterification of unrefined green seed canola oil. Hence, route 2 was employed for the synthesis of HPW-MAS-7 and HPW-MAS-9 composites with varying wt %'s of HPW loadings of the composites and calcined at 500 °C.

5.7 Influence of $H_3PW_{12}O_{40}$ loading (wt %) in the HPW-MAS-7 and HPW-MAS-9 composites obtained by route 2 on biodiesel synthesis

To study the influence of the HPW loading on the methyl ester yield, HPW-MAS-7 and HPW-MAS-9 composites with varying HPW loadings of 15, 25, and 35 wt % were investigated to catalyze the simultaneous esterification and transesterification of unrefined green seed canola oil under a 20:1 molar ratio of methanol to oil with 2.57 wt % catalyst (grams of a catalyst based on

the weight of oil) and at 150 °C and 4 MPa for 8 h. With the increase in HPW loading up to 25 wt % in composites, the increase in millimoles of H^+ and methyl ester is observed (Figure 5.17).

HPW-MAS-9 with 25 wt % of HPW loading is found to be the most active among the tested composites and gives a methyl ester yield of 89 ± 3.0 wt %. Further, an increase in the HPW loading to 35 wt % did not increase the methyl ester yield significantly.

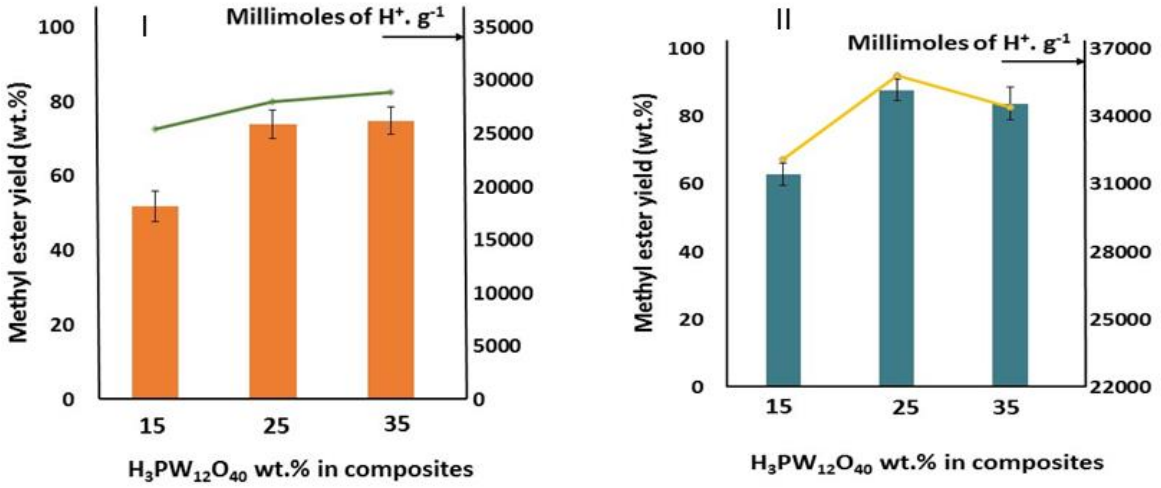

Figure 5.17**.** Catalytic activity of (I) HPW-MAS-7 and (II) HPW-MAS-9 composites with varying HPW loading as a function of Brønsted acidity. Conditions- 20:1 methanol to oil molar ratio, 0.9 g of catalyst (2.57 wt.% of catalyst based on 35 g of oil) , 150 °C, 8 hours, 4 MPa.

The increase in the HPW loading resulted in a decrease in surface area since HPW contributes to the sample weight. As a consequence, the number of available active sites decreased and led to the insignificant rise in the catalytic activity, whereas the HPW-MAS-7 composite with HPW loading of 25 and 35 wt % showed similar activity. Hence, subsequent reactions for both the composites were studied with HPW loading of 25 wt % for the optimization of reaction parameters and reusability study.

5.8 Comparison of efficiencies (in terms methyl ester wt %) of HPW-MAS-7 and HPW-MAS-8 (25 wt % HPW loading) composites

For similar reaction conditions, the compared efficiencies of composites provide insights into the textural properties and surface chemistry of the composites and their influence on the ability to catalyze the transesterification reaction effectively. The difference in the catalytic activity

of the two composites can be an outcome of the particle size of the composite, the pore size of the composites, and the increase in hydrophobicity with the increase in Brønsted acidity.

5.8.1 Influence of particle size

The major difference between the structures of both the composites is particle size. The average particle diameter of the HPW-MAS-9 composite was 6 times greater than the HPW-MAS-7 composite (Table 5.4). As a result, the surface area available for the reaction was smaller than the HPW-MAS-7 composite. Hence, a better reaction rate and decreased mass transfer flux are observed in the case of the HPW-MAS-7 composite. A higher activity is observed for the HPW-MAS-9 composite. This could be due to the fact that a catalytic site is used multiple times during the transesterification reaction.

Table 5.4. Comparison of HPW-MAS-7 and HPW-MAS-9 composites (obtained by route 2 with 25 wt. % of HPW loading) based on the textural and surface chemistry properties.

Catalysts	BET surface area (m^2/g)	Particle size (μm)	Pore size (nm)	Mass Transfer Flux ($mol/m^2.s$)	Reaction Rate ($mol/m^2.s$)	Weisz - Prater Criteria
HPW-MAS-7 500 °C	842	19	6	0.17	1.23×10^{-10}	2.1×10^{-6}
HPW-MAS-9 500 °C	810	118	8	2.5×10^{-2}	1.08×10^{-10}	7.2×10^{-6}

5.8.2 Brønsted acidity and hydrophobicity of the composites

A higher density of H^+ is observed for HPW-MAS-9 (35830 ± 826 mmol of H^+/ g) than for the HPW-MAS-7 composite (27792 ± 549 mmol of H^+/g). Hence, it promotes more of hydrophobic environment for the enrichment of hydrophobic reactants like triglyceride molecule. As a result, higher transesterification yield is observed for HPW-MAS-9 composite. Moreover, the hydrophobic environment protects Lewis sites from the poisoning effect of water. Thus, it supports that the HPW-MAS-9 composite was more hydrophobic than HPW-MAS-7.

5.8.3 BET surface area and pore size

The HPW-MAS-7 composite possesses higher surface area than HPW-MAS-9 composites, but it exhibits the lower activity as compared to the HPW-MAS-9. The influence of the BET surface area of the HPW-MAS-7 composite on the reaction is very limited. This is due to the low density of acid catalytic sites as implied by surface acidity analysis and a high silicon to aluminum molar ratio (SiO_2/Al_2O_3 = 60). On the other hand, the HPW-MAS-9 composite was found to effectively catalyze the reaction, which is reasonably related to the high density of the catalytic sites and low silicon to aluminum molar ratio (SiO_2/Al_2O_3 = 50) and favored the generation of strong Si-(OH)-Al sites. The low surface area exhibited by HPW-MAS-9 can be due to the decrease in mesostructuration/crystallization quality with the increase in Al content (Pega et al. 2008).

To explain the effect of the composite pore size on the activity of the catalysts, the maximum diameter of the major fatty acid in green seed canola oil (oleic acid C18:1) was computed using ChemBio3D Ultra 12.0 software (Appendix A, Figure A.5). The maximum diameter by definition is the longest part of the molecule and helps to ascertain that all molecules can travel through the pores of the composite material. The pore size of the HPW-MAS-9 composite is 4 times larger than that of oleic acid. Hence, it facilitates the diffusion of these bulky molecules into the composite pores to react with the acidic sites embedded in the pores and transformed to the product. Accordingly, the catalytic activity was higher when compared to that of the HPW-MAS-7 composite. However, the pore size of the HPW-MAS-7 composite was 3 times larger than the maximum diameter of the C18:1. Thus, there was adequate space for the molecule to pass through the pores but not enough active sites to react.

To summarize the comparison, from the mass transfer flux values, a lengthened diffusion path of reactants from the bulk to the surface of the HPW-MAS-9 composite is observed. At the macroscopic level, the size of the composite particles did not have an impact on the catalytic efficiency as the reaction did not take place exclusively on the surface of the composite. As a result, the higher activity could be mostly related to a number of active sites present inside the pores of the composite. In case of the MAS-7 composite, despite the decreased mass transfer flux, a low activity was observed, and this could be attributed to the low density of acid catalytic sites.

5.8.4 Optimization of the reaction conditions for the transesterification reaction

The influences of the weight of the catalyst, reaction time, and methanol to oil molar ratio on the ester yield were studied via response surface design of experiments for the HPW-MAS-9 composite with 25 wt % HPW loading. The temperature was kept constant at 180 °C. The methyl ester yield was measured at different combinations of catalyst weight, methanol to oil ratio, and time of reaction. The catalysts' weights were varied from 1 to 10 wt %, reaction time from 4 to 10 h, and methanol to oil molar ratio from 6:1 to 25:1 (Appendix A, Table A.2). The maximum ester yield obtained was 95.4 ± 1.4 wt % with optimal settings of the factors being 5.5 wt % of the catalysts (based on the weight of green seed canola oil), 15.5:1 methanol to oil molar ratio, and reaction time of 10 h at 180 °C and 4 MPa. For the HPW-MAS-7 composite, the maximum ester yield obtained was 85 ± 2.2 wt % at similar operating conditions. The regression equation in uncoded units, Pareto chart, and the main effects of the plot are provided in Appendix A (Eq. A.1, Figures A.6 and A.7).

5.9 Stability study of composite

The composite stability study was investigated by recycling the solids recovered from the reaction media and by characterizing the spent catalysts. The solids were separated by filtration after each catalytic run. The catalysts were regenerated by washing with tetrahydrofuran and subsequently drying at 110 °C.

From the results displayed in Figure 5.18, it is found that the HPW-MAS-7 and HPW-MAS-9 composites almost retained their catalytic activity after four runs. Also, hardly any change in the Brønsted acid density of regenerated catalysts is observed after each catalytic run.

In order to determine the leaching of the HPW from the composite framework, the concentration of the catalysts before and after the reaction run was obtained from the HPW standard calibration curve. Hardly any leaching of the HPW from the framework is observed. This is because keggin units exist in the framework structure via chemical interaction rather than the physical adsorption as evident from TEM and ^{29}Si NMR results.

The catalytic activity of the present composite catalyst for the simultaneous esterification and transesterification has been compared with other composites/hybrid catalysts in the reported literature in Table 5.5.

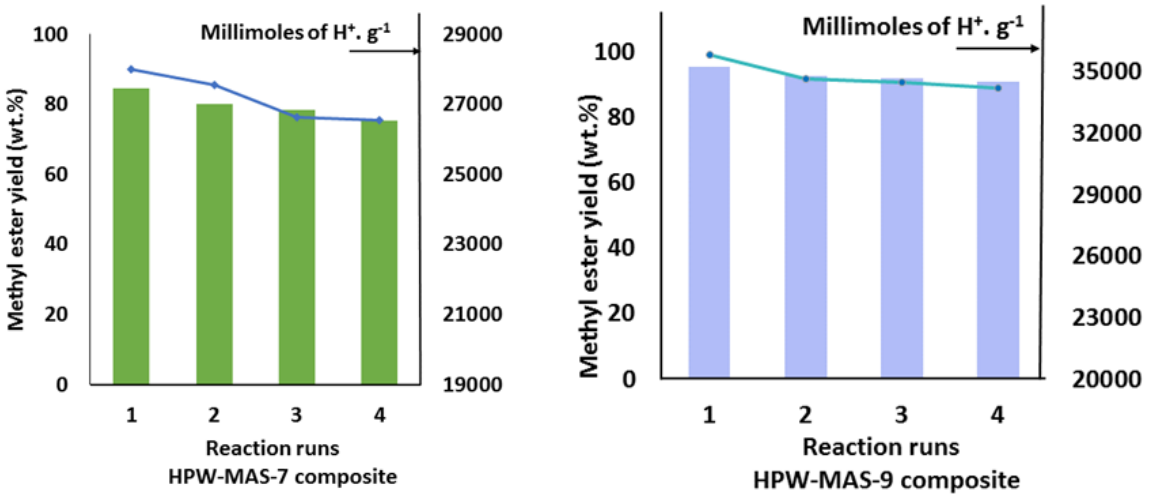

*HPW-MAS-7 composite - Methyl ester yield (wt %) ± 1.03; Millimoles of H^+/ g ± 826
*HPW-MAS-9 composite - Methyl ester yield (wt %) ± 1.1; Millimoles of H+/g ± 549

Figure 5.18. Reusability study of HPW-MAS composites (with 25 wt. % HPW loading) towards transesterification of green seed canola oil with methanol. Optimized Conditions- 15.5:1 methanol to oil molar ratio, 1.9 g of catalysts (5.5 wt. % catalyst based on 35 g of oil), 180 °C, 10 hours, 4 MPa.

The HPW-MAS-9 composite catalyst exhibited a high biodiesel yield of 95.4 ± 1.4 wt % for the simultaneous esterification and transesterification of unrefined green seed canola oil (10.8 mg KOH/g) under moderate conditions.

From Table 5.5, it is observed that 80–85% methyl esters were obtained for Zr-periodic mesoporous silica with crude palm oil at a high temperature and catalyst loading (Sánchez-Vázquez et al., 2013). The $Mg_{20}F_{39}$TPA-1.0 hybrid shows considerable catalytic activity and gives a methyl ester yield of 93 ± 0.7% (Yang et al., 2017). For $H_3PW_{12}O_{40}/Ta_2O_5$-10.8, 51.4% of methyl palmitate was obtained with model feedstock at a very high molar ratio, and a decrease in activity was observed after the second run (Xu et al., 2008). With Ta_2O_5/SiO_2–[$H_3PW_{12}O_{40}$/Me] for soybean oil with 20% myristic acid, the yield of methyl linolenate, methyl palmitate, and methyl oleate reached 81.2%, 65.9%, and 53.9% after 24 h using a very high methanol to oil molar ratio (Xu et al., 2009). However, under the same conditions, the methyl myristic yield reached more than 99%, indicating more reactivity towards the esterification reaction.

Table 5.5. Composite/hybrid catalysts for the biodiesel production

	Biodiesel production				
Hybrids/Composites catalysts	Feedstocks	Reaction conditions	Activity	Recyclability	Reference
Zr-periodic mesoporous silica	Crude palm oil	48.5:1 methanol to oil molar ratio, 12.8 wt % catalysts, 209 °C, 6 h.	80-85 % of methyl esters	Insignificant loss in activity after two cycles	(Sánchez-Vázquez et al., 2013)
$Mg_{20}F_{39}$TPA-1.0 (TPA- tungstophosphoric acid)	Jatropha oil	30: 1 methanol to oil molar ratio, 8 wt % catalysts, 130 °C, 12 h.	93 ±0.7 %	Negligible loss in activity after five cycles	(Yang et al., 2017)
$H_3PW_{12}O_{40}/Ta_2O_5$-10.8	Tripalmitin	90:1 methanol to palmitate ratio, 2 wt % catalysts, 65 °C, 6 h.	51.4 % of methyl palmitate	A decrease in the yield was observed after the second run.	(Xu et al., 2008)
Ta_2O_5/SiO_2–$[H_3PW_{12}O_{40}/Me]$ SiO_2-$[H_3PW_{12}O_{40}/Me]$	Soybean oil with 20 wt.% of myristic acid	90:1 methanol to oil ratio, 2 wt. % catalysts, 65 °C, 24 h.	Methyl linoleate 81.2 %, methyl palmitin 65.9 %, methyl oleate 53.9 % Methyl linoleate 9.3%, methyl palmitin 10.5%, methyl oleate 53.9%	Similar level of activity after four cycles.	(Xu et al., 2009)
HPW-MAS-9 with 25 wt.% HPW loading	Unrefined green seed canola oil	15.5:1 methanol to oil ratio, 5.5 wt % catalysts, 180 °C, 10 hours.	95.4 ± 1.4 wt% methyl ester	Retained catalytic activity after four runs.	This work

Compared to the esterification reaction, the transesterification reaction of oil proceeds more slowly. This is because transesterification involves consecutive steps and requires higher activation. Hence, in the literature, most of the catalytic activity of the catalysts for the biodiesel production is reported mainly via esterification reaction under mild conditions but at a very high methanol to oil molar ratio and longer reaction duration.

The present composite exhibits promising activity towards the biodiesel production via simultaneous esterification and transesterification of the unrefined green seed canola oil at a moderate methanol to oil molar ratio, catalyst loading, and reaction time at 180 °C giving methyl ester yield of 95.4 ± 1.4 wt %. The FFA content of resulting biodiesel was found to be 0.2 ± 0.01 wt %. The triglyceride, diglyceride, and monoglyceride content were 1.2 ± 0.8 wt %, 1.4 ±0.1 wt % and 1.9 ± 1.5 wt %, respectively.

Optimized HPW-MAS-9 composite with 25 wt % HPW loading catalysts can be used for the pre-treatment in alkaline catalysis. However, the leaching of alkali catalysts such as KCO_3 and $CaCO_3$ in glycerol phase may take place during the transesterification reaction. In the case of biodiesel production using CaO as a heterogeneous catalysts, Colombo et al. (2017) found a high concentration of calcium in the biodiesel product formed by the reaction between CaO and glycerol. For this purpose, a further step in the purification of biodiesel is required to remove the leached CaO catalysts by passing the biodiesel through a column packed with cation-exchange resin.

5.10 Conclusions

The sequential introduction of HPW in the preparation of these composites affected the surface morphologies of these catalysts. HPW-MAS composites obtained by route 2 exhibited a larger BET surface area and well-ordered structure decreasing the mass transfer limitation of the bulky triglyceride molecules. HPW-MAS 2D hexagonal composites with long-range orderliness exhibited higher catalytic activity with respect to ones obtained by route 1, and thus suggested that the ordered, transitional periodicity is beneficial in catalysis. The synthesized composites were found to be stable at a calcination temperature of 500 °C without any decomposed keggin structure.^{31}P NMR, ^{29}Si MAS NMR, and Raman spectroscopy confirmed the stronger interactions between the keggin unit and aluminosilicates in the composites and, hence, inhibited the leaching of HPW from the composite framework. ^{29}Si MAS NMR study indicated more surface reactions

or interaction of Q_3 silanols at the pore edge with HPW in favor of the catalytic activity. The inherent Brønsted acidity and Lewis acidity of these composites contributed to the catalytic activity. These HPW-MAS-7 and HPW-MAS-9 composites can be used multiple times without any loss of reactivity**.**

Compared to HPW-MAS-7, HPW-MAS-9 composite with HPW loading of 25 wt % demonstrated potential catalytic activity and hence, was the choice of catalyst for kinetic and mechanistic studies detailed in the next section.

CHAPTER 6

Kinetic Modeling, Mechanistic, and Thermodynamic Studies of HPW-MAS-9 Catalysed Transesterification Reaction for Biodiesel Synthesis

The content of this chapter has been published in Fuel Processing Technology and cited as

Kurhade, A., Dalai, A.K., 2019. Kinetic modeling, mechanistic, and thermodynamic studies of HPW-MAS-9 catalysed transesterification reaction for biodiesel synthesis. Fuel Process. Technol. 196, 106164. https://doi.org/10.1016/j.fuproc.2019.106164

Contribution of the Ph.D. Candidate

Experiments and modelling were carried out by Ankeeta Kurhade. Majak Mapoiur helped with the coding in Matlab. The manuscript was drafted by Ankeeta Kurhade based on the suggestions provided by Dr.Ajay K.Dalai.

Contribution of this Chapter to Overall Ph.D. Research

This section provides the kinetics, mechanistic, and thermodynamic studies of the transesterification reaction of green seed canola oil and methanol catalyzed by self-assembled HPW-MAS-9 mesoporous composite. The potential energy profile for the stepwise transesterification mechanism over the composite catalysts to yield biodiesel has been deduced, which makes this study unique. The results provide a basic understanding of the reaction mechanism influencing the kinetics over acid-catalyzed transesterification.

6.1 Abstract

The kinetics and reaction mechanism of methanolysis of unrefined green seed canola oil using heterogeneous HPW-MAS-9 composite catalyst have been investigated. The activity coefficients of the reactant and product species were estimated using the UNIQUAC method. Eley-Rideal reaction pathway with the surface reaction of adsorbed methanol as the rate controlling step was found to be a reliable presentation of the observed kinetics.

Other kinetic models deduced from pseudo-homogenous (PH) and Langmuir-Hinshelwood-Hougen-Watson (LHHW) were rejected based on statistical analysis. The positive values of ΔH^{0} and ΔG^{0} indicated that the reaction is endothermic and non-spontaneous. E_a (activation energy), $\Delta H^{\ddagger}$ (enthalpy of activation), $\Delta G^{\ddagger}$ (free energy of reaction), and $\Delta S^{\ddagger}$ (entropy of activation) for the reaction was found to be 72.5 kJ/mol, 68.9 kJ/mol, 58.3 kJ/mol, and 0.04 kJ/mol K, respectively. Intricate mechanistic details for the stepwise transesterification reactions were deduced from the kinetic and thermodynamic parameters. On the basis of the $\Delta S^{\ddagger}$, the reaction of triglyceride to diglyceride followed the dissociative pathway (S_N1 mechanism), whereas the reactions of diglyceride to monoglyceride and monoglyceride to glycerol proceeded via the associative pathway (S_N 2 mechanism).

6.2 Introduction

Biofuel synthesis methods –whether biodiesel, hydrogenated renewable diesel or ethanol are efficient, renewable pathways that comply with Canada's targets for GHG reductions. Second generation biodiesels are synthesized from non-edible feedstocks that go through a set of esterification and transesterification reactions to yield methyl esters in the presence of catalysts. Traditional alkaline catalysts are effective for biodiesel production from refined vegetable oils; but, the process tends to be uneconomical because of high feedstock cost, undesired side reactions and competition with food resources (Su and Guo, 2014). On the contrary, heterogeneous solid acid catalysts, promote transesterification and esterification reaction from low-quality, unrefined feedstock without any side reactions like saponification; thus, making them desirable alternatives.

Among solid acid catalysts, heteropolyacids are widely used for acid-catalyzed reactions owing to their high Brønsted acidity (Gagea et al., 2009; Hoo and Abdullah, 2014; Tropecêlo et al.,2010). The incorporation of heteropolyacids like 12-tungstophosphoric acid (HPW) onto various supports like functionalized SBA-15 with ionic liquid, Zr-Beta zeolite, and zirconia for the acid catalyzed reactions have been stated in literature (Alcañiz-Monge et al., 2018; Hung et al., 2019; Winoto et al., 2019). The modification of these catalytic materials has also been studied in literature (Alcañiz-Monge et al., 2018; Nikseresht et al., 2017).

In our recent study, the direct incorporation of HPW in the synthesis of MAS-9 aluminosilicate (HPW-MAS-9 composite with 25 wt. % HPW loading) had shown a promising catalytic activity for methyl ester synthesis from unrefined green seed canola oil. Also, the

composite catalysts can be used multiple times without any leaching of the HPW or loss of reactivity, thus, making them potentially efficient heterogeneous catalysts. Owing to this, efforts are made in the present work to investigate the kinetics and gain insights into mechanistic details of the transesterification reaction using this HPW-MAS-9 composite catalyst.

A few kinetic models for the transesterification reaction using a heterogeneous solid base or solid acid catalysts have been cited in the literature. Dossin et al. (2006) proposed an Eley-Rideal mechanism based on three steps with the methanol adsorption as the slowest step. The authors reported that the adsorbed methanol interacts with ethyl acetate from the bulk when catalyzed by magnesium oxide on the solid base. Van De Steene et al. (2012) investigated pseudo-homogeneous (PH), Langmuir–Hinshelwood--Hougen–Watson (LHHW) and Eley–Rideal (ER) mechanisms for the methanolysis of ethyl acetate catalyzed by Lewatit K1221. Wang et al. (2019) employed power law and Eley- Rideal (ER) models to describe the esterification of palmitic acid with methanol catalyzed by phosphotungstic acid based poly (ionic liquid). Kapil et al. (2011) developed three models for the transesterification of glycerol tributyrate using hydrotalcite catalysts. The reaction pathways included Langmuir-Hinshelwood-Hougen–Watson (LHHW), Hattori, and Eley-Rideal (ER) models based on assumptions of adsorption of methanol, quasi-steady state, and surface reaction as the rate-determining step.

The transesterification reactions involving methanol and vegetable oil using heterogeneous solid acid catalysts are a complicated heterogeneous liquid-liquid-solid reaction with three consecutive steps (Xiao et al., 2010). The transesterification reaction of vegetable oil with methanol was found to be reversible (Lukić et al., 2013). The overall transesterification process involves the intrinsic reaction, inter-liquid mass transfer, and liquid-solid mass transfer resistance. Hence, most of the kinetic studies employ pseudo-homogeneous model for esterification or transesterification reactions that is simple and involves fewer constants to be approximated (Banchero and Gozzelino, 2018; Kaur and Ali, 2014; Lukić et al., 2013). Gaurav et al. (2019) considered only the pseudo-homogeneous model for simultaneous transesterification and esterification of canola oil with added free fatty acid using $HSiW/Al_2O_3$ solid acid catalyst. Pan et al. (2019) also employed a pseudo-homogenous model for heterogeneously catalyzed esterification reaction of oleic acid over acidic ionic functionalized (IL)-mesoporous melamine-formaldehyde polymer (MMFP-IL).Some investigators proposed that the heterogeneous and homogenous reactions probably follow a similar reaction pathway (Bozek-Winkler and Gmehling, 2006; López et al., 2007).

Most studies in literature for the transesterification of vegetable oil and methanol limit the thermodynamic study only to the estimation of activation energies. In literature, only a few reports are available stating the $\Delta H^{\ddagger}$ (enthalpy of activation), $\Delta G^{\ddagger}$ (free energy of reaction), and $\Delta S^{\ddagger}$ (entropy of activation) for transesterification reactions. However, these values are estimated mostly for the overall transesterification reaction. To potentially determine the rate that controls the overall transesterification of unrefined green seed canola oil using HPW–MAS-9 composite, a less complex pseudo-homogeneous (PH) model and adsorption models such as Langmuir-Hinshelwood-Hougen-Watson (LHHW) and Eley-Rideal (ER) are studied in the current investigation. In addition to reaction kinetics, the thermodynamic parameters for the stepwise transesterification reactions are evaluated using the best model based on statistical analysis.

In the present work, the thermodynamic parameters $\Delta H^{\ddagger}$, $\Delta S^{\ddagger}$ and $\Delta G^{\ddagger}$ have been calculated for the stepwise forward and reverse transesterification reactions, thus providing the details for the reaction pathways. The model of these mechanisms plays an important role in finding the kinetic and thermodynamic parameters. The optimal values obtained from the model aid in designing and controlling of heterogeneous reactions using solid acid composite catalysts.

6.3 Experimental

HPW-MAS-9 composite catalyst with 25 wt % HPW loading was synthesized by one-pot – surfactant (Pluronic123) template-assisted self-assembly mechanism. The detailed synthesis procedure is reported in our previous work (Kurhade et al., 2019). The composite was calcined at 500 °C.

The transesterification reactions were performed in a 100 mL batch reactor (Parr Instrument Co., IL, USA) at 150 °C, 165 °C, and 180 °C using 35 g of unrefined green seed canola oil, 15.7 methanol to oil molar ratio and 5.5 wt.% of catalyst (based on weight of oil).The reactions were performed for 600 minutes. Samples were collected at an interval of 15 minutes for the first hour and thereafter at an interval of 60 minutes. 1 mL of the sample was withdrawn from the reaction system with the stirrer on, without stopping the reaction. The amount of the reaction volume decreased slightly at the time of data collection, without disturbing much the concentration of species. The samples were analyzed using HPLC (Agilent Technologies) with two phenogel columns (5µ 100 Å 300 × 7.8 mm) attached to the guard column. The column and detector

temperatures were maintained at 24 °C and 35 °C, respectively. The injection volume of the sample was 20 µL. Tetrahydrofuran solvent was used for a mobile phase. Triglyceride (TG), diglyceride (DG), monoglyceride (MG), and methyl ester (ME) concentrations were expressed as mol/L Methanol (MeOH) concentrations were determined on the basis of the number of moles of methanol consumed and the moles of the methyl ester formed. Glycerol (GL) concentrations were estimated using equation (1)

$$n_{TG_0} + n_{DG_0} + n_{MG_0} = n_{TG_t} + n_{DG_t} + n_{MG_t} \quad \text{.....(6.1)}$$

$n_{TG_0}, n_{DG_0}, n_{MG_0}$, represents the moles of TG, DG and MG present initially, whereas n_{TG_i}, n_{DG_i}, n_{MG_i} are the moles of TG, DG and MG at time = *t.*

6.4 Methodology

The overall strategy to determine the kinetic rate constants based on PH and adsorption models is shown in Figure 6.1.

The change in the reactant concentration with time is termed as a kinetic rate. The expressions for the rate of reaction were derived in terms of activities of species for methyl ester synthesis for the various reaction mechanisms.

The non-ideality of the reaction mixture in the transesterification reaction was assessed. The activity of species was correlated with its concentration (Eq. 6.2). The UNIQUAC method described here was employed to determine the activity coefficient (γ_i) of species *i* using group contribution (Sadhukhan et al., 2014). The contribution made by one group within a molecule is assumed to be independent of that made by any other group in that molecule. *nspc* represents the total number of species. Table 6.1 provides the activity coefficients of species at different temperatures at steady state.

$$[i] = C_i \gamma_i \; \forall i \in nspc \quad \text{.....(6.2)}$$

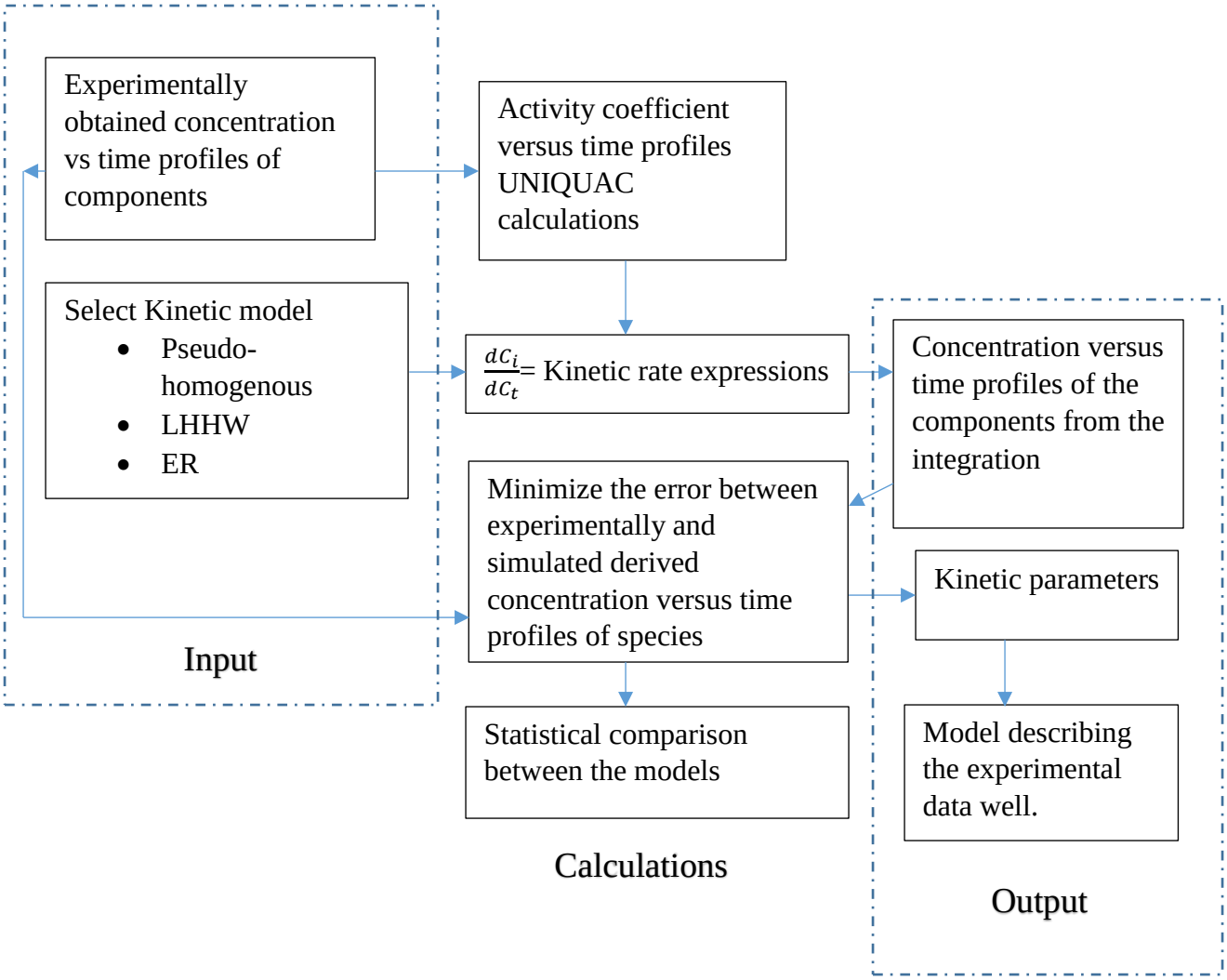

Figure 6.1. Methodology to determine the mechanism.

Table 6.1. Activity coefficients of species at different temperatures at steady state

Temperature	TG	DG	MG	MeOH	GL	ME
423K	1.40	0.52	5.70	1.03	2.19	6.12
438K	1.29	0.49	4.30	1.05	1.31	2.80
453K	1.37	0.52	0.68	1.04	1.14	1.93

The activity coefficient (γ_i) consists of two parts (Eq. 3), the first part is the combinatorial part (γ_i^C), contributed by the molecular size shape and the second part is the residual part (γ_i^R) due to the interactions of molecule (Kapil et al., 2011).

$$\text{n}\,\gamma_i = \ln \gamma_i^C + \ln \gamma_i^R \;\forall i \in nspc \quad \text{(6.3)}$$

γ_i^C is evaluated using the mole fraction x_i , volume or segment fraction Φ_i and area fraction θ_i of species *i* (Eq.6.4).

$$\ln \gamma_i^C = \ln \frac{\Phi_i}{x_i} + 5q_i \ln \frac{\theta_i}{\Phi_i} + l_i - \frac{\Phi_i}{x_i}\sum_{i'}^{nspc} x_i, l_i\,, \;\forall i \in nspc \quad \text{(6.4)}$$

s_i , q_i represents the molecular van der Waals area and volume parameters. They are estimated from the summation of the group (p) van der Waals surface area S_P and volume Q_p (Eqs. 6.5, 6. 6).

$$\theta_i = \frac{x_i q_i}{\sum_{i'}^{nspc} x_i, q_i} \quad \Phi_i = \frac{x_i s_i}{\sum_{i'}^{nspc} x_i, s_i} \;\; \forall i \in nspc \quad \text{(6.5)}$$

$$q_i = \sum_p^g v_p^{(i)} Q_p \;\; S_i = \sum_p^g v_p^{(i)} S_P \;\; \forall i \in nspc \quad \text{(6.6)}$$

$$l_i = 5(s_i - q_i) - (s_i - 1) \;\; \forall i \in nspc \quad \text{(6.7)}$$

The number of p group present in the molecule *i* is denoted by $v_p^{(i)}$. l_i represents group parameters in Eq. (6.4).

γ_i^R is estimated using Eq. (6.8), wherein Γ_p is the group residual activity coefficient. $\Gamma_p^{(i)}$, and Γ_p are the corresponding area parameters in Eqs. (6.9) - (6.11).

$$\ln \gamma_i^R = \sum_p^g (\ln \Gamma_p - \ln \Gamma_p^{(i)})\, v_p^{(i)} \quad \forall i \in nspc \quad \text{..... (6.8)}$$

$$\ln \Gamma_p = Q_P \left\{1 - \ln\left(\sum_m^g \theta_m \Psi_{m,p}\right) - \sum_m^g \frac{\theta_m \Psi_{p,m}}{\sum_n^g \theta_n \Psi_{n,m}}\right\} \quad \forall m, n, p, \in g \text{.....(6.9)}$$

$$\theta_p = \frac{Q_p X_p}{\sum_p Q_P X_P} \quad \text{..... (6.10)}$$

$$X_p = \frac{\sum_i x_i}{\sum_i x_i \sum_p v_p^{(i)}} \text{.....(6.11)}$$

$$\ln \Gamma_p^{(i)} = Q_P \left\{1 - \ln\left(\sum_m^g \theta_m^{(i)} \Psi_{m,p}\right) - \sum_m^g \frac{\theta_m^{(i)} \Psi_{p,m}}{\sum_n^g \theta_n^{(i)} \Psi_{n,m}}\right\} \quad \forall m, n, p, \in g \; and \forall \; i \; \in nspc \text{ .....(6.12)}$$

$$\Psi_{m,n} = \exp\left(-\frac{a_{m,n}}{T}\right) \text{.....(6.13)}$$

$\Psi_{m,n}$ is the group interaction parameter in species i related to $a_{m,n}$. $a_{m,n}$ is interaction energy between groups m and n at temperature T.

The ordinary differential equations (ODEs) (Tables 6.2 and 6.4) were solved by an ODE45 using MATLAB R 2018a. The built in "ode45" employs 4th and 5th order Runge-Kutta formula to solve the differential equations. The bulk concentration profiles of species are obtained as a function of time. The initial values for TG, DG, MG, ME, MeOH, and GL are provided in Appendix E. The difference between the calculated values and experimental values was defined as C_{error} matrix given by Eq. (6.14) (Issariyakul and Dalai, 2012) .

$$C_{error} = \left|C_{cal} - C_{exp}\right| \text{.....(6.14)}$$

The summation of all elements in C_{error} matrix was defined as *"err"* function. To minimize the error the built in "*fminsearch"* command was used. The "*fminsearch"* command accepts the

initial guess values of rate and equilibrium constants, and returns scalar err and minimizes it by adjusting the rate constants (Issariyakul and Dalai, 2012).

The kinetic models were statistically compared using P_{12} criterion as defined in the Eq. (6.15) (Kapil et al., 2011). χ_1^2 and χ_2^2 in the equation are Chi-square. n_1 and n_2 represents the number of constants or parameters , for model 1 and 2. N represents the number of experimental points.

$$P_{12} = \frac{\chi_1^2/(N-n_1)}{\chi_2^2/(N-n_2)} \quad \text{.....(6.15)}$$

If $P_{12} < 1$, model 1 fits the data better compared to model 2 and conversely. χ^2 is calculated using Eq. 6.16.

$$\chi^2 = \sum_{t=1}^{n\ time} \sum_{i=1}^{nspc} \frac{(C_i(t) - C_i^{Exp}(t))^2}{C_i^{Exp}(t)} \quad \text{.....(6.16)}$$

6.5 Kinetic modeling

The transesterification reaction can be represented by the following stoichiometric Eq. set (6.17)

$$\mathrm{TG} + \mathrm{MeOH} \underset{k_2}{\overset{k_1}{\rightleftharpoons}} \mathrm{DG} + \mathrm{ME} \quad \&$$

$$\mathrm{DG} + \mathrm{MeOH} \underset{k_4}{\overset{k_3}{\rightleftharpoons}} \mathrm{MG} + \mathrm{ME} \quad \&$$

$$\mathrm{MG} + \mathrm{MeOH} \underset{k_6}{\overset{k_5}{\rightleftharpoons}} \mathrm{GL} + \mathrm{ME} \quad \text{.....(6.17)}$$

To yield a high conversion of triglyceride, 15.7:1 methanol to green seed canola oil molar ratio was maintained. The concentration of the methanol approximately remains constant as it is one of the excess reactants. Thus, the transesterification reaction depends on the limiting reagent triglyceride. The kinetics was evaluated via the pseudo-first order reaction in the absence of the internal and external mass transfer (Please see Appendix G). Four kinetics models based on pseudo-homogeneous (PH), Langmuir-Hinshelwood-Hougen-Watson (LHHW) and Eley-Rideal (ER) type reaction mechanisms with the assumptions of pseudo-homogeneous behaviour of surface species,

surface reactions and adsorption of methanol as rate controlling steps and were evaluated, as follows:

- Pseudo –homogeneous
- Langmuir-Hinshelwood-Hougen–Watson surface reaction as rate controlling
- Eley-Rideal surface reaction as rate determining
- Eley –Rideal methanol adsorption as rate determining

6.5.1 PH model

The pseudo homogeneous considers that the surface of a catalyst is at pseudo-homogeneous sate such that concentration of species on the catalysts remains constant.

Table 6.2**.** Reaction rate expressions for PH model.

Assumptions	Equation set (6.18) Overall reaction rate
The surface of the catalyst is at pseudo-homogeneous state. The concentration of the catalyst surface species remains constant.	$r_{TG} = \frac{d[TG]}{dt} = -k_1\,[TG][MeOH] + k_2[ME][DG]$
	$r_{DG} = \frac{d[DG]}{dt} = k_1\,[TG][MeOH] + k_4[MG][ME] - k_2[DG][ME] - k_3[DG][MeOH$
	$r_{MG} = \frac{d[MG]}{dt} = \mathrm{k_3[DG][MeOH]+k_6\,[GL][ME] - k_4[MG][ME] - k_5[MG][MeOH]}$
	$r_{ME} = \frac{d[ME]}{dt} = \mathrm{k_1\,[TG][MeOH] + k_3[DG][MeOH]+k_5[MG][MeOH] - k_2[DG][ME] - k_4[MG][ME] - k_6\,[GL][ME]}$
	$r_{GL} = \frac{d[GL]}{dt} = \mathrm{k_5\,[MG][MeOH] - k_6\,[GL][ME]}$
	$r_{MeOH} = -r_{ME}$

Hence, it does not account for the adsorption terms for any of the species. The kinetic rate expressions for the PH model are provided in Table 6.2 (Eq. set 6.18).

6.5.2 LHHW kinetic mechanism

The elementary reactions in LHHW reaction pathway for the first reversible reaction in transesterification are given in Table 6.3 (Eq. set 6.19). The LHHW model is based on the fractional coverage of all the reacting species for the transesterification reaction. The adsorbed MeOH and adsorbed TG on the surface of the catalyst (active sites) react to form adsorbed DG and ME, respectively. Subsequently, the DG formed reacts with adsorbed MeOH to form MG, which also reacts to form GL. LHHW model based on the surface reaction or adsorption of methanol as the rate controlling step has been previously described in literature (Eze, 2014). In this case, diffusion and mass transport rates are faster than surface reactions. The surface reaction tends to be the slowest step. The kinetic rate expressions for the LHHW reaction pathway based on surface reaction as slowest step are presented in Table 6.4 (Eq. set 6.21).

Table 6.3. Elementary reactions in LHHW and ER mechanism.

	Equation set (6.19) LHHW	
1.	$TG + \emptyset \leftrightarrow TG\emptyset$	TG adsorption
2.	$MeOH + \emptyset \leftrightarrow MeOH\emptyset$	MeOH adsorption
3.	$TG\emptyset + MeOH\emptyset \leftrightarrow DG\emptyset + ME\emptyset$	Surface reaction
4.	$DG\emptyset \leftrightarrow DG + \emptyset$	DG desorption
5.	$ME\emptyset \leftrightarrow ME + \emptyset$	ME desorption
	Equation set (6.20) ER	
1.	$MeOH + \emptyset \leftrightarrow MeOH\emptyset$	Adsorption of MeOH
2.	$TG + MeOH\emptyset \leftrightarrow DG\emptyset + ME$	Surface reaction
3.	$DG\emptyset \leftrightarrow DG + \emptyset$	Desorption of DG

Table 6.4. Reaction rate expressions for LHHW and ER models.

LHHW mechanism surface reaction as rate determining equation	
Assumptions	Equation set (6.21) Overall reaction rate
TG, DG, MG, ME, GL, and MeOH species are adsorbed on the catalysts surface. Since, the catalyst was used in the powder form, it was assumed that the diffusion steps are relatively fast. Surface reaction of adsorbed TG with adsorbed methanol is rate limiting.	$r_{TG} = \frac{d[TG]}{dt} = \frac{-k_1 K_{TG} K_{MeOH}[TG][MeOH] + k_2 K_{DG} K_{ME}[DG][ME]}{(1 + K_{TG}[TG] + K_{DG}[DG] + K_{MG}[MG] + K_{MeOH}[MeOH] + K_{ME}[ME] + K_{GL}[GL])^2}$ $r_{DG} = \frac{d[DG]}{dt} = \frac{k_1 K_{TG} K_{MeOH}[TG][MeOH] + k_4 K_{MG} K_{ME}[MG][ME] - k_2 K_{DG} K_{ME}[DG][ME] - k_3 K_{DG} K_{MeOH}[DG][MeOH]}{(1 + K_{TG}[TG] + K_{DG}[DG] + K_{MG}[MG] + K_{MeOH}[MeOH] + K_{ME}[ME] + K_{GL}[GL])^2}$ $r_{MG} = \frac{d[MG]}{dt} = \frac{k_3 K_{DG} K_{MeOH}[DG][MeOH] + k_6 K_{GL} K_{ME}[GL][ME] - k_4 K_{MG} K_{ME}[MG][ME] - k_5 K_{MG} K_{MeOH}[MG][MeOH]}{(1 + K_{TG}[TG] + K_{DG}[DG] + K_{MG}[MG] + K_{MeOH}[MeOH] + K_{ME}[ME] + K_{GL}[GL])^2}$ $r_{ME} = \frac{k_1 K_{TG} K_{MeOH}[TG][MeOH] + k_3 K_{DG} K_{MeOH}[DG][MeOH] + k_5 K_{MG} K_{MeOH}[MG][MeOH] - k_2 K_{DG} K_{ME}[DG][ME] - k_4 K_{MG} K_{ME}[MG][ME] - k_6 K_{GL} K_{ME}[GL][ME]}{(1 + K_{TG}[TG] + K_{DG}[DG] + K_{MG}[MG] + K_{MeOH}[MeOH] + K_{ME}[ME] + K_{GL}[GL])^2}$ $r_{GL} = \frac{d[GL]}{dt} = \frac{k_5 K_{MG} K_{MeOH}[MG][MeOH] - k_6 K_{GL} K_{ME}[GL][ME]}{(1 + K_{TG}[TG] + K_{DG}[DG] + K_{MG}[MG] + K_{MeOH}[MeOH] + K_{ME}[ME] + K_{GL}[GL])^2}$ $r_{MeOH} = -r_{ME}$
ER mechanism surface reaction as rate determining equation	
Assumptions	Equation set (6.22) Overall reaction rate

The adsorbed species is MeOH and reacts with TG in the bulk phase. Due to significantly higher MeOH concentration, only methanol adsorption term was mathematically significant. Hence, adsorption term corresponding to ester term was not included.	$r_{TG} = \frac{-k_1[TG]K_{MeOH}[MeOH] + k_2[ME]K_{DG}[DG]}{(1 + K_{DG}[DG] + K_{MG}[MG] + K_{MeOH}[MeOH] + K_{GL}[GL])}$ $r_{DG} = \frac{k_1 K_{MeOH}[TG][MeOH] + k_4 K_{MG}[MG][ME] - k_2 K_{DG}[DG][ME] - k_3 K_{MeOH}[DG][MeOH]}{(1 + K_{DG}[DG] + K_{MG}[MG] + K_{MeOH}[MeOH] + K_{GL}[GL])}$ $r_{MG} = \frac{k_3 K_{MeOH}[DG][MeOH] + k_6 K_{GL}[GL][ME] - k_4 K_{MG}[MG][ME] - k_5 K_{MeOH}[MG][MeOH]}{(1 + K_{DG}[DG] + K_{MG}[MG] + K_{MeOH}[MeOH] + K_{GL}[GL])}$ $r_{ME} = \frac{k_1 K_{MeOH}[TG][MeOH] + k_3 K_{MeOH}[DG][MeOH] + k_5 K_{MeOH}[MG][MeOH] - k_2 K_{ME}[DG][ME] - k_4 K_{MG}[MG][ME] - k_6 K_{GL}[GL][ME]}{(1 + K_{DG}[DG] + K_{MG}[MG] + K_{MeOH}[MeOH] + K_{GL}[GL])}$ $r_{GL} = \frac{k_5 K_{MeOH}[MG][MeOH] - k_6 K_{GL}[GL][ME]}{(1 + K_{DG}[DG] + K_{MG}[MG] + K_{MeOH}[MeOH] + K_{GL}[GL])}$ $r_{MeOH} = -r_{ME}$

ER mechanism with methanol adsorption as rate limiting step	
Assumptions	Equation set (6.23) Overall reaction rate
The equilibrium constant for the adsorption of	$r_{TG} = \frac{k_{MeOH}\left([MeOH] - \frac{[ME][DG]}{K_{eq}[TG]}\right)}{\left(1 + \frac{K_{MeOH}[ME][DG]}{K_{eq}[TG]} + K_{DG}[DG] + K_{MG}[MG] + K_{GL}[GL]\right)}$

methanol is assumed to be constant and equal to unity.

$$r_{DG} = \frac{k_{MeOH}([MeOH] - \frac{[MG][ME]}{K_{eq}[DG]})}{(1 + \frac{K_{MeOH}[MG][ME]}{K_{eq}[DG]} + K_{DG}[DG] + K_{MG}[MG] + K_{GL}[GL])}$$

$$r_{MG} = \frac{k_{MeOH}([MeOH] - \frac{[GL][ME]}{K_{eq}[MG]})}{(1 + \frac{K_{MeOH}[GL][ME]}{K_{eq}[MG]} + K_{DG}[DG] + K_{MG}[MG] + K_{GL}[GL])}$$

$$r_{ME} = -(r_{TG} + r_{DG} + r_{MG})$$

$$r_{GL} = -r_{MG}$$

$$r_{MeOH} = -r_{ME}$$

6.5.3 ER kinetic mechanism

Table 6.3 (Eq. set 6.20) shows the ER reaction scheme. ER reaction mechanism assumes that reaction takes place via chemisorption of one reactant species. The adsorbed molecule reacts with another reactant in the bulk phase. Since methanol is smaller reactant molecule and is polar in nature, it is chemisorbed on the surface of the catalyst. The adsorbed MeOH reacts with TG from the bulk and yields ME and DG. DG diffuses into the bulk phase after desorption. Likewise, reactions of DG and MG take place with the adsorbed MeOH.

ER kinetic model with the surface reaction as rate controlling step is shown in Table 6.4 (Eq. set 6.22). When the adsorption of methanol is assumed to be the slowest, the kinetic rate expressions are given in Table 6.4 (Eq. set 6.23). The model assumes that the surface reaction of adsorbed MeOH and bulk TG is in equilibrium with the adsorption and desorption of DG, MG and GL species.

6.6 Results & discussions

6.6.1 Thermodynamic analysis

The equilibrium constant (K_{eq}) for transesterification reaction was calculated using Eq. (6.24).

$$K_{eq} = K_c K_{eq} = \frac{x_{MG} x_{GL}}{x_{TG} x_{MeOH}} \frac{\gamma_{ME} \gamma_{GL}}{\gamma_{TG} \gamma_{MEOH}} = exp\left(\frac{-\Delta G^{0}_{R,T}}{RT}\right) \quad \text{.....(6.24)}$$

Wherein x_i and γ_i represents the mole fraction and activity coefficient of the species *i*, respectively. K_{eq} was determined to be 12.7, 16.13, and 19.8 at temperatures of 150 °C, 165 °C, and 180 °C, respectively. The thermodynamic parameters such as enthalpy (ΔH°) and entropy (ΔS°) were calculated from the graph of $\ln K_{eq}$ vs. $^{1}/_{T}$ (K^{-1}) (Appendix A, Figure A.8).

$$\ln K_{eq} = \frac{\Delta S^{0}}{R} - \frac{\Delta H^{0}}{R}\frac{1}{T} \quad \text{.....(6.25)}$$

The plot of $\ln K_{eq}$ vs. $^{1}/_{T}$ follows the linear relationship and gives linear regression

$$\ln K_{eq} = \frac{(-2830)}{T} + 9.2392 \quad \text{.....(6.26)}$$

By solving Eqs. (6.25) and (6.26), $\Delta H^{0} = 23.5$ kJ/mol and $\Delta S^{0} = 0.076$ kJ/mol K were determined from the slope and intercept of the graph. The standard state Gibbs free energy was calculated using the equation $\Delta G^{0} = \Delta H^{0} - T\Delta S^{0}$ and found to be 0.73 kJ/mol. The change in enthalpy and Gibbs free energy for the transesterification reaction using HPW-MAS-9 composite catalysts is positive, indicating that the reaction is endothermic and non-spontaneous. The reaction equilibrium increased with the increased in temperature, which also indicated that methanolysis of green seed canola oil is an endothermic reaction. This is in accordance to the studies investigated in literature for the transesterification reaction using heterogeneous catalysts (Baroi and Dalai, 2013; Xiao et al., 2010).

6.6.2 PH model

Table 6.5. Kinetic rate constants for pseudo-homogeneous model.

		150 °C	165 °C	180 °C
TG ⇌ DG	k_1	6.5×10^{-4}	8.6×10^{-4}	1.7×10^{-3}
	k_2	3.7×10^{-3}	2.0×10^{-3}	1.3×10^{-3}
DG ⇌ MG	k_3	1.8×10^{-3}	2.7×10^{-3}	4.0×10^{-3}
	k_4	1.1×10^{-3}	2.6×10^{-3}	3.9×10^{-3}
MG ⇌ GL	k_5	1.2×10^{-3}	1.3×10^{-3}	1.4×10^{-3}
	k_6	2.0×10^{-4}	1.6×10^{-3}	5.2×10^{-5}

As observed from Table 6.5, the kinetic constant for conversion of TG to DG was the lowest among all the forward reactions and can be considered as the rate determining step. The forward rate constants increase from 6.5×10^{-4} to 8.6×10^{-4} then to 1.7×10^{-3} as the reaction temperature increase from 150 °C to 165 and to 180 °C, respectively. The reaction between diglyceride and methanol is fastest with high values of k_3. The PH fitted kinetics at 150 °C, 165 °C and 180 °C are shown in Figures 6.2, 6.3 and 6.4, respectively.

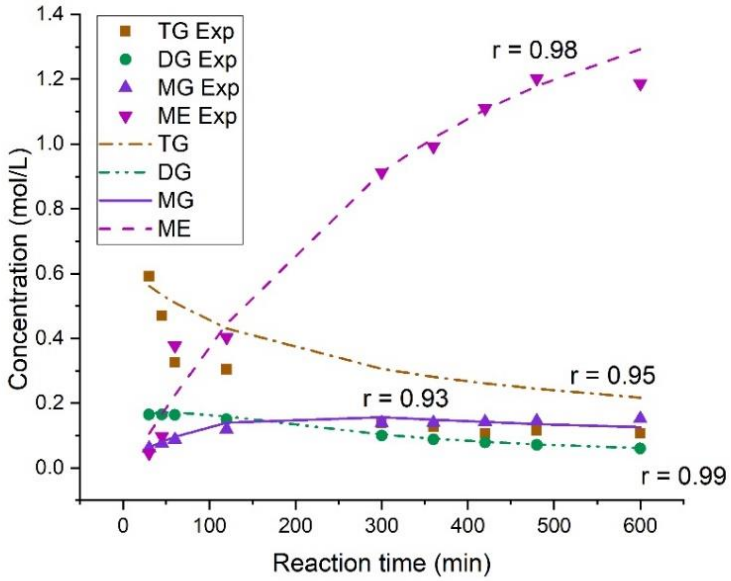

Figure 6.2. Fitted PH model for the concentrations of TG, DG, MG, and ME during transesterification of green seed canola oil at 150 °C.

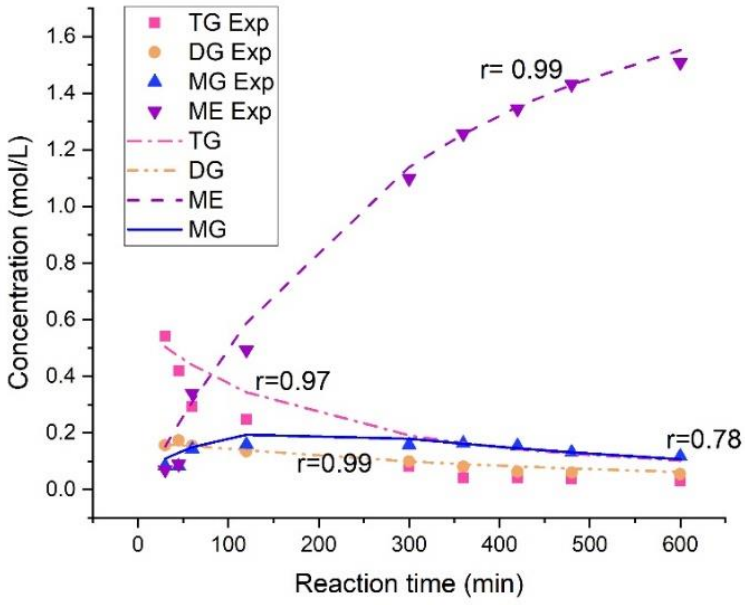

Figure 6.3. Fitted PH model for the concentrations of TG, DG, MG, and ME during transesterification of green seed canola oil at 165 °C.

The model data for DG, ME exhibits a close fit to the experimental data with the Pearson coefficient of more than 0.95, whereas TG differs slightly at 150 °C and 165 °C. MG is found to be weakest fitted at 165 °C and 180 °C with Pearson coefficient of 0.78 and 0.7, respectively (Appendix A, Table A.3).

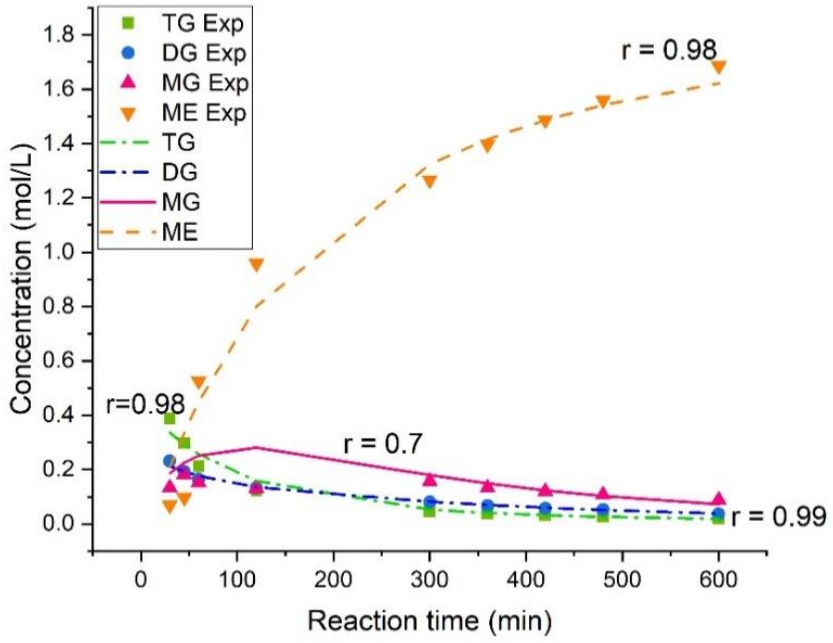

Figure 6.4. Fitted PH model for the concentrations of TG, DG, MG and ME during transesterification of green seed canola oil at 180 °C.

6.6.3 LHHW model with surface reaction as rate controlling

Table 6.6 depicts the rate constants for LHHW reaction pathway with surface reaction as the slowest step. The rate constant k_1 is the smallest amidst all the forward reaction rate constants. This suggests that the reaction of adsorbed triglyceride with adsorbed methanol is the slowest step. Hence, the reaction $\mathrm{TG} \rightarrow \mathrm{DG}$ is the rate controlling step that governs the kinetics. The rate constant k_1 increases as the temperature increases. This implies that the reaction is favored at the high reaction temperature. As the reaction progresses from $\mathrm{TG} \rightarrow \mathrm{DG}, \mathrm{DG} \rightarrow \mathrm{MG}$, and $\mathrm{MG} \rightarrow \mathrm{GL}$, the forward reaction rate constants also increases. The reaction between the adsorbed methanol and monoglyceride is faster with the reaction rate constant (k_5) values of 1.20, 2.87 and 3.56 at 150° C, 165 °C, and 180 °C, respectively.

Table 6.6. Kinetic rate constants and adsorption equilibrium constants for LHHW reaction pathway with surface reaction as rate controlling.

		150 °C	165 °C	180 °C
$TG \rightleftharpoons DG$	k_1	0.022	0.06	0.125
	k_2	0.001	0.04	0.047
$DG \rightleftharpoons MG$	k_3	0.218	0.23	0.860
	k_4	0.079	0.05	0.193
$MG \rightleftharpoons GL$	k_5	1.197	2.28	3.556
	k_6	0.234	1.07	0.668
	K_{TG}	1.890	1.34	0.512
	K_{DG}	0.610	0.3	0.102
	K_{MG}	0.108	0.02	0.020
	K_{ME}	2.026	1.5	0.857
	K_{GL}	0.040	0	0.000
	K_{MeOH}	1.497	0.48	0.163

The values of the rate constants for the reverse transesterification are not zero. Hence, the consecutive reactions $TG \rightarrow DG, DG \rightarrow MG$, and $MG \rightarrow GL$ are reversible in nature. However, the forward rate constants are higher than those for the reverse reactions. The reaction $TG \rightarrow DG$ is less reversible at 180 °C as implied by the low values of rate constant k_2. The LHHW fitted kinetics at 150 °C, 165 °C and 180 °C are depicted in Figure. 6.5, 6.6 and 6.7. It can be seen that the simulated data fits closely to the experimental values except for the triglyceride concentrations at 150 °C and 165 °C. At a high temperature of 180°C, the simulated triglyceride concentration shows a close fit to the experimental data. The simulated and experimental data for DG and MeOH correlate well and the Pearson's correlation coefficients are found to be more than 0.9. The model data for MG differs at 165 °C and 180 °C likewise in PH plots.

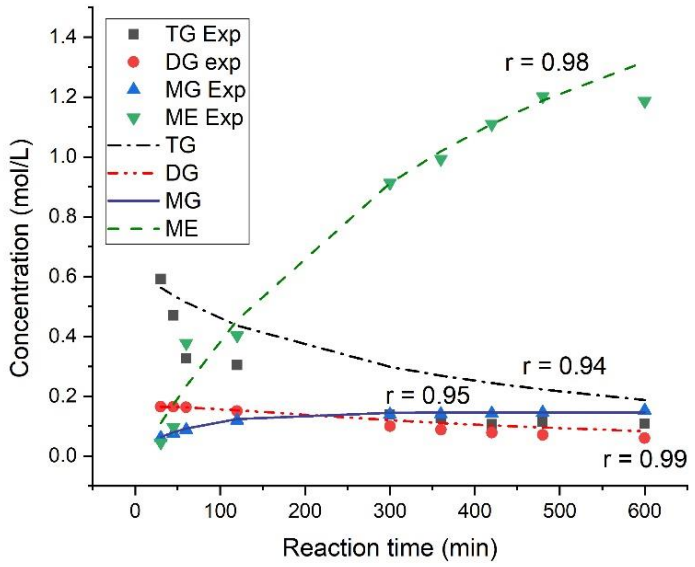

Figure 6.5. Fitted LHHW model for the concentrations of TG, DG, MG and ME during transesterification of green seed canola oil at 150 ° C.

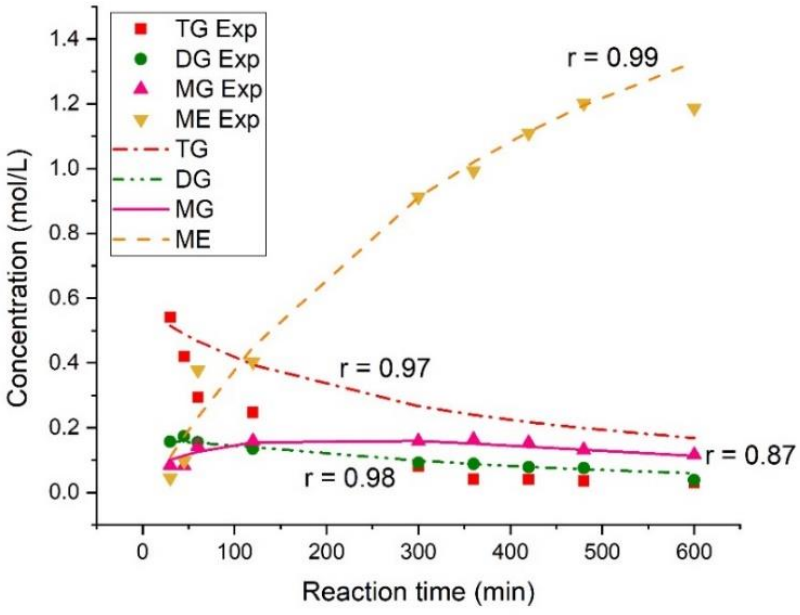

Figure 6.6 Fitted LHHW model for the concentrations of TG, DG, MG and ME during transesterification of green seed canola oil at 165 °C.

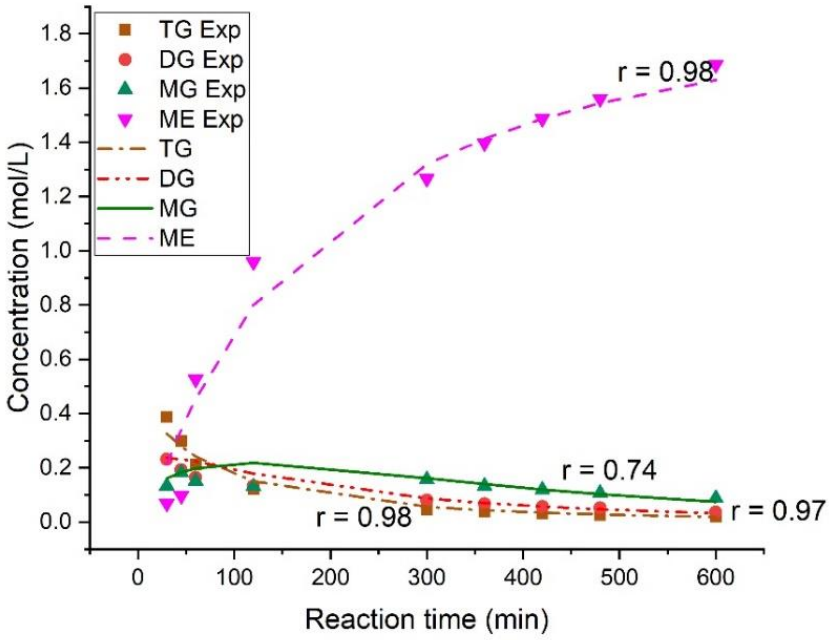

Figure 6.7. Fitted LHHW model for the concentrations of TG, DG, MG and ME during transesterification of green seed canola oil at 180 °C.

6.6.4 ER model with surface reaction as rate controlling

Similar to LHHW mechanism (surface reaction as rate limiting), the rate constant k_1 is found to be the smallest among all the forward constants. The reaction between the bulk triglyceride and adsorbed methanol is the slowest step. As a result, the reaction TG $\leftrightarrow$ DG is the rate limiting step. High values of k_3 are observed, which suggests the reaction between the adsorbed diglyceride and adsorbed methanol is faster. According to Lukić et al. (2013) the increase in the concentration of ME is caused by a complex phased transition during the reaction. The DG, MG and the small amount of esters products act as solubilizing agent, influencing the better dispersion of oil and methanol phase. The adsorption process is an exothermic reaction. The value of the adsorption constants decreased with the increased in the reaction temperature (Table 6.7).

Table 6.7. Kinetic rate constants and adsorption equilibrium constants for ER reaction mechanism with surface reaction as rate limiting.

		150 °C	165 °C	180 °C
TG ⇌ DG	k_1	0.0024 ± 0.0002	0.004 ± 0.0005	0.0092 ± 0.0003
	k_2	0.0011 ± 0.0004	0.0014 ± 0.0004	0.0014 ±0.0004
DG ⇌ MG	k_3	0.0097 ± 0.0002	0.012 ±0.001	0.0150 ± 0.003
	k_4	0.0010 ± 0.0003	0.0012 ± 0.0004	0.0016 ± 0.0002
MG ⇌ GL	k_5	0.0067 ± 0.0009	0.0077 ± 0.0012	0.0093 ± 0.0004
	k_6	0.0017± 0.0002	0.0019 ± 0.0001	0.0026 ± 0.0003
	K_{DG}	0.36 ±0.02	0.30 ± 0.01	0.218 ± 0.006
	K_{MG}	0.12 ± 0.003	0.12 ± 0.005	0.0723 ± 0.008
	K_{GL}	0.05 ± 0.03	0.0063 ± 0.00012	0.0007 ± 0.00069
	K_{MeOH}	1.63 ± 0.15	1.2 ± 0.1	0.479 ±0.101

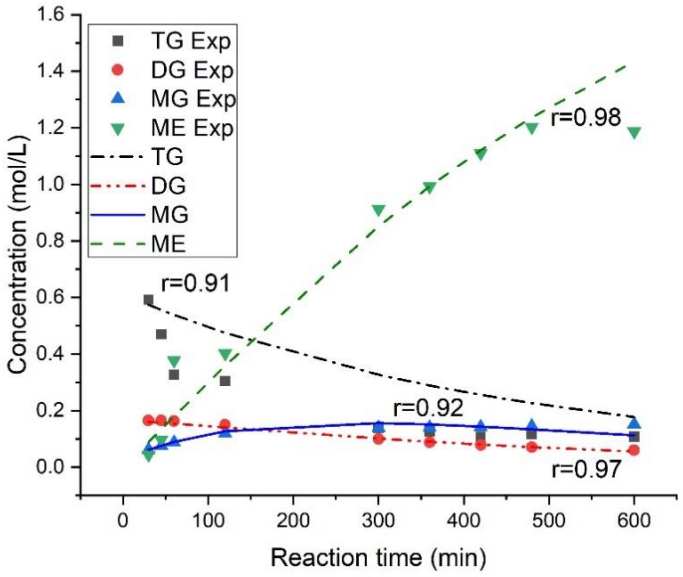

Figure 6.8. Fitted ER model for the concentrations of TG, DG, MG and ME during transesterification of green seed canola oil at 150 °C.

Similar observations were reported by Xiao et al. (2010), wherein the adsorption constants for methanol and glycerol decreased with the increase in temperature. The adsorption coefficients of DG, MG, and glycerol are not found to be high. It is observed that adsorption constant of glycerol is lowest at 150 °C compared to DG, MG and negligible at 165 °C and 180 °C. Macleod (2008) reported that the increase adsorption of these species will increase the rate of reverse reaction and the equilibrium composition will be slightly closer to the reactant side. In such case, it will be difficult to meet ASTM D6751 or EN 14214 standards specified for glyceride content.

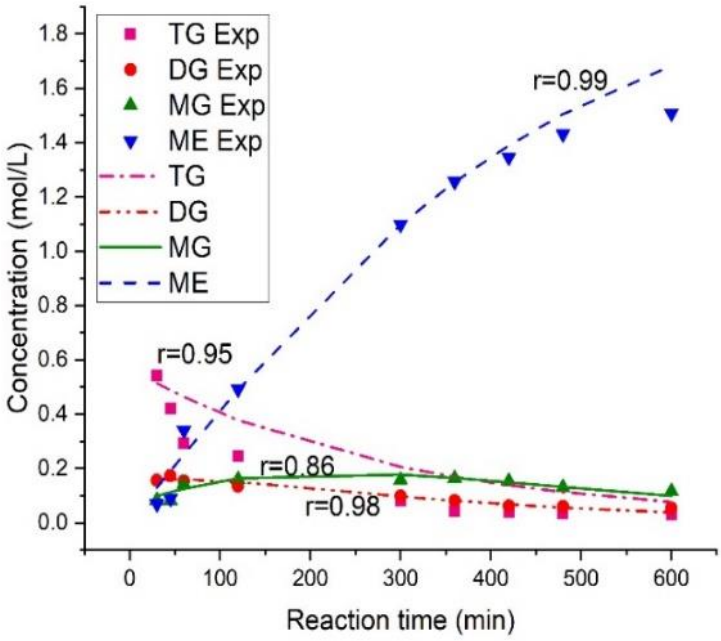

Figure 6.9. Fitted ER model for the concentrations of TG, DG, MG and ME during transesterification of green seed canola oil at 165 °C

The ER fitted reaction kinetics at 150 °C, 165 °C and 180 °C are depicted in Figs. 6.8, 6.9 and 6.10, respectively. In the ER plots, the model data for the TG, DG, and ME fit the experimental data well with the Pearson's coefficient more than 0.9 except for the MG at 165 °C and 180 °C. The lack of fit for MG is dominant at a high reaction temperature of 180°C. This deviation might be because of the influence of the temperature on the adsorption of MG on the surface of the catalysts (Hoo and Abdullah, 2015). The species are weakly adsorbed at high temperatures as compared to the adsorption at low temperatures.

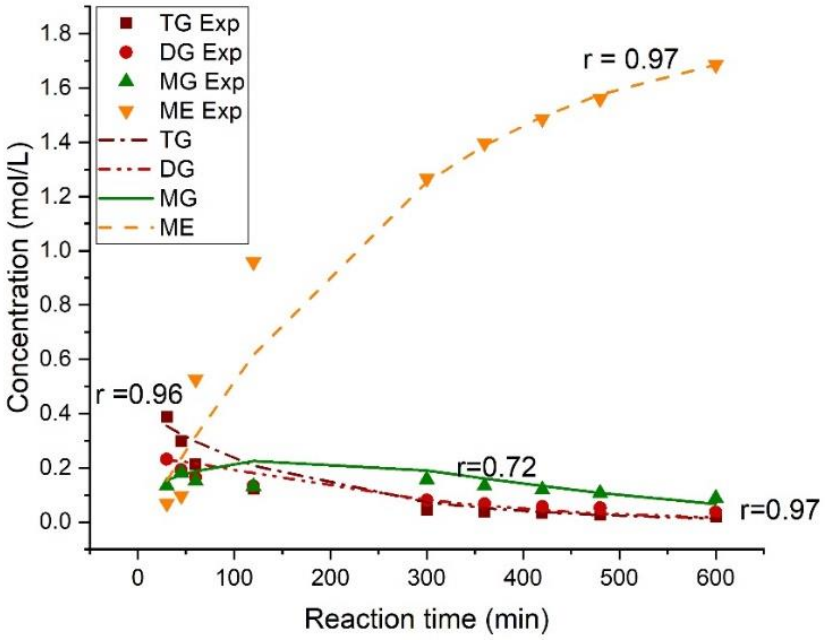

Figure 6.10. Fitted ER model for the concentrations of TG, DG, MG and ME during transesterification of green seed canola oil at 180 °C.

6.6.5 ER reaction mechanism with methanol adsorption as rate controlling

The ER reaction pathway with the adsorption of methanol as the slowest step involved three constant, the rate constant for MeOH (k_{MeOH}), the adsorption equilibrium constant for the overall transesterification reaction (K_{eq}), and the adsorption constant for MeOH (K_{MeOH}). A negative value for K_{MeOH} was observed. The predicted data fitted weakly to that of the experimental data with negative Pearson's coefficient. Hence, the rate expressions were in disagreement with the experimental data. Also, the adsorption constant cannot be negative. Similar observation was stated by Ilgen and Akin (2012) for the transesterification reaction of canola oil and methanol on KOH/MgO catalyst. As a result, the adsorption–based ER model was discarded. This implies that the accessibility of the catalytic sites by methanol is not limited due to the excess concentration of methanol.

6.6.6 Statistical Comparison between kinetic models

The three kinetic models with the assumptions of the pseudo-state, surface reaction as rate limiting, are distinguished by calculating their P_{12} ratio (Table 6.8). The complexity of the model increases as the number of the parameters increases in the model. It minimizes the limit on χ^2 for the statistical significance of the fit (Kapil et al., 2011).

Table 6.8. P_{12} ratio obtained by regression of 108 experimental points using equation.

Model 1	Model 2	P_{12}
Pseudo	LHHW (surface reaction)	0.97
Pseudo	ER (surface reaction)	1.14
LHHW (surface reaction)	ER (surface reaction)	1.17

The least number of constants are involved in pseudo-homogeneous model. For the adsorption based model, the ER reaction pathway with the surface reaction as the slowest step involves a lesser number of parameters compared to LHHW (surface reaction). The complexity of LHHW model increases as it assumes the adsorption of all the reactant species.

On analysing the P_{12} values in Table 6.8, the subsequent order of models describes the experimental data well ER (surface reaction) > pseudo > LHHW. The probability for pseudo homogeneous and LHHW describing the data set is found to be almost equal. The ER model with the surface reaction as the rate controlling step correlates the experimental values well than the pseudo and LHHW models. This also complies with the mechanism reported by Xiao et al.(2010), where in the surface reaction of palm oil with adsorbed methanol using KF/Ca-Mg-Al hydrotalcite solid base catalysts was found to be rate limiting step. Also, the surface reaction of the ethyl acetate and adsorbed methanol as the slowest step has been proposed by Van De Steene et al. (2012) for the methanolysis of ethyl acetate using Lewatit K1221. However, in some kinetic studies, it has been proposed that methanol adsorption is the rate determining step. Kapil et al. (2011) found that the adsorption of methanol as the slowest step in LHHW model represents the experimental data well with hydrotalcite catalysts. Galván Muciño et al. (2016) reported methanol adsorption as a

rate-limiting step in ER reaction pathway for the methanolysis of safflower oil on K_2O/NaX catalysts. The mechanism and rate-limiting steps depend on the employed catalysts for the reaction.

6.7 Activation energy and thermodynamic parameters

The ER reaction pathway with surface reaction as rate controlling, which correlates the experimental data well, was selected for determining the activation energies and thermodynamic parameters ($\Delta H^{\ddagger}$, $\Delta S^{\ddagger}$, $\Delta G^{\ddagger}$) of the stepwise transesterification of green seed canola oil and methanol catalysed by HPW-MAS-9 composite catalysts. The activation energies were estimated using the Arrhenius equation

$$k = A \times Exp\left(\frac{-E_a}{RT}\right) \quad \text{.....(6.27)}$$

The entropy of activation ($\Delta S^{\ddagger}$) and enthalpy of the activation ($\Delta H^{\ddagger}$) were calculated using the Eyring –Polanyi equation.

$$\ln\frac{k}{T} = -\frac{\Delta H^{\ddagger}}{R}\frac{1}{T} + \ln\frac{k_B}{h} + \frac{\Delta S^{\ddagger}}{R} \quad \text{.....(6.28)}$$

Where in Boltzmann constant $k_B = 1.38 \times 10^{-23}$ J/K Planck's constant $h = 6.62 \times 10^{-34}$ J.s. The values of $\Delta H^{\ddagger}$ and $\Delta S^{\ddagger}$ were determined from the slope and the intercept of the graph ln (k/T) vs. $(1/T)$.

Table 6.9 provides the activation energies and, $\Delta H^{\ddagger}$, $\Delta S^{\ddagger}$, and $\Delta G^{\ddagger}$ for forward and reverse transesterification reactions.

The reaction of TG → DG is observed to be the slowest step with an activation energy of 72.5 kJ/mol. It governs the rate of the overall transesterification reaction. Xiao et al. (2010) developed the ER reaction pathway with the surface reaction of TG and MeOH on KF/Ca-Mg-Al hydrotalcite solid base catalysts as the slowest step. The model fitted the experimental data well and the reaction possessed an activation of 111.6 kJ/mol (Table 6.10) (Xiao et al., 2010). Sulfamic acid catalysed transesterification of waste cooking oil followed pseudo –second order kinetics with the activation energy of 80.3 kJ/mol (Gao et al., 2019). In case of KOH/ZSM-5-Fe_3O_4, CaO , HSiW/Al_2O_3 , 20-CeO2/Li/SBA-15, and Sr:Zr mixed oxide catalysts, the activation energies were found to be 122.7 kJ/mol, 78.4 kJ/mol, 61.4 kJ/mol, 57.7 kJ/mol, and 48.2 kJ/mol, respectively (Gaurav et al., 2019; Kaur and Ali, 2014; Latchubugata et al., 2018; Malhotra and Ali, 2018;

Rezayan and Taghizadeh, 2018). The activation energy in the present work was well within the reported range of 33-84 kJ/mol for the transesterification reaction of vegetable oil feedstock.

Table 6.9. Activation energies and thermodynamic parameters of the stepwise transesterification reactions.

Reaction	E_a (kJ/mol)	$\Delta H^{\ddagger}$ (kJ/mol)	$\Delta S^{\ddagger}$ (kJ/mol K)	$\Delta G^{\ddagger}$ (kJ/mol)
$\mathrm{TG + MeOH \rightarrow DG + ME}$	72.5	68.9	0.04	58.3
$\mathrm{TG + MeOH \leftarrow DG + ME}$	12.8	9.1	-0.11	42.3
$\mathrm{DG + MeOH \rightarrow MG + ME}$	22.8	19.2	-0.07	40.0
$\mathrm{DG + MeOH \leftarrow MG + ME}$	26.4	22.8	-0.08	46.8
$\mathrm{MG + MeOH \rightarrow GL + ME}$	17.9	14.3	-0.08	39.5
$\mathrm{MG + MeOH \leftarrow GL + ME}$	22.7	19.1	-0.08	44.3

The forward reactions of $\mathrm{DG \rightarrow MG}$ and $\mathrm{MG \rightarrow GL}$ are more favored as the activation energies for these reactions are lower than their reversible reactions. The forward reaction between the green seed canola oil and methanol should obtain the activation energy level before formation of activated complex. Similarly, for the reversible reactions, the glycerides and methanol must also acquire an energy level. A lesser energy was required by forward reactions of DG to MG and MG to GL to form the activated complex than their reverse reactions.

The $\Delta H^{\ddagger}$, $\Delta S^{\ddagger}$, $\Delta G^{\ddagger}$ for the reaction of TG to DG is determined to be 68.9 kJ/mol, 0.04 kJ/mol K and 58.3 kJ/mol, respectively.

These values are comparable with those reported in literature (Table 6.10), except for $\Delta S^{\ddagger}$ values, which was found to be positive for the reaction in the present study. $\Delta H^{\ddagger} = 45.9$ kJ/mol, $\Delta S^{\ddagger} = -0.121$ kJ/mol K, and $\Delta G^{\ddagger} = 88.2$ kJ/mol were observed for the 2Sr:Zr catalyzed transesterification of waste cooking oil (Kaur and Ali, 2014). Similarly, for the transesterification of waste cooking oil and methanol with 20-CeO_2/Li/SBA-15, Malhotra and Ali (2018) found $H^{\ddagger}$, $\Delta S^{\ddagger}$, and $\Delta G^{\ddagger}$ values to be 59.4 kJ/mol, -0.108 kJ/mol K and 95.9 kJ/mol, respectively. The positive value of the enthalpy of activation indicated that in order to reach the transition state and to proceed in the forward direction, the reaction requires external heating. This holds true in the case of all the forward and reversible transesterification reactions.

Table 6.10. Activation energies and thermodynamic parameters reported in the literature.

Catalyst	Feedstock	Kinetic model	E_a (kJ/mol)	$\Delta H^{\ddagger}$ (kJ/mol)	$\Delta G^{\ddagger}$ (kJ/mol)	$\Delta S^{\ddagger}$ (kJ/mol K)	Reference
KF/Ca-Mg-Al hydrotalcite	Palm oil	Eley -Rideal with surface reaction of adsorbed methanol as rate limiting	111.6	-	-	-	(Xiao et al., 2010)
Sulfamic acid	Waste cooking oil	Pseudo -second order	80.3	-	-	-	(Gao et al., 2019)
KOH/ZSM-5-Fe_3O_4	Canola oil	Pseudo-first order	122.7	-	-	-	(Rezayan and Taghizadeh, 2018)
CaO	Palm oil	Pseudo-first order	78.4	-	-	-	(Latchubugata et al., 2018)
HSiW/Al_2O_3	Canola oil	Pseudo - homogenous	61.4	-	-	-	(Gaurav et al., 2019)
20-CeO_2/Li/SBA-15	Waste cooking oil	Pseudo-first order	57.7	59.4	95.9	-0.108	(Malhotra and Ali, 2018)
Sr:Zr mixed oxide	waste cooking oil	Pseudo-first order	48.2	45.97	88.23	-0.121	(Kaur and Ali, 2014)
HPW-MAS-9 with 25wt.% HPW loading	Green seed canola oil	Eley -Rideal with surface reaction of adsorbed methanol as rate limiting	72.5	68.7	58.3	0.04	This work

The positive value of the activation of entropy indicated the formation of an activated complex via dissociation mechanism. Hence, the reactants in the ground state possessed more rigid and ordered structure than the activated complex and that is why the rate of reaction of TG to DG was slowest. The rest of the forward and reversible reactions observed a negative entropy of activation. $-\Delta S^{\ddagger}$ suggesting that the transition state possesses a more ordered structure compared to the reactants in their ground state. Thus, the reaction DG → MG and MG → GL followed an associative path. Figure 6.11 illustrates the free energy profile and the reaction pathway for the consecutive steps of the transesterification reaction. The dissociative pathway is analogous to two-step S_N 1 substitution, whereas the associative pathway is analogous to concerted S_N 2 nucleophilic substitution.

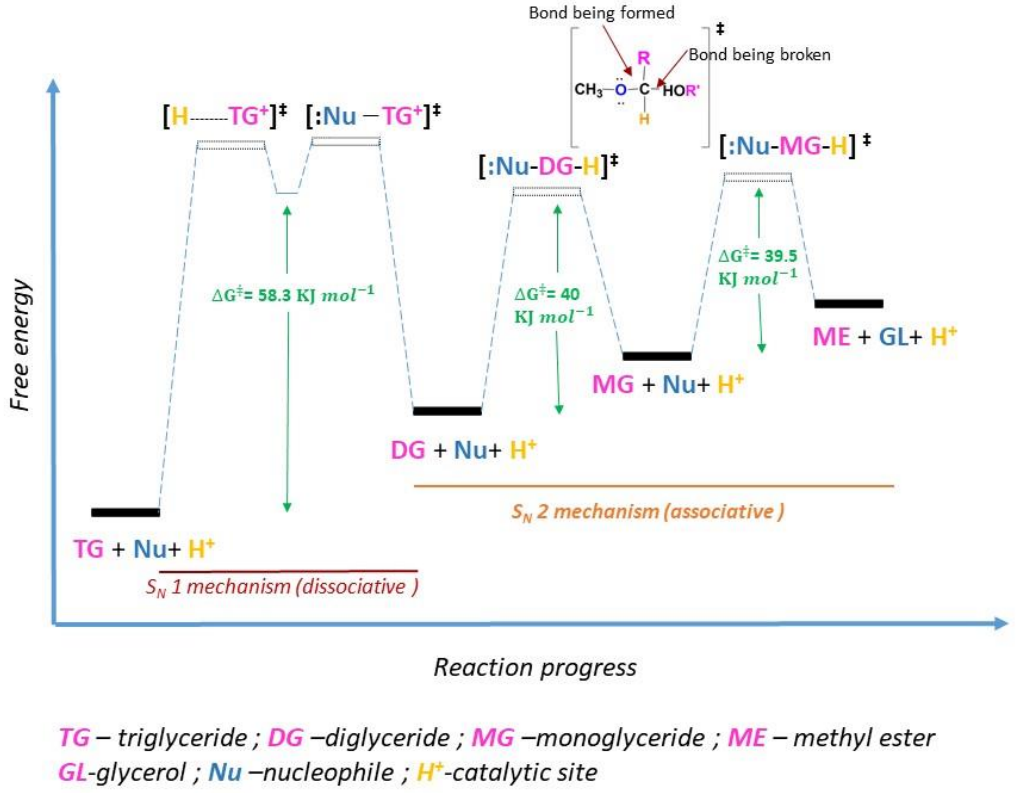

Figure 6.11**.** Free energy diagram for the stepwise transesterification reaction of green seed canola oil and methanol using HPW-MAS-9 catalysts.

This suggests that TG → DG follows the S_N 1 substitution mechanism in which the carbonyl bond breaks first leading to the formation of carbocation before the nucleophile approaches. In the

second step, the nucleophile attacks the carbocation. In case of $DG \rightarrow MG$ and $MG \rightarrow GL$, the reactions follow concerted $S_N 2$ nucleophilic substitution. It is one step mechanism in which the addition of nucleophile and the departure of the leaving group takes place in a single step. The H^+ (catalytic site) and the hydroxyl oxygen from the methanol attack the oxygen and carbonyl group.

6.7.1 Reaction mechanism considerations

On the basis of the P_{12} values and fitted experimental data, the suggested mechanism for the transesterification reaction using HPW-MAS-9 catalyst could be the ER mechanism. Methanol must be adsorbed on the active site of the catalyst and reacting with the bulk triglyceride. In the case of the pseudo homogenous mechanism, it is the triglyceride which gets adsorbed and protonated on the active site and then interacts with the methanol from the bulk. This contradiction is due to the occurrence of the physical adsorption step in the reaction pathway before any elemental steps taking place on the acidic sites. In case of the solid acid catalyzed esterification reaction, Kirumakki et al. (2006) reported that the acetic acid adsorbs on the surface of the zeolite and then interacts with the alcohol in the bulk. Koster et al. (2001) claimed that the ethanolysis of acetic acid using MCM-41-16 proceeded via acetic acid protonation and then followed the LHHW pathway. In case of phosphotungstic acid based poly (ionic liquid) catalysed esterification of palmitic acid with methanol, Wang et al. (2019) proposed that the palmitic acid adsorbs on the catalyst surface before reacting with the methanol. Although, it is unlikely that the methanol will directly interact with the active site of the catalyst, López et al. (2007) indicated that the methanol adsorption on the reaction sites must be accounted (order of reaction of methanol being < 1). The partial reaction order of the methanol tends to zero at higher methanol concentration.

In the ER mechanism, considering both reactants physical adsorption, methanol being in excess, its adsorption will be more pronounced than the triglyceride. The adsorption of methanol will be more likely to experience the saturation effects. Hence, in accordance to Van De Steene et al. (2012) the overall rate of reaction for the transesterification would require to take into account the methanol adsorption term and not for the triglyceride, provided that the protonation of triglyceride is not experiencing the saturation effects. The adsorption term for the methanol is significant and is accounted for the developed model in the present work.

6.8 Model verification

Simulated data and the experimental data at time periods other than the ones used to build the ER model are compared in the Table 6.11. The deviation was found to be less than 5 % for the reaction time of 180 and 540 minutes, whereas for a reaction time of 15 min the deviation was found to be 6.8 %. Since the deviation is less than 10%, the kinetic model can predict the concentrations of species in the reaction. Xiao et al. (2010) found that ER reaction pathway with the assumption of surface reaction of triglyceride with adsorbed methanol could predict the conversion of transesterification reaction with a deviation of less than 10%.

Table 6.11. Verification of model calculations for reaction temperature of 180 °C using 35 g of green seed canola oil, 18.9 g of methanol, 5.5wt. % of catalysts (based on the weight of green seed canola oil).

Reaction time (min)	15	180	540
Model	0.82	1.39	1.77
Experimental	0.76	1.45	1.79
Error %	6.8	3.9	1.5

6.9 Conclusions

The ER model with the surface reaction of triglyceride and adsorbed methanol as the slowest step described the kinetic behavior of the methanolysis of green seed canola oil using HPW-MAS-9 composite catalysts. The simulated data correlated well with the experimental findings. The reactions were found to be endothermic in nature, whereas the positive value of $\Delta G^{\ddagger}$ implied that HPW-MAS-9 catalyzed transesterification reaction is non-spontaneous and the transition state is at higher energy level compared to the reactants. A positive value of $\Delta S^{\ddagger}$ indicated that $\mathrm{TG} \rightarrow \mathrm{DG}$ followed a dissociative pathway. The reaction of TG to DG followed the two-step S_N 1 substitution. The rest of the forward and reverse reaction steps followed the associative mechanism, indicated by the negative value of $\Delta S^{\ddagger}$.The reactions of $\mathrm{DG} \rightleftharpoons \mathrm{MG}$ and $\mathrm{MG} \rightleftharpoons \mathrm{GL}$ proceeded via S_N 2 nucleophilic substitution.

CHAPTER 7

Techno-economic and Life Cycle Assessment for Heterogeneous Catalysed Biodiesel Production from Green Seed Canola

A version of this section will be submitted for publication in a journal.

Contribution of the Ph.D. Candidate

The process economic evaluations and life cycle assessment were performed by Ankeeta Kurhade in discussion with Dr.Ajay K. Dalai. The content of this chapter was written by Ankeeta Kurhade as per the guidance and suggestions provided by Dr.Ajay K.Dalai.

Contribution of this Chapter to Overall Ph.D. Research

Renewable or tax credits are needed to make the biodiesel process economically feasible. Despite, the limited economic feasibility, the biodiesel synthesis from green seed canola oil shows the promising potential with its zero carbon burden, desirable environmental profile, and providing market for green seed canola seeds.

7.1 Abstract

Green seed in canola is a downgrading factor that causes annual losses of more than $ 150 million and is of major concern in North America. Green seed canola oil serves as a feedstock alternative for the production of biodiesel, avoiding land use and food vs fuel drawbacks for conventional biofuel crops. The present study assessed the techno–economic feasibility and environmental impact of the biodiesel production from green seed canola oil using Aspen PlusV10 and SimaPro 9.0. Both deterministic and stochastic models were tested for the economic evaluation of the biodiesel processing plant, producing 7308 tonnes of biodiesel per year. Under the current scenario, the minimum selling price of the biodiesel is estimated to be $ 1.2/kg inclusive of tax incentives, with the venture likely to be 88% profitable as projected by stochastic model. Based on

the outcome of Life -cycle assessment (LCA), the process indicated a zero burden to the climate change. The overall study showed that the renewable or tax credits are needed to make the biodiesel process economically viable and, despite the limited economic feasibility, the biodiesel synthesis from green seed canola oil has a promising potential with its zero carbon burden, desirable environmental profile, and providing market for green seed canola seeds.

7.2 Introduction

Agriculture Canada's canola group is looking forward for market diversification in the wake of the loss of Chinese market. One of the ways to incentivise farmers to continue growing canola is to increase the federal biodiesel mandate from two percent to five percent. In addition, biodiesel fuels are sourced through biological processes such as agricultural and anaerobic digestion, instead of being sourced from geological processes based on the formation of fossil fuels such as oil and coal. This would also aid in reductions in greenhouse gas emissions. Biodiesel is an alternative to fossil fuels to produce energy. The amount of carbon released in burning biodiesel is equivalent to the amount of carbon sequestered during the growth of plants (Azapagic and Stichnothe, 2010).

Biodiesel has more oxygen content compared to conventional petrol diesel and no sulfur. It generates less carbon monoxide, smoke and particulates (Gebremariam and Marchetti, 2018). However, the major drawback with biodiesel as a fuel is its high production cost and less energy content than fossil diesel (Anuar and Abdullah, 2016; Gebremariam and Marchetti, 2018). Biodiesel derived from rapeseed oil, soybean oil and palm oil form the largest sector in the market. Soybean oil is the preferred source in United States due to its high production and ease of availability, whereas in Canada, canola is the preferred choice. For on farm biodiesel production, the cost of production for canola or soybean is the main factor. The biodiesel industry faces the major challenges when the demand for the feedstock fluctuates or the feedstock is more expensive than processing cost. Moreover, the subsidies, taxes, and policies from the government play an important role in the economics of biodiesel (Anuar and Abdullah, 2016). However, most governmental policies are short–termed and their restoration is unclear. The uncertainty results in curtailing the investment in new plants, holding back purchases of raw material and renewable fuel deliverables which in turn would impact the economy. The environmental impact and the economy could be improved only if the policies are smart and have a multi-year extension. The other

alternatives to improve the economics of the biodiesel production include using cheaper alternative feedstocks and using technologies with minimum overall energy input.

In terms of economics, the profitability of biodiesel plant using different low cost feedstock varies. Kookos (2018) carried out the techno-economic assessment for the biodiesel production from the spent coffee ground oil using NaOH as catalyst. The study indicated that the process is economically competitive only when the annual production capacity is greater than 42000 tonnes/year, which is difficult to achieve because the availability of the raw materials limits the capacity. Budiman Abdurakhman et al. (2018) found that the catalytic membrane reactor process is more profitable than the conventional alkaline process when waste cooking oil is used as feedstock for the biodiesel process. However, more selective membrane towards biodiesel and better separation techniques for biodiesel and FFA are still required for improving the economics of the process. In another study, Martinovic et al. (2018) conducted a comparative economic study of the single and two-step production of biodiesel with supercritical methanol based on simulations in Aspen Plus 8.8. The two-step process requires lower investment and overall cost of production cost, but higher process energy inputs than the single-step process. The reduction in cost using cheaper feedstock is compromised against the cost incurred in additional energy inputs or steps involved in pre-treatment or product quality improvement. In such a scenario, the heterogeneous solid acid catalysts do offer several advantages in terms of reusability, recoverability and having minimal process steps needed for separation of products and purification reducing the environmental impacts.

It is not only important for the alternative routes or technologies to be economically competitive but also requires them to be sustainable providing minimal risk to the environment. Life cycle analysis is a tool that evaluates environmental impacts of production stages and products (Carvalho et al., 2019). The Life-cycle assessment (LCA) method as described by the International organisation for Standardization (ISO, 2006) consists of four stages, definition of goal and scope, life-cycle inventory, life-cycle impact assessment, and interpretation of results (Amouri et al. 2016.; Carvalho et al., 2019). Ajayebi et al. (2013) conducted a life cycle assessment of biodiesel production from algae and jatropha and found that both the processes showed reduction in 10-25% in fossil energy depletion and 36-40% in greenhouse gas emissions as compared to fossil diesel impacts. In another study, Gue et al. (2019) assessed the microalgal biodiesel sustainability via

material circularity indicator (MCI) and Life-cycle assessment (LCA) framework and compared it with jatropha based biodiesel. MCI framework incorporates material flow and utilisation of an end–product. The study revealed that jatropha has a lower environmental impact compared to microalgal biodiesel, whereas the circularity of microalgae biodiesel was better than jatropha. Microalgae biodiesel has 4.28% recycled materials in the form of CO_2 and 95.72% in the form of nutrients. Amouri et al. (2016) conducted the life cycle analysis of castor-bean based biodiesel. The analysis showed *Ricinus communis* as promising feedstock for the biodiesel production with a positive contribution to a climate change reduction.

The main objective of this study was to evaluate the techno-economic viability and LCA for heterogeneously catalyzed biodiesel synthesis from green seed canola oil. The study will help define whether the green seed canola can serve as a potential feedstock for the biodiesel process.

7.3 Methods and approaches

7.3.1 Simulation

Aspen PlusV10 simulation package was used to design, optimize and simulate the production of biodiesel from green seed canola oil using HPW-MAS-9 catalysts. Information on methanol and glycerol is available in the Aspen Plus component library. Triolein was chosen to represent the green seed canola oil in Aspen Plus simulation, since oleic acid is the major fatty acid in green seed canola oil. Correspondingly, methyl oleate was selected as the biodiesel product. Equilibrium model was used for the calculations in simulation. The group contribution method UNIFAC (Dortmund) was used to predict vapor – liquid equilibria. Sensitivity analysis was carried out to estimate the optimal operating conditions.

7.3.2 Process Description

The process uses green seed canola oil (GSC), methanol, and HPW-MAS-9 catalysts as feed streams and yields 7308 tonnes/year of biodiesel with 99.9% purity and 766 tonnes/year of glycerol by-product with 96% purity. The purity of the biodiesel was obtained in accordance to ASTM standard i.e., 99.65 wt %. The stream properties are summarised in Table.7.1. Recycle, fresh methanol stream, and catalyst are first mixed in mixer M101 and then mixed with GSC oil stream in mixer M102 before sending it to the reactor. The reaction mixture is then pumped through pump P100 to obtain a pressure of 2 MPa so that the mixture is in the liquid phase. The mixture

stream (A4) is then preheated in exchanger H100 by exchanging heat with hot glycerol (A15). The stream A5 is further preheated by exchanging heat with stream A11 in heat exchanger H101. The mixture is pumped through the pump P101 to obtain the desired pressure of 4 MPa and is heated to 180 °C. The methyl ester synthesis took place in a conversion reactor R100 by transesterification reaction catalysed by HPW-MAS-9 composite catalyst at the optimized reaction conditions obtained from Chapter 4 to achieve a triglyceride conversion of 95%. The methanol to oil molar ratio is 15.6:1. The outlet stream from the reactor contains methyl ester, methanol, catalyst and glycerol. Separator S100 separates the solid catalyst while the stream A10 after exchanging the heat in H100 is fed to the flash drum F100 (stream A12) to recover the excess methanol. The separation of the glycerol and methanol takes place in the flash drum. The operating temperature of the flash drum is set to 82.5 °C based on the sensitivity analysis to control the flowrate of the glycerol in stream A13. Stream A13 containing methanol is cooled and recycled back to mixer M100. The bottom stream from the flash drum is cooled by exchanging heat in H100 and is fed to the decanter D100 to separate glycerol. Stream A17 containing fatty acid methyl esters (FAME), unused oil is preheated to 190 °C by exchanging heat with a hot stream to A19 through heat exchanger H104 before feeding to the distillation column. The distillation column operates with 7 equilibrium stages with total condenser and kettle boiler. The distillate flowrate is 2.85 kmol/hr. The top stream is rich in biodiesel and the bottom stream contains unreacted GSC.

7.3.3 Sensitivity Analysis

Sensitivity analysis using Aspen Plus V10 was performed on the process unit. Sensitivity analysis on Flash drum (F-100) was carried out to find the optimal temperature setting for the methanol recovery conditions.

The analysis was performed in a temperature range of 75.5 - 92.5 °C. Figures 7.1 and 7.2 show that the mass flow rates of both methanol and glycerol in the A13 recycle stream increase as the temperature of flash drum increases. The increase in the mass flow rate of the glycerol in A13 stream is comparatively sharper after 84 °C. In order to maintain the recycle stream purity, the operating temperature of flash drum was set to 82.5 °C.

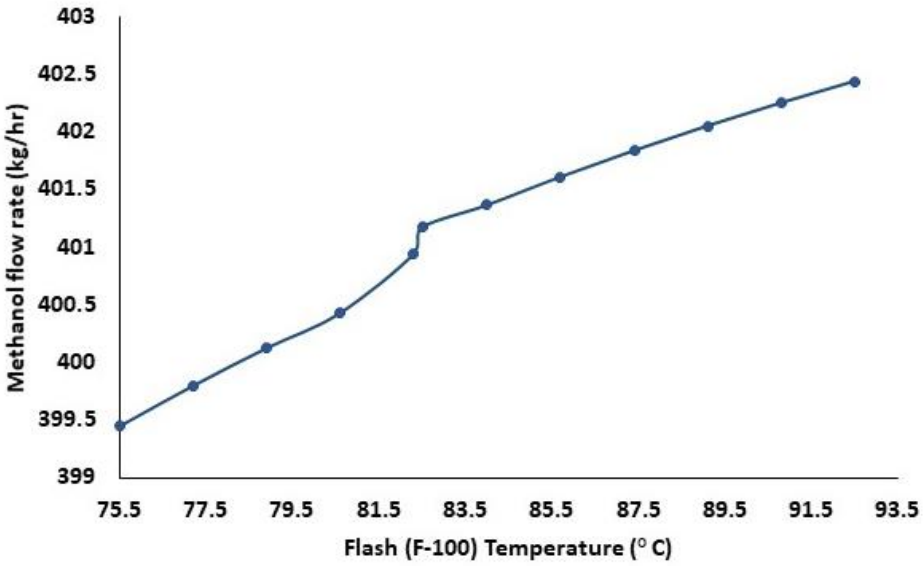

Figure 7.1. Sensitivity analysis of Flash drum F100 temperature on molar flow rate of methanol in stream A13.

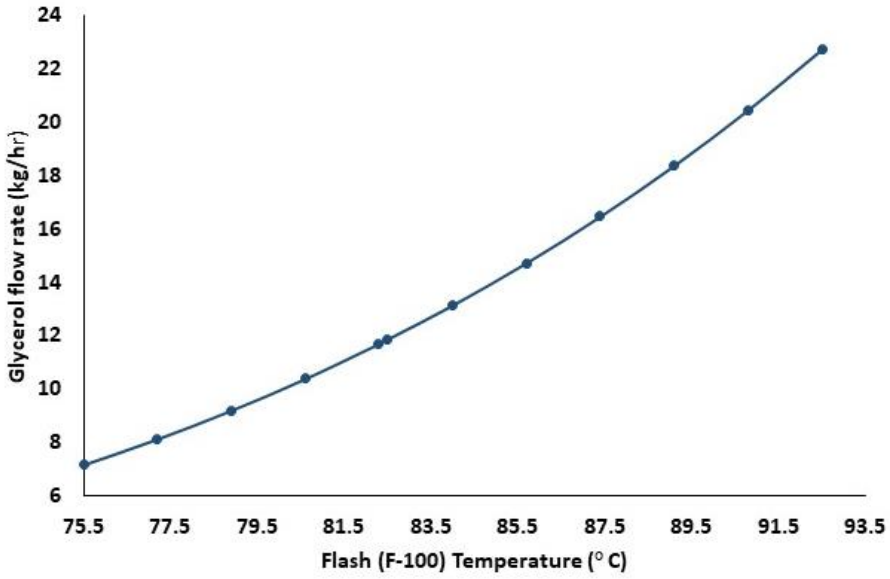

Figure 7.2. Sensitivity analysis of Flash drum F100 temperature on molar flow rate of methanol in stream A13.

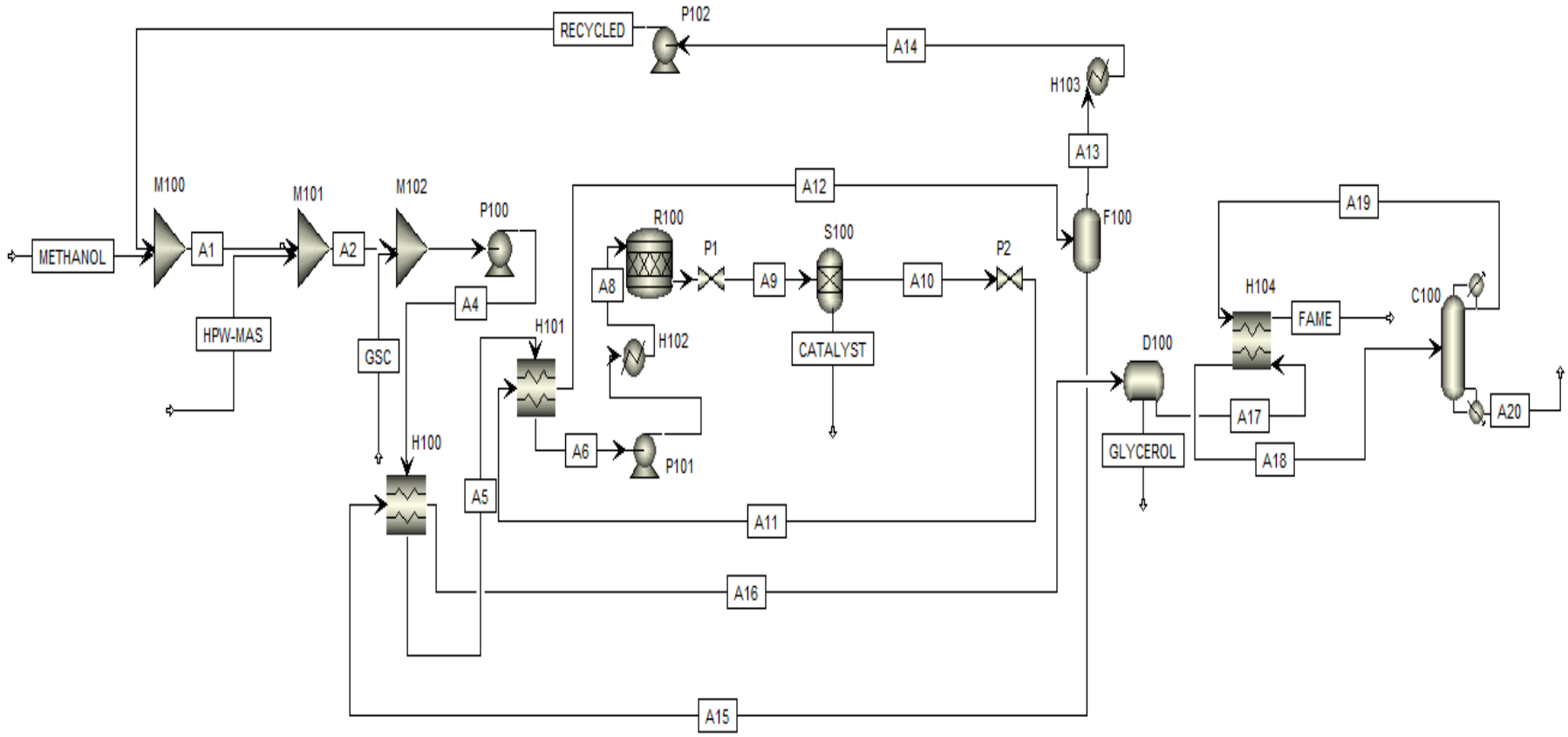

Figure 7.3. Process flow diagram for biodiesel production from green seed canola oil using HPW-MAS-9 catalyst.

Table 7.1. Stream properties of the biodiesel production plant illustrated in Figure 7.3.

	Feed		Product					
	GSC	HPW-MAS	Methanol	Recycle	A20 (Unreacted reactants)	Catalyst	Fame	Glycerol
Temperature (°C)	25	25	25	25	289.2	140	29	25
Pressure (Mpa)	0.1	0.1	0.1	0.1	0.01	0.7	0.05	0.1
Mole Flows (kmol/hr)	1.0	0.2	3.0	12.65	0.09	0.19	2.85	1.06
Mass Flows (Kg/hr)	885.4	48.7	96.1	413	55.6	48.7	834.9	91.0
TRIOL-01	885.4	0	0	0	44.3	0	1.02E-04	1.87E-14
METHA-01	0	0	96.1	401	1.63E-17	0	1.21	3.55
METHY-01	0	0	0	0.24	11.31	0	833.7	7.87E-04
GLYCE-01	0	0	0	11.87	1.77E-05	0	0.044	87.4
HPW-MAS	0	48.7	0	0	0	48.7	0	0
Mass Fractions								
TRIOL-01	1	0	0	5.37E-15	0.80	0	1.23E-07	2.05E-16
METHA-01	0	0	1	0.97	2.93E-19	0	0.0014	0.039
METHY-01	0	0	0	5.80E-04	0.20	0	0.999	8.65E-06
GLYCE-01	0	0	0	2.87E-02	3.18E-07	0	5.26E-05	0.96
HPW-MAS	0	1	0	0	0	1	0	0

7.4 Techno-economic analysis

7.4.1 Deterministic model

Economic assessment based on the deterministic model is used to determine the cash flow of this biodiesel plant. Equipment mapping and sizing was carried out using Aspen Process Economic Analyzer (APEA).The capacity of the biodiesel plant is assumed to be 7308 tonnes/year of biodiesel production. The plant is assumed to operate 8000 hours per year (i.e. 24 hours per day during 333 days per year, remaining 35 days for maintenance tasks) on a three eight-hour shifts cycle.

The bare module costs of the equipment were estimated using CAPCOST program and the Chemical engineering plant cost index (CEPCI) of 603.31 for 2018. The fixed capital investment (FCI) of the biodiesel plant is $ 2.1 M. Table 7.2 depicts the manufacturing cost summary. Land cost and working capital cost are assumed equal to 5% and 15% of FCI, respectively. The direct manufacturing, indirect manufacturing, and general expenses are calculated based on the details provided in Ulrich and Vasudevan (2004).

The number of operators per shift is estimated on the basis of the details provided in Ulrich and Vasudevan (2004). The average annual salary for the chemical equipment operator is obtained from the US Bureau of Labor Statistics, May 2018. The price of methanol and green seed canola oil (after applying discount for CGC grade 3 of damaged canola) are $ 0.27/kg and $ 0.47/kg, respectively. With, the inclusion of tax credit of $ 0.29/kg, the biodiesel selling price is approximately equal to $ 1.2 /kg. Salvage value is estimated to be 5 % of FCI. Based on the data in Table 7.3, the discounted cash flow rate of return (DCFROR), discounted payback period and net present value (NPV) are estimated using CAPCOST. The plot of cumulative discounted cash flow versus the years of plant operation provides the profitability criteria of DCFROR, NPV, and payback period (Figure 7.4). DCFROR tells how efficiently money is being used. If DCFROR is higher than the internal discount rate, the project is regarded to be profitable. For the current case, (DCFROR) is 24.3 %, greater than the internal discount rate. Project net present value (NPV) is $ 5.1 M, based on cost-of-money i equal to 5%. Discounted payback period time from start up until recovery of discounted fixed capital is 3.0 years. Net pay out time (NPT) from startup to discounted break-even is 3.8 years. Discounted break- even point (DBEP), time from project initiation to discounted total cash recovery is 5.9 years.

Table 7.2. Manufacturing cost summary of biodiesel plant

Particulars	In million $
Total module cost	1.60
Auxiliary cost	0.48
Fixed capital investment (FCI)	2.08
Land cost	0.10
Working capital	0.31
Total capital investment	2.39
Direct manufacturing expenses (DME)	
Raw materials	5.89
Operating labour	0.28
Total utility costs	0.08
Maintenance and repairs (M& R) 4% of FCI	0.08
Operating supplies (10% of M & R)	0.008
Laboratory charges (10% of operating labour)	0.028
Total (A_{DME})	6.37
Indirect manufacturing expenses (IME)	
Overhead, packaging, storage (50% of operating labor + maintenance)	0.22
Local taxes (1.5% of FCI)	0.03
Insurance (0.5% of FCI)	0.01
Total (A_{IME})	0.27
Total manufacturing expense (A_{ME}= A_{DME} + A_{IME})	6.63
General expenses	
Administrative costs (25% of overhead)	0.01
Distribution and selling (10% of total expense)	0.8
Research and development (3% of total expense)	0.24
Total general expense AGE	1.07
Depreciation (10% of FCI)	0.21
Total expenses	8.07
Revenue from sales	9.49

Net annual profit (A_{NP})	1.41
Income taxes (42% of net profit), A_{IT}	0.59
Net annual profit after taxes (A_{NP}-A_{IT})	0.82

Table 7.3. Discounted feasibility criteria

Net Present Value (millions)	5.1
Discounted Cash Flow Rate of Return	24.3 %
Discounted Payback Period (years)	3.0

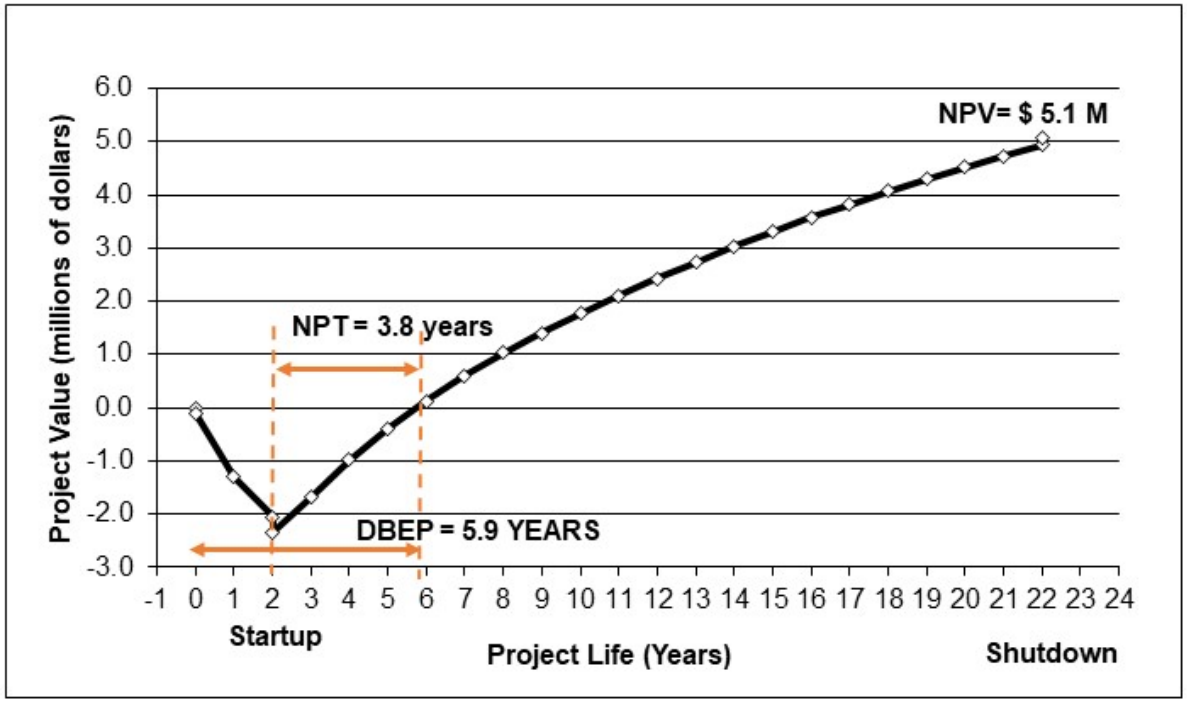

Figure 7.4. Cash flow profile for biodiesel plant.

7.4.2 Profitability of the biodiesel process

The economic feasibility of the biodiesel production process depends on the various factors to list a few such as the production technology, the inputs and the outputs as well as the plant

capacity (Gebremariam and Marchetti, 2018). It also depends on the regional fluctuating data and makes each case unique (Navarro-Pineda et al., 2017).

West et al. (2008) modelled and evaluated four biodiesel processes using waste vegetable oil as feedstock: alkali catalysed reaction wherein FFA was first pretreated with acid catalyst, homogenous acid catalysed reaction, heterogeneous acid catalysed reaction, and supercritical methanol process. For the plant capacity of 8000 tonnes/year, 10 % depreciation rate, and 50% income tax rate, a negative tax rate of return was observed for all the process except for the heterogeneous- catalysed reaction.

Glisic et al.(2016) comparatively analysed the economics of green diesel and biodiesel from waste cooking oil. The authors investigated the impact of NPV on three processes: catalytic hydrogenation, supercritical non catalytic, and homogenous alkali catalysed transesterification and found that the economics of these processes depends on the unit capacity and cost of the feedstock. The study revealed that unit capacities of the process below 100,000 tonnes/year result in negative NPV after 10 years of project.

Similarly, Kookos (2018) found that biodiesel production from the spent coffee ground oil using NaOH is not profitable. The minimum selling price for biodiesel was found to be $ 3.6 /kg for the production capacity of 1000 tonnes/year. In the present study, the minimum selling price of biodiesel is estimated at $ 1.09/kg when NPV is zero.

Based on the type of feedstock and plant capacity, the outcomes for economic feasibility for the process varies and these uncertainties are the major sources of concern. In order to account for the economic viability of the biodiesel process in the present study, the stochastic modelling approach is considered.

7.4.3 Stochastic model

In practicality, the factors affecting the profitability of the process vary over the years of plant operation. Stochastic model uses a probabilistic approach to quantify the risk. It incorporates Monte-Carlo simulation to determine the uncertainty on the values of DCFROR, NPV, and discounted payback period. Monte-Carlo simulation assigns the probability distributions to parameters and repeatedly choses variable from these distributions and uses the values to calculate variable-dependent functions. The fluctuations in fixed capital investment, working capital, income

tax rate, price of product, salvage value, and raw material price are considered in this model. Table 7.4 describes the probable variation of these parameters over chemical plant life. For instance, the FCI for the current case is $ 2, 083,380. It can fluctuate from $ 1,875,402 (90% of $ 2,083,380) to $ 2,604,225. The probability distribution and a random number are assigned to all the parameters listed in Table 7.4. The random number can be generated using Rand () function in Microsoft's excel program. The value of the parameter is then calculated using probability distribution function (Turton et al., 2012).

$$P(x) = \frac{(x-a)^2}{(c-a)(b-a)} \; for \; x \leq b \quad \text{.....(7.1)}$$

$$P(x) = \frac{(b-a)}{(c-a)} + \frac{(x-b)(2c-x-b)}{(c-a)(c-b)} \; for \; x > b \quad \text{.....(7.2)}$$

Table 7.4. Variation of key factors affecting the profitability of the process.

	Lower Limit (%)	Upper Limit (%)	Base Value
FCI	-10	25	$ 2,083,380
Price of Product	-10	20	$ 9,489,640
Working Capital	-10	20	$ 312,507
Income Tax Rate*	-20	20	42%
Interest Rate*	-10	20	5%
Raw Material Price	-10	20	$ 5,889,460
Salvage Value	-80	20	$ 104169

Where a,b, and c are the estimates of the lowest, most likely and highest value that the parameter could take and $P(x)$ is random number. Eqs 7.1 and 7.2 can be solved for x, having two solutions. The value outside the interval is rejected. The profitability of (NPV, DCFROR) the project is then calculated once values have been assigned to all the parameters. A smooth

probability curve or histogram is generated (Turton et al., 2012). CAPCOST software is used to generate a smooth curve with 1000 data points. The profitability of the project can then be analysed.

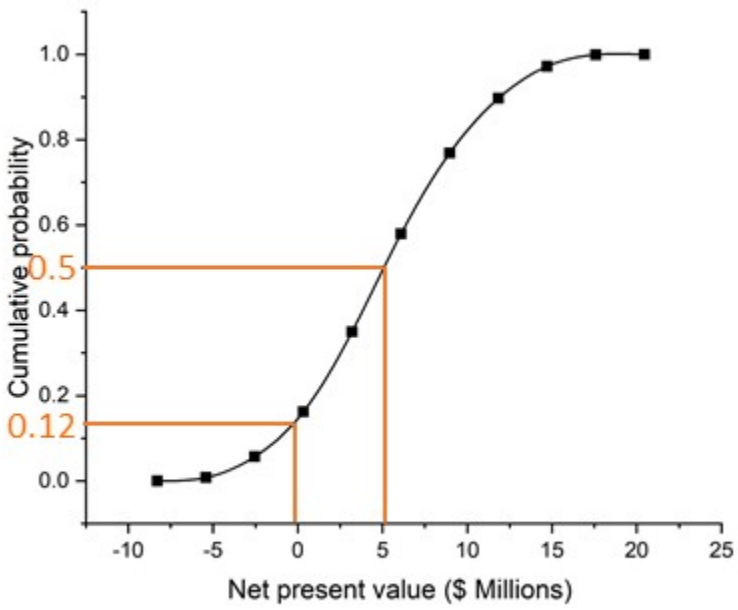

Figure 7.5. Cumulative probability of NPV obtained via 1000-point Monte Carlo simulation

Figure 7.5 shows cumulative probability distributions for the values of NPV, DCFROR, and discounted payback period. From Figure 7.5, there is about 12 % that the project will not be profitable and the median NPV is about 5.1. The lowest value of NPV for the current biodiesel plant is $ -8.3 M, while the highest value of NPV is $ 20.5 M.

7.5 Life cycle assessment (LCA)

Life cycle analysis software SimaPro 9.0 was used to perform the analysis using Impact 2002+ method developed by Jolliet et al. (2003). This method employs two approaches: i) mid–point categories and ii) damage-oriented categories. Mid-point categories is based on quantitative modeling and classify the LCA results into 14 midpoint categories which include carcinogens and non-carcinogens, ozone layer depletion, respiratory inorganics, and organics, ionizing radiation, aquatic and terrestrial ecotoxicity, aquatic acidification and eutrophication, global warming, land

occupation, and non-renewable energy. Damage-oriented categories are build on cause-effect chain and are classified into four damage categories: i) ecosystem quality, ii) human health, iii) resources, and iv) climate change (Li et al., 2014). Impact 2002+ method links all the life cycle inventory results by midpoint categories to damage categories. The damage categories and 14 mid point categories are shown in Figure 7.6.

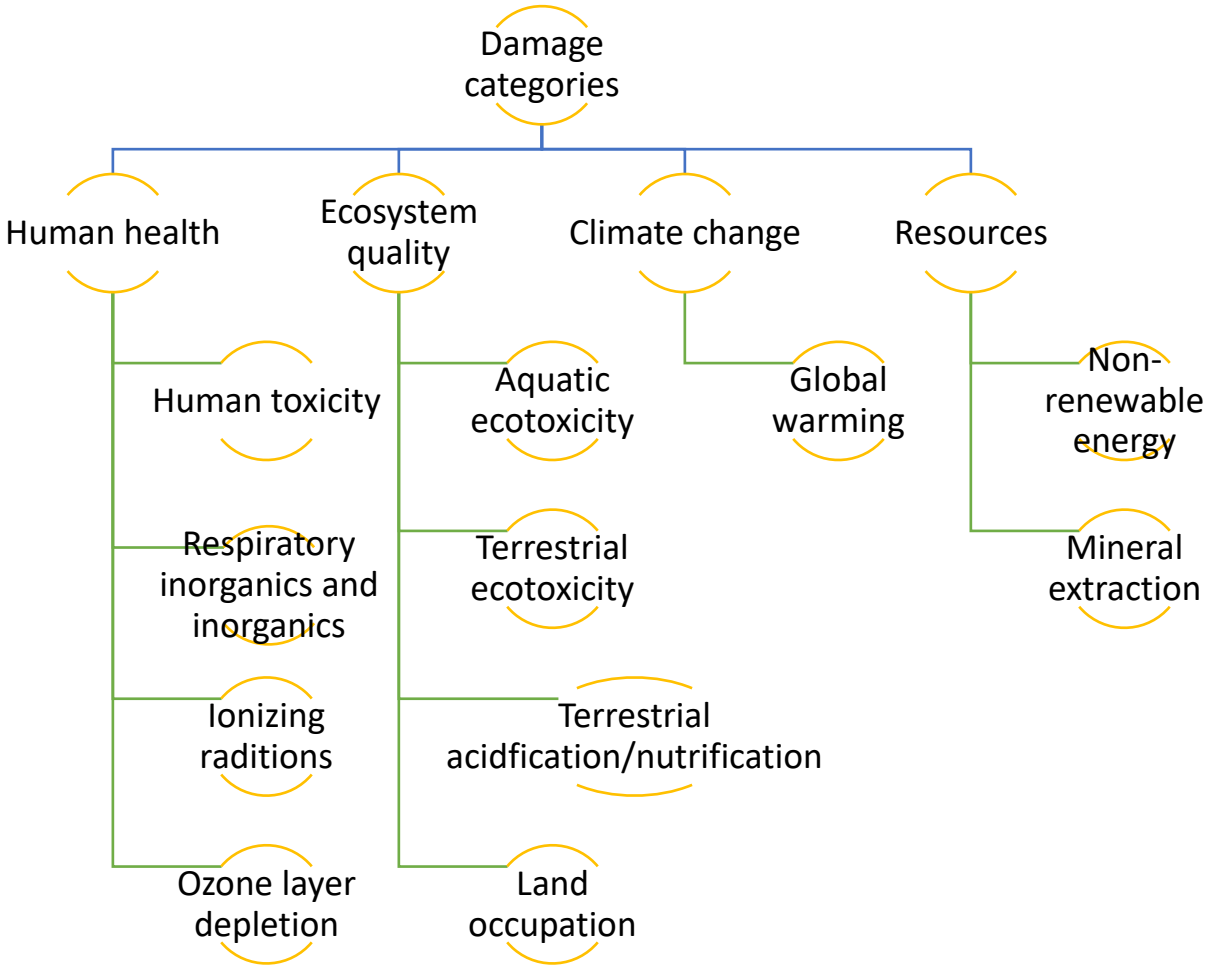

Figure 7.6. Impact 2002+ categories

7.5.1 System boundary and inventory

The plant under the study collects the green, wet or spring thrashed canola from the local farmers as a feedstock for biodiesel production. These low-grade canola seeds were considered as the by-products of canola cultivation. Hence, the agricultural production of canola seeds was not

accounted. It was assumed that the biodiesel facility is co-located at the oilseed crusher. The system boundaries include the inputs in transportation of the seeds to the biodiesel plant, oil extraction, biodiesel production, and transportation of fuel to station.

Extraction of canola oil

The information concerning the canola seed conversion into canola oil was taken from the Ecoinvent database in Simapro. Several steps are involved in the extraction of canola oil. The process usually includes cleaning, preconditioning, flaking, and cooking of seeds before running through extraction press. The obtained press cake is solvent extracted to remove the remaining oil. Most of canola crushing facilities in North America utilize natural gas as their source of thermal energy. Table 7.5 shows the inventory for the canola oil extraction data. The oil content in the seed was taken on an average of 42.8 % based on report of Canola Council of Canada. The transportation of the canola seeds from the farm to seed crushing facility is assumed to be by truck over 100 km distance. The electricity consumed during canola oil extraction was assumed to be converted to waste heat based on study carried out by X. Li and Mupondwa (2014).

Table 7.5. Inventory data for green seed canola oil extraction

Source: Ecoinvent database, Simapro 9.0

	Input	
Seed	19405	tonnes
Seed transportation by truck	1940500	tkm
Electricity	82927.3504	kWh
Heat (Natural gas)	1.1112E+10	kJ
Heat (steam)	8292735043	kJ
hexane (oil extraction)	9951.3	kg
water	1547.9	kg
heat , waste emission	331709.4	MJ
	Output	
Canola oil	7761.8	tonnes
Canola meal	4657.1	tonnes

Biodiesel production

The inventory for the biodiesel production was obtained from the process flow sheet and mass/energy balance simulated in Aspen Plus V10. Table 7.6 depicts the input and output parameters for the biodiesel process. The catalysts employed in the process was tungstophosphoric acid supported on mesoporous aluminosilicate. The GHG emission and energy use associated with the catalyst was not taken into the account due to lack of information in database. No transportation was considered from oil extraction facility to biodiesel plant as it was assumed that the extraction facility is co-located with the biodiesel plant. The transportation distance from biodiesel facility to fuel station was assumed to be 240 km.

Table 7.6. Input and output parameters for the biodiesel process

	Input	
Oil	7762	tonnes
Electricity	594616	kW
cooling water	83528	tonnes
Steam	2944904	lb
Methanol	4357	tonnes
transportation by truck	1752480	tkm
	Output	
Biodiesel	7308	tonnes
glycerine	766	tonnes
oil waste	388.9	tonnes

The LCA results are analysed based on climate change, ecosystem quality, human health, and resources.

7.5.2 GHG emission contribution for each input canola-derived biodiesel production

Figures 7.7 and 7.8 depict the GHG emission contribution (tonnes of CO_2 eq. per tonne of biodiesel) of each input in canola oil extraction and green seed canola derived biodiesel. The process steam, natural gas, and transportation were the main three contributors to GHG emission in the green seed canola oil extraction. The LCA was developed using the system expansion method

whereby the by-product green seed canola meal from the extraction process provides credit to CO_2 emissions in GSC oil extraction such that the total emission GHG emission amounts to – 0.8 tonnes of CO_2 eq. per tonne of oil. The valorisation of the pressed green seed cake could be achieved for the biogas production for the heat and electricity generation.

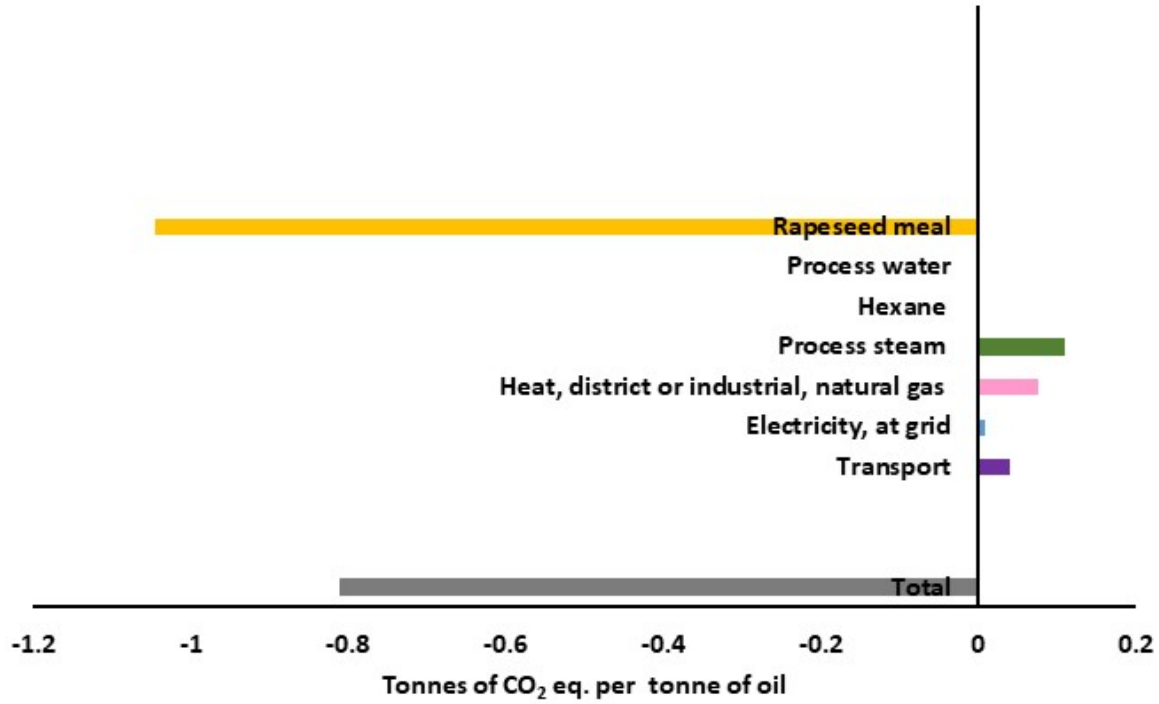

Figure 7.7. GHG emission contribution (tonnes of CO_2 eq. per tonne of oil) of each input in green seed canola oil extraction.

The top three contributor to the global warming potential of biodiesel were methanol, transportation, and electricity. Methanol contribution was mainly from the natural gas consumption during the production process. The electricity requirement for the process is satisfied with the electricity taken from the national grid. The transesterification by-product glycerol and the canola oil production gave credits to CO_2 emissions resulting into net emission of -0.5 tonnes of CO_2 eq. per tonne of biodiesel derived. As per the results obtained, the biodiesel process from the green seed canola oil indicates a zero burden to the climate change. However, this research does not consider the use of the biodiesel in the vehicle owing to the lack of primary data in fuel combustion.

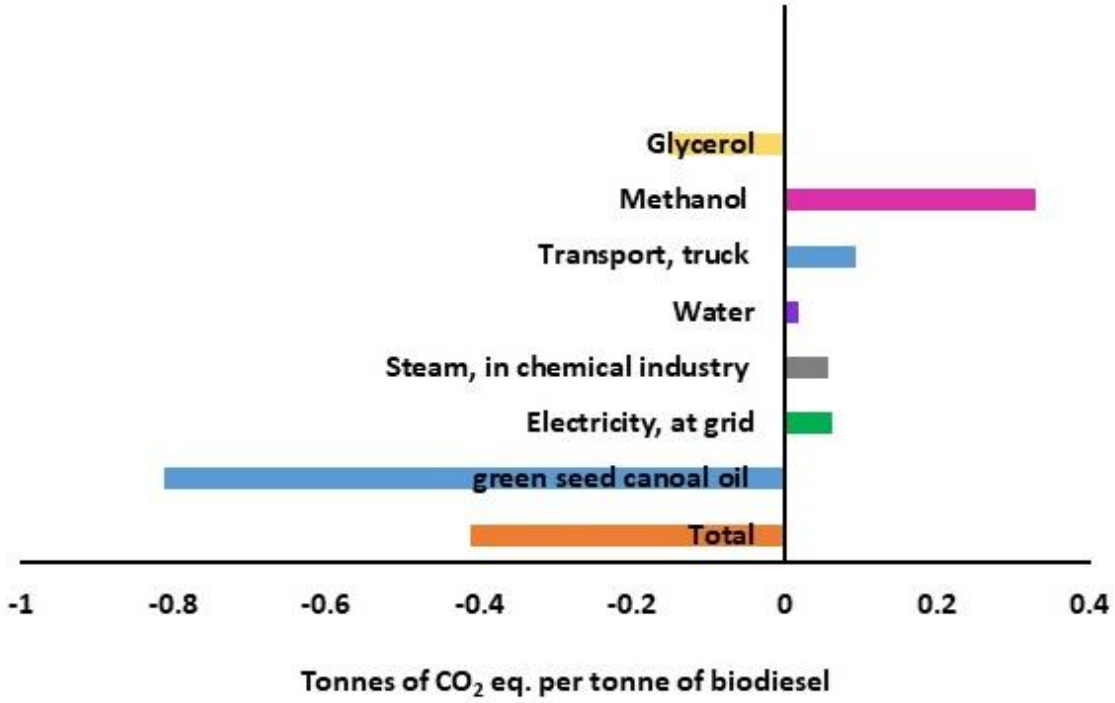

Figure 7.8. GHG emission contribution (tonnes of CO_2 eq. per tonne of biodiesel) of each input in green seed canola derived biodiesel

In the case of biodiesel production from the rapeseed as feedstock, González-García et al. (2013) found that the agricultural activities associated with the rapeseed production had a major impact on environment with GHG emissions due to extensive use of fertilizer. The GHG emission for the rapeseed oil-derived biodiesel was found to be 3.2 tonnes of CO_2 eq. per tonne of biodiesel using conventional transesterification process. For the biodiesel production from soybean oil, the GHG emissions are estimated to be 2.1 tonnes of CO_2 per tonne of biodiesel (Pradhan et al., 2009). Similar observation was also noted for the biodiesel production from cotton seed wherein the agriculture activities significantly contributed to the environmental impact with GHG emissions estimated to 1.5 tonnes of CO_2 eq. per tonne of biodiesel (Lima et al., 2017).

In such a scenario, the waste feedstock could serve as a viable alternative for sustainable biodiesel process avoiding the intensive agricultural inputs and in turn providing the valorisation of these waste materials.

7.5.3 Impact on ecosystem quality and human health

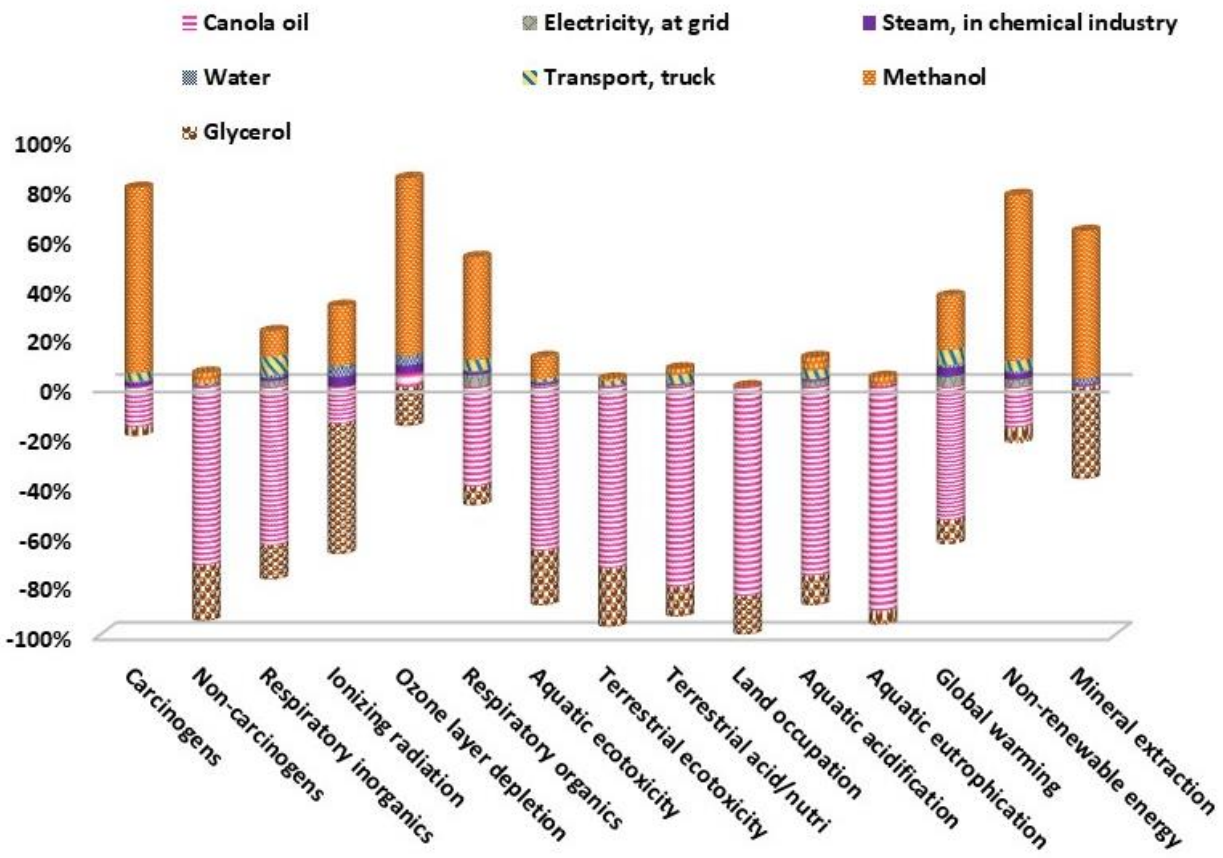

Figure 7.9. Relative contributions of input and outputs in biodiesel process to each impact categories

The relative contributions of each inputs in biodiesel process to each impact category (ecosystem quality and human health) are shown in Figure 7.9. According to figure 7.9, the methanol production was the main hot spots in the impact categories assessed. The methanol production had a major impact on human health (carcinogens + ozone layer depletion), climate change, and resources (non-renewable energy content and mineral extraction). This is because of the fact that the methanol production process involves steam reforming, which is mainly dependent from the natural gas. Concerning the impact categories under the assessment, the canola oil production as well as the by-product glycerine presented a positive environmental impact.

7.5.4 Comparison with fossil diesel and biodiesel from soybean oil

A comparison among the diesel mix at refinery and biodiesel from green seed canola oil, and soybean oil was carried out in order to asses the viability of the biodiesel process from green seed canola oil as alternative fuel. All the inputs and outputs were referred to the production of 1 tonne of biodiesel or fossil diesel.

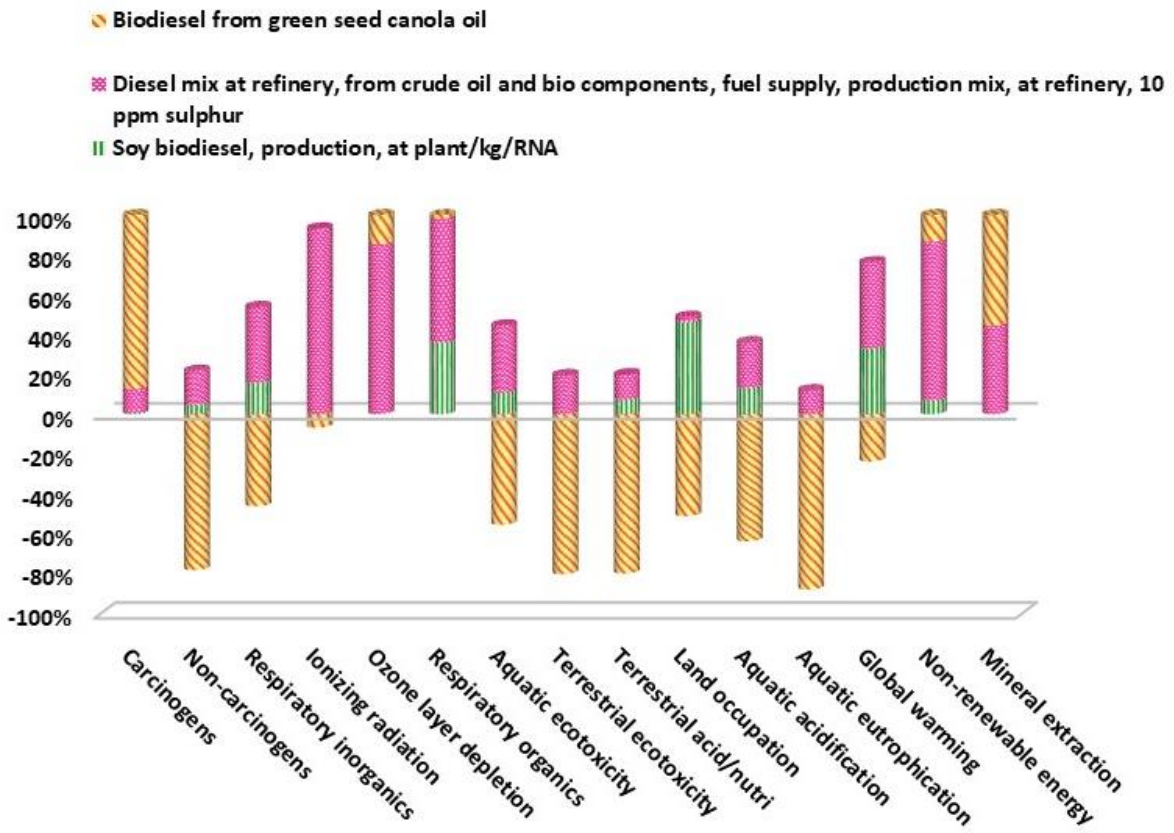

Figure 7.10. Comparison among biodiesel from green seed canola oil, diesel mix, and soybean oil

In each impact category, the total impacts associated with the biodiesel production from the green seed canola oil are much lower than those associated with diesel mix and soy biodiesel except for carcinogenic category which is associated with the methanol production (Figure 7.10). The diesel mix shows the highest effect on the global warming potential followed by soy biodiesel. The effects of the global warming are produced primarily because of the use of fossil resources. Also, the agricultural stages such as pesticides, fertilizers, machineries associated with the cultivation of biomass contribute to this impact category. Concerning the non-renewable energy category, the

diesel mix and biodiesel from green seed canola oil are mainly dependent on non–renewables. It is to be noted that the soy biodiesel production uses alkaline-catalyzed process and consumes less methanol, which is why the contribution to non-renewable energy content was smaller.

Biodiesel production from the green seed canola oil, as observed, has a much more beneficial environment profile than the current process of biomass diesel or diesel fuel.

The findings of the LCA are accurate only on the basis of the research assumptions and are associated with significant uncertainty that must be considered to be critical to the understanding of the results of the study (Guldbrandsson and Bergmark, 2012). The inventories are specific to the regions and the impact assessment would vary due to differences in the regions from which these data sets are collected.

7.6 Conclusions

The techno-economic investigation demonstrated that biodiesel production from green seed canola oil is competitive with the selling price of biodiesel equivalent to $ 1.2/kg, including tax incentives. The stochastic model predicted that the project was 88 % likely to be profitable. In terms of sustainability, the process indicated a zero burden to climate change. Based on the LCA outcomes, green seed canola oil biodiesel production showed a better environmental profile, offering an appealing alternative to the other biodiesel options analyzed.

CHAPTER 8

Conclusions and Recommendations

8.1 Overall discussion and conclusions

The overall research focussed on the development of HPW-based solid acid catalysts supported on γ-Al_2O_3 and mesoporous aluminosilicates like MAS-7 and MAS-9, for the production of biodiesel.

Chapter 2 helped to recognize the potential supports for application in heterogeneous catalysis and the knowledge gaps associated with this research.

The suitability of γ- alumina as a support for the immobilisation of the heteropolyacid was tested in Chapter 3. From this study, it was found that the surface acidity of γ-alumina plays a role in the immobilization of HPW. Porous oxide materials with acidic characteristics was therefore determined to be appropriate for heteropolyacid heterogenization. However, a high HPW loading of 45 wt % was needed to catalyze the reaction with methyl ester yields of 90.0 ± 2.8 wt % and 74.0 ± 1.9 wt % for the transesterification of canola and green seed canola oil, respectively. This can be explained by the fact that the apparent Brønsted acidity occurred at the loading of 45 wt % and provided the optimal B/L (Brønsted to Lewis) ratio. However, the alumina-based solid acid catalyst lacked the desirable catalytic activity for the simultaneous transesterification and esterification of low-grade green seed canola oil. This could be due to the hydrolysis of esters due to the FFA content in the feedstock and the presence of water, as well as the limited availability of Brønsted sites on the catalysts surface.

In Chapter 4, mesoporous aluminosilicates such as MAS-7 and MAS-9 supports were employed for the heterogenization of HPW for biodiesel production from green seed canola oil. In cases of MAS-7 and MAS-9, improved catalytic activity was achieved with lower HPW loading compared to γ-Al_2O_3.

MAS-7 and MAS-9 supports also contributed to the catalytic activity and therefore a low loading was sufficient to make the catalysts reactive. Results from this phase of the work demonstrated MAS-7 and MAS- 9 to be promising supports for HPW owing to their high hydrothermal stability, acidity and large surface area. The interaction of HPW with the mesoporous framework plays a key role in endowing chemical properties desirable for simultaneous esterification and transesterification reactions. Furthermore, the study demonstrated that the activity of these catalysts is a result of synergism between HPW and the MAS support. W in octahedral co-ordination and Al in tetrahedral co-ordination contributed to the catalytic activity.

In Chapter 5, the direct incorporation of HPW in MAS-7 and MAS-9 framework was undertaken. Results from this phase of the research showed that the textural properties and reactivity of the catalysts can be advanced by direct incorporation of HPW in the synthesis step of the aluminosilicates MAS-7 and MAS-9. 40% and 90% increases in surface area were observed for HPW-MAS-7 and HPW-MAS-9 composites with 25 wt % HPW loadings compared to their supported counterparts. An improvement in pore size was observed for HPW-MAS-7 catalysts. Synthesis of stable and bifunctional HPW-MAS composite catalysts with intact HPW has been proven successfully in this work. The sequential introduction of HPW in the preparation of these composites affected the surface morphologies of these catalysts. Route 2 resulted in HPW–MAS 2D hexagonal composites with long-range orderliness. The results indicated that the ordered, transitional periodicity is beneficial in catalysis.^{29}Si MAS NMR, and Raman spectroscopy confirmed the stronger interactions between the keggin unit and aluminosilicates in the composites and hence, inhibited the leaching of HPW from the composite framework. Furthermore, the catalytic activity of HPW-MAS-7 and HPW-MAS-9 was directly proportional to the acid strength. The findings also indicated that HPW-MAS-9 catalysts outperform HPW-MAS-7 catalysts, and therefore MAS-9 is the better choice of support for HPW for the acid-catalyzed transesterification reaction.

In Chapter 6, kinetic, mechanistic and thermodynamics studies were undertaken on the optimized HPW-MAS-9 composite obtained from phase 4 of this research work. The kinetic behaviour of the HPW-MAS-9 catalysed transesterification reaction of low-grade green seed canola oil and methanol is best described by the ER model with the surface reaction of triglyceride and adsorbed methanol as the slowest step. The mechanistic details indicated that the reaction of TG to DG proceeded via two-step S_N1 substitution, whereas the reactions of $DG \rightleftharpoons MG$ and $MG \rightleftharpoons$

GL took place via $S_N 2$ nucleophilic substitution. The understanding of the reaction mechanisms is of importance for designing these heterogeneously catalyzed reaction systems.

Chapter 7 explored the techno-economic feasibility of scaling up this process along with the life cycle assessment. From the techno-economic analysis it was concluded that the biodiesel production is profitable provided that there is a tax credit $ 0.29/kg. The life cycle assessment of biodiesel production using green seed canola oil indicated a zero burden with respect to climate change. Using green canola seeds for biodiesel production can contribute a non-negligible proportion of renewable energy to society and reduce the environmental effects associated with the disposal of green canola seeds.

Overall, it was concluded that HPW-MAS-9 catalysts with 25 wt % HPW result in high methyl ester yield due to their unique physicochemical properties.

8.2 Recommendations

Studies on computational modelling of supported heteropolyacid systems would assist in gaining insights into the complicated mechanism of solid acids, such as electron hopping.

Research on *in situ* characterization during the transesterification/esterification reaction would assist in predicting the actual behaviour of these catalytic systems and needs to be carried out.

Immobilisation of the heteropolyacid on the support via linkers (organosiloxane) could be a focus of research in the future.

In order to realize the prospective industrial application, an appropriate cost estimate and life cycle assessment for the catalysts must be developed. To make a reliable evaluation in an LCA analysis, high-quality data is essential, and this task requires a great deal of time and effort.

REFERENCES

Agarwal, M., Chauhan, G., Chaurasia, S.P., Singh, K., 2012. Study of catalytic behavior of KOH as homogeneous and heterogeneous catalyst for biodiesel production. J. Taiwan Inst. Chem. Eng. 43, 89–94.

Ajayebi, A., Gnansounou, E., Kenthorai Raman, J., 2013. Comparative life cycle assessment of biodiesel from algae and jatropha: A case study of India. Bioresour. Technol. 150, 429–437.

Alcañiz-Monge, J., Bakkali, B. El, Trautwein, G., Reinoso, S., 2018. Zirconia-supported tungstophosphoric heteropolyacid as heterogeneous acid catalyst for biodiesel production. Appl. Catal. B Environ. 224, 194–203

Amouri, M., Mohellebi, F., Zaïd, T.A., Aziza, M., 2017. Sustainability assessment of Ricinus communis biodiesel using LCA Approach. Clean Technol. Environ. Policy 19, 749–760.

Anuar, M.R., Abdullah, A.Z., 2016. Challenges in biodiesel industry with regards to feedstock, environmental, social and sustainability issues: A critical review. Renew. Sustain. Energy Rev. 58, 208-223.

Araujo, Lucia Regina Raddi de, Cynthia Fraga Scofield, Nídia Maria Ribeiro Pastura, W. de A.G., 2006. H_3PO_4/Al_2O_3 catalysts: characterization and catalytic evaluation of oleic acid conversion to biofuels and biolubricant. Mater. Res. 9, 181–184.

Atia, H., Armbruster, U., Martin, A., 2008. Dehydration of glycerol in gas phase using heteropolyacid catalysts as active compounds. J. Catal. 258, 71–82.

Avramidou, K. V., Zaccheria, F., Karakoulia, S.A., Triantafyllidis, K.S., Ravasio, N., 2017. Esterification of free fatty acids using acidic metal oxides and supported polyoxometalate (POM) catalysts. Mol. Catal. 439, 60–71.

Azapagic, A., Stichnothe, H., 2010. Life cycle sustainability assessment of biofuels, in: Handbook of Biofuels Production: Processes and Technologies. pp. 37–60.

Badday, A.S., Abdullah, A.Z., Lee, K.T., 2013. Ultrasound-assisted transesterification of crude Jatropha oil using alumina-supported heteropolyacid catalyst. Appl. Energy 105, 380–388.

Bala, D.D., Misra, M., Chidambaram, D., 2017. Solid-acid catalyzed biodiesel production, part I:

biodiesel synthesis from low quality feedstock. J. Clean. Prod. 142, 4169–4177.

Balzer, R., Drago, V., Schreinerc, W.H., Probsta, L.F.D., 2014. Synthesis and structure-activity relationship of a WO_3 catalyst for the total oxidation of BTX. J. Braz. Chem. Soc. 25, 2026–2031.

Banchero, M., Gozzelino, G., 2018. A simple pseudo-homogeneous reversible kinetic model for the esterification of different fatty acids with methanol in the presence of Amberlyst-15. Energies. 11, 1843.

Baroi, C., Dalai, A.K., 2014. Esterification of free fatty acids (FFA) of Green Seed Canola (GSC) oil using H-Y zeolite supported 12-Tungstophosphoric acid (TPA). Appl. Catal. A Gen. 485, 99–107.

Baroi, C., Dalai, A.K., 2013. Simultaneous esterification, transesterification and chlorophyll removal from green seed canola oil using solid acid catalysts. Catal. Today 207, 74–85.

Baroi, C., Dalai, A.K., 2012. TPA supported on SBA-15 as solid acid catalysts for the biodiesel production, in: ACS Symposium Series. pp. 93–109.

Baroi, C., Mahto, S., Niu, C., Dalai, A.K., 2014. Biofuel production from green seed canola oil using zeolites. Appl. Catal. A Gen. 469, 18–32.

Bart, J.C.J., Palmeri, N., Cavallaro, S., 2010. Biodiesel science and technology: from soil to oil, Woodhead Publishing.

Beale, A., O'Brien, M., Weckhuysen, B., 2012. Characterization of Solid Materials and Heterogeneous Catalysts. John Wiley & Sons.

Benedictto, G.P., Sotelo, R.M., Dalla Costa, B.O., Fetter, G., Basaldella, E.I., 2018. Potassium-containing hydroxylated hydrotalcite as efficient catalyst for the transesterification of sunflower oil. J. Mater. Sci. 53, 12828–12836.

Bérubé, F., Kaliaguine, S., 2008. Calcination and thermal degradation mechanisms of triblock copolymer template in SBA-15 materials. Microporous Mesoporous Mater. 115, 469–479.

Bhatt, N., Patel, A., 2011. Supported 12-tungstophosphoricacid: A recoverable solid acid catalyst for liquid phase Friedel-Crafts alkylation of phenol. J. Taiwan Inst. Chem. Eng. 42, 356–362.

Bozek-Winkler, E., Gmehling, J., 2006. Transesterification of methyl acetate and n-butanol catalyzed by Amberlyst 15. Ind. Eng. Chem. Res. 45, 6648–6654.

BP statistical review of world energy, 2019: https://www.bp.com/content/dam/bp/business-sites/en/global/corporate/pdfs/energy-economics/statistical-review/bp-stats-review-2019-full-report.pdf

Brahmkhatri, V., Patel, A., 2011a. 12-Tungstophosphoric acid anchored to SBA-15: An efficient, environmentally benign reusable catalysts for biodiesel production by esterification of free fatty acids. Appl. Catal. A Gen. 403, 161–172.

Brahmkhatri, V., Patel, A., 2011b. Biodiesel production by esterification of free fatty acids over 12-tungstophosphoric acid anchored to MCM-41. Ind. Eng. Chem. Res. 50, 6620–6628.

Budiman Abdurakhman, Y., Adi Putra, Z., Bilad, M.R., Md Nordin, N.A.H., Wirzal, M.D.H., 2018. Techno-economic analysis of biodiesel production process from waste cooking oil using catalytic membrane reactor and realistic feed composition. Chem. Eng. Res. Des. 134, 564–574.

Caliman, E., Dias, J.A., Dias, S.C.L., Prado, A.G.S., 2005. Solvent effect on the preparation of $H_3PW_{12}O_{40}$ supported on alumina. Catal. Today 107, 816–825.

Canola council of Canada: https://www.canolacouncil.org/

Carvalho, F.S., Fornasier, F., Leitão, J.O.M., Moraes, J.A.R., Schneider, R.C.S., 2019. Life cycle assessment of biodiesel production from solaris seed tobacco. J. Clean. Prod. 230, 1085–1095.

Cattaneo, A.S., Ferrara, C., Villa, D.C., Angioni, S., Milanese, C., Capsoni, D., Grandi, S., Mustarelli, P., Allodi, V., Mariotto, G., Brutti, S., Quartarone, E., 2016. SBA-15 mesoporous silica highly functionalized with propylsulfonic pendants: A thorough physico-chemical characterization. Microporous Mesoporous Mater. 219, 219–229.

Chen, T.L., Ji, J., Xiao, S.X., Cai, T.X., Yan, G.S., 1992. The electronic structure of Keggin anion $(PW_{12}O_{40})^{3-}$ and catalytic properties. Int. J. Quantum Chem. 44, 1015–1025.

Chen, Y., Cao, Y., Zheng, G.P., Dong, B.B., Zheng, X.C., 2014. Comparative study on the structural and catalytic properties of mesoporous hexagonal silica anchored with $H_3PW_{12}O_{40}$: Green synthesis of benzoic acid from benzaldehyde, in: Advanced Powder Technology. pp.

1351–1356.

Chen, Y., Zhang, X.L., Chen, X., Dong, B.B., Zheng, X.C., 2013. MCM-41 supported 12-tungstophosphoric acid mesoporous materials: Preparation, characterization, and catalytic activities for benzaldehyde oxidation with H_2O_2. Solid State Sci. 24, 21–25.

Colombo, K., Ender, L., Barros, A.A.C., 2017. The study of biodiesel production using CaO as a heterogeneous catalytic reaction. Egypt. J. Pet. 2, 341-349

Cullity, B., Stock, S., 2001. Elements of X-ray Diffraction.

da Conceição, L.R. V., Carneiro, L.M., Giordani, D.S., de Castro, H.F., 2017. Synthesis of biodiesel from macaw palm oil using mesoporous solid catalyst comprising 12-molybdophosphoric acid and niobia. Renew. Energy 113, 119–128.

Dimian, A.C., Rothenberg, G., 2016. An effective modular process for biodiesel manufacturing using heterogeneous catalysis. Catal. Sci. Technol. 6, 6097–6108.

Dossin, T.F., Reyniers, M.F., Marin, G.B., 2006. Kinetics of heterogeneously MgO-catalyzed transesterification. Appl. Catal. B Environ. 62, 35–45.

Dufaud, V., Lefebvre, F., 2010. Inorganic hybrid materials with encapsulated polyoxometalates. Materials 3(1), 682-703.

Eze, V.C., 2014. The use of mesoscale oscillatory baffled reactors for rapid screening of heterogeneously catalysed biodiesel production reactions. PhD Thesis.School of Chemical Engineering and Advanced Materials, Newcastle University, United Kingdom.

Gagea, B.C., Lorgouilloux, Y., Altintas, Y., Jacobs, P.A., Martens, J.A., 2009. Bifunctional conversion of n-decane over HPW heteropoly acid incorporated into SBA-15 during synthesis. J. Catal. 265, 99–108.

Galván Muciño, G.E., Romero, R., Ramírez, A., Ramos, M.J., Baeza-Jiménez, R., Natividad, R., 2016. Kinetics of transesterification of safflower oil to obtain biodiesel using heterogeneous catalysis. Int. J. Chem. React. Eng. 14, 929–938.

Gao, Y., Chen, Y., Gu, J., Xin, Z., Sun, S., 2019. Butyl-biodiesel production from waste cooking oil: Kinetics, fuel properties and emission performance. Fuel 236, 1489–1495.

Gaurav, A., Dumas, S., Mai, C.T.Q., Ng, F.T.T., 2019. A kinetic model for a single step biodiesel production from a high free fatty acid (FFA) biodiesel feedstock over a solid heteropolyacid catalyst. Green Energy Environ.

Gebremariam, S.N., Marchetti, J.M., 2018. Economics of biodiesel production. Energy Convers. Manag. 168, 74-84.

Glisic, S.B., Pajnik, J.M., Orlović, A.M., 2016. Process and techno-economic analysis of green diesel production from waste vegetable oil and the comparison with ester type biodiesel production. Appl. Energy 170, 176–185.

González-García, S., García-Rey, D., Hospido, A., 2013. Environmental life cycle assessment for rapeseed-derived biodiesel. Int. J. Life Cycle Assess. 18, 61–76.

Gopinath, S., Vinoth Kumar, P., Sahaya Murphin Kumar, P., Yasar Arafath, K.A., Sivanesan, S., Baskaralingam, P., 2018. Cs-tungstosilicic acid/Zr-KIT-6 for esterification of oleic acid and transesterification of non-edible oils for green diesel production. Fuel 234, 824–835.

Grinenval, E., Rozanska, X., Baudouin, A., Berrier, E., Delbecq, F., Sautet, P., Basset, J.M., Lefebvre, F., 2010. Controlled interactions between anhydrous keggin-type heteropolyacids and silica support: Preparation and characterization of well-defined silica-supported polyoxometalate species. J. Phys. Chem. C 114, 19024–19034.

Groen, J.C., Peffer, L.A.A., Pérez-Ramírez, J., 2003. Pore size determination in modified micro- and mesoporous materials. Pitfalls and limitations in gas adsorption data analysis. Microporous Mesoporous Mater. 60, 1–17.

Gue, I.H. V., Ubando, A.T., Cuello, J.L., Culaba, A.B., 2019. Assessing microalgal biodiesel sustainability via MCI and LCA frameworks, in: 2018 IEEE 10th International Conference on Humanoid, Nanotechnology, Information Technology, Communication and Control, Environment and Management, HNICEM 2018. pp. 1–5.

Guldbrandsson, F., Bergmark, P., 2012, Opportunities and limitations of using life cycle assessment methodology in the ICT sector. In 2012 Electronics Goes Green 2012+ (pp. 1-6). IEEE.

Guo, Y., Li, K., Yu, X., Clark, J.H., 2008. Mesoporous $H_3PW_{12}O_{40}$-silica composite: Efficient and

reusable solid acid catalyst for the synthesis of diphenolic acid from levulinic acid. Appl. Catal. B Environ. 81, 182–191.

Gupta, P., Paul, S., 2014. Solid acids: Green alternatives for acid catalysis. Catal. Today 236, 153-70.

Haas, M.J., McAloon, A.J., Yee, W.C., Foglia, T.A., 2006. A process model to estimate biodiesel production costs. Bioresour. Technol. 97, 671–678.

Han, Y., Xiao, F.S., Wu, S., Sun, Y., Meng, X., Li, D., Lin, S., Deng, F., Ai, X., 2001. A novel method for incorporation of heteroatoms into the framework of ordered mesoporous silica materials synthesized in strong acidic media. J. Phys. Chem. B 105, 7963–7966.

Hanif, M.A., Nisar, S., Rashid, U., 2017. Supported solid and heteropoly acid catalysts for production of biodiesel. Catal. Rev. Sci. Eng. 59, 165–188.

Hernández-Cortéz, J.G., López, T., Aguilar, D.H., Quintana, P., 2003. Thermal Stability and Hydrolysis Catalysts Effect on Sol-Gel Zirconia in the Presence of Heteropolyacids, in: Emerging Fields in Sol-Gel Science and Technology. pp. 221–229.

Hernández-Cortez, J.G., Martinez, L., Soto, L., López, A., Navarrete, J., Manríquez, M., Lara, V.H., López-Salinas, E., 2010. Liquid phase alkylation of benzene with dec-1-ene catalyzed on supported 12-tungstophosphoric acid. Catal. Today 150, 346–352.

Holclajtner-Antunović, I., Mioč, U.B., Todorović, M., Jovanović, Z., Davidović, M., Bajuk-Bogdanović, D., Laušević, Z., 2010. Characterization of potassium salts of 12-tungstophosphoric acid. Mater. Res. Bull. 45, 1679–1684.

Hoo, P., Abdullah, A.Z., 2015. Kinetics Modeling and Mechanism Study for Selective Esterification of Glycerol with Lauric Acid using 12-Tungstophosphoric Acid Post-Impregnated SBA-15. Ind. Eng. Chem. Res. 54, 7852–7858.

Hoo, P.Y., Abdullah, A.Z., 2014. Direct synthesis of mesoporous 12-tungstophosphoric acid SBA-15 catalyst for selective esterification of glycerol and lauric acid to monolaurate. Chem. Eng. J. 250, 274–287.

Hung, C. Te, Liu, L.L., Wang, J.J., Wu, P.H., Wang, C. Bin, Tsai, T.C., Liu, S. Bin, 2019. Acidity

and alkylation activity of 12-tungstophosphoric acid supported on ionic liquid-functionalized SBA-15. Catal. Today 327, 10–18.

Ilgen, O., Akin, A.N., 2012. Determination of reaction orders for the transesterification of canola oil with methanol by using KOH/MgO as a heterogeneous catalyst. Appl. Catal. B Environ. 126, 342–346.

Isernia, L.F., 2013. FTIR study of the relation, between extra-framework aluminum species and the adsorbed molecular water, and its effect on the acidity in ZSM-5 steamed zeolite. Mater. Res. 16, 792–802.

Issariyakul, T., Dalai, A.K., 2012. Comparative kinetics of transesterification for biodiesel production from palm oil and mustard oil. Can. J. Chem. Eng. 90, 342–350.

Issariyakul, T., 2011. Development of Biodiesel Production Processes from Various Vegetable Oils.PhD Thesis. Division of Environmental Engineering, University of Saskatchewan, Canada.

Jacobson, K., Gopinath, R., Meher, L.C., Dalai, A.K., 2008. Solid acid catalyzed biodiesel production from waste cooking oil. Appl. Catal. B Environ. 85, 86–91.

Jolliet, O., Margni, M., Charles, R., Humbert, S., Payet, J., Rebitzer, G., Rosenbaum, R., 2003. IMPACT 2002+: a new life cycle impact assessment methodology. Int J LCA, 8(6), 324.

Kapil, A., Wilson, K., Lee, A.F., Sadhukhan, J., 2011. Kinetic modeling studies of heterogeneously catalyzed biodiesel synthesis reactions. Ind. Eng. Chem. Res. 50, 4818–4830.

Kaur, M., Malhotra, R., Ali, A., 2018. Tungsten supported Ti/SiO_2 nanoflowers as reusable heterogeneous catalyst for biodiesel production. Renew. Energy 116, 109–119.

Kaur, N., Ali, A., 2014. One-pot transesterification and esterification of waste cooking oil via ethanolysis using Sr:Zr mixed oxide as solid catalyst. RSC Adv. 4, 43671–43681.

Kawashima, H., Yamashita, Y., Saito, I., 1997. Solid-state ^{13}C NMR of pyridine-swollen coal. Energy and Fuels 11, 709–715.

Kirumakki, S.R., Nagaraju, N., Chary, K.V.R., 2006. Esterification of alcohols with acetic acid over zeolites Hβ, HY and HZSM5. Appl. Catal. A Gen. 299, 185–192.

Kookos, I.K., 2018. Technoeconomic and environmental assessment of a process for biodiesel production from spent coffee grounds (SCGs). Resour. Conserv. Recycl. 134, 156–164.

Koster, R., Van der Linden, B., Poels, E., Blieky, A., 2001. The mechanism of the gas-phase esterification of acetic acid and ethanol over MCM-41. J. Catal. 204, 333–338.

Kozhevnikov, I. V., 2007. Sustainable heterogeneous acid catalysis by heteropoly acids, in: Journal of Molecular Catalysis A: Chemical. Wiley-VCH Verlag GmbH & Co. KGaA, Weinheim, Germany, pp. 86–92.

Kozhevnikov, I. V., 1995. Heteropoly Acids and Related Compounds as Catalysts for Fine Chemical Synthesis. Catal. Rev. 37, 311–352.

Kozhevnikov, I. V., Kloetstra, K.R., Sinnema, A., Zandbergen, H.W., Van Bekkum, H., 1996. Study of catalysts comprising heteropoly acid $H_3PW_{12}O_{40}$ supported on MCM-41 molecular sieve and amorphous silica. J. Mol. Catal. A Chem. 114, 287–298.

Kurhade, A., Zhu, J., Dalai, A.K., 2019. Meso-structured HPW-MAS-7 and HPW-MAS-9 composite catalysts for biodiesel synthesis from unrefined green seed canola oil. Ind. Eng. Chem. Res. 58, 15772–15786.

Kurhade, A., Zhu, J., Hu, Y., Dalai, A.K., 2018. Surface investigation of tungstophosphoric acid supported on ordered mesoporous aluminosilicates for biodiesel synthesis. ACS Omega 3, 14064–14075.

Ladera, R., Finocchio, E., Rojas, S., Busca, G., Fierro, J.L.G., Ojeda, M., 2013. Supported WO_x -based catalysts for methanol dehydration to dimethyl ether. Fuel 113, 1–9.

Latchubugata, C.S., Kondapaneni, R.V., Patluri, K.K., Virendra, U., Vedantam, S., 2018. Kinetics and optimization studies using Response Surface Methodology in biodiesel production using heterogeneous catalyst. Chem. Eng. Res. Des. 135, 129–139.

Lau, P.C., Kwong, T.L., Yung, K.F., 2016. Effective heterogeneous transition metal glycerolates catalysts for one-step biodiesel production from low grade non-refined Jatropha oil and crude aqueous bioethanol. Sci. Rep. 6, 23822.

Lee, A.F., Bennett, J.A., Manayil, J.C., Wilson, K., 2014. Heterogeneous catalysis for sustainable

biodiesel production via esterification and transesterification. Chem. Soc. Rev. 43 (22),7887-7916.

Lee, H.V., Juan, J.C., Yun Hin, T.Y., Ong, H.C., 2016. Environment-friendly heterogeneous alkaline-Based mixed metal oxide catalysts for biodiesel production. Energies 9, 611.

Léonardelli, S., Facchini, L., Fretigny, C., Tougne, P., Legrand, A.P., 1992. Silicon-29 Nuclear Magnetic Resonance Study of Silica. J. Am. Chem. Soc. 114, 6412–6418.

Leung, D.Y.C., Wu, X., Leung, M.K.H., 2010. A review on biodiesel production using catalyzed transesterification. Appl. Energy 87,1083-1095.

Li, K., Hu, J., Li, W., Ma, F., Xu, L., Guo, Y., 2009. Design of mesostructured $H_3PW_{12}O_{40}$-silica materials with controllable ordered and disordered pore geometries and their application for the synthesis of diphenolic acid. J. Mater. Chem. 19, 8628–8638.

Li, X., Mupondwa, E., 2014. Life cycle assessment of camelina oil derived biodiesel and jet fuel in the Canadian Prairies. Sci. Total Environ. 481, 17–26.

Lima, Â.M.F., Torres, E.A., Kiperstok, A., de Freitas Moreira Santos, G., 2017. Environmental impacts of the biodiesel production chain of cotton seed in Bahia, Brazil. Clean Technol. Environ. Policy 19, 1523–1534.

Lin, S., Wang, L., Xiao, F.S., 2004. Design and control of acidic strength in ordered mesoporous aluminosilicates by using preformed zeolite precursors, in: Studies in Surface Science and Catalysis: Elsevier, pp.1513-1518.

Liu, K., Wang, R., Yu, M., 2018. An efficient, recoverable solid base catalyst of magnetic bamboo charcoal: Preparation, characterization, and performance in biodiesel production. Renew. Energy 127, 531–538.

Liu, Y., Pinnavaia, T.J., 2002. Aluminosilicate mesostructures with improved acidity and hydrothermal stability. J.Mater.Chem. 12, 3179–3190.

López, D.E., Goodwin, J.G., Bruce, D.A., 2007. Transesterification of triacetin with methanol on Nafion® acid resins. J. Catal. 245, 381–391.

Lukić, I., Kesić, Ž., Maksimović, S., Zdujić, M., Liu, H., Krstić, J., Skala, D., 2013. Kinetics of

sunflower and used vegetable oil methanolysis catalyzed by CaO·ZnO. Fuel 113, 367–378.

Luque, R., Melero, J.A., 2012. Advances in biodiesel production: Processes and technologies, Woodhead Publishing.

Maciel, G.E., Haw, J.F., Chuang, I.S., Hawkins, B.L., Early, T.A., McKay, D.R., Petrakis, L., 1983. NMR Studies of Pyridine on Silica-Alumina. J. Am. Chem. Soc. 105, 5529–5535.

Macleod, C., 2008. Evaluation of Heterogeneous Catalysts for Biodiesel Production. PhD Thesis School of Chemical Engineering and Advanced Materials, Newcastle University, United Kingdom.

Madhusudhan Rao, P., Wolfson, A., Kababya, S., Vega, S., Landau, M. V., 2005. Immobilization of molecular H3PW12O40 heteropolyacid catalyst in alumina-grafted silica-gel and mesostructured SBA-15 silica matrices. J. Catal. 232, 210–225.

Malhotra, R., Ali, A., 2018. Lithium-doped ceria supported SBA−15 as mesoporous solid reusable and heterogeneous catalyst for biodiesel production via simultaneous esterification and transesterification of waste cottonseed oil. Renew. Energy 119, 32–44.

Mansir, N., Taufiq-Yap, Y.H., Rashid, U., Lokman, I.M., 2017. Investigation of heterogeneous solid acid catalyst performance on low grade feedstocks for biodiesel production: A review. Energy Convers. Manag. 141,171-182.

Marchena, C.L., Gomez, S., Saux, C., Pierella, L.B., Pizzio, L.R., 2015. Tungstophosphoric acid heterogenized onto NH4 ZSM5 as an efficient and recyclable catalyst for the photocatalytic degradation of dyes. Quim. Nova 38, 518–525.

Marchetti, J.M., Errazu, A.F., 2008. Technoeconomic study of supercritical biodiesel production plant. Energy Convers. Manag. 49, 2160–2164.

Margeta, K., Zabukovec, N., Siljeg, M., Farkas, A., 2013. Natural Zeolites in Water Treatment – How Effective is Their Use, in: Water Treatment. pp. 81–112.

Martinovic, F.L., Kiss, F.E., Micic, R.D., Simikić, M., Tomić, M.D., 2018. Comparative techno-economic analysis of single-step and two-step biodiesel production with supercritical methanol based on process simulation. Chem. Eng. Res. Des. 132, 751–765.

Maskill, H., 1996 Mechanisms of organic reactions. Oxford University Press

Meng, J., Cao, Y., Zheng, G., Li, J., Wu, H., Guan, X., Zheng, X., 2014. Assembling of Al-MCM-48 supported H 3 PW 12 O 40 mesoporous materials and their catalytic performances in the green synthesis of benzoic acid. Mater. Res. Bull. 60, 20–27.

Misono, M., 2001. Unique acid catalysis of heteropoly compounds (heteropolyoxometalates) in the solid state. Chem. Commun. 1, 1141–1153.

Mochida, I., Choi, K.H., 2007. Current Progress in Catalysts and Catalysis for Hydrotreating, in: Practical Advances in Petroleum Processing: Springer, New York, pp.257-296

Moffat, J.B., 2001. Metal – Oxygen Clusters: The Surface and Catalytic Properties of Heteropoly Oxometalates. Springer Science and Buisness Media.

Mokaya, R., 1999. Improving the stability of mesoporous MCM-41 silica via thicker more highly condensed pore walls. J. Phys. Chem. B 103, 10204–10208.

Mukai, S.R., Lin, L., Masuda, T., Hashimoto, K., 2001. Key factors for the encapsulation of Keggin-type heteropoly acids in the supercages of Y-type zeolite. Chem. Eng. Sci. 56, 799–804.

Narkhede, N., Singh, S., Patel, A., 2015. Recent progress on supported polyoxometalates for biodiesel synthesis via esterification and transesterification. Green Chem. 17,89-107.

Navarro-Pineda, F.S., Ponce-Marbán, D. V, Sacramento-Rivero, J.C., Barahona-Pérez, L.F., 2017. An economic model for estimating the viability of biodiesel production from Jatropha curcas L. J. Chem. Technol. Biotechnol. 92, 971–980.

Nikseresht, A., Daniyali, A., Ali-Mohammadi, M., Afzalinia, A., Mirzaie, A., 2017. Ultrasound-assisted biodiesel production by a novel composite of Fe(III)-based MOF and phosphotangestic acid as efficient and reusable catalyst. Ultrason. Sonochem. 37, 203–207.

Noshadi, I., Amin, N.A.S., Parnas, R.S., 2012. Continuous production of biodiesel from waste cooking oil in a reactive distillation column catalyzed by solid heteropolyacid: Optimization using response surface methodology (RSM). Fuel 94, 156–164.

Nowińska, K., Fórmaniak, R., Kaleta, W., Wącław, A., 2003. Heteropoly compounds incorporated

into mesoporous material structure. Appl. Catal. A Gen. 256, 115–123.

Okuhara, T., Mizuno, N., Misono, M., 1996. Catalytic Chemistry of Heteropoly Compounds. Adv. Catal. 41, 113–252.

Olejniczak, Z., Sulikowski, B., Kubacka, A., Ga˛siorga˛sior, M., 2000. Heterogenization of 12-tungstophosphoric acid on stabilized zeolite Y, Topics in Catalysis 11(1-4), 391-400.

Oliveira, C.F., Dezaneti, L.M., Garcia, F.A.C., de Macedo, J.L., Dias, J.A., Dias, S.C.L., Alvim, K.S.P., 2010. Esterification of oleic acid with ethanol by 12-tungstophosphoric acid supported on zirconia. Appl. Catal. A Gen. 372, 153–161.

Pan, H., Li, H., Zhang, H., Wang, A., Yang, S., 2019. Acidic ionic liquid-functionalized mesoporous melamine-formaldehyde polymer as heterogeneous catalyst for biodiesel production. Fuel 239, 886–895.

Patel, A., Narkhede, N., 2012. 12-tungstophosphoric acid anchored to zeolite Hβ: Synthesis, characterization, and biodiesel production by esterification of oleic acid with methanol. Energy and Fuels 26, 6025–6032.

Pega, S., Boissière, C., Chaumonnot, A., Sanchez, C., 2008. Tuning pore size and acidity of mesostructured aluminosilicates made by spray drying: design of new catalysts. Stud. Surf. Sci. Catal. 174, 471–476.

Pérez-Pariente, J., Díaz, I., Mohino, F., Sastre, E., 2003. Selective synthesis of fatty monoglycerides by using functionalised mesoporous catalysts. Appl. Catal. A Gen. 254, 173–188.

Pradhan, A., Shrestha, D.S., Mcaloon, A., Yee, W., Haas, M., Duffield, J.A., Shapouri, H., 2009. Energy life-cycle assessment of soybean biodiesel. Transactions of the ASABE, 54(3), 1031-1039.

Pruszko, R., 2015. Chapter 20 – Biodiesel Production, in: Bioenergy. pp. 339–359.

Ramis, G., Busca, G., Cristiani, C., Lietti, L., Forzatti, P., Bregani, F., 1992. Characterization of Tungsta–Titania Catalysts. Langmuir 8, 1744–1749.

Ren, Y., Yue, B., Gu, M., He, H., 2010. Progress of the application of mesoporous silica-supported

heteropolyacids in heterogeneous catalysis and preparation of nanostructured metal oxides. Materials 3, 764–785.

Renewables, 2018: https://www.iea.org/renewables2018/

Rezayan, A., Taghizadeh, M., 2018. Synthesis of magnetic mesoporous nanocrystalline KOH/ZSM-5-Fe_3O_4 for biodiesel production: Process optimization and kinetics study. Process Saf. Environ. Prot. 117, 711–721.

Roberge, D.M., Hausmann, H., Hölderich, W.F., 2002. Dealumination of zeolite beta by acid leaching: A new insight with two-dimensional multi-quantum and cross polarization ^{27} Al MAS NMR. Phys. Chem. Chem. Phys. 4, 3128–3135.

Ross-Medgaarden, E.I., Knowles, W. V., Kim, T., Wong, M.S., Zhou, W., Kiely, C.J., Wachs, I.E., 2008. New insights into the nature of the acidic catalytic active sites present in ZrO_2-supported tungsten oxide catalysts. J. Catal. 256, 108–125.

Sadhukhan, J., Ng, K.S., Hernandez, E.M., 2014. Biorefineries and Chemical Processes: Design, Integration and Sustainability Analysis, Biorefineries and Chemical Processes: Design, Integration and Sustainability Analysis.

Saifuddin, N., Samiuddin, A., Kumaran, P., 2015b. A Review on Processing Technology for Biodiesel Production. Trends Appl. Sci. Res. 10, 1–37.

Sánchez-Vázquez, R., Pirez, C., Iglesias, J., Wilson, K., Lee, A.F., Melero, J.A., 2013. Zr-Containing Hybrid Organic-Inorganic Mesoporous Materials: Hydrophobic Acid Catalysts for Biodiesel Production. Chem. Cat. Chem. 5, 994–1001.

Satterfield, C.N., 1970. Mass transfer in heterogeneous catalysis. MIT press, Cambridge

Scharff, Y., Asteris, D., Fédou, S., 2013. Catalyst technology for biofuel production: Conversion of renewable lipids into biojet and biodiesel. OCL - Oilseeds fats, Crop. lipids 20, D502.

Schoenfeldt, N.J., 2008. Synthesis and characterization of γ-alumina supportedmanganese oxides prepared by grafting and impregnation for applications in heterogeneous catalysis. The University of Iowa, ProQuest Dissertations Publishing.

Sharma, P., Vyas, S., Patel, A., 2004. Heteropolyacid supported onto neutral alumina:

Characterization and esterification of 1° and 2° alcohol. J. Mol. Catal. A Chem. 214, 281–286.

Shi, W., Zhao, J., Yuan, X., Wang, S., Wang, X., Huo, M., 2012. Effects of Brønsted and Lewis acidities on catalytic activity of heteropolyacids in transesterification and esterification reactions. Chem. Eng. Technol. 35, 347–352.

Shringarpure, P.A., Patel, A., 2011. Supported undecatungstophosphate: An efficient recyclable bi-functional catalyst for esterification of alcohols as well as selective oxidation of styrene. Chem. Eng. J. 173, 612–619.

Si, U., Mas, C.P., Zhao, X.S., Lu, G.Q., Whittaker, a K., Millar, G.J., Zhu, H.Y., 1997. Comprehensive Study of Surface Chemistry of MCM-41 Comprehensive Study of Surface Chemistry of MCM-41 Using. J. Phys. Chem. B 5647, 6525–6531.

Sinkler, W., Bradley, S.A., Ziese, U., De Jong, K.P., 2006. 3D-TEM study of gamma alumina catalyst supports, in: Microscopy and Microanalysis. pp. 52–53.

Su, F., Guo, Y., 2014. Advancements in solid acid catalysts for biodiesel production. Green Chem.16, 2934-2957.

Surasit, C., Yoosuk, B., Pohmakotr, M., Tantirungrotechai, J., 2017. biodiesel synthesis from palm fatty acid distillate using tungstophosphoric acid supported on cesium-containing niobia. J. Am. Oil Chem. Soc. 94, 465–474.

Topcrop manager: https://www.topcropmanager.com/crushing-the-green-seed-problem-in-canola-21343/).

Trombetta, M., Busca, G., Storaro, L., Lenarda, M., Casagrande, M., Zambon, A., 2000. Surface acidity modifications induced by thermal treatments and acid leaching on microcrystalline H-BEA zeolite. A FTIR, XRD and MAS-NMR study. Phys. Chem. Chem. Phys. 2, 3529–3537.

Tropecêlo, A.I., Casimiro, M.H., Fonseca, I.M., Ramos, A.M., Vital, J., Castanheiro, J.E., 2010. Esterification of free fatty acids to biodiesel over heteropolyacids immobilized on mesoporous silica. Appl. Catal. A Gen. 390, 183–189.

Turton, R., Bailie, R.C., Whiting, W.B. and Shaeiwitz, J.A., 2012. Analysis, synthesis and design

of chemical processes,fourth ed.Pearson Education.

Ulrich, G.D., Vasudevan, P.T., 2004. Chemical engineering process design and economics, a practical guide, second ed. Process publishing, Durham.

Van De Steene, E., De Clercq, J., Thybaut, J.W., 2012. Adsorption and reaction in the transesterification of ethyl acetate with methanol on Lewatit K1221. J. Mol. Catal. A Chem. 359, 57–68.

Vicente, G., Martínez, M., Aracil, J., Esteban, A., 2005. Kinetics of sunflower oil methanolysis. Ind. Eng. Chem. Res. 44, 5447–5454.

Wachs, I.E., 1996. Raman and IR studies of surface metal oxide species on oxide supports: Supported metal oxide catalysts. Catal. Today 27, 437–455.

Wang, G., Nicholson, P.S., 2004. Influence of Acidity on the Stability and Rheological Properties of Ionically Stabilized Alumina Suspensions in Ethanol. J. Am. Ceram. Soc. 84, 1977–1980.

Wang, H., Li, Y., Yu, F., Wang, Q., Xing, B., Li, D., Li, R., 2019. A stable mesoporous super-acid nanocatalyst for eco-friendly synthesis of biodiesel. Chem. Eng. J. 364, 111–122.

Wang, Y., Zhao, D., Chen, G., Liu, S., Ji, N., Ding, H., Fu, J., 2019. Preparation of phosphotungstic acid based poly(ionic liquid) and its application to esterification of palmitic acid. Renew. Energy 317–324.

Wang, Y.T., Yang, X.X., Xu, J., Wang, H.L., Wang, Z.B., Zhang, L., Wang, S.L., Liang, J.L., 2019. Biodiesel production from esterification of oleic acid by a sulfonated magnetic solid acid catalyst. Renew. Energy 139, 688–695.

West, A.H., Posarac, D., Ellis, N., 2008. Assessment of four biodiesel production processes using HYSYS.Plant. Bioresour. Technol. 99, 6587–6601.

Winoto, H.P., Fikri, Z.A., Ha, J.M., Park, Y.K., Lee, H., Suh, D.J., Jae, J., 2019. Heteropolyacid supported on Zr-Beta zeolite as an active catalyst for one-pot transformation of furfural to Γ-valerolactone. Appl. Catal. B Environ. 241, 588–597.

Wong, Y.C., Tan, Y.P., Taufiq-Yap, Y.H., Ramli, I., 2014. Effect of calcination temperatures of CaO/Nb_2O_5 mixed oxides catalysts on biodiesel production. Sains Malaysiana,43, 783-790.

Wu, H.Y., Zhang, X.L., Chen, X., Chen, Y., Zheng, X.C., 2014. Preparation, characterization and catalytic properties of MCM-48 supported tungstophosphoric acid mesoporous materials for green synthesis of benzoic acid. J. Solid State Chem. 211, 51–57.

Wu, M., Zhang, X., Su, X., Li, X., Zheng, X., Guan, X., Liu, P., 2016a. 3D graphene aerogel anchored tungstophosphoric acid catalysts: Characterization and catalytic performance for levulinic acid esterification with ethanol. Catal. Commun. 85, 66–69.

Wu, M., Zhao, Q.Q., Li, J., Su, X.L., Wu, H.Y., Guan, X.X., Zheng, X.C., 2016b. Tungstophosphoric acid-based mesoporous materials anchored to MCM-41: characterization and catalytic performance in esterification of levulinic acid with ethanol. J. Porous Mater. 23, 1329–1338.

Wu, M., Zhao, Q.Q., Li, J., Wu, H.Y., Zheng, X.C., Guan, X.X., Liu, P., 2016c. Esterification of levulinic acid into hexyl levulinate over dodecatungstophosphoric acid anchored to Al-MCM-41. J. Exp. Nanosci. 11, 1331–1347.

Xia, C., Liu, B.S., Guo, Y.H., 2014. LaxNiyOz/MAS-9 catalysts with high Ni 0 dispersion and hydrothermal stability for CH_4/CO_2 reforming. Ind. Eng. Chem. Res. 53, 2189–2196.

Xiao, F.S., 2005. Ordered mesoporous materials with improved stability and catalytic activity. Top. Catal. 35, 9–24.

Xiao, Y., Gao, L., Xiao, G., Lv, J., 2010. Kinetics of the transesterification reaction catalyzed by solid base in a fixed-bed reactor. Energy and Fuels 24, 5829–5833.

Xie, W., Li, H., 2006. Alumina-supported potassium iodide as a heterogeneous catalyst for biodiesel production from soybean oil. J. Mol. Catal. A Chem. 255, 1–9.

Xu, L., Wang, Y., Yang, X., Hu, J., Li, W., Guo, Y., 2009. Simultaneous esterification and transesterification of soybean oil with methanol catalyzed by mesoporous Ta_2O_5/SiO_2-$[H_3PW_{12}O_{40}/R]$ (R = Me or Ph) hybrid catalysts. Green Chem. 11, 314–317.

Xu, L., Wang, Y., Yang, X., Yu, X., Guo, Y., Clark, J.H., 2008. Preparation of mesoporous polyoxometalate-tantalum pentoxide composite catalyst and its application for biodiesel production by esterification and transesterification. Green Chem. 10, 746–755.

Xu, L., Yin, M.L., Liu, S., 2014. Agx@WO_3 core-shell nanostructure for LSP enhanced chemical sensors. Sci. Rep. 4, 6745.

Yadav, G.D., 2005. Synergism of clay and heteropoly acids as nano-catalysts for the development of green processes with potential industrial applications. Catal. Surv. from Asia 9, 117-137.

Yamazoe, S., Hitomi, Y., Shishido, T., Tanaka, T., 2008. XAFS study of tungsten L_1- and L_3-edges: structural analysis of WO_3 species loaded on TiO_2 as a catalyst for photo-oxidation of NH3. J. Phys. Chem. C 112, 6869–6879.

Yang, K.L., Huang, S., Pan, H., Zhang, H., Liu, X.F., Yang, S., 2017. Polyoxometalate-MgF_2 hybrids as heterogeneous solid acid catalysts for efficient biodiesel production. RSC Adv. 7, 33335–33343.

Yun, H.S., Kuwabara, M., Zhou, H.S., Honma, I., 2004. One-step synthesis of mesoporous PWA/SiO_2 composite materials using triblock copolymer templates. J. Mater. Sci. 39, 2341–2347.

Zabeti, M., Daud, W.M.A.W., Aroua, M.K., 2010. Biodiesel production using alumina-supported calcium oxide: An optimization study. Fuel Process. Technol. 91, 243–248.

Zabeti, M., Wan Daud, W.M.A., Aroua, M.K., 2009. Activity of solid catalysts for biodiesel production: A review. Fuel Process. Technol. 90, 770–777.

Zaera, F., 2014. New advances in the use of infrared absorption spectroscopy for the characterization of heterogeneous catalytic reactions. Chem. Soc. Rev. 43,7624-7663.

Zheng, X.C., Li, N., Wu, M., Guan, X.X., Zhang, X.L., 2017. Synthesis of biofuel via levulinic acid esterification over porous solid acid consisting of tungstophosphoric acid and reduced graphene oxide. Res. Chem. Intermed. 43, 6651–6664.

Zillillah, Ngu, T.A., Li, Z., 2014. Phosphotungstic acid-functionalized magnetic nanoparticles as an efficient and recyclable catalyst for the one-pot production of biodiesel from grease via esterification and transesterification. Green Chem. 16, 1202–1210.

APPENDIX A

Additional data

Table A.1. The fitting data for the W-L_3 XANES spectra using Athena Software

Catalysts	Area Peak 1	Area Peak 2	R-factor	Chi-square	Reduced chi square
HPW/MAS-9	15.96	10.23	0.0001287	0.01773	0.000341
H_2WO_4	19.894	12.875	0.0010871	0.14882	0.0015832
Na_2WO_4	4.78	7.124	0.0001974	0.01585	0.000283

Table A.2. The minimum and maximum limits of each factors used.

Factor	Unit	Minimum	Maximum
Catalyst weight	Weight %	1	10
Methanol : oil ratio		6:1	25:1
Time	Hour	4	10

Table A.3. Pearson correlation coefficient for the curve representing the species' concentrations for the fitted kinetic models.

Species	Goodness of fit (Pearson correlation r)								
	PH model			LHHW surface reaction			ER surface reaction		
	150°C	165°C	180°C	150°C	165°C	180°C	150°C	165°C	180°C
TG	0.95	0.97	0.98	0.94	0.97	0.98	0.91	0.95	0.96
DG	0.99	0.99	0.99	0.99	0.98	0.97	0.97	0.98	0.97
MG	0.93	0.78	0.7	0.95	0.87	0.74	0.92	0.86	0.72
ME	0.98	0.99	0.98	0.98	0.99	0.98	0.98	0.99	0.97

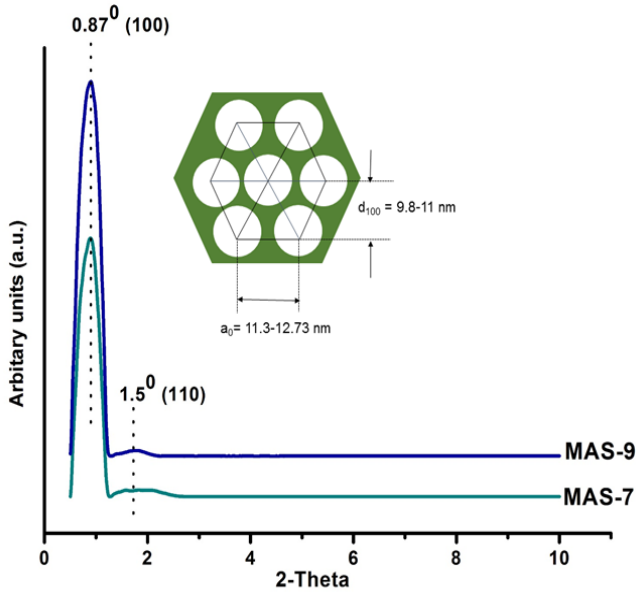

Figure A.1. Low angle XRD patterns for MAS-7 and MAS-9

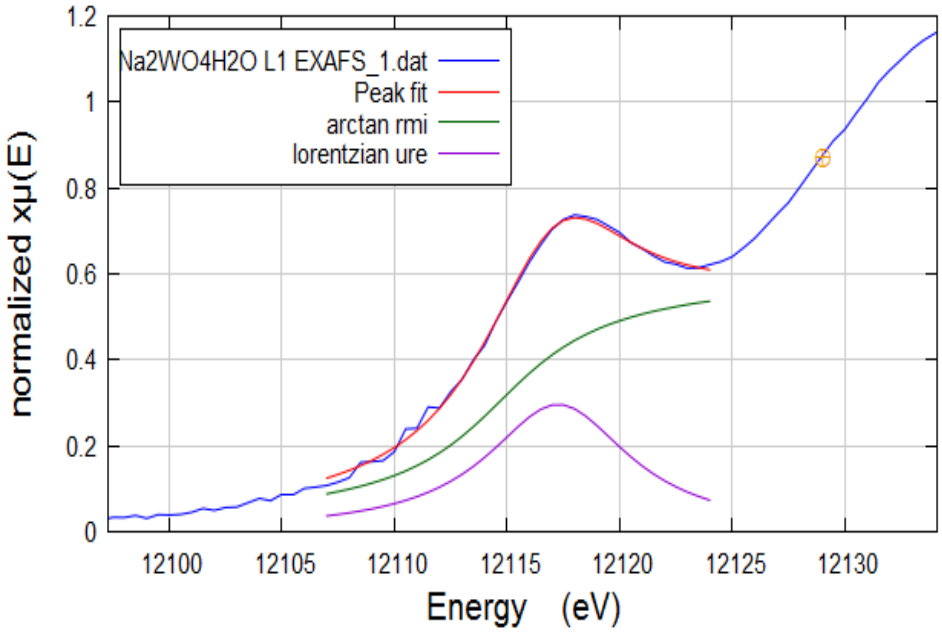

Figure A.2. Curve –fitted W L_1- edge XANES spectra of Na_2WO_4

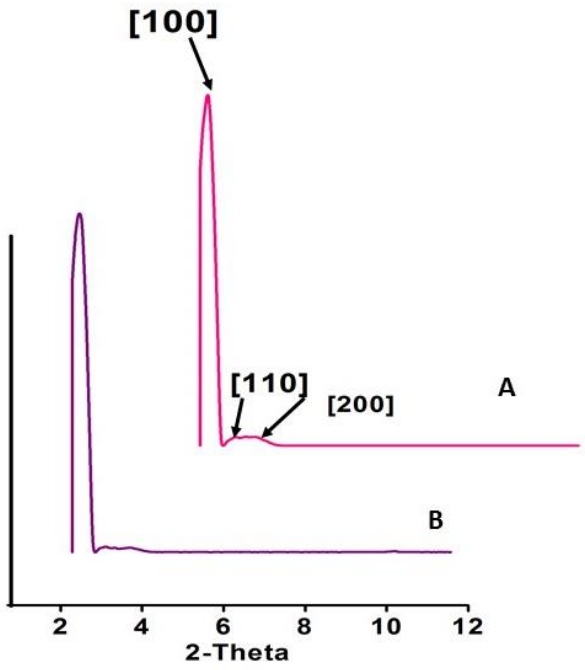

Figure A.3. Small angle XRD of composites A) HPW-MAS-7 2 500^0C, and B) HPW-MAS-7 1 500^0C.

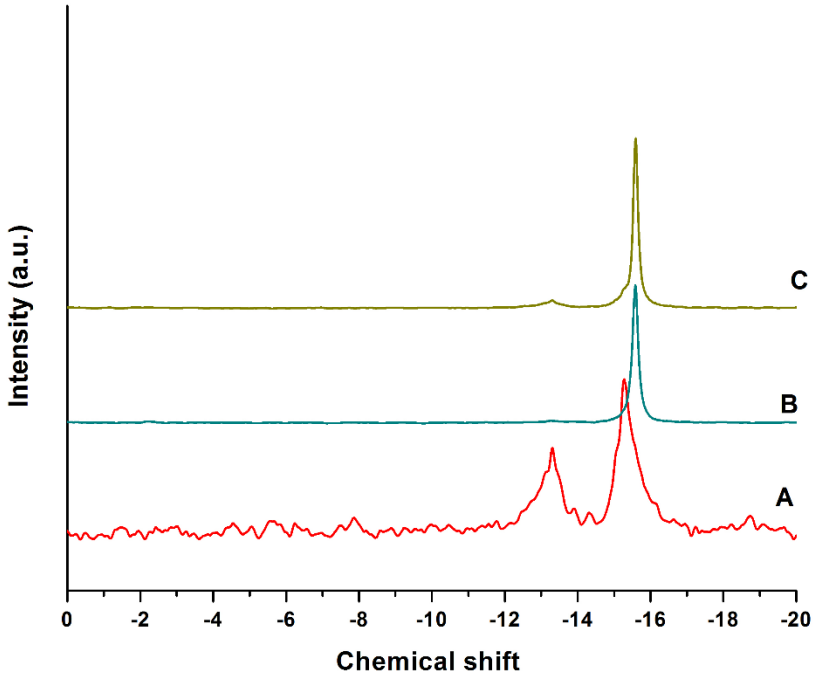

Figure A.4. ^{31}P NMR spectra of A) HPW-MAS-9 2 500°C composite, B) mechanical mixture of HPW + HPW-MAS-9 2 500°C (50/50 (w/w)) and, C) mechanical mixture of HPW + HPW-MAS-9 2 500°C (10/90 (w/w)).

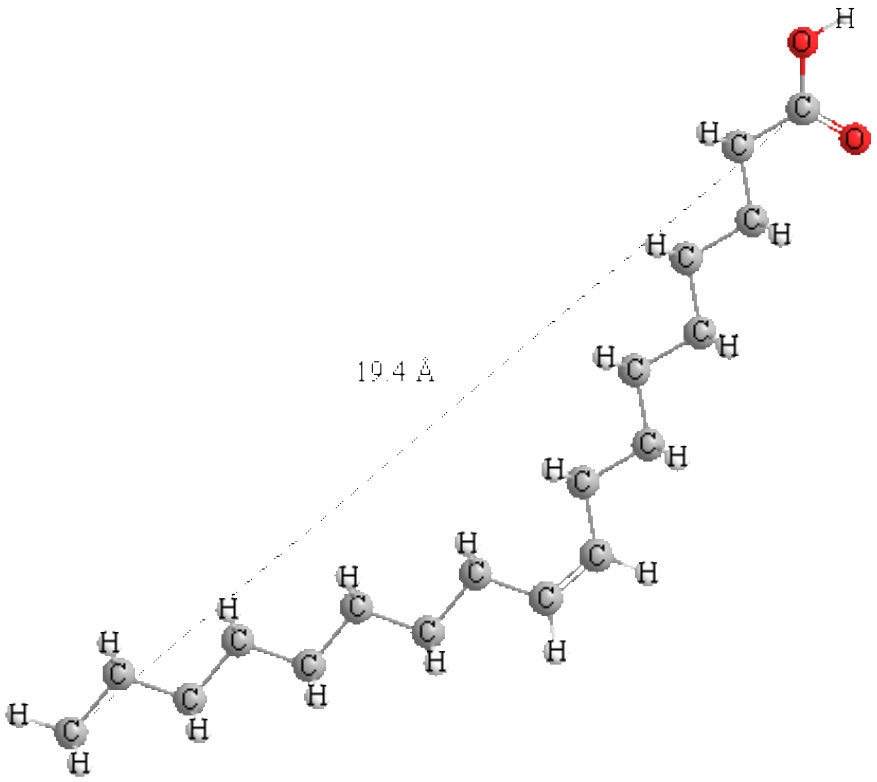

Figure A.5. Model of the Oleic acid (major fatty acid in green seed canola oil) and determination of the chain length (d_{oleic} = 1.94 nm)

The quadratic model equation (Multiple Regression equation) was derived using Response Surface DOE for determining the combinations of these three factors giving best ester yield. The model has R square (adjusted) value of 99.74%, meaning it is capable of explaining 99.74% of variations in the yield results. It also has R square value (for prediction) of 99.36%, meaning it is capable of explaining 99.36% of variations in the predicted yield. Regression equation in uncoded units

Yield (wt.%)=-2.75+3.21 catalyst+2.02 methanol :oil ratio +12.82 time-0.25 catalyst*catalyst-0.061methanol : oil ratio*methanol: oil ratio - 0.635 time*time -0.035 catalyst weight *methanol: oil ratio+ 0.049 catalyst weight*time + 0.045 methanol: oil ratio*time …….(A.1)

Main effects plot of yield (Figure S4) and Pareto chart (Figure S5) reveals that the model is affected largely by the time of reaction rather than the catalyst weight and molar ratio of alcohol and oil. Hence, increase in reaction time further can result in further increase in the yield at 6.09 g catalyst weight and 18.66:1 molar ratio of alcohol: oil.

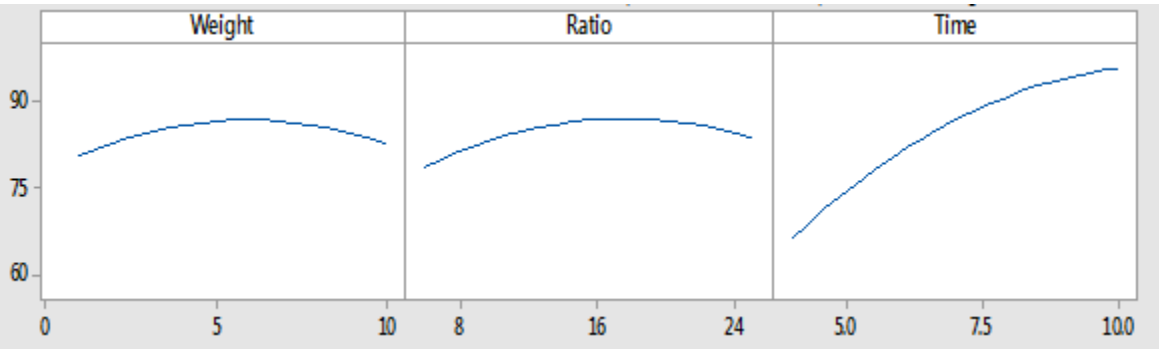

Figure A.6. The main effect plots for methyl ester yield.

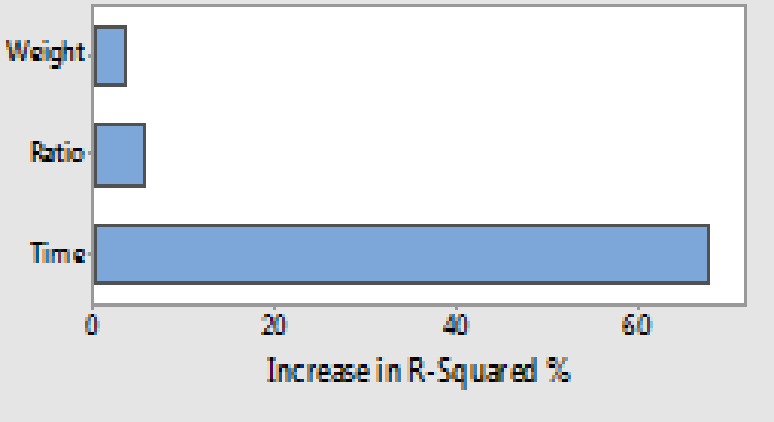

Figure A.7. Pareto chart

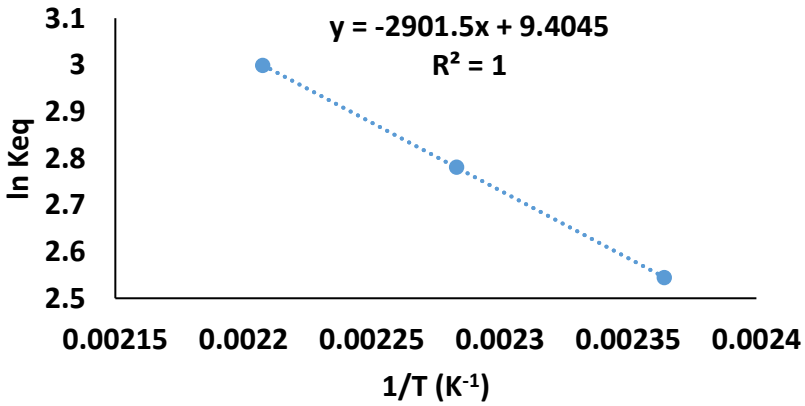

Figure A.8. Plot of ln $K_{eq.}$ $vs.$ $^{1}/_{T}$ (K^{-1})

APPENDIX B

Aspen plus simulation results for biodiesel plant

```
 + + +
```

TABLE OF CONTENTS

TABLE OF CONTENTS

RUN CONTROL SECTION

RUN CONTROL INFORMATION

THIS COPY OF ASPEN PLUS LICENSED TO UNIVERSITY OF SASKATCHEW

TYPE OF RUN: NEW

INPUT FILE NAME: _2952mgp.inm

OUTPUT PROBLEM DATA FILE NAME: _2952mgp
LOCATED IN:

PDF SIZE USED FOR INPUT TRANSLATION:
NUMBER OF FILE RECORDS (PSIZE) = 0
NUMBER OF IN-CORE RECORDS = 256
PSIZE NEEDED FOR SIMULATION = 256

CALLING PROGRAM NAME: apmain
LOCATED IN: C:\Program Files (x86)\AspenTech\Aspen Plus V10.0\Engine\\xeq

SIMULATION REQUESTED FOR ENTIRE FLOWSHEET

DESCRIPTION

General Simulation with Metric Units : C, bar, kg/hr, kmol/hr, Gcal/hr, cum/hr. Property Method: None Flow basis for input: Mole

FLOWSHEET SECTION

FLOWSHEET CONNECTIVITY BY STREAMS

STREAM	SOURCE	DEST	STREAM	SOURCE	DEST
METHANOL	----	M100	GSC	----	M102
HPW-MAS	----	M101	A1	M100	M101
A3	M102	P100	A4	P100	$H100H02
S3	R100	P1	A9	P1	S100
CATALYST	S100	----	A10	S100	P2
A11	P2	$H101HTR	A13	F100	H103
A15	F100	$H100HTR	A14	H103	P102
A17	D100	$H104H01	GLYCEROL	D100	----
A2	M101	M102	A19	C100	$H104HTR
A20	C100	----	A18	$H104H01	C100
FAME	$H104HTR	----	A8	H102	R100
A12	$H101HTR	F100	A6	$H101H02	P101
A7	P101	H102	A16	$H100HTR	D100
A5	$H100H02	$H101H02	RECYCLED	P102	M100
$H101Q02	$H101H02	$H101HTR	$H104Q01	$H104H01	$H104HTR
$H100Q02	$H100H02	$H100HTR			

FLOWSHEET CONNECTIVITY BY BLOCKS

BLOCK	INLETS	OUTLETS
M100	METHANOL RECYCLED	A1
M102	A2 GSC	A3
P100	A3	A4
R100	A8	S3
P1	S3	A9
S100	A9	CATALYST A10
P2	A10	A11
F100	A12	A13 A15
H103	A13	A14
D100	A16	A17 GLYCEROL
M101	HPW-MAS A1	A2
C100	A18	A19 A20
H102	A7	A8
P101	A6	A7
P102	A14	RECYCLED
$H101H02	A5	A6 $H101Q02
$H101HTR	A11 $H101Q02	A12
$H104H01	A17	A18 $H104Q01
$H104HTR	A19 $H104Q01	FAME
$H100H02	A4	A5 $H100Q02
$H100HTR	A15 $H100Q02	A16

FLOWSHEET SECTION

CONVERGENCE STATUS SUMMARY

DESIGN-SPEC SUMMARY

DESIGN SPEC	ERROR	TOLERANCE	ERR/TOL	VARIABLE	STAT	CONV BLOCK
DS-1	0.18932E-01	0.10000	0.18932	12.519	#	$OLVER04

TEAR STREAM SUMMARY

STREAM ID	VARIABLE ID	MAXIMUM ERR/TOL	MAX. ERR. RELATIVE	ABSOLUTE ERROR	STAT	CONV BLOCK
A1	METHA-01MOLEFLOW	0.93704	0.93704E-04	0.40390E-06	#	$OLVER01

\# = CONVERGED
* = NOT CONVERGED
LB = AT LOWER BOUNDS
UB = AT UPPER BOUNDS

DESIGN-SPEC: DS-1

SAMPLED VARIABLES:
METHANOL : METHA-01MOLEFLOW IN STREAM A1 SUBSTREAM MIXED

SPECIFICATION:
MAKE METHANOL APPROACH 15.5000
WITHIN 0.100000

MANIPULATED VARIABLES:
VARY : METHA-01MOLEFLOW IN STREAM RECYCLED SUBSTREAM MIXED
LOWER LIMIT = 12.5037 KMOL/HR
UPPER LIMIT = 12.5190 KMOL/HR
FINAL VALUE = 12.5189 KMOL/HR

VALUES OF ACCESSED FORTRAN VARIABLES:
VARIABLE VALUE AT START FINAL VALUE UNITS

```
                    OF LOOP
    --------      --------------      -----------     -----
    METHANOL        15.5189            15.5189        KMOL/HR

 CONVERGENCE BLOCK:  $OLVER01
 ----------------------------
    Tear Stream  :  A1
    Tolerance used:  0.100D-03
    Trace molefrac:  0.100D-05

    MAXIT =  100 WAIT =   2

 ASPEN PLUS   PLAT: WINDOWS   VER: 36.0                    04/25/2019  PAGE
4

                              FLOWSHEET SECTION

 CONVERGENCE BLOCK:  $OLVER01 (CONTINUED)
    METHOD: BROYDEN       STATUS: CONVERGED
    TOTAL NUMBER OF ITERATIONS:    10
    NUMBER OF ITERATIONS ON LAST OUTER LOOP:     3

                          *** FINAL VALUES ***

VAR#  TEAR STREAM VAR  STREAM   SUBSTREA COMPONEN ATTRIBUT ELEMENT
UNIT         VALUE       PREV VALUE       ERR/TOL
----  ---------------  -------- -------- -------- -------- -------- ------
----- ------------   ------------   ------------
   1  TOTAL MOLEFLOW   A1       MIXED
KMOL/HR        15.6486        15.6472         0.9278
   2  MOLE-FLOW        A1       MIXED    TRIOL-01
KMOL/HR      2.5039-15      2.5039-15         0.1430
   3  MOLE-FLOW        A1       MIXED    METHA-01
KMOL/HR        15.5189        15.5175         0.9370
   4  MOLE-FLOW        A1       MIXED    METHY-01
KMOL/HR      8.0900-04      8.0899-04      5.4403-02
   5  MOLE-FLOW        A1       MIXED    GLYCE-01
KMOL/HR         0.1289         0.1289        -0.1740
   6  MOLE-FLOW        A1       MIXED    HPW-MAS
KMOL/HR         0.0            0.0             0.0
   7  PRESSURE         A1       MIXED                                    BAR
1.0000         1.0000         0.0
   8  MASS ENTHALPY    A1       MIXED
KCAL/KG     -1775.6108     -1775.6106     -9.3074-04

                          *** ITERATION HISTORY ***

    TEAR STREAMS AND TEAR VARIABLES:

    ITERATION   MAX-ERR/TOL VAR#  STREAM ID      VARIABLE
SUBSTREA COMPONEN ATTRIBUT ELEMENT
    ---------   ----------- ----  ---------      ---------------- -------
- -------- -------- -------
```

```
          1       1.282         5  A1             MOLE-FLOW        MIXED
GLYCE-01
          2      -1.006         5  A1             MOLE-FLOW        MIXED
GLYCE-01
          3      0.9370         3  A1             MOLE-FLOW        MIXED
METHA-01

 CONVERGENCE BLOCK:  $OLVER04
 ----------------------------
     SPECS: DS-1
     MAXIT=   30 STEP-SIZE=   0.10000E-03% OF RANGE
                 MAX-STEP=       100.    % OF RANGE
                 XTOL=       1.000000E-08
     THE NEW ALGORITHM WAS USED WITH BRACKETING=NO
     METHOD: SECANT        STATUS: CONVERGED
     TOTAL NUMBER OF ITERATIONS:     7
     NUMBER OF ITERATIONS ON LAST OUTER LOOP:     1

                          *** FINAL VALUES ***


VAR#  MANIPUL/TEAR-VAR VARIABLE DESCRIPTION
UNIT         VALUE       PREV VALUE       ERR/TOL                        ------
----- ------------   ------------   ------------
   1  METHA-01MOLEFLOW RECYCLED.MIXED.METHA-01MOLEFLOW
KMOL/HR        12.5189        12.5189         0.1893

                          *** ITERATION HISTORY ***
```

FLOWSHEET SECTION

CONVERGENCE BLOCK: $OLVER04 (CONTINUED)

DESIGN-SPEC ID: DS-1
ITERATED: METHA-01MOLEFLOW IN STREAM RECYCLED SUBSTREAM MIXED

ITERATION	VARIABLE	ERROR	ERR/TOL
1	12.52	0.1893E-01	0.1893

COMPUTATIONAL SEQUENCE

SEQUENCE USED WAS:
$OLVER01 M101 M102 P100 $H100H02 $H101H02 P101 H102 R100 P1 S100 P2
| $H101HTR F100 H103 P102
| $OLVER04 M100
| (RETURN $OLVER04)
(RETURN $OLVER01)
$H100HTR D100 $H104H01 C100 $H104HTR

OVERALL FLOWSHEET BALANCE

*** MASS AND ENERGY BALANCE ***

	IN	OUT	GENERATION	RELATIVE DIFF.
CONVENTIONAL COMPONENTS (KMOL/HR)				
TRIOL-01	1.00000	0.500000E-01	-0.950000	-0.403079E-08
METHA-01	3.00000	0.148546	-2.85000	0.484689E-03
METHY-01	0.00000	2.85000	2.85000	-0.790713E-07
GLYCE-01	0.00000	0.950002	0.950000	-0.213694E-05
HPW-MAS	0.188740	0.188740	0.00000	0.00000
TOTAL BALANCE				
MOLE(KMOL/HR)	4.18874	4.18729	0.195156E-15	0.346598E-03
MASS(KG/HR)	1030.27	1030.22		0.449727E-04
ENTHALPY(GCAL/HR)	-0.676618	-0.685524		0.129911E-01

*** CO2 EQUIVALENT SUMMARY ***

FEED STREAMS CO2E	0.00000	KG/HR
PRODUCT STREAMS CO2E	0.00000	KG/HR

NET STREAMS CO2E PRODUCTION	0.00000	KG/HR
UTILITIES CO2E PRODUCTION	0.00000	KG/HR
TOTAL CO2E PRODUCTION	0.00000	KG/HR

PHYSICAL PROPERTIES SECTION

COMPONENTS

ID	TYPE	ALIAS	NAME
TRIOL-01	C	C57H104O6	TRIOLEIN
METHA-01	C	CH4O	METHANOL
METHY-01	C	C19H36O2	METHYL-OLEATE
GLYCE-01	C	C3H8O3	GLYCEROL
HPW-MAS	C	H2O	WATER

U-O-S BLOCK SECTION

BLOCK: H100 MODEL: MHEATX

HOT SIDE:	INLET STREAM	OUTLET STREAM
	A15	A16
COLD SIDE:	INLET STREAM	OUTLET STREAM
	A4	A5

PROPERTIES FOR STREAM A4
PROPERTY OPTION SET: UNIF-DMD DORTMUND MOD. UNIFAC / REDLICH-KWONG-SOAVE

PROPERTIES FOR STREAM A15
PROPERTY OPTION SET: UNIF-DMD DORTMUND MOD. UNIFAC / REDLICH-KWONG-SOAVE

*** MASS AND ENERGY BALANCE ***

	IN	OUT	RELATIVE DIFF.
TOTAL BALANCE			
MOLE(KMOL/HR)	20.8345	20.8345	0.00000
MASS(KG/HR)	2425.00	2425.00	0.00000
ENTHALPY(GCAL/HR)	-2.05303	-2.05303	0.00000

*** CO2 EQUIVALENT SUMMARY ***

FEED STREAMS CO2E	0.00000	KG/HR
PRODUCT STREAMS CO2E	0.00000	KG/HR
NET STREAMS CO2E PRODUCTION	0.00000	KG/HR
UTILITIES CO2E PRODUCTION	0.00000	KG/HR
TOTAL CO2E PRODUCTION	0.00000	KG/HR

*** INPUT DATA ***

SPECIFICATIONS FOR STREAM A4 :

ONE PHASE TP FLASH	SPECIFIED PHASE IS	LIQUID
SPECIFIED TEMPERATURE	C	60.0000
PRESSURE DROP	BAR	0.0
MAXIMUM NO. ITERATIONS		30
CONVERGENCE TOLERANCE		0.000100000

U-O-S BLOCK SECTION

BLOCK: H100 MODEL: MHEATX (CONTINUED)

SPECIFICATIONS FOR STREAM A15 :
ONE PHASE FLASH SPECIFIED PHASE IS LIQUID
PRESSURE DROP BAR 0.0
MAXIMUM NO. ITERATIONS 30
CONVERGENCE TOLERANCE 0.000100000

*** RESULTS ***

INLET STREAM	DUTY GCAL/HR	OUTLET TEMPERATURE C	OUTLET PRESSURE BAR	OUTLET VAPOR FRAC
A4	0.26519E-01	60.00	20.000	0.0000
A15	-0.26519E-01	35.69	0.10000	0.0000

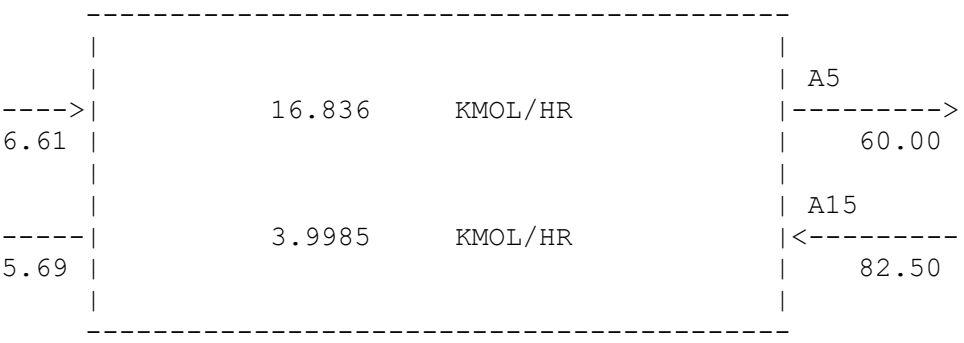

BLOCK: H101 MODEL: MHEATX

	INLET STREAM	OUTLET STREAM
HOT SIDE:	A11	A12
COLD SIDE:	A5	A6

PROPERTIES FOR STREAM A5
PROPERTY OPTION SET: UNIF-DMD DORTMUND MOD. UNIFAC / REDLICH-KWONG-SOAVE

PROPERTIES FOR STREAM A11

U-O-S BLOCK SECTION

BLOCK: H101 MODEL: MHEATX (CONTINUED)

*** MASS AND ENERGY BALANCE ***

	IN	OUT	RELATIVE DIFF.
TOTAL BALANCE			
MOLE(KMOL/HR)	33.4831	33.4831	0.00000
MASS(KG/HR)	2838.24	2838.24	0.00000
ENTHALPY(GCAL/HR)	-2.63318	-2.63318	0.168652E-15

*** CO2 EQUIVALENT SUMMARY ***

FEED STREAMS CO2E	0.00000	KG/HR
PRODUCT STREAMS CO2E	0.00000	KG/HR
NET STREAMS CO2E PRODUCTION	0.00000	KG/HR
UTILITIES CO2E PRODUCTION	0.00000	KG/HR
TOTAL CO2E PRODUCTION	0.00000	KG/HR

*** INPUT DATA ***

SPECIFICATIONS FOR STREAM A5 :
ONE PHASE TP FLASH SPECIFIED PHASE IS LIQUID

SPECIFIED TEMPERATURE	C	100.000
PRESSURE DROP	BAR	0.0
MAXIMUM NO. ITERATIONS		30
CONVERGENCE TOLERANCE		0.000100000

SPECIFICATIONS FOR STREAM A11 :
TWO PHASE FLASH

PRESSURE DROP	BAR	0.0
MAXIMUM NO. ITERATIONS		30
CONVERGENCE TOLERANCE		0.000100000

*** RESULTS ***

INLET STREAM	DUTY GCAL/HR	OUTLET TEMPERATURE C	OUTLET PRESSURE BAR	OUTLET VAPOR FRAC
A5	0.36193E-01	100.00	20.000	0.0000

U-O-S BLOCK SECTION

BLOCK: H101 MODEL: MHEATX (CONTINUED)

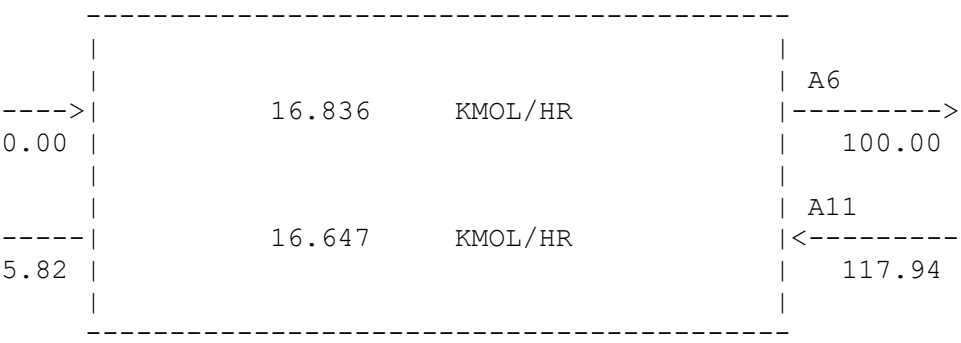

BLOCK: H104 MODEL: MHEATX

HOT SIDE:	INLET STREAM	OUTLET STREAM
	A19	FAME
COLD SIDE:	INLET STREAM	OUTLET STREAM
	A17	A18

PROPERTIES FOR STREAM A17
PROPERTY OPTION SET: UNIF-DMD DORTMUND MOD. UNIFAC / REDLICH-KWONG-SOAVE

PROPERTIES FOR STREAM A19
PROPERTY OPTION SET: UNIF-DMD DORTMUND MOD. UNIFAC / REDLICH-KWONG-SOAVE

*** MASS AND ENERGY BALANCE ***

	IN	OUT	RELATIVE DIFF.
TOTAL BALANCE			
MOLE(KMOL/HR)	5.78815	5.78815	0.00000
MASS(KG/HR)	1725.48	1725.48	0.00000
ENTHALPY(GCAL/HR)	-0.936771	-0.936771	0.237032E-15

U-O-S BLOCK SECTION

BLOCK: H104 MODEL: MHEATX (CONTINUED)

*** CO2 EQUIVALENT SUMMARY ***

FEED STREAMS CO2E	0.00000	KG/HR
PRODUCT STREAMS CO2E	0.00000	KG/HR
NET STREAMS CO2E PRODUCTION	0.00000	KG/HR
UTILITIES CO2E PRODUCTION	0.00000	KG/HR
TOTAL CO2E PRODUCTION	0.00000	KG/HR

*** INPUT DATA ***

SPECIFICATIONS FOR STREAM A17 :

ONE PHASE TP FLASH SPECIFIED PHASE IS	LIQUID	
SPECIFIED TEMPERATURE	C	190.000
SPECIFIED PRESSURE	BAR	1.00000
MAXIMUM NO. ITERATIONS		30
CONVERGENCE TOLERANCE		0.000100000

SPECIFICATIONS FOR STREAM A19 :

ONE PHASE FLASH SPECIFIED PHASE IS	LIQUID	
PRESSURE DROP	BAR	0.0
MAXIMUM NO. ITERATIONS		30
CONVERGENCE TOLERANCE		0.000100000

*** RESULTS ***

INLET STREAM	DUTY GCAL/HR	OUTLET TEMPERATURE C	OUTLET PRESSURE BAR	OUTLET VAPOR FRAC
A17	0.80070E-01	190.00	1.0000	0.0000
A19	-0.80070E-01	29.04	0.50000	0.0000

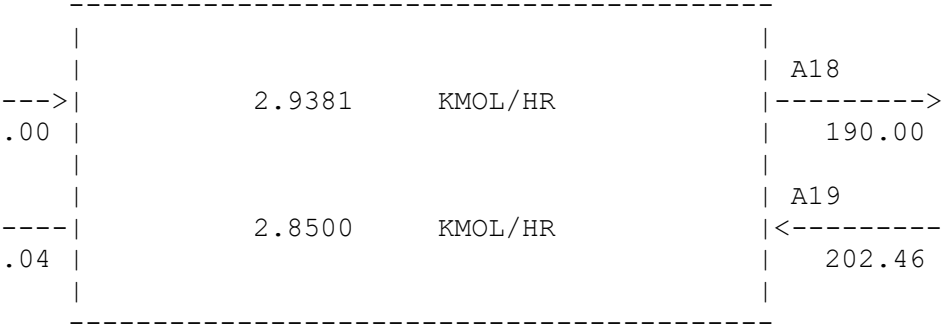

U-O-S BLOCK SECTION

BLOCK: C100 MODEL: RADFRAC

INLETS - A18 STAGE 2
OUTLETS - A19 STAGE 1
A20 STAGE 7
PROPERTY OPTION SET: UNIF-DMD DORTMUND MOD. UNIFAC / REDLICH-KWONG-SOAVE

*** MASS AND ENERGY BALANCE ***

	IN	OUT	RELATIVE DIFF.
TOTAL BALANCE			
MOLE(KMOL/HR)	2.93815	2.93815	0.00000
MASS(KG/HR)	890.530	890.530	-0.127662E-15
ENTHALPY(GCAL/HR)	-0.444851	-0.435259	-0.215607E-01

*** CO2 EQUIVALENT SUMMARY ***

FEED STREAMS CO2E	0.00000	KG/HR
PRODUCT STREAMS CO2E	0.00000	KG/HR
NET STREAMS CO2E PRODUCTION	0.00000	KG/HR
UTILITIES CO2E PRODUCTION	0.00000	KG/HR
TOTAL CO2E PRODUCTION	0.00000	KG/HR

****
**** INPUT DATA ****
****

**** INPUT PARAMETERS ****

NUMBER OF STAGES	7
ALGORITHM OPTION	STANDARD
ABSORBER OPTION	NO
INITIALIZATION OPTION	STANDARD
HYDRAULIC PARAMETER CALCULATIONS	NO
INSIDE LOOP CONVERGENCE METHOD	BROYDEN
DESIGN SPECIFICATION METHOD	NESTED
MAXIMUM NO. OF OUTSIDE LOOP ITERATIONS	25
MAXIMUM NO. OF INSIDE LOOP ITERATIONS	10
MAXIMUM NUMBER OF FLASH ITERATIONS	30
FLASH TOLERANCE	0.000100000
OUTSIDE LOOP CONVERGENCE TOLERANCE	0.000100000

U-O-S BLOCK SECTION

BLOCK: C100 MODEL: RADFRAC (CONTINUED)

**** COL-SPECS ****

MOLAR VAPOR DIST / TOTAL DIST		0.0
MOLAR REFLUX RATIO		3.00000
MOLAR DISTILLATE RATE	KMOL/HR	2.85000

**** PROFILES ****

P-SPEC	STAGE	1	PRES, BAR	0.50000
		2		0.100000

****
**** RESULTS ****
****

*** COMPONENT SPLIT FRACTIONS ***

	OUTLET STREAMS	
	A19	A20
COMPONENT:		
TRIOL-01	.23118E-05	1.0000
METHA-01	1.0000	0.0000
METHY-01	.98662	.13385E-01
GLYCE-01	.99960	.40246E-03

*** SUMMARY OF KEY RESULTS ***

TOP STAGE TEMPERATURE	C	202.457
BOTTOM STAGE TEMPERATURE	C	289.215
TOP STAGE LIQUID FLOW	KMOL/HR	8.55000
BOTTOM STAGE LIQUID FLOW	KMOL/HR	0.088146
TOP STAGE VAPOR FLOW	KMOL/HR	0.0
BOILUP VAPOR FLOW	KMOL/HR	13.9774
MOLAR REFLUX RATIO		3.00000
MOLAR BOILUP RATIO		158.570
CONDENSER DUTY (W/O SUBCOOL)	GCAL/HR	-0.31587
REBOILER DUTY	GCAL/HR	0.32546

**** MAXIMUM FINAL RELATIVE ERRORS ****

DEW POINT	0.75898E-04	STAGE= 7	
BUBBLE POINT	0.30884E-04	STAGE= 1	
COMPONENT MASS BALANCE	0.41914E-07	STAGE= 6	COMP=TRIOL-01
ENERGY BALANCE	0.52391E-05	STAGE= 1	

U-O-S BLOCK SECTION

BLOCK: C100 MODEL: RADFRAC (CONTINUED)

**** PROFILES ****

NOTE REPORTED VALUES FOR STAGE LIQUID AND VAPOR RATES ARE THE FLOWS FROM THE STAGE INCLUDING ANY SIDE PRODUCT.

STAGE	TEMPERATURE C	PRESSURE BAR	ENTHALPY KCAL/MOL LIQUID	ENTHALPY KCAL/MOL VAPOR	HEAT DUTY GCAL/HR
1	202.46	0.50000	-144.51	-47.951	-0.3158
2	257.25	0.10000	-136.34	-116.98	
3	257.59	0.10000	-136.27	-117.70	
4	257.59	0.10000	-136.27	-117.70	
5	257.59	0.10000	-136.27	-117.70	
6	257.62	0.10000	-136.49	-117.70	
7	289.22	0.10000	-265.57	-112.40	0.3254

STAGE	FLOW RATE KMOL/HR LIQUID	FLOW RATE KMOL/HR VAPOR	FEED RATE KMOL/HR LIQUID	FEED RATE KMOL/HR VAPOR	FEED RATE KMOL/HR MIXED	PRODUCT RATE KMOL/HR LIQUID	PRODUCT RATE KMOL/HR VAPOR
1	11.40	0.000		.31838-01		2.8500	
2	18.16	11.37	2.9063				
3	18.23	18.07					
4	18.23	18.14					
5	18.22	18.14					
6	14.07	18.13					
7	0.8815E-01	13.98				.88146-01	

**** MASS FLOW PROFILES ****

STAGE	FLOW RATE KG/HR LIQUID	FLOW RATE KG/HR VAPOR	FEED RATE KG/HR LIQUID	FEED RATE KG/HR VAPOR	FEED RATE KG/HR MIXED	PRODUCT RATE KG/HR LIQUID	PRODUCT RATE KG/HR VAPOR
1	3340.	0.000		1.6199		834.9471	
2	5414.	3338.	888.9097				
3	5433.	5359.					
4	5433.	5378.					
5	5432.	5378.					
6	4201.	5376.					
7	55.58	4145.				55.5824	

U-O-S BLOCK SECTION

BLOCK: C100 MODEL: RADFRAC (CONTINUED)

**** MOLE-X-PROFILE ****

STAGE	TRIOL-01	METHA-01	METHY-01	GLYCE-01
1	0.40558E-07	0.13218E-01	0.98661	0.16717E-03
2	0.27529E-02	0.27887E-04	0.99715	0.67747E-04
3	0.27433E-02	0.73368E-07	0.99723	0.27904E-04
4	0.27434E-02	0.19302E-09	0.99725	0.11491E-04
5	0.27441E-02	0.50780E-12	0.99725	0.47298E-05
6	0.36478E-02	0.13373E-14	0.99635	0.19475E-05
7	0.56724	0.57730E-17	0.43276	0.21762E-05

**** MOLE-Y-PROFILE ****

STAGE	TRIOL-01	METHA-01	METHY-01	GLYCE-01
1	0.12723E-14	0.97400	0.25870E-01	0.12626E-03
2	0.40669E-07	0.10655E-01	0.98918	0.16598E-03
3	0.41540E-07	0.28023E-04	0.99990	0.68066E-04
4	0.41547E-07	0.73724E-07	0.99997	0.28029E-04
5	0.41559E-07	0.19396E-09	0.99999	0.11537E-04
6	0.55407E-07	0.51027E-12	1.0000	0.47422E-05
7	0.93638E-04	0.13457E-14	0.99990	0.19461E-05

**** K-VALUES ****

STAGE	TRIOL-01	METHA-01	METHY-01	GLYCE-01
1	0.31374E-07	73.684	0.26221E-01	0.75528
2	0.14774E-04	382.09	0.99201	2.4499
3	0.15143E-04	381.95	1.0027	2.4393
4	0.15145E-04	381.95	1.0027	2.4391
5	0.15145E-04	381.95	1.0027	2.4391
6	0.15189E-04	381.56	1.0037	2.4350
7	0.16510E-03	233.09	2.3106	0.89420

**** MASS-X-PROFILE ****

STAGE	TRIOL-01	METHA-01	METHY-01	GLYCE-01
1	0.12258E-06	0.14457E-02	0.99850	0.52550E-04
2	0.81771E-02	0.29976E-05	0.99180	0.20930E-04
3	0.81484E-02	0.78861E-08	0.99184	0.86205E-05
4	0.81484E-02	0.20747E-10	0.99185	0.35500E-05
5	0.81506E-02	0.54581E-13	0.99185	0.14612E-05
6	0.10816E-01	0.14349E-15	0.98918	0.60058E-06
7	0.79652	0.29335E-18	0.20348	0.31783E-06

**** MASS-Y-PROFILE ****

STAGE	TRIOL-01	METHA-01	METHY-01	GLYCE-01
1	0.28967E-13	0.80248	0.19722	0.29900E-03
2	0.12263E-06	0.11627E-02	0.99879	0.52056E-04
3	0.12406E-06	0.30287E-05	0.99998	0.21144E-04
4	0.12408E-06	0.79676E-08	0.99999	0.87063E-05
5	0.12411E-06	0.20961E-10	1.0000	0.35834E-05

6	0.16547E-06	0.55145E-13	1.0000	0.14730E-05
7	0.27959E-03	0.14541E-15	0.99972	0.60437E-06

U-O-S BLOCK SECTION

BLOCK: C100 MODEL: RADFRAC (CONTINUED)

****
***** HYDRAULIC PARAMETERS *****
****

*** DEFINITIONS ***

MARANGONI INDEX = SIGMA - SIGMATO
FLOW PARAM = (ML/MV)*SQRT(RHOV/RHOL)
QR = QV*SQRT(RHOV/(RHOL-RHOV))
F FACTOR = QV*SQRT(RHOV)
WHERE:
SIGMA IS THE SURFACE TENSION OF LIQUID FROM THE STAGE
SIGMATO IS THE SURFACE TENSION OF LIQUID TO THE STAGE
ML IS THE MASS FLOW OF LIQUID FROM THE STAGE
MV IS THE MASS FLOW OF VAPOR TO THE STAGE
RHOL IS THE MASS DENSITY OF LIQUID FROM THE STAGE
RHOV IS THE MASS DENSITY OF VAPOR TO THE STAGE
QV IS THE VOLUMETRIC FLOW RATE OF VAPOR TO THE STAGE

	TEMPERATURE C	
STAGE	LIQUID FROM	VAPOR TO
1	202.46	258.25
2	257.25	257.59
3	257.59	257.59
4	257.59	257.59
5	257.59	257.62
6	257.62	289.22
7	289.22	289.22

	MASS FLOW KG/HR		VOLUME FLOW CUM/HR		MOLECULAR WEIGHT	
STAGE	LIQUID FROM	VAPOR TO	LIQUID FROM	VAPOR TO	LIQUID FROM	VAPOR TO
1	3339.8	3339.8	4.5046	949.73	292.96	292.96
2	5414.2	5358.7	7.8689	7886.1	298.09	296.47
3	5433.3	5377.7	7.8996	7913.8	298.10	296.49
4	5433.3	5377.7	7.8996	7913.7	298.11	296.49
5	5431.9	5376.3	7.8976	7912.0	298.11	296.49
6	4200.6	4145.0	6.1301	6475.3	298.64	296.55

7	55.582	0.0000	0.11005	0.0000	630.57

	DENSITY KG/CUM		VISCOSITY CP		SURFACE TENSION DYNE/CM
STAGE	LIQUID FROM	VAPOR TO	LIQUID FROM	VAPOR TO	LIQUID FROM
1	741.42	3.5166	0.43365	0.71616E-02	17.046
2	688.06	0.67951	0.28553	0.70535E-02	13.232
3	687.80	0.67954	0.28485	0.70533E-02	13.208
4	687.80	0.67955	0.28484	0.70532E-02	13.207
5	687.80	0.67952	0.28484	0.70536E-02	13.207

U-O-S BLOCK SECTION

BLOCK: C100 MODEL: RADFRAC (CONTINUED)

	DENSITY KG/CUM		VISCOSITY CP		SURFACE TENSION DYNE/CM
STAGE	LIQUID FROM	VAPOR TO	LIQUID FROM	VAPOR TO	LIQUID FROM
6	685.23	0.64012	0.28496	0.74373E-02	13.204
7	505.08		0.31702		10.890

STAGE	MARANGONI INDEX DYNE/CM	FLOW PARAM	QR CUM/HR	REDUCED F-FACTOR (GM-L)**.5/MIN
1		0.68870E-01	65.563	29683.
2	-4.0899	0.31752E-01	247.95	0.10834E+06
3	-.24160E-01	0.31757E-01	248.87	0.10873E+06
4	-.47632E-03	0.31757E-01	248.87	0.10873E+06
5	-.19202E-03	0.31757E-01	248.81	0.10870E+06
6	-.25405E-02	0.30974E-01	198.00	86346.
7	-2.3141		0.0000	0.0000

****
***** TRAY SIZING CALCULATIONS *****
****

****
*** SECTION 1 ***
****

STARTING STAGE NUMBER		2
ENDING STAGE NUMBER		6
FLOODING CALCULATION METHOD		GLITSCH6

DESIGN PARAMETERS

PEAK CAPACITY FACTOR		1.00000
SYSTEM FOAMING FACTOR		1.00000
FLOODING FACTOR		0.80000
MINIMUM COLUMN DIAMETER	METER	0.30480
MINIMUM DC AREA/COLUMN AREA		0.100000
HOLE AREA/ACTIVE AREA		0.100000

TRAY SPECIFICATIONS

TRAY TYPE	SIEVE
NUMBER OF PASSES	1

TRAY SPACING	METER	0.60960

U-O-S BLOCK SECTION

BLOCK: C100 MODEL: RADFRAC (CONTINUED)

***** SIZING RESULTS @ STAGE WITH MAXIMUM DIAMETER *****

STAGE WITH MAXIMUM DIAMETER		4
COLUMN DIAMETER	METER	1.50000
DC AREA/COLUMN AREA		0.029012
DOWNCOMER VELOCITY	M/SEC	0.042800
FLOW PATH LENGTH	METER	1.29820
SIDE DOWNCOMER WIDTH	METER	0.10090
SIDE WEIR LENGTH	METER	0.75145
CENTER DOWNCOMER WIDTH	METER	0.0
CENTER WEIR LENGTH	METER	MISSING
OFF-CENTER DOWNCOMER WIDTH	METER	0.0
OFF-CENTER SHORT WEIR LENGTH	METER	MISSING
OFF-CENTER LONG WEIR LENGTH	METER	MISSING
TRAY CENTER TO OCDC CENTER	METER	0.0

**** SIZING PROFILES ****

STAGE	DIAMETER METER	TOTAL AREA SQM	ACTIVE AREA SQM	SIDE DC AREA SQM
2	1.5000	1.7671	1.6646	0.51269E-01
3	1.5000	1.7671	1.6646	0.51269E-01
4	1.5000	1.7671	1.6646	0.51269E-01
5	1.5000	1.7671	1.6646	0.51269E-01
6	1.5000	1.7671	1.6646	0.51269E-01

**** ADDITIONAL SIZING PROFILES ****

STAGE	FLOODING FACTOR	PRES. DROP BAR	DC BACKUP METER	DC BACKUP/ (TSPC+WHT)
2	36.91	0.3603E-02	0.1443	21.86
3	37.05	0.3607E-02	0.1444	21.86
4	37.05	0.3607E-02	0.1444	21.86
5	37.04	0.3606E-02	0.1444	21.86
6	29.73	0.3365E-02	0.1425	21.57

STAGE	HEIGHT OVER WEIR METER	DC REL FROTH DENS	TR LIQ REL FROTH DENS	FRA APPR TO SYS LIMIT
2	0.3267E-01	0.6050	0.3256	24.81
3	0.3283E-01	0.6049	0.3248	24.92
4	0.3283E-01	0.6049	0.3248	24.92
5	0.3282E-01	0.6049	0.3248	24.91
6	0.2400E-01	0.6048	0.3786	19.78

BLOCK: D100 MODEL: DECANTER

INLET STREAM: A16
FIRST LIQUID OUTLET: A17
SECOND LIQUID OUTLET: GLYCEROL
PROPERTY OPTION SET: UNIF-DMD DORTMUND MOD. UNIFAC / REDLICH-KWONG-SOAVE

U-O-S BLOCK SECTION

BLOCK: D100 MODEL: DECANTER (CONTINUED)

*** MASS AND ENERGY BALANCE ***

	IN	OUT	RELATIVE DIFF.
TOTAL BALANCE			
MOLE(KMOL/HR)	3.99855	3.99855	0.00000
MASS(KG/HR)	981.529	981.529	-0.524328E-07
ENTHALPY(GCAL/HR)	-0.674169	-0.682636	0.124041E-01

*** CO2 EQUIVALENT SUMMARY ***

FEED STREAMS CO2E	0.00000	KG/HR
PRODUCT STREAMS CO2E	0.00000	KG/HR
NET STREAMS CO2E PRODUCTION	0.00000	KG/HR
UTILITIES CO2E PRODUCTION	0.00000	KG/HR
TOTAL CO2E PRODUCTION	0.00000	KG/HR

*** INPUT DATA ***

LIQUID-LIQUID SPLIT, TP SPECIFICATION		
SPECIFIED TEMPERATURE	C	25.0000
SPECIFIED PRESSURE	BAR	1.00000
CONVERGENCE TOLERANCE ON EQUILIBRIUM		0.10000E-03
MAXIMUM NO ITERATIONS ON EQUILIBRIUM		30
EQUILIBRIUM METHOD		EQUATION-SOLVING
KLL COEFFICIENTS FROM		OPTION SET OR EOS
KLL BASIS		MOLE
KEY COMPONENT(S):	GLYCE-01	

*** RESULTS ***

OUTLET TEMPERATURE	C	25.000
OUTLET PRESSURE	BAR	1.0000
CALCULATED HEAT DUTY	GCAL/HR	-0.84675E-02
MOLAR RATIO 1ST LIQUID / TOTAL LIQUID		0.73480

L1-L2 PHASE EQUILIBRIUM :

COMP	F	X1	X2	K
TRIOL-01	0.012505	0.017018	0.198984-16	0.116929-14
METHA-01	0.037150	0.012822	0.10456	8.15478
METHY-01	0.71276	0.97000	0.250303-05	0.258044-05
GLYCE-01	0.23759	0.00016222	0.89544	5,519.97

U-O-S BLOCK SECTION

BLOCK: F100 MODEL: FLASH2

INLET STREAM: A12
OUTLET VAPOR STREAM: A13
OUTLET LIQUID STREAM: A15
PROPERTY OPTION SET: UNIF-DMD DORTMUND MOD. UNIFAC / REDLICH-KWONG-SOAVE

*** MASS AND ENERGY BALANCE ***

	IN	OUT	RELATIVE DIFF.
TOTAL BALANCE			
MOLE(KMOL/HR)	16.6472	16.6472	0.00000
MASS(KG/HR)	1394.77	1394.77	0.252679E-13
ENTHALPY(GCAL/HR)	-1.29051	-1.25830	-0.249625E-01

*** CO2 EQUIVALENT SUMMARY ***

FEED STREAMS CO2E	0.00000	KG/HR
PRODUCT STREAMS CO2E	0.00000	KG/HR
NET STREAMS CO2E PRODUCTION	0.00000	KG/HR
UTILITIES CO2E PRODUCTION	0.00000	KG/HR
TOTAL CO2E PRODUCTION	0.00000	KG/HR

*** INPUT DATA ***

TWO PHASE TP FLASH		
SPECIFIED TEMPERATURE	C	82.5000
SPECIFIED PRESSURE	BAR	0.100000
MAXIMUM NO. ITERATIONS		30
CONVERGENCE TOLERANCE		0.000100000

*** RESULTS ***

OUTLET TEMPERATURE	C	82.500
OUTLET PRESSURE	BAR	0.10000
HEAT DUTY	GCAL/HR	0.32214E-01
VAPOR FRACTION		0.75981

V-L PHASE EQUILIBRIUM :

COMP	F(I)	X(I)	Y(I)	K(I)
TRIOL-01	0.30035E-02	0.12505E-01	0.19796E-15	0.15831E-13
METHA-01	0.76094	0.37150E-01	0.98975	26.642
METHY-01	0.17125	0.71276	0.63959E-04	0.89735E-04

GLYCE-01 0.64809E-01 0.23759 0.10189E-01
0.42885E-01

U-O-S BLOCK SECTION

BLOCK: H102 MODEL: HEATER

INLET STREAM: A7
OUTLET STREAM: A8
PROPERTY OPTION SET: UNIF-DMD DORTMUND MOD. UNIFAC / REDLICH-KWONG-
SOAVE

*** MASS AND ENERGY BALANCE ***

	IN	OUT	RELATIVE DIFF.
TOTAL BALANCE			
MOLE(KMOL/HR)	16.8359	16.8359	0.00000
MASS(KG/HR)	1443.47	1443.47	0.00000
ENTHALPY(GCAL/HR)	-1.33727	-1.25762	-0.595623E-01

*** CO2 EQUIVALENT SUMMARY ***

FEED STREAMS CO2E	0.00000	KG/HR
PRODUCT STREAMS CO2E	0.00000	KG/HR
NET STREAMS CO2E PRODUCTION	0.00000	KG/HR
UTILITIES CO2E PRODUCTION	0.00000	KG/HR
TOTAL CO2E PRODUCTION	0.00000	KG/HR

*** INPUT DATA ***

TWO PHASE TP FLASH

SPECIFIED TEMPERATURE	C	180.000
SPECIFIED PRESSURE	BAR	40.0000
MAXIMUM NO. ITERATIONS		30
CONVERGENCE TOLERANCE		0.000100000

*** RESULTS ***

OUTLET TEMPERATURE	C	180.00
OUTLET PRESSURE	BAR	40.000
HEAT DUTY	GCAL/HR	0.79651E-01
OUTLET VAPOR FRACTION		0.0000

V-L PHASE EQUILIBRIUM :

COMP	F(I)	X(I)	Y(I)	K(I)

```
      TRIOL-01          0.59397E-01    0.59397E-01    0.28115E-05
0.38536E-04
      METHA-01          0.92169        0.92169        0.98290
0.86821
      METHY-01          0.48052E-04    0.48052E-04    0.53282E-06
0.90275E-02
      GLYCE-01          0.76550E-02    0.76550E-02    0.13714E-04
0.14586E-02
      HPW-MAS           0.11211E-01    0.11211E-01    0.17080E-01
1.2404
```

U-O-S BLOCK SECTION

BLOCK: H103 MODEL: HEATER

INLET STREAM: A13
OUTLET STREAM: A14
PROPERTY OPTION SET: UNIF-DMD DORTMUND MOD. UNIFAC / REDLICH-KWONG-SOAVE

*** MASS AND ENERGY BALANCE ***

	IN	OUT	RELATIVE DIFF.
TOTAL BALANCE			
MOLE(KMOL/HR)	12.6486	12.6486	0.00000
MASS(KG/HR)	413.242	413.242	0.536463E-14
ENTHALPY(GCAL/HR)	-0.610648	-0.733598	0.167599

*** CO2 EQUIVALENT SUMMARY ***

FEED STREAMS CO2E	0.00000	KG/HR
PRODUCT STREAMS CO2E	0.00000	KG/HR
NET STREAMS CO2E PRODUCTION	0.00000	KG/HR
UTILITIES CO2E PRODUCTION	0.00000	KG/HR
TOTAL CO2E PRODUCTION	0.00000	KG/HR

*** INPUT DATA ***

TWO PHASE TP FLASH

SPECIFIED TEMPERATURE	C	25.0000
SPECIFIED PRESSURE	BAR	1.00000
MAXIMUM NO. ITERATIONS		30
CONVERGENCE TOLERANCE		1.00000

*** RESULTS ***

OUTLET TEMPERATURE	C	25.000
OUTLET PRESSURE	BAR	1.0000
HEAT DUTY	GCAL/HR	-0.12295
OUTLET VAPOR FRACTION		0.0000

V-L PHASE EQUILIBRIUM :

COMP	F(I)	X(I)	Y(I)	K(I)
METHA-01	0.98975	0.98975	1.0000	0.17219
METHY-01	0.63959E-04	0.63959E-04	0.67560E-09	0.18002E-05
GLYCE-01	0.10189E-01	0.10189E-01	0.14521E-07	0.24289E-06

U-O-S BLOCK SECTION

BLOCK: M100 MODEL: MIXER

INLET STREAMS: METHANOL RECYCLED
OUTLET STREAM: A1
PROPERTY OPTION SET: UNIF-DMD DORTMUND MOD. UNIFAC / REDLICH-KWONG-SOAVE

*** MASS AND ENERGY BALANCE ***

	IN	OUT	RELATIVE DIFF.
TOTAL BALANCE			
MOLE(KMOL/HR)	15.6486	15.6472	0.927754E-04
MASS(KG/HR)	509.369	509.322	0.910648E-04
ENTHALPY(GCAL/HR)	-0.904441	-0.904358	-0.911579E-04

*** CO2 EQUIVALENT SUMMARY ***

FEED STREAMS CO2E	0.00000	KG/HR
PRODUCT STREAMS CO2E	0.00000	KG/HR
NET STREAMS CO2E PRODUCTION	0.00000	KG/HR
UTILITIES CO2E PRODUCTION	0.00000	KG/HR
TOTAL CO2E PRODUCTION	0.00000	KG/HR

*** INPUT DATA ***

ONE PHASE FLASH SPECIFIED PHASE IS LIQUID
MAXIMUM NO. ITERATIONS 32
CONVERGENCE TOLERANCE 0.00075000
OUTLET PRESSURE BAR 1.00000

BLOCK: M101 MODEL: MIXER

INLET STREAMS: HPW-MAS A1
OUTLET STREAM: A2
PROPERTY OPTION SET: UNIF-DMD DORTMUND MOD. UNIFAC / REDLICH-KWONG-SOAVE

*** MASS AND ENERGY BALANCE ***

	IN	OUT	RELATIVE DIFF.
TOTAL BALANCE			
MOLE(KMOL/HR)	15.8359	15.8359	0.00000
MASS(KG/HR)	558.017	558.017	0.407467E-14
ENTHALPY(GCAL/HR)	-0.917242	-0.917242	-0.435741E-14

U-O-S BLOCK SECTION

BLOCK: M101 MODEL: MIXER (CONTINUED)

*** CO2 EQUIVALENT SUMMARY ***

FEED STREAMS CO2E	0.00000	KG/HR
PRODUCT STREAMS CO2E	0.00000	KG/HR
NET STREAMS CO2E PRODUCTION	0.00000	KG/HR
UTILITIES CO2E PRODUCTION	0.00000	KG/HR
TOTAL CO2E PRODUCTION	0.00000	KG/HR

*** INPUT DATA ***

TWO PHASE FLASH	
MAXIMUM NO. ITERATIONS	30
CONVERGENCE TOLERANCE	0.000100000
OUTLET PRESSURE BAR	1.00000

BLOCK: M102 MODEL: MIXER

INLET STREAMS:	A2 GSC
OUTLET STREAM:	A3
PROPERTY OPTION SET:	UNIF-DMD DORTMUND MOD. UNIFAC / REDLICH-KWONG-SOAVE

*** MASS AND ENERGY BALANCE ***

	IN	OUT	RELATIVE DIFF.
TOTAL BALANCE			
MOLE(KMOL/HR)	16.8359	16.8359	0.00000
MASS(KG/HR)	1443.47	1443.47	-0.157519E-14
ENTHALPY(GCAL/HR)	-1.41013	-1.41013	0.157464E-14

*** CO2 EQUIVALENT SUMMARY ***

FEED STREAMS CO2E	0.00000	KG/HR
PRODUCT STREAMS CO2E	0.00000	KG/HR
NET STREAMS CO2E PRODUCTION	0.00000	KG/HR
UTILITIES CO2E PRODUCTION	0.00000	KG/HR
TOTAL CO2E PRODUCTION	0.00000	KG/HR

*** INPUT DATA ***

TWO PHASE FLASH	
MAXIMUM NO. ITERATIONS	30
CONVERGENCE TOLERANCE	0.000100000
OUTLET PRESSURE:	MINIMUM OF INLET STREAM PRESSURES

U-O-S BLOCK SECTION

BLOCK: P1 MODEL: VALVE

INLET STREAM: S3
OUTLET STREAM: A9
PROPERTY OPTION SET: UNIF-DMD DORTMUND MOD. UNIFAC / REDLICH-KWONG-SOAVE

*** MASS AND ENERGY BALANCE ***

	IN	OUT	RELATIVE DIFF.
TOTAL BALANCE			
MOLE(KMOL/HR)	16.8359	16.8359	0.00000
MASS(KG/HR)	1443.47	1443.47	0.00000
ENTHALPY(GCAL/HR)	-1.26442	-1.26442	0.00000

*** CO2 EQUIVALENT SUMMARY ***

FEED STREAMS CO2E	0.00000	KG/HR
PRODUCT STREAMS CO2E	0.00000	KG/HR
NET STREAMS CO2E PRODUCTION	0.00000	KG/HR
UTILITIES CO2E PRODUCTION	0.00000	KG/HR
TOTAL CO2E PRODUCTION	0.00000	KG/HR

*** INPUT DATA ***

VALVE OUTLET PRESSURE	BAR	6.89476
VALVE FLOW COEF CALC.		NO

FLASH SPECIFICATIONS:

PHASE	LIQUID
MAX NUMBER OF ITERATIONS	30
CONVERGENCE TOLERANCE	0.000100000

*** RESULTS ***

VALVE PRESSURE DROP	BAR	33.1052

BLOCK: P100 MODEL: PUMP

INLET STREAM: A3
OUTLET STREAM: A4
PROPERTY OPTION SET: UNIF-DMD DORTMUND MOD. UNIFAC / REDLICH-KWONG-SOAVE

*** MASS AND ENERGY BALANCE ***

	IN	OUT	RELATIVE DIFF.

U-O-S BLOCK SECTION

BLOCK: P100 MODEL: PUMP (CONTINUED)

TOTAL BALANCE			
MOLE(KMOL/HR)	16.8359	16.8359	0.00000
MASS(KG/HR)	1443.47	1443.47	0.00000
ENTHALPY(GCAL/HR)	-1.41013	-1.40538	-0.337393E-02

*** CO2 EQUIVALENT SUMMARY ***

FEED STREAMS CO2E	0.00000	KG/HR
PRODUCT STREAMS CO2E	0.00000	KG/HR
NET STREAMS CO2E PRODUCTION	0.00000	KG/HR
UTILITIES CO2E PRODUCTION	0.00000	KG/HR
TOTAL CO2E PRODUCTION	0.00000	KG/HR

*** INPUT DATA ***

OUTLET PRESSURE BAR	20.0000
DRIVER EFFICIENCY	1.00000

FLASH SPECIFICATIONS:
LIQUID PHASE CALCULATION
NO FLASH PERFORMED

MAXIMUM NUMBER OF ITERATIONS	30
TOLERANCE	0.000100000

*** RESULTS ***

VOLUMETRIC FLOW RATE CUM/HR	3.09966
PRESSURE CHANGE BAR	19.0000
NPSH AVAILABLE METER	18.5870
FLUID POWER KW	1.63593
BRAKE POWER KW	5.53320
ELECTRICITY KW	5.53320
PUMP EFFICIENCY USED	0.29566
NET WORK REQUIRED KW	5.53320
HEAD DEVELOPED METER	416.045

BLOCK: P101 MODEL: PUMP

INLET STREAM: A6
OUTLET STREAM: A7
PROPERTY OPTION SET: UNIF-DMD DORTMUND MOD. UNIFAC / REDLICH-KWONG-SOAVE

*** MASS AND ENERGY BALANCE ***

	IN	OUT	RELATIVE DIFF.
TOTAL BALANCE			
MOLE(KMOL/HR)	16.8359	16.8359	0.00000
MASS(KG/HR)	1443.47	1443.47	0.00000

```
       ENTHALPY(GCAL/HR )       -1.34266        -1.33727       -0.401727E-
02


 ASPEN PLUS   PLAT: WINDOWS   VER: 36.0                    04/25/2019  PAGE
27

                              U-O-S BLOCK SECTION

 BLOCK:  P101     MODEL: PUMP (CONTINUED)

                      ***  CO2 EQUIVALENT SUMMARY ***
    FEED STREAMS CO2E             0.00000      KG/HR
    PRODUCT STREAMS CO2E          0.00000      KG/HR
    NET STREAMS CO2E PRODUCTION   0.00000      KG/HR
    UTILITIES CO2E PRODUCTION     0.00000      KG/HR
    TOTAL CO2E PRODUCTION         0.00000      KG/HR

                           ***  INPUT DATA  ***
    OUTLET PRESSURE  BAR                                    40.0000
    DRIVER EFFICIENCY                                        1.00000

    FLASH SPECIFICATIONS:
    LIQUID PHASE CALCULATION
    NO FLASH PERFORMED
    MAXIMUM NUMBER OF ITERATIONS                            30
    TOLERANCE                                               0.000100000

                           ***  RESULTS  ***
    VOLUMETRIC FLOW RATE  CUM/HR                            3.33841
    PRESSURE CHANGE  BAR                                   20.0000
    NPSH AVAILABLE   METER                                379.725
    FLUID POWER  KW                                         1.85467
    BRAKE POWER  KW                                         6.27305
    ELECTRICITY  KW                                         6.27305
    PUMP EFFICIENCY USED                                    0.29566
    NET WORK REQUIRED  KW                                   6.27305
    HEAD DEVELOPED METER                                  471.675

 BLOCK:  P102     MODEL: PUMP
 ------------------------------
   INLET STREAM:          A14
   OUTLET STREAM:         RECYCLED
   PROPERTY OPTION SET:   UNIF-DMD  DORTMUND MOD. UNIFAC / REDLICH-KWONG-
SOAVE

                      ***  MASS AND ENERGY BALANCE  ***
                                  IN              OUT        RELATIVE
DIFF.
    TOTAL BALANCE
       MOLE(KMOL/HR )            12.6486         12.6486         0.00000
       MASS(KG/HR   )            413.242         413.242         0.00000
       ENTHALPY(GCAL/HR )      -0.733598       -0.733598         0.00000
```

```
                    ***  CO2 EQUIVALENT SUMMARY ***
   FEED STREAMS CO2E             0.00000      KG/HR
   PRODUCT STREAMS CO2E          0.00000      KG/HR
   NET STREAMS CO2E PRODUCTION   0.00000      KG/HR
   UTILITIES CO2E PRODUCTION     0.00000      KG/HR
   TOTAL CO2E PRODUCTION         0.00000      KG/HR


 ASPEN PLUS   PLAT: WINDOWS   VER: 36.0                  04/25/2019  PAGE
28

                              U-O-S BLOCK SECTION

 BLOCK:  P102     MODEL: PUMP (CONTINUED)

                           ***  INPUT DATA  ***
   OUTLET PRESSURE  BAR                                    1.00000
   DRIVER EFFICIENCY                                       1.00000

   FLASH SPECIFICATIONS:
   LIQUID PHASE CALCULATION
   NO FLASH PERFORMED
   MAXIMUM NUMBER OF ITERATIONS                            30
   TOLERANCE                                               0.000100000

                           ***  RESULTS  ***
   VOLUMETRIC FLOW RATE  CUM/HR                            0.51368
   PRESSURE CHANGE  BAR                                    0.0
   NPSH AVAILABLE   METER                                 10.5634
   FLUID POWER  KW                                         0.0
   BRAKE POWER  KW                                         0.0
   ELECTRICITY  KW                                         0.0
   PUMP EFFICIENCY USED                                    0.29566
   NET WORK REQUIRED  KW                                   0.0
   HEAD DEVELOPED METER                                    0.0

 BLOCK:  P2       MODEL: VALVE
 ------------------------------
   INLET STREAM:          A10
   OUTLET STREAM:         A11
   PROPERTY OPTION SET:   UNIF-DMD  DORTMUND MOD. UNIFAC / REDLICH-KWONG-
SOAVE

                     ***  MASS AND ENERGY BALANCE  ***
                                  IN              OUT        RELATIVE
DIFF.
    TOTAL BALANCE
      MOLE(KMOL/HR )           16.6472         16.6472         0.00000
      MASS(KG/HR   )           1394.77         1394.77         0.00000
      ENTHALPY(GCAL/HR )      -1.25432        -1.25432         0.00000

                     ***  CO2 EQUIVALENT SUMMARY ***
   FEED STREAMS CO2E             0.00000      KG/HR
   PRODUCT STREAMS CO2E          0.00000      KG/HR
```

NET STREAMS CO2E PRODUCTION	0.00000	KG/HR
UTILITIES CO2E PRODUCTION	0.00000	KG/HR
TOTAL CO2E PRODUCTION	0.00000	KG/HR

*** INPUT DATA ***

VALVE OUTLET PRESSURE	BAR	3.00000
VALVE FLOW COEF CALC.		NO

U-O-S BLOCK SECTION

BLOCK: P2 MODEL: VALVE (CONTINUED)

FLASH SPECIFICATIONS:

NPHASE	2
MAX NUMBER OF ITERATIONS	30
CONVERGENCE TOLERANCE	0.000100000

*** RESULTS ***

VALVE PRESSURE DROP	BAR	3.89476

BLOCK: R100 MODEL: RSTOIC

INLET STREAM: A8
OUTLET STREAM: S3
PROPERTY OPTION SET: UNIF-DMD DORTMUND MOD. UNIFAC / REDLICH-KWONG-SOAVE

*** MASS AND ENERGY BALANCE ***

	IN	OUT	GENERATION	RELATIVE DIFF.
TOTAL BALANCE				
MOLE(KMOL/HR)	16.8359	16.8359	0.195156E-15	0.00000
MASS(KG/HR)	1443.47	1443.47		0.157519E-15
ENTHALPY(GCAL/HR)	-1.25762	-1.26442		0.538009E-02

*** CO2 EQUIVALENT SUMMARY ***

FEED STREAMS CO2E	0.00000	KG/HR
PRODUCT STREAMS CO2E	0.00000	KG/HR
NET STREAMS CO2E PRODUCTION	0.00000	KG/HR
UTILITIES CO2E PRODUCTION	0.00000	KG/HR
TOTAL CO2E PRODUCTION	0.00000	KG/HR

*** INPUT DATA ***

STOICHIOMETRY MATRIX:

REACTION # 1:

SUBSTREAM MIXED :							
TRIOL-01	-1.00	METHA-01	-3.00	METHY-01	3.00	GLYCE-01	1.00

REACTION CONVERSION SPECS: NUMBER= 1
REACTION # 1:
SUBSTREAM:MIXED KEY COMP:TRIOL-01 CONV FRAC: 0.9500

```
   ONE    PHASE  TP  FLASH   SPECIFIED PHASE IS  LIQUID
   SPECIFIED TEMPERATURE C                                  180.000
   SPECIFIED PRESSURE    BAR                                 40.0000
   MAXIMUM NO. ITERATIONS                                    30
   CONVERGENCE TOLERANCE                                      0.000100000

 ASPEN PLUS   PLAT: WINDOWS   VER: 36.0                  04/25/2019  PAGE
30

                              U-O-S BLOCK SECTION

 BLOCK:  R100     MODEL: RSTOIC (CONTINUED)
   SIMULTANEOUS REACTIONS
   GENERATE COMBUSTION REACTIONS FOR FEED SPECIES          NO

                            ***  RESULTS  ***
   OUTLET TEMPERATURE    C                                    180.00
   OUTLET PRESSURE       BAR                                  40.000
   HEAT DUTY             GCAL/HR                             -0.68027E-02



   REACTION EXTENTS:

      REACTION          REACTION
      NUMBER            EXTENT
                        KMOL/HR
      1                 0.95000

 BLOCK:  S100     MODEL: SEP
 ---------------------------
   INLET STREAM:          A9
   OUTLET STREAMS:        CATALYST    A10
   PROPERTY OPTION SET:   UNIF-DMD  DORTMUND MOD. UNIFAC / REDLICH-KWONG-
SOAVE

                       ***  MASS AND ENERGY BALANCE  ***
                                    IN              OUT        RELATIVE
DIFF.
    TOTAL BALANCE
       MOLE(KMOL/HR )            16.8359         16.8359         0.00000
       MASS(KG/HR   )            1443.47         1443.47         0.00000
       ENTHALPY(GCAL/HR )       -1.26442        -1.26680        0.187535E-
02

                       ***  CO2 EQUIVALENT SUMMARY ***
    FEED STREAMS CO2E             0.00000      KG/HR
    PRODUCT STREAMS CO2E          0.00000      KG/HR
    NET STREAMS CO2E PRODUCTION   0.00000      KG/HR
    UTILITIES CO2E PRODUCTION     0.00000      KG/HR
    TOTAL CO2E PRODUCTION         0.00000      KG/HR
```

*** INPUT DATA ***

FLASH SPECS FOR STREAM CATALYST
TWO PHASE TP FLASH
PRESSURE DROP BAR 0.0
MAXIMUM NO. ITERATIONS 30
CONVERGENCE TOLERANCE 0.000100000

U-O-S BLOCK SECTION

BLOCK: S100 MODEL: SEP (CONTINUED)

FLASH SPECS FOR STREAM A10
TWO PHASE TP FLASH
PRESSURE DROP BAR 0.0
MAXIMUM NO. ITERATIONS 30
CONVERGENCE TOLERANCE 0.000100000

FRACTION OF FEED
SUBSTREAM= MIXED
STREAM= CATALYST CPT= HPW-MAS FRACTION= 1.00000

*** RESULTS ***

HEAT DUTY GCAL/HR -0.23757E-02

COMPONENT = TRIOL-01

STREAM	SUBSTREAM	SPLIT FRACTION
A10	MIXED	1.00000

COMPONENT = METHA-01

STREAM	SUBSTREAM	SPLIT FRACTION
A10	MIXED	1.00000

COMPONENT = METHY-01

STREAM	SUBSTREAM	SPLIT FRACTION
A10	MIXED	1.00000

COMPONENT = GLYCE-01

STREAM	SUBSTREAM	SPLIT FRACTION
A10	MIXED	1.00000

COMPONENT = HPW-MAS

STREAM	SUBSTREAM	SPLIT FRACTION
CATALYST	MIXED	1.00000

STREAM SECTION

A1 A10 A11 A12 A13

STREAM ID	A1	A10	A11	A12	A13
FROM :	M100	S100	P2	H101	F100
TO :	M101	P2	H101	F100	H103
CONV. MAX. REL. ERR:	9.3704-05	0.0	0.0	0.0	0.0
SUBSTREAM: MIXED					
PHASE:	LIQUID	MIXED	MIXED	MIXED	VAPOR
COMPONENTS: KMOL/HR					
TRIOL-01	2.5039-15	5.0000-02	5.0000-02	5.0000-02	2.5039-15
METHA-01	15.5175	12.6675	12.6675	12.6675	12.5189
METHY-01	8.0899-04	2.8508	2.8508	2.8508	8.0900-04
GLYCE-01	0.1289	1.0789	1.0789	1.0789	0.1289
HPW-MAS	0.0	0.0	0.0	0.0	0.0
TOTAL FLOW:					
KMOL/HR	15.6472	16.6472	16.6472	16.6472	12.6486
KG/HR	509.3224	1394.7716	1394.7716	1394.7716	413.2423
CUM/HR	0.6348	32.9290	101.3425	62.9159	3734.5232
STATE VARIABLES:					
TEMP C	24.9963	139.5085	117.9388	105.8245	82.5000
PRES BAR	1.0000	6.8948	3.0000	3.0000	0.1000
VFRAC	0.0	0.4053	0.5731	0.3645	1.0000
LFRAC	1.0000	0.5947	0.4269	0.6355	0.0
SFRAC	0.0	0.0	0.0	0.0	0.0
ENTHALPY:					
KCAL/MOL	-57.7969	-75.3473	-75.3473	-77.5214	-48.2778
KCAL/KG	-1775.6106	-899.3007	-899.3007	-925.2498	-1477.6988
GCAL/HR	-0.9044	-1.2543	-1.2543	-1.2905	-0.6106
ENTROPY:					
CAL/MOL-K	-58.0531	-108.6116	-107.7906	-113.4413	-25.0385
CAL/GM-K	-1.7835	-1.2963	-1.2865	-1.3540	-0.7664

DENSITY:					
KMOL/CUM	24.6473	0.5055	0.1643	0.2646	3.3869-03
KG/CUM	802.2809	42.3570	13.7630	22.1688	0.1107
AVG MW	32.5505	83.7843	83.7843	83.7843	32.6709

STREAM SECTION

A14 A15 A16 A17 A18

STREAM ID	A14	A15	A16	A17	A18
FROM :	H103	F100	H100	D100	H104
TO :	P102	H100	D100	H104	C100
SUBSTREAM: MIXED					
PHASE:	LIQUID	LIQUID	LIQUID	LIQUID	LIQUID
COMPONENTS: KMOL/HR					
TRIOL-01	2.5039-15	5.0000-02	5.0000-02	5.0000-02	5.0000-02
METHA-01	12.5189	0.1485	0.1485	3.7672-02	3.7672-02
METHY-01	8.0900-04	2.8500	2.8500	2.8500	2.8500
GLYCE-01	0.1289	0.9500	0.9500	4.7662-04	4.7662-04
HPW-MAS	0.0	0.0	0.0	0.0	0.0
TOTAL FLOW:					
KMOL/HR	12.6486	3.9985	3.9985	2.9381	2.9381
KG/HR	413.2423	981.5293	981.5293	890.5296	890.5296
CUM/HR	0.5137	1.2576	1.2108	1.0925	1.2659
STATE VARIABLES:					
TEMP C	25.0000	82.5000	35.6879	25.0000	190.0000
PRES BAR	1.0000	0.1000	0.1000	1.0000	1.0000
VFRAC	0.0	0.0	0.0	0.0	0.0
LFRAC	1.0000	1.0000	1.0000	1.0000	1.0000
SFRAC	0.0	0.0	0.0	0.0	0.0
ENTHALPY:					
KCAL/MOL	-57.9983	-161.9713	-168.6033	-178.6572	-151.4052

KCAL/KG	-1775.2250	-659.8378	-686.8553	-589.4482	-499.5349
GCAL/HR	-0.7336	-0.6477	-0.6742	-0.5249	-0.4449
ENTROPY:					
CAL/MOL-K	-58.2124	-352.6139	-372.5677	-464.8211	-392.6170
CAL/GM-K	-1.7818	-1.4365	-1.5178	-1.5336	-1.2954
DENSITY:					
KMOL/CUM	24.6234	3.1794	3.3023	2.6893	2.3210
KG/CUM	804.4699	780.4502	810.6237	815.1046	703.4838
AVG MW	32.6709	245.4714	245.4714	303.0923	303.0923

STREAM SECTION

A19 A2 A20 A3 A4

STREAM ID	A19	A2	A20	A3	A4
FROM :	C100	M101	C100	M102	P100
TO :	H104	M102	----	P100	H100
SUBSTREAM: MIXED					
PHASE:	LIQUID	LIQUID	LIQUID	LIQUID	LIQUID
COMPONENTS: KMOL/HR					
TRIOL-01	1.1559-07	2.5039-15	5.0000-02	1.0000	1.0000
METHA-01	3.7672-02	15.5175	5.0887-19	15.5175	15.5175
METHY-01	2.8119	8.0899-04	3.8146-02	8.0899-04	8.0899-04
GLYCE-01	4.7643-04	0.1289	1.9182-07	0.1289	0.1289
HPW-MAS	0.0	0.1887	0.0	0.1887	0.1887
TOTAL FLOW:					
KMOL/HR	2.8500	15.8359	8.8146-02	16.8359	16.8359
KG/HR	834.9471	558.0174	55.5825	1443.4666	1443.4666
CUM/HR	1.1261	0.6389	0.1100	3.0997	3.1153
STATE VARIABLES:					
TEMP C	202.4575	25.4375	289.2153	20.8707	26.6058

```
   PRES   BAR             0.5000     1.0000     0.1000     1.0000
20.0000
   VFRAC                   0.0        0.0        0.0        0.0        0.0
   LFRAC                   1.0000     1.0000     1.0000     1.0000
1.0000
   SFRAC                   0.0        0.0        0.0        0.0        0.0
 ENTHALPY:
   KCAL/MOL             -144.5087   -57.9217  -265.5749   -83.7575   -
83.4749
   KCAL/KG              -493.2646 -1643.7519  -421.1658  -976.9078  -
973.6117
   GCAL/HR                -0.4118    -0.9172 -2.3409-02    -1.4101    -
1.4054
 ENTROPY:
   CAL/MOL-K            -375.1824   -57.7083  -735.5033  -133.2062  -
132.4167
   CAL/GM-K               -1.2806    -1.6377    -1.1664    -1.5537    -
1.5444
 DENSITY:
   KMOL/CUM                2.5307    24.7872     0.8010     5.4315
5.4043
   KG/CUM                741.4174   873.4385   505.0805   465.6849
463.3540
 AVG MW                  292.9639    35.2375   630.5709    85.7374
85.7374
```

STREAM SECTION

A5 A6 A7 A8 A9

STREAM ID	A5	A6	A7	A8	A9
FROM :	H100	H101	P101	H102	P1
TO :	H101	P101	H102	R100	S100
SUBSTREAM: MIXED					
PHASE:	LIQUID	LIQUID	LIQUID	LIQUID	LIQUID
COMPONENTS: KMOL/HR					
TRIOL-01	1.0000	1.0000	1.0000	1.0000	5.0000-02
METHA-01	15.5175	15.5175	15.5175	15.5175	12.6675
METHY-01	8.0899-04	8.0899-04	8.0899-04	8.0899-04	2.8508
GLYCE-01	0.1289	0.1289	0.1289	0.1289	1.0789
HPW-MAS	0.1887	0.1887	0.1887	0.1887	0.1887
TOTAL FLOW:					
KMOL/HR	16.8359	16.8359	16.8359	16.8359	16.8359
KG/HR	1443.4666	1443.4666	1443.4666	1443.4666	1443.4666
CUM/HR	3.2110	3.3384	3.3557	3.6498	2.0701
STATE VARIABLES:					
TEMP C	60.0000	100.0000	105.0670	180.0000	180.2424
PRES BAR	20.0000	20.0000	40.0000	40.0000	6.8948
VFRAC	0.0	0.0	0.0	0.0	0.0
LFRAC	1.0000	1.0000	1.0000	1.0000	1.0000
SFRAC	0.0	0.0	0.0	0.0	0.0
ENTHALPY:					
KCAL/MOL	-81.8998	-79.7501	-79.4297	-74.6987	-75.1027
KCAL/KG	-955.2403	-930.1666	-926.4299	-871.2496	-875.9623
GCAL/HR	-1.3789	-1.3427	-1.3373	-1.2576	-1.2644
ENTROPY:					
CAL/MOL-K	-127.5242	-121.5442	-120.8374	-109.6643	-107.8528
CAL/GM-K	-1.4874	-1.4176	-1.4094	-1.2791	-1.2579

```
 DENSITY:
   KMOL/CUM               5.2432     5.0431     5.0171     4.6128
8.1328
   KG/CUM               449.5395   432.3809   430.1538   395.4913
697.2815
 AVG MW                  85.7374    85.7374    85.7374    85.7374
85.7374

 ASPEN PLUS   PLAT: WINDOWS   VER: 36.0                  04/25/2019  PAGE
36

                                STREAM SECTION

 CATALYST FAME GLYCEROL GSC HPW-MAS
 ----------------------------------

 STREAM ID               CATALYST   FAME       GLYCEROL   GSC        HPW-
MAS
 FROM :                  S100       H104       D100       ----       ----
 TO   :                  ----       ----       ----       M102       M101

 SUBSTREAM: MIXED
 PHASE:                  LIQUID     LIQUID     LIQUID     LIQUID
LIQUID
 COMPONENTS: KMOL/HR
   TRIOL-01               0.0     1.1559-07  2.1100-17     1.0000     0.0
   METHA-01               0.0     3.7672-02     0.1109     0.0        0.0
   METHY-01               0.0        2.8119  2.6542-06     0.0        0.0
   GLYCE-01               0.0     4.7643-04     0.9495     0.0        0.0
   HPW-MAS                0.1887     0.0        0.0        0.0
0.1887
 TOTAL FLOW:
   KMOL/HR                0.1887     2.8500     1.0604     1.0000
0.1887
   KG/HR                 48.6950   834.9471    90.9997   885.4492
48.6950
   CUM/HR              3.8854-03     0.9630  7.2398-02     0.9733  3.4209-
03
 STATE VARIABLES:
   TEMP   C             139.5085    29.0359    25.0000    25.0000
25.0000
   PRES   BAR            6.8948     0.5000     1.0000     1.0000
1.0000
   VFRAC                  0.0        0.0        0.0        0.0        0.0
   LFRAC                  1.0000     1.0000     1.0000     1.0000
1.0000
   SFRAC                  0.0        0.0        0.0        0.0        0.0
 ENTHALPY:
   KCAL/MOL             -66.1174  -172.6036  -148.7313  -492.8915   -
68.2626
   KCAL/KG             -256.2690  -589.1635 -1733.1370  -556.6571  -
264.5836
   GCAL/HR           -1.2479-02    -0.4919    -0.1577    -0.4929 -1.2884-
02
```

ENTROPY:					
CAL/MOL-K	-32.9402	-448.0778	-136.1525	-1323.5578	-38.9668
CAL/GM-K	-0.1277	-1.5295	-1.5866	-1.4948	-0.1510
DENSITY:					
KMOL/CUM	48.5773	2.9596	14.6468	1.0274	55.1730
KG/CUM	1.2533+04	867.0627	1256.9308	909.7461	1.4235+04
AVG MW	258.0000	292.9639	85.8162	885.4492	258.0000

STREAM SECTION

METHANOL RECYCLED S3

STREAM ID	METHANOL	RECYCLED	S3
FROM :	----	P102	R100
TO :	M100	M100	P1
SUBSTREAM: MIXED			
PHASE:	LIQUID	LIQUID	LIQUID
COMPONENTS: KMOL/HR			
TRIOL-01	0.0	2.5039-15	5.0000-02
METHA-01	3.0000	12.5189	12.6675
METHY-01	0.0	8.0900-04	2.8508
GLYCE-01	0.0	0.1289	1.0789
HPW-MAS	0.0	0.0	0.1887
TOTAL FLOW:			
KMOL/HR	3.0000	12.6486	16.8359
KG/HR	96.1265	413.2423	1443.4666
CUM/HR	0.1212	0.5137	2.0693
STATE VARIABLES:			
TEMP C	25.0000	25.0000	180.0000
PRES BAR	1.0000	1.0000	40.0000
VFRAC	0.0	0.0	0.0
LFRAC	1.0000	1.0000	1.0000
SFRAC	0.0	0.0	0.0
ENTHALPY:			
KCAL/MOL	-56.9475	-57.9983	-75.1027
KCAL/KG	-1777.2692	-1775.2250	-875.9623
GCAL/HR	-0.1708	-0.7336	-1.2644
ENTROPY:			
CAL/MOL-K	-57.3985	-58.2124	-108.0544
CAL/GM-K	-1.7913	-1.7818	-1.2603
DENSITY:			
KMOL/CUM	24.7462	24.6234	8.1359
KG/CUM	792.9208	804.4699	697.5474
AVG MW	32.0422	32.6709	85.7374

PROBLEM STATUS SECTION

BLOCK STATUS

```
********************************************************************************
**
 *
*
 * Calculations were completed normally
*
 *
*
 * All Unit Operation blocks were completed normally
*
 *
*
 * All streams were flashed normally
*
 *
*
 * All Convergence blocks were completed normally
*
 *
*
 * Properties estimation was completed normally
*
 *
*

********************************************************************************
**
```

APPENDIX C

Calculation related to synthesis recipe of MAS-9 and MAS-7

MAS-9

Molar batch composition:

1.0 Na_2O: 1.0 Al_2O_3: 50 SiO_2: 7 $(TPA)_2O$: 1800 H_2O

Source materials:

Sodium aluminate: 53.49 wt % Al_2O_3, 46.51 wt % Na_2O

TEOS, Sigma Aldrich: 28.846 wt %

Sodium hydroxide: J.T.Baker, 97% NaOH, 3 wt % H_2O

Tetrapropylammonium hydroxide solution, Aldrich

Deionized water

1 mole Al_2O_3 = 102g Al_2O_3

For 102 grams of Al_2O_3

$$= 102\ g\ Al_2O_3\ \times \frac{100\ g\ sodium\ aluminate}{53.49} = 190.68\ g$$

In 190.68 grams of sodium aluminate

$$= 190.68 \times \frac{40.48\ gNa_2O}{100} \times \frac{1\ mole}{61.98\ gNa_2O} = 1.24\ mol\ Na_2O$$

Compound formula – 1.24 Na_2O: Al_2O_3

$$1\ mole\ of\ SiO_2 \times \frac{60g}{1\ mole} = 60g\ SiO_2$$

$$= 60.086 \times \frac{100\ g\ TEOS}{28.846} = 208.29g$$

$$1\ mole\ NaOH \times \frac{40g}{1\ mole} = 40g$$

1 mole of TPAOH = 203 g

For 203 g TPAOH,

$$= 203 \times \frac{100\ (40\%)}{40} = 1015\ g\ TEOH$$

In 1015 g TPAOH

$$= 1015 \times \frac{60\ gH_2O}{100g\ TPAOH} \times \frac{1\ mole}{18\ gH_2O} = 16.19\ mol\ H_2O$$

Compound formula of tetrapropylammonium hydroxide; TPAOH·16.19 H_2O

Chemical equations

(1.24 Na_2O: Al_2O_3) = 1.24 Na_2O + Al_2O_3

2 TPAOH = $(TPA)_2O$ + H_2O

2 (TPAOH·16.19 H_2O) = $(TPA)_2O$ + 32.28 H_2O

Table C.1. Mole composition to form ZSM -5 precursor solution.

1.24 Na_2O + Al_2O_3	Na_2O -1.24 Na_2O	1.0 Al_2O_3 -1.0 Al_2O_3	50 SiO_2	7 $(TPA)_2O$	1800 H_2O
50 SiO_2			- 50 SiO_2		1800 H_2O
14 (TPAOH+ 16.19 H_2O)					1800 H_2O -226.66
1573.34 H_2O					= 1573.34 H_2O

Compound	Moles	Formula weight	Mass
1.24 $Na_2O + Al_2O_3$	1	177.94	177.94
TEOS	50	208.3	10415
TPAOH+ 16.19 H_2O	14	494.42	6921.88
H_2O	1573.46	18	28320.12
Total			45819.94

On 100g basis

$NaOAl_2$ – 0.4 g

TEOS- 22.7 g

TPAOH- 15.10 g

H_2O- 61.8 g

Similarly, calculations were done for MAS-7

APPENDIX D

Calibration curves for HPLC and GC; Determination of methanol to oil molar ratio

Calibration curves for HPLC

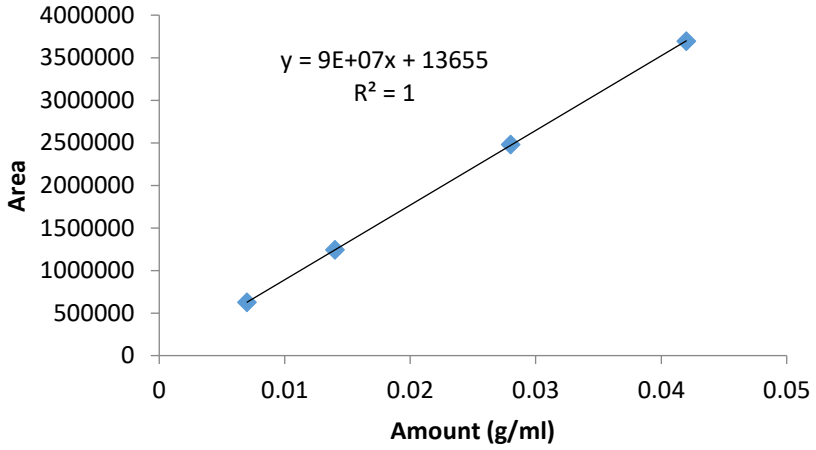

Figure D.1. Calibration curve for triglyceride (TG).

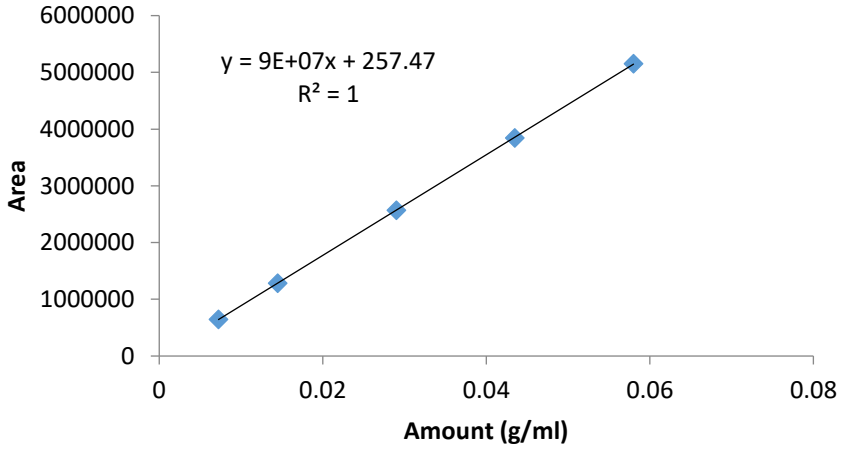

Figure D.2. Calibration curve for diglyceride (DG

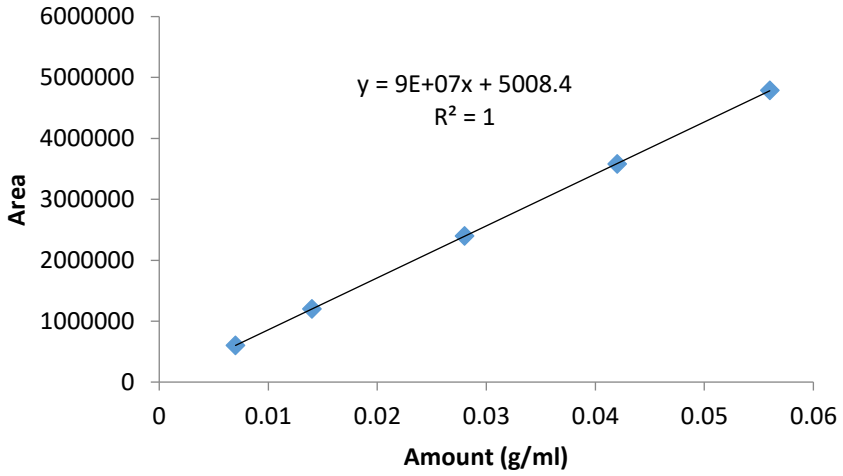

Figure D.3. Calibration curve for monoglyceride (MG).

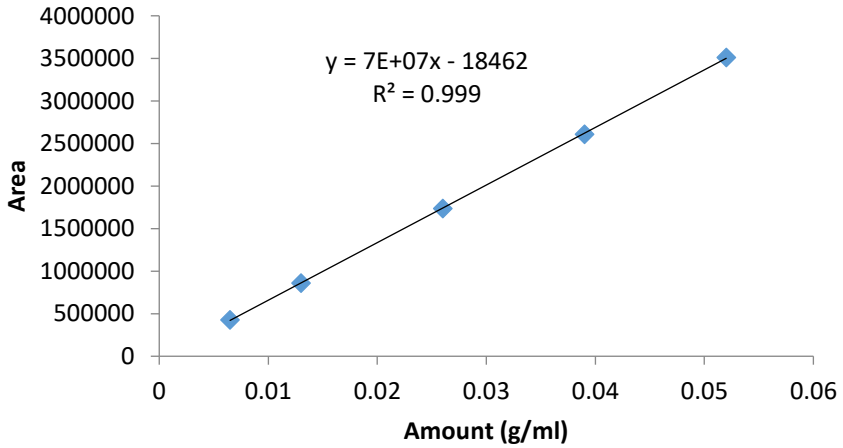

Figure D.4. Calibration curve for free fatty acid (FFA).

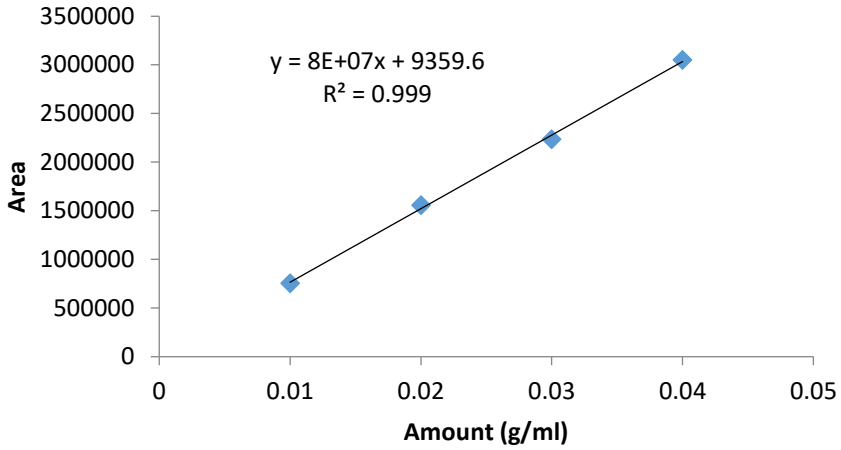

Figure D.5. Calibration curve for esters.

Calibration curves for GC

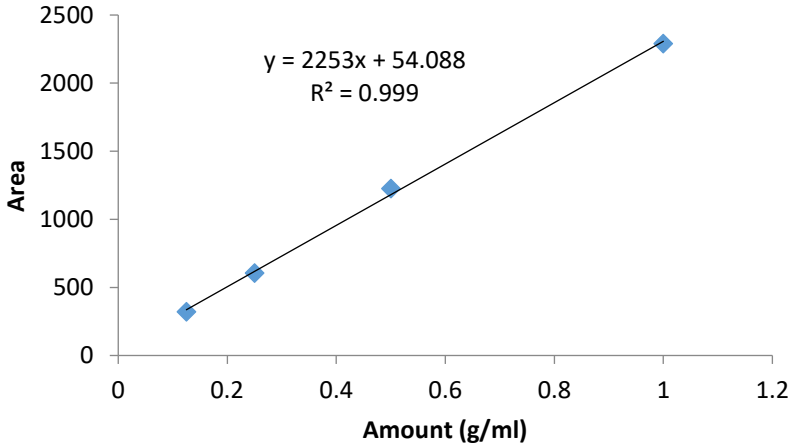

Figure D.6. Calibration curve for C14:0 methyl myristate

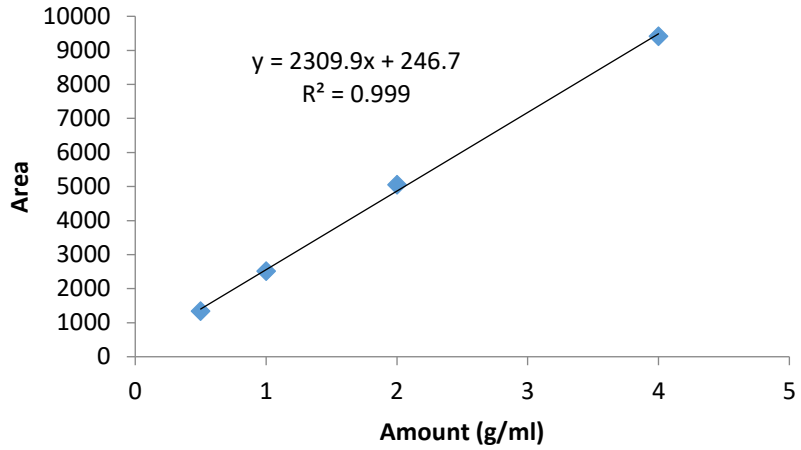

Figure D.7. Calibration curve for C16:0 methyl palmitate

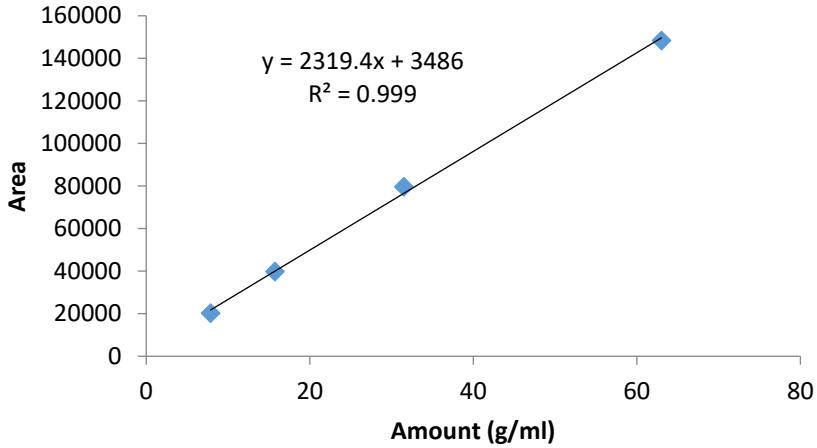

Figure D.8. Calibration curve for C18:0 + C18:1 methyl stearate + methyl oleate.

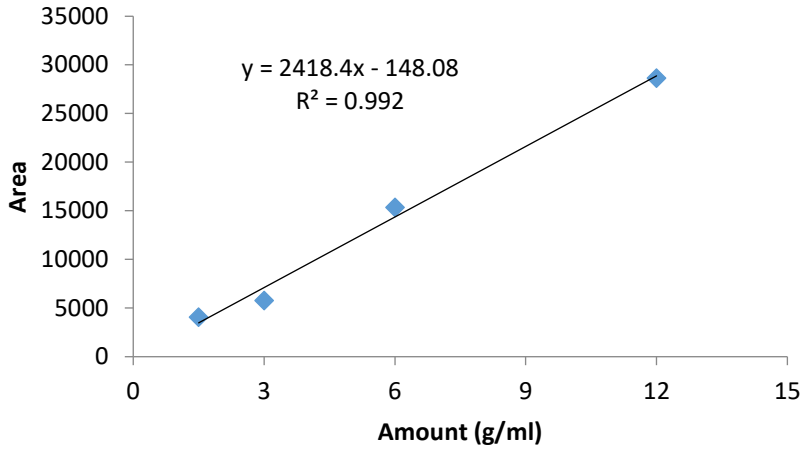

Figure D.9. Calibration curve for C18:2 methyl linoleate.

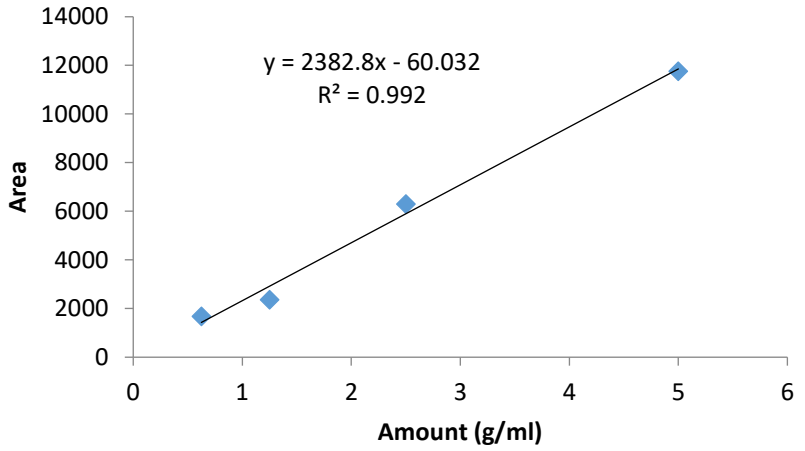

Figure D.10. Calibration curve for C18:3 methyl linolenate.

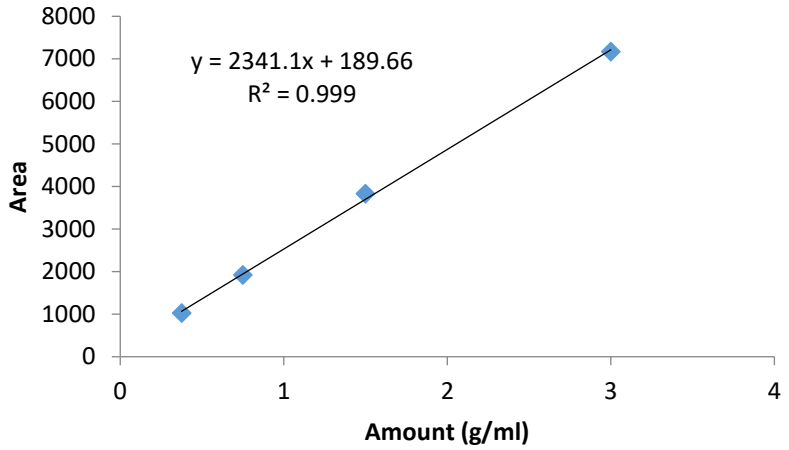

Figure D.11. Calibration curve for C20:0 methyl arachidate.

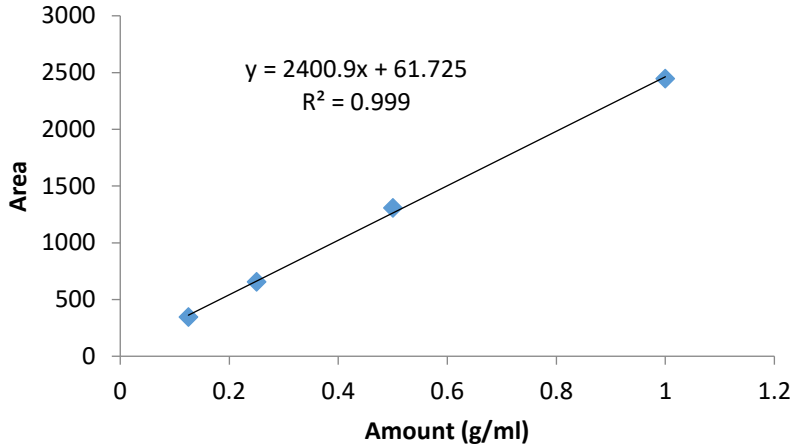

Figure D.12**.** Calibration curve for C20:1 methyl cis-11 eicosenoate.

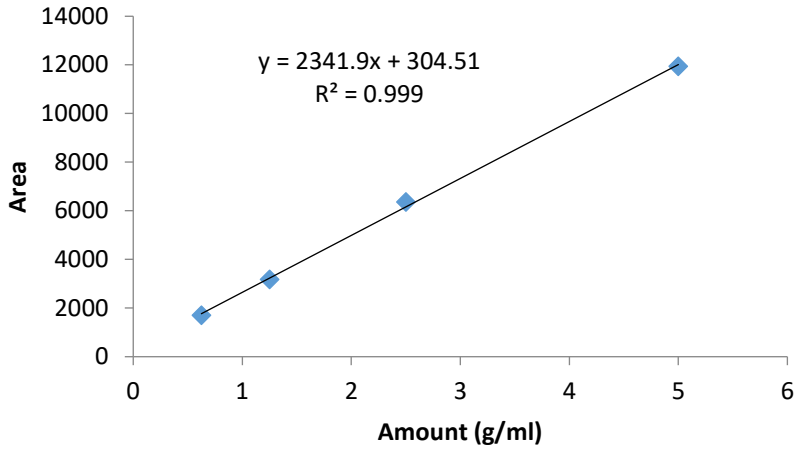

Figure D.13**.** Calibration curve for C22:1 methyl cis-13 docosenoate.

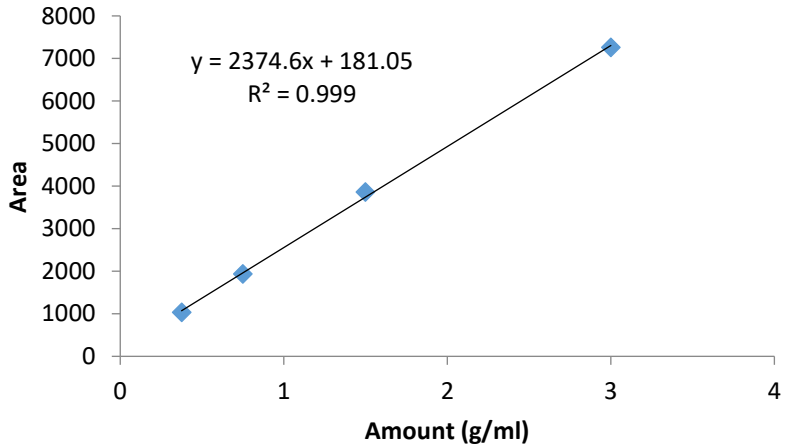

Figure D.14**.** Calibration curve for C24:0 methyl tetracosanoate.

Determination of methanol to oil molar ratio

Fatty acid methyl ester (FAME) mix rapeseed oil standard was used as a reference for gas chromatography. In the calibration sample, the concentration of each FAME was known and equaled to 1 mg/ml.acid compositions of esters were determined using an Agilent Gas Chromatography system (7890 A)

Table D.1. Fatty acid composition of green seed canola oil.

Carbon number	Fatty acid	Molecular weight	Weight fraction	Fatty acid %	$\sum x_i F_{Ai}$
C14:0	Methyl myristate	228.9	0.001	0.10	0.23
C16:0	Methyl palmitate	257.118	0.053	5.26	13.52
C18:0	methyl stearate	285.16	0.02	2.00	5.70
C18:1	methyl oleate	283.09	0.7	70.00	198.16
C18:2	Methyl linoleate	280.44	0.19	19.14	53.67
C18:3	Methyl linolenate	278.46	0.006	0.63	1.75
C20:0	Methyl arachidate	312.5	0.005	0.52	1.63
C20:1	Methyl cis-11-eicosenoate	310.5	0.019	1.85	5.75
C22:0	Methyl behenate	340.58	0.002	0.23	0.78
C22:1	Methyl cis-13-docosenoate	338	0	0.00	0.00
C24:0	Methyl tetracosanoate	367.38	0.002	0.24	0.87
	Total		0.999	99.96	282.06

A relative peak areas for each fatty acid was calculated using Eq.D.1

$$Relative\ area = \frac{Area\ of\ the\ peak\ in\ studied\ sample}{Area\ of\ the\ peak\ in\ calibrated\ sample} \times 100 \quad \text{.....(D.1)}$$

The molar fraction of each FAME in the studied sample was obtained from the relative peak area. The molar fraction of each fatty acid was assumed to be equal to the molar fraction of each corresponding FAME derived from the oil by transesterification. The average molecular weight of the fatty acid (MW_{FA}), triglyceride (MW_{TG}), diglyceride (MW_{DG}), monoglyceride (MW_{MG}) and FAME (MW_{FAME}) from green seed oil were determined using Eqs D.2.

$MW_{FA} = \sum_i x_{FAi} M_{FAi}$ = 282.06

$MW_{TG} = 3\sum_i x_{FAi} M_{FAi} + M_{glycerol} - 3M_{OH}$ = 884.18 …… (D.2)

$MW_{DG} = 2(\sum_i x_{FAi} M_{FAi}) + 56$ = 620.12

$MW_{MG} = (\sum_i x_{FAi} M_{FAi}) + 74$ = *356*

$MW_{FAME} = (\sum_i x_{FAi} M_{FAi}) + 14$ = 296

Weight of FFA per gram of oil:

$m_{FFA} = N_{FFA} M_{FA} = 1.92 \times 10^{-4} \times 282.06 = 0.054\ g\ of\ FFA$…….. (D.3)

No of moles of triglyceride per gram of oil:

$N_{trig} = \frac{1 - m_{FFA}}{M_{trig}} = \frac{0.946}{884} = 0.00106\ mol$……. (D.4)

Methanol to oil molar ratio:

$weight\ of\ methanol = 32 \times 0.00106 \times ratio \times weight\ of\ oil$…….... (D.5)

APPENDIX E

Code for Matlab programming

Matlab code was defined as described by Issariyakul (2011).

Eley-Rideal mechanism with surface reaction as rate limiting

```
function dCdt=KinODE(t,Cinput,K)
 global k1 k2 k3 k4 k5 k6 j7 j8 j9 j10;
% ************ Define Concentration and Rate Constant Parameters
**************
C1 = Cinput(1);
C2 = Cinput(2);
C3 = Cinput(3);
C4 = Cinput(4);
C5 = Cinput(5);
C6 = Cinput(6);
k1 = K(1);
k2 = K(2);
k3 = K(3);
k4 = K(4);
k5 = K(5);
k6 = K(6);
j7= K(7);
j8=K(8);
j9= K(9);
j10=K(10);
% ************ Ordinary Differential Equations **************
dCdt = [(-k1*C1*j10*C6+k2*C4*j7*C2)/(1+j10*C6+j7*C2+j8*C3+j9*C5);...
(k1*C1*j10*C6-k2*j7*C2*C4-
k3*C2*j10*C6+k4*j8*C3*C4)/(1+j10*C6+j7*C2+j8*C3+j9*C5);...
(k3*C2*j10*C6-k4*j8*C3*C4-
k5*C3*j10*C6+k6*j9*C5*C4)/(1+j10*C6+j7*C2+j8*C3+j9*C5);...
(k1*C1*j10*C6+k3*C2*j10*C6+k5*C3*j10*C6-k2*j7*C2*C4-k4*j8*C3*C4-
k6*j9*C5*C4)/(1+j10*C6+j7*C2+j8*C3+j9*C5);...
(k5*C3*j10*C6-k6*j9*C5*C4)/(1+j10*C6+j7*C2+j8*C3+j9*C5);...
(k2*j7*C2*C4+k4*j8*C3*C4+k6*j9*C5*C4-k1*C1*j10*C6-k3*C2*j10*C6-
k5*C3*j10*C6)/(1+j10*C6+j7*C2+j8*C3+j9*C5)];

unction error=err(KI)
% ************ Reaction Time; Unit - Minutes **************
texp=[30 45 60 120 300 360 420 480 600];
% ************ Concentrations; Unit - mol/L **************
TG=[0.3870 0.2973 0.2130 0.1217 0.0450 0.0387 0.0323 0.0262 0.0188];
DG=[0.2309 0.1935 0.1652 0.1328 0.0813 0.0677 0.0576 0.0520 0.0368];
MG=[0.1340 0.1823 0.1515 0.1313 0.1571 0.1333 0.1201 0.1073 0.0878];
ME=[0.069 0.0968 0.5268 0.9588 1.2659 1.3971 1.4860 1.5597 1.6857];
GL=[0.026 0.050 0.1756 0.3196 0.4220 0.4657 0.4953 0.5199 0.5619];
MeOH=[5.556 5.528 5.098 4.6662 4.3591 4.2279 4.1390 4.0653 3.9393];
% ************ Define Concentration and Step Time **************
CExp = [TG; DG; MG; ME; GL; MeOH];
Cini = CExp(:,1);
```

```
tspan=(15:15:600);
% ************ Solving Ordinary Differential Equations **************
[t,C] = ode45(@KinODE,tspan,Cini,[],KI);
disp(C);
TGc=C(:,1)';
DGc=C(:,2)';
MGc=C(:,3)';
MEc=C(:,4)';
GLc=C(:,5)';
MeOHc=C(:,6)';

TGcal=[TGc(t==30),TGc(t==45),TGc(t==60),TGc(t==120),TGc(t==300),TGc(t==360),TG
c(t==420),TGc(t==480),TGc(t==600)];

DGcal=[DGc(t==30),DGc(t==45),DGc(t==60),DGc(t==120),DGc(t==300),DGc(t==360),DG
c(t==420),DGc(t==480),DGc(t==600)];

MGcal=[MGc(t==30),MGc(t==45),MGc(t==60),MGc(t==120),MGc(t==300),MGc(t==360),MG
c(t==420),MGc(t==480),MGc(t==600)];

MEcal=[MEc(t==30),MEc(t==45),MEc(t==60),MEc(t==120),MEc(t==300),MEc(t==360),ME
c(t==420),MEc(t==480),MEc(t==600)];

GLcal=[GLc(t==30),GLc(t==45),GLc(t==60),GLc(t==120),GLc(t==300),GLc(t==360),GL
c(t==420),GLc(t==480),GLc(t==600)];

MeOHcal=[MeOHc(t==30),MeOHc(t==45),MeOHc(t==60),MeOHc(t==120),MeOHc(t==300),Me
OHc(t==360),MeOHc(t==420),MeOHc(t==480),MeOHc(t==600)];

Ccal = [TGcal; DGcal; MGcal; MEcal; GLcal; MeOHcal];
% ************ Define Error Parameter **************
CError = abs(Ccal-CExp);
n=1;
error = sum(sum(CError))/n;

% ************ Reaction Time; Unit - Minutes **************

texp=[30 45 60 120 300 360 420 480 600];

% ************ Concentrations; Unit - mol/L **************

TG=[0.5411 0.4195 0.2938 0.2467 0.0815 0.0414 0.0408 0.0365 0.0309];
DG=[0.1567 0.1737 0.1549 0.1349 0.09926 0.08163 0.06275 0.0600 0.05491];
MG=[0.0841 0.0822 0.1431 0.1595 0.1585 0.1636 0.1536 0.1318 0.1169];
ME=[0.06966 0.0898 0.3405 0.49277 1.09825 1.2561  1.3445 1.4311 1.5078];
GL=[0.0232 0.0300 0.1135 0.1643 0.3661 0.4187 0.4482 0.4770 0.5026];
MeOH=[5.555 5.351 5.2844 5.1322 4.5267 4.3688 4.2804 4.1938 4.1171];
```

% ************ Initial Guess for Rate Constants **************

```
KI = [0.0065  0.0014  0.0200  0.0009  0.0129  0.0028  0.2057  0.0849  0.0065  1.5130];
```

% ************ Regression **************

```
[k,fval] = fminsearch(@err,KI);
```

```
% ************ Optional Regression Command **************
%[k,fval] = fminunc(@err,KI);
% ************ Define Concentration and Step Time **************
CExp = [TG; DG; MG; ME; GL; MeOH];
Cini = CExp(:,1);
tspan = (15:15:600);
% ************ Solving Ordinary Differential Equations **************
[t,C]=ode45(@KinODE,tspan,Cini,[],k);
[t,C]=ode45(@KinODE,tspan,Cini,[],k);
TGc=C(:,1)';
DGc=C(:,2)';
MGc=C(:,3)';
MEc=C(:,4)';
GLc=C(:,5)';
MeOHc=C(:,6)';
TGcal=[TGc(t==30),TGc(t==45),TGc(t==60),TGc(t==120),TGc(t==300),TGc(t==360),TG
c(t==420),TGc(t==480),TGc(t==600)];

DGcal=[DGc(t==30),DGc(t==45),DGc(t==60),DGc(t==120),DGc(t==300),DGc(t==360),DG
c(t==420),DGc(t==480),DGc(t==600)];

MGcal=[MGc(t==30),MGc(t==45),MGc(t==60),MGc(t==120),MGc(t==300),MGc(t==360),MG
c(t==420),MGc(t==480),MGc(t==600)];

MEcal=[MEc(t==30),MEc(t==45),MEc(t==60),MEc(t==120),MEc(t==300),MEc(t==360),ME
c(t==420),MEc(t==480),MEc(t==600)];

GLcal=[GLc(t==30),GLc(t==45),GLc(t==60),GLc(t==120),GLc(t==300),GLc(t==360),GL
c(t==420),GLc(t==480),GLc(t==600)];

MeOHcal=[MeOHc(t==30),MeOHc(t==45),MeOHc(t==60),MeOHc(t==120),MeOHc(t==300),Me
OHc(t==360),MeOHc(t==420),MeOHc(t==480),MeOHc(t==600)];

Ccal = [TGcal; DGcal; MGcal; MEcal; GLcal; MeOHcal];

% ************ Define Error Parameter **************
```

% ************ Number of Data Point for each Species **************

```
N = 9;

% ************ Pearson Correlation Coefficient **************

for i = 1:10

r(i) = (N*sum(CExp(i,:).*Ccal(i,:))-sum(CExp(i,:))*sum(Ccal(i,:)))/sqrt((N*sum(CExp(i,:).^2)-
(sum(CExp(i,:)))^2)*(N*sum(Ccal(i,:).^2)-(sum(Ccal(i,:)))^2));

end


disp(C);

disp('Rate constants: k1, k2, k3, k4, k5, k6');

disp(k); disp('Pearson correlation coefficient: TG, DG, MG, ME, GL, MeOH');

disp(r);

plot(texp,CExp(1,:),'ro',texp,TGcal,'bo',t,C(:,1),'b-');


plot(texp,CExp(2,:),'ro',texp,DGcal,'bo',t,C(:,2),'b-');


plot(texp,CExp(3,:),'ro',texp,MGcal,'bo',t,C(:,3),'b-');


plot(texp,CExp(4,:),'ro',texp,MEcal,'bo',t,C(:,4),'b-');


plot(texp,CExp(6,:),'ro',texp,MeOHcal,'bo',t,C(:,6),'b-');

plot(texp,CExp(5,:),'ro',texp,GLcal,'bo',t,C(:,5),'b-');
```

APPENDIX F

Permissions to use manuscripts

1. Permission to use published manuscript "Physiochemical characterization and support interaction of alumina-supported heteropolyacid catalyst for biodiesel production".

License Number	4717850348614
License date	Nov 28, 2019
Licensed Content Publisher	John Wiley and Sons
Licensed Content Publication	Asia-Pacific Journal of Chemical Engineering
Licensed Content Title	Physiochemical characterization and support interaction of alumina-supported heteropolyacid catalyst for biodiesel production
Licensed Content Author	Ajay K. Dalai, Ankeeta Kurhade
Licensed Content Date	Sep 9, 2018
Licensed Content Volume	13
Licensed Content Issue	6
Licensed Content Pages	13
Type of Use	Dissertation/Thesis
Requestor type	Author of this Wiley article
Format	Print and electronic
Portion	Full article
Will you be translating?	No
Title of your thesis / dissertation	Synthesis and characterization of supported solid acid catalysts for conversion of green seed canola oil to biodiesel
Expected completion date	Nov 2019
Expected size (number of pages)	298
Requestor Location	University of Saskatchewan 1424, 14 street east Saskatoon, SK S7H 0A8 Canada Attn: Ankeeta Kurhade
Publisher Tax ID	EU826007151
Total	**0.00 CAD**

2. Permission to use published manuscript “Surface Investigation of Tungstophosphoric Acid Supported on Ordered Mesoporous Aluminosilicates for Biodiesel Synthesis. ACS Omega 3”.

ACS Chemistry for Life®

Dear Dr. Kurhade:

Thank you for contacting ACS Publications Support.

Your permission request is granted and there is no fee for this reuse. In your planned reuse, you must cite the ACS article as the source, add this direct link (https://pubs.acs.org/doi/abs/10.1021%2Facs.accounts.5b00438) and include a notice to readers that further permissions related to the material excerpted should be directed to the ACS.

I hope this information helped. Please let me know if I can be of further assistance.

Sincerely,

Kryxie J. Ramirez
ACS Customer Services & Information
https://help.acs.org

Incident Information:

Incident #: 2985492
Date Created: 2019-09-03T10:02:35
Priority: 3
Customer: Ankeeta Kurhade
Title: Permission to use article in my thesis
Description: Hello,
I am writing to seek the permission to use article in my thesis. Please find the link to the ACS article below

- https://pubs.acs.org/doi/10.1021/acsomega.8b01931
- I wish to use the entire article for my dissertation.
- The content will be reused in my thesis titled " Blodiesel Production using Supported Solid Acid Catalyst."

Thank you.
Regards
Ankeeta Kurhade

3. Permission to use published manuscript “Meso-Structured HPW-MAS-7 & HPW-MAS-9 Composite Catalysts for Biodiesel Synthesis from Unrefined Green Seed Canola Oil”.

Copyright Clearance Center RightsLink®

Home | Account Info | Help

ACS Publications
Most Trusted. Most Cited. Most Read.

Title:	Meso-Structured HPW-MAS-7 and HPW-MAS-9 Composite Catalysts for Biodiesel Synthesis from Unrefined Green Seed Canola Oil
Author:	Ankeeta Kurhade, Jianfeng Zhu, Ajay K. Dalai
Publication:	Industrial & Engineering Chemistry Research
Publisher:	American Chemical Society
Date:	Mar 1, 2019

Logged in as:
Ankeeta Kurhade
University of Saskatchewan
Account #:
3001511060
LOGOUT

PERMISSION/LICENSE IS GRANTED FOR YOUR ORDER AT NO CHARGE

This type of permission/license, instead of the standard Terms & Conditions, is sent to you because no fee is being charged for your order. Please note the following:

- Permission is granted for your request in both print and electronic formats, and translations.
- If figures and/or tables were requested, they may be adapted or used in part.
- Please print this page for your records and send a copy of it to your publisher/graduate school.
- Appropriate credit for the requested material should be given as follows: "Reprinted (adapted) with permission from (COMPLETE REFERENCE CITATION). Copyright (YEAR) American Chemical Society." Insert appropriate information in place of the capitalized words.
- One-time permission is granted only for the use specified in your request. No additional uses are granted (such as derivative works or other editions). For any other uses, please submit a new request.

4. Permission to use published manuscript “Kinetic Modeling, Mechanistic, and Thermodynamic Studies of HPW-MAS-9 Catalysed Transesterification Reaction for biodiesel synthesis”.

Copyright Clearance Center RightsLink®

Home | Account Info | Help

Title: Kinetic modeling, mechanistic, and thermodynamic studies of HPW-MAS-9 catalysed transesterification reaction for biodiesel synthesis

Author: Ankeeta Kurhade,Ajay K. Dalai

Publication: Fuel Processing Technology

Publisher: Elsevier

Date: 15 December 2019

Logged in as:
Ankeeta Kurhade
University of Saskatchewan
Account #:
3001511060

LOGOUT

APPENDIX G

Sample calculations for absence of external and internal mass transfer limitations

Sample calculation for effective diffusivity

Empirical correlations can be used to estimate diffusivity for dilute solutions of the diffusing solute

$$D_{12} = 7.4 \times 10^{-10} \frac{T(\phi M_2)^{0.5}}{\mu V_B^{0.6}} \quad \text{..... (G.1)}$$

Where:

Subscript 1 = triolein and 2 = methanol

D_{12} = Diffusivity of triolein in mixture cm^2/s ; T is the temperature in K ; M_2 is the molecular weight of methanol , μ is the viscosity of the solution in posies ; V_B- molar volume of the diffusing triolein cm^3/gmol estimated using Tyn and Calus method $V_B = 0.285 \times V_c^{1.048}$; ϕ – association factor (1.9 for methanol)

$$V_B = 0.285 \times V_c^{1.048} \quad \text{.....(G.2)}$$

$V_C = 3230\ cm^3/gmol$

Molar volume V_B = 1356 $cm^3/gmol$

$$D_{12} = 7.4 \times 10^{-10} \frac{453(1.9 \times 32)^{0.5}}{0.195(1356)^{0.6}} = 9.2\ \times 10^{-8}\ cm^2/s \quad \text{.....(G.3)}$$

Effective diffusivity

Assuming diffusion through a randomly oriented system of long cylindrical pores, tortuosity factor is 3 (Satterfield, 1970).

Typical value of 0.4 for pellet porosity was used [Fogler, 2006]

$$D_{12,eff} = D_{12} \times \frac{\theta}{\tau} = 1.2 \times 10^{-8}\ cm^2/\text{s} \quad \text{.....(G.4)}$$

Where:

θ is porosity of catalyst ; τ is tortuosity factor.

Effect of interparticle mass transfer resistance

Assuming an extreme case, the Sherwood number was set to a constant value of 2, which corresponds to the Sherwood number in a quiescent flow as per the analogy $sh = 2 + 0.6\,Re^{0.5}Pr^{0.33}$ $0 \leq Re < 776.06$ $0 \leq Pr < 250$

$sh = k_{Coil}\frac{D_p}{D_{12}}$…… (G.5)

Where:

k_{Coil} is defined as the mass transfer coefficient of oil; D_p is the particle diameter

$k_{coil} = \frac{2\times9.2\times10^{-12}}{1.18\times10^{-4}} = 1.57\times10^{-7} m/s$……(G.6)

The oil is a limiting reactant present in the excess methanol.

The reaction is considered to take place instantaneously at the external surface such that the concentration of oil in the liquid in contact with the solid surface is zero.

For dilute concentration of the oil, the flux is expressed as $W_{oil} = k_{coil}.\ C_{oil}$, mol/m^2.s where in C_{oil} is the bulk concentration of the oil.

$W_{oil} = 9.37\times10^{-5} > r'' = 1.39\times10^{-10}$ …… (G.7)

The mass transfer rate was found to be higher than the initial rate of reaction.

Weiz –Prater Criterion for internal diffusion

Catalysts – HPW-MAS-9 composite with 25wt % HPW loading at the optimized reaction conditions

$C_{WP} = r'(obs)\times\rho_c\times R^2/D_{12,eff}C_{AS}$……(G.8)

Where;

$r'(obs)$- observed rate of reaction, mol/g.s ; ρ_c - density of the catalyst pellet , bulk density $\rho_B = \rho_C(1-\emptyset)$; R^2- radius of the catalyst pellet ; C_{AS} - is the reactant concentration at the catalysts surface

No mass transfer limitations- $C_{Ab} = C_{As} = C_A$

$c_{wp} = 1.12 \times 10^{-7} \times 4.17 \times 10^{5} \times (8 \times 10^{-6})^2/(1.2 \times 10^{-12} \times 601) = 0.00414$ …(G.9)

C_{WP} value was found to be less than one and therefore the internal mass transfer effects could be neglected.

APPENDIX H

Sample calculation for BET surface area

Catalysts adsorption isotherms, surface area and pore size

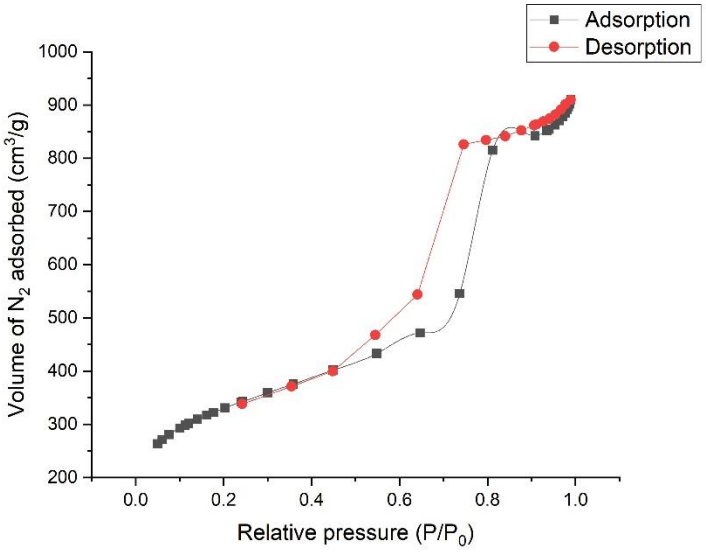

Figure H.1. Adsorption-desorption isotherm for HPW-MAS-7 2 400 °C

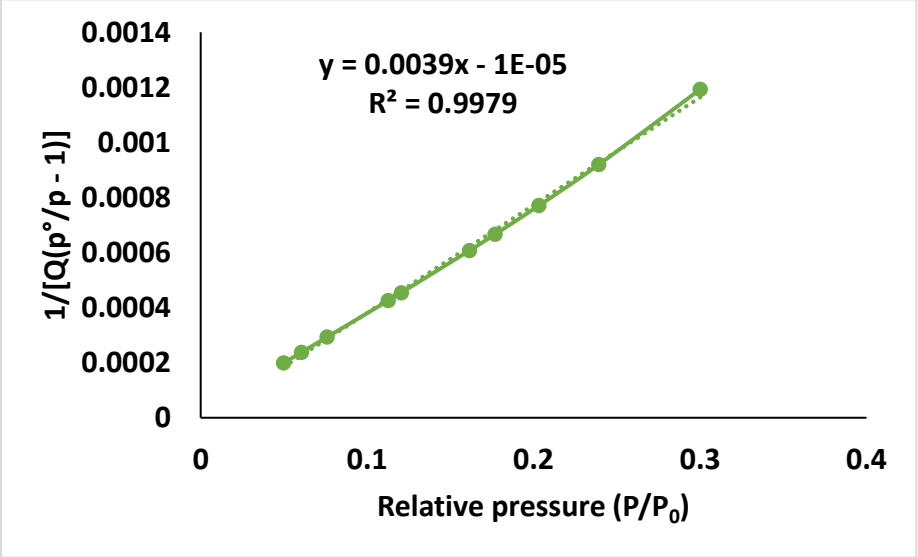

Figure H.2. BET plot for the calculations of the catalyst surface area (HPW-MAS-7 2 400°C).

BET surface area of the catalysts can be calculated from the BET plot using equation

$$S_{BET} = \frac{A_C \times N_A}{(22414\ cm^3 STP) \times (S+I)} \quad \text{.....(H.1)}$$

Where:

N_A : Avogadro's number, 6.022×10^{23} per mole

s_{BET}: Brunauer–Emmett–Teller surface area

S: slope of the BET plot (g/cm^3) ; I: intercept of the BET plot (g/cm^3)

A_C: cross-sectional area of N_2 $(0.162\ nm^2)$; M_W: molecular mass of N_2 $(g.mol^{-1})$

For example, BET surface area of HPW-MAS-7 2 400°C from Figure G.2 is

$$s_{BET} = \frac{0.162 \times (6.023 \times 10^{23})}{(22414\ cm^3\ STP) \times (10^{18}\ {}^{nm^2}/_{m^2}) \times (0.0039 - 0.00001)} \frac{m^2}{\text{g}} = 1119.4\ m^2/\text{g} \quad \text{.....(H.2)}$$

Micropore volume

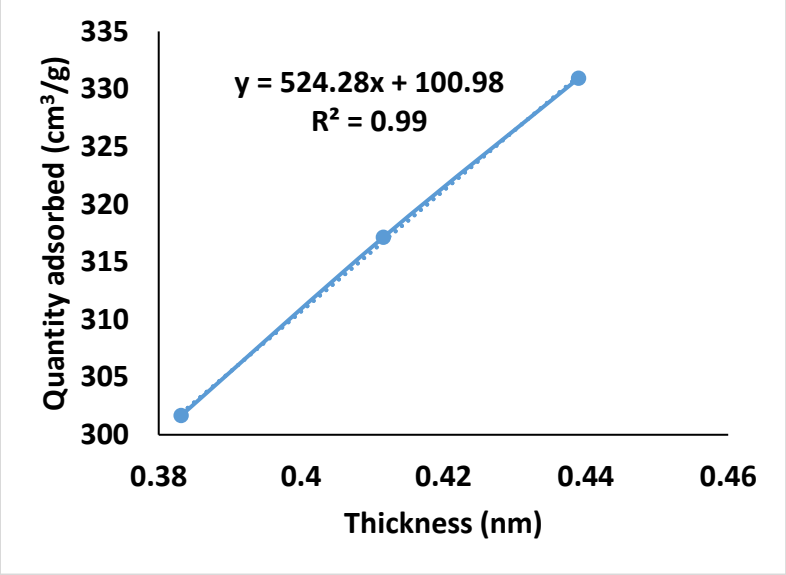

Figure H.3. t-plot for calculation of micropore volume.

$$V = I \times \frac{D\ cm^3 liquid}{cm^3\ STP} \quad \text{.....(H.3)}$$

Where

D = density conversion factor

$V = 100.98 \times 0.0015468 = 0.1561\ {}^{cm^3}/_{g}$……..(H.4)

Pore size

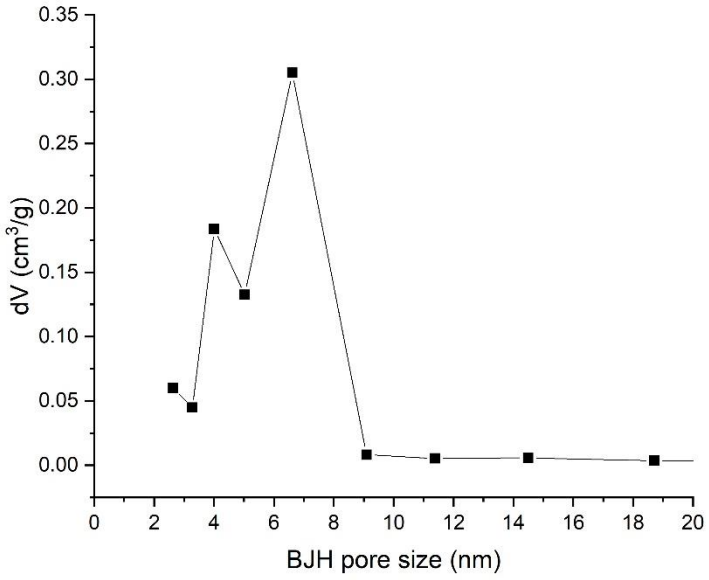

Figure H.4. BJH pore size distribution of catalysts HPW-MAS-7 2 400 °C.

The pore size can be calculated as follows

$r_p = r_k + t$……...(H.5)

$w_p = 2 \times (r_k + t)$……(H.6)

where :

w_p- pore width (diameter)

r_p - pore radius

r_k - hydraulic radius

t - thickness of adsorbed layer

$r_k = -\gamma v / RT ln \frac{p}{p_0}$……...(H.7)

where:

γ- surface tension

v- liquid volume

$$t(nm) = 3.54[-\frac{5}{ln^{p}/_{p_0}}]^{0.333} \quad \text{.....(H.8)}$$

APPENDIX I

Sample calculations for activity coefficients using UNIQUAC method

The UNIQUAC calculations were carried out as stated by Sadhukhan et al. (2014).

Triglyceride, diglyceride, monoglyceride, methanol, glycerol and methyl ester indicated by species i = 1-6, respectively

6 groups, CH_3, CH_2, CH, CH=CH, COO and OH, present are denoted by their secondary group number, p = 1, 2, 3, 6, 77 and 14, respectively (Sadhukhan et al., 2014).

Table I.1. $v_p^{(i)}$ matrix of group p in specie *i* (Sadhukhan et al., 2014).

		Specie					
		1	**2**	**3**	**4**	**5**	**6**
Group	**1**	3	2	1	1	0	2
	2	8	6	4	0	2	2
	3	1	1	1	0	1	0
	6	0	0	0	0	0	0
	77	3	2	1	0	0	1
	14	0	1	2	1	3	0
	sum	15	12	9	2	6	5

Table I.2. Group (p) van der Waals surface area S_P and volume Q_p (Sadhukhan et al., 2014).

	Group					
	1	**2**	**3**	**6**	**77**	**14**
Q_p	0.848	0.540	0.228	0.867	1.20	1.20
S_P	0.901	0.674	0.446	1.116	1.38	1.0

Table I.3. Mole fraction x_i of specie *i*.

		Specie					
		1	**2**	**3**	**4**	**5**	**6**
Conc.	x_i	0.00297	0.00581	0.0139	0.6223	0.0887	0.266

Table I.4. Binary energy of interaction between two groups (Sadhukhan et al., 2014).

	Group						
Group		**1**	**2**	**3**	**6**	**77**	**14**
	1	0	0	0	86	387.1	986.5
	2	0	0	0	86	387.1	986.5
	3	0	0	0	86	387.1	986.5
	6	-35.36	-35.36	-35.36	0	48.33	524.1
	77	529	529	529	1397	0	88.63
	14	156.4	156.4	156.4	457	190.3	0

s_i , $q_i and\ l_i$ are calculated using equations H.1-H.3.

$$\theta_i = \frac{x_i q_i}{\sum_{i\prime}^{nspc} x_i, q_i} \quad \Phi_i = \frac{x_i s_i}{\sum_{i\prime}^{nspc} x_i, s_i} \quad \forall i \in nspc \text{.....(I.1)}$$

$$q_i = \sum_p^g v_p^{(i)} Q_p \quad S_i = \sum_p^g v_p^{(i)} S_P \quad \forall i \in nspc \text{ .....(I.2)}$$

$$l_i = 5(s_i - q_i) - (s_i - 1) \quad \forall i \in nspc \text{.....(I.3)}$$

$$\ln \gamma_i^C = \ln \frac{\Phi_i}{x_i} + 5 q_i \ln \frac{\theta_i}{\Phi_i} + l_i - \frac{\Phi_i}{x_i} \sum_{i'}^{nspc} x_i, l_i \text{ , } \forall i\ nspc \text{.....(I.4)}$$

Table I.5. gives the molecular van der Waals area, volume and group parameters, s_i , $q_i and\ l_i$ for the different species using Equations I.5 (Sadhukhan et al., 2014).

	Specie					
	1	**2**	**3**	**4**	**5**	**6**
q_i	10.69	8.76	6.83	2.05	4.90	3.97
s_i	12.68	10.05	7.42	1.90	4.79	4.53
l_i	-1.71	-2.59	-3.47	-1.63	-4.35	-0.76

Table I.6. Volume or segment fraction Φ, area fraction θ_i and combinatorial activity coefficient γ_i^c for a given mole fraction $_i x$ of specie *i* in Table I.3.

Φ	0.012	0.019	0.0341	0.392	0.141	0.400
θ	0.010	0.017	0.0322	0.432	0.148	0.359
$\ln\gamma_i^c$	-1.154	-0.831	-0.505	-0.044	-0.100	0.0257

For a temperature of 453 K (180 °C), $\Psi_{m,n}$ group interaction parameters are generated using $a_{m,n}$ from Table I.4.

$$\Psi_{m,n} = \exp\left(-\frac{a_{m,n}}{T}\right) \quad \text{(I.5)}$$

$$\Psi_{1,6} = \exp\left(-\frac{86.02}{453}\right) = 0.826$$

$$\Psi_{1,6} = \exp\left(-\frac{-35.36}{453}\right) = 1.08$$

Table H.7. Secondary group interaction parameter Ψ estimated from $a_{m,n}$ in Table I.4 for the operating temperature of 453K.

	1	2	3	6	77	14
1	1	1	1	0.826	0.4254	0.056
2	1	1	1	0.826	0.425	0.056
3	1	1	1	0.826	0.425	0.056
6	1.109	1.1085	1.108	1	0.89	0.217
77	0.214	0.214	0.214	0.0171	1	0.772
14	0.634	0.634	0.634	0.264	0.5743	1

$$\ln \Gamma_p = Q_P \left\{1 - \ln\left(\sum_m^g \theta_m \Psi_{m,p}\right) - \sum_m^g \frac{\theta_m \Psi_{p,m}}{\sum_n^g \theta_n \Psi_{n,m}}\right\} \quad \forall m, n, p, \in g \text{.....(I.6)}$$

$$\theta_p = \frac{Q_p X_p}{\sum_p Q_P X_P} \text{ .....(I.7)}$$

$$X_p = \frac{\sum_i x_i}{\sum_i x_i \sum_p v_p^{(i)}} \text{.....(I.8)}$$

Table I.8. Group residual activity coefficient using Eqs H.6- H.8.

	Group					
	1	**2**	**3**	**6**	**77**	**14**
X_p	0.355	0.246	0.033	0	0.089	0.275
θ_m	0.342	0.152	0.0086	0	0.122	0.375
$\sum_m^g \frac{\theta_m \Psi_{p,m}}{\sum_n^g \theta_n \Psi_{n,m}}$	0.807	0.767	0.767	0.558	0.567	0.533
$\sum_m^g \theta_m \Psi_{m,p}$	0.860	0.921	0.921	0.940	0.9.00	1.311
$\ln \Gamma_p$	0.299	0.185	0.078	0.556	0.800	0.381

Table I.9. Mole fraction of p group amongst all groups within each specie.

		Specie					
		1	**2**	**3**	**4**	**5**	**6**
Group	**1**	0.2	0.167	0.111	0.5	0	0.4
	2	0.533	0.5	0.444	0.0	0.33	0.4
	3	0.067	0.0833	0.111	0.0	0.17	0.0
	6	0.0	0.00	0	0.0	0.0	0.0
	77	0.2	0.1667	0.11	0.0	0.0	0.2
	14	0.0	0.0833	0.22	0.5	0.5	0.0

Table I.10. Matrix of area fraction associated to a particular group p over the sum of all different groups in given specie.

		Specie					
		1	**2**	**3**	**4**	**5**	**6**
Group	**1**	0.238	0.193	0.124	0.414	0	0.426
	2	0.404	0.369	0.316	0	0.22	0.272
	3	0.021	0.026	0.034	0	0.046	0
	6	0	0	0	0	0	0
	77	0.336	0.274	0.175	0	0	0.302
	14	0	0.137	0.351	0.586	0.734	0

Table I.11. Matrix $\theta_m^{(i)}\Psi_{m,p}$ for specie i=1.

		Group P					
		1	**2**	**3**	**4**	**5**	**6**
Group M	**1**	0.237	0.237	0.237	0.257	0.074	0.168
	2	0.404	0.404	0.404	0.437	0.125	0.286
	3	0.021	0.0213	0.021	0.0230	0.00663	0.015
	6	0	0	0	0	0	0
	77	0.143	0.1432	0.1432	0.302	0.336	0.221
	14	0	0	0	0	0	0

Table I.12. $\sum_m^g \theta_m^{(i)}\Psi_{m,p}$

		Group					
		1	**2**	**3**	**6**	**77**	**14**
Species	**1**	0.708	0.708	0.708	0.447	0.424	0.235
	2	0.708	0.708	0.708	0.414	0.413	0.267
	3	0.708	0.708	0.708	0.440	0.404	0.407
	4	0.736	0.736	0.736	0.401	0.382	0.498
	5	0.701	0.701	0.701	0.411	0.374	0.532
	6	0.756	0.756	0.756	0.459	0.408	0.221

Table I.13. $\sum_m^g \frac{\theta_m^{(i)} \Psi_{m,p}}{\sum_n^g \theta_m^{(i)} \Psi_{m,p}}$

		Group					
		1	2	3	6	77	14
Species	1	1.27	1.27	1.27	1.73	1.08	1.18
	2	1.28	1.28	1.28	1.75	1.11	1.20
	3	1.29	1.29	1.29	1.76	1.03	1.21
	4	1.28	1.28	1.28	1.77	1.17	1.23
	5	1.33	1.33	1.33	1.83	1.19	1.26
	6	1.23	1.23	1.23	1.69	1.10	1.18

Table I.14. Group residual activity coefficient in a reference solution containing only molecules of type *i*,

		Group					
		1	**2**	**3**	**6**	**77**	**14**
Species	**1**	0.060	0.038	0.016	0.069	0.927	1.516
	2	0.052	0.033	0.014	0.117	0.933	1.345
	3	0.046	0.029	0.012	0.051	0.708	0.826
	4	0.026	0.016	0.007	0.127	0.960	0.575
	5	0.022	0.014	0.006	0.049	0.960	0.443
	6	0.043	0.028	0.012	0.077	0.960	1.615

Table I.15. $\ln \gamma_i^R$, residual activity coefficient and γ_i, activity coefficient for mole fraction of specie *i*.

	Specie					
	1	**2**	**3**	**4**	**5**	**6**
$\ln \gamma_i^C$	-1.155	-0.832	-0.506	-0.045	-0.100	0.026
$\ln \gamma_i^R$	1.471	0.173	0.113	0.079	0.230	0.634
γ_i	1.372	0.517	0.675	1.035	1.139	1.934